

THÈSE

Université Lille 1 : Sciences et Technologies
École Doctorale Sciences de la Matière, du Rayonnement
et de l'Environnement (EDSMRE)
Spécialité « Molécules et Matière Condensée »

Titre:

Deactivation Modeling of Cobalt Fischer-Tropsch Catalysts in Different Reactor Configurations

Par :

Majid SADEQZADEH

Date de soutenance : 6 Décembre 2012

À Unité de Catalyse et de Chimie du Solide, Lille, France, devant le jury composé de:

Daniel BIANCHI	Professeur, Université Claude-Bernard Lyon 1, France	Rapporteur
Enrico TRONCONI	Professeur, Politecnico di Milano, Italy	Rapporteur
Francis LUCK	Research Manager, Direction Scientifique, TOTAL S.A., France	Examineur
Guy B. MARIN	Professeur, Ghent University, Belgium	Examineur
Daniel SCHWEICH	Directeur de recherche CNRS (LGPC, CPE Lyon), France	Examineur
Daniel CURULLA FERRE	Project Manager, Energies Nouvelles, TOTAL S.A., France	Examineur
Pascal FONGARLAND	Professeur, Université Claude-Bernard Lyon 1, France	Directeur de thèse
Andrei KHODAKOV	Directeur de recherches CNRS (UCCS, EC Lille), France	Directeur de thèse

Acknowledgement

This work has been realized in the Unité de Catalyse et Chimie du Solide (UCCS), a joint laboratory between CNRS, Université Lille 1 : Sciences et Technologies, Ecole Centrale de Lille, and Ecole Nationale Supérieure de Chimie de Lille (ENSCL). I would like to thank Lionel Montagne the director of the UCCS to host me there.

The project was carried out in the framework of a research project between TOTAL S.A. and Ecole Centrale de Lille. I would therefore acknowledge the project funding by TOTAL and especially the useful help of Francis Luck and Daniel Currula Ferre. I would also thank Ecole Centrale de Lille for the work contract.

I would like to express my gratitude to Andrei Khodakov and Pascal Fongarland, my directors of thesis, for their advice during these years. I appreciate their constant availability and infinite patience.

I would thank Enrico Tronconi from Politecnico di Milano and Daniel Bianchi from Institut de recherches sur la catalyse et l'environnement de Lyon who accepted to report this work. I also thank Daniel Schweich, and Guy B. Marin for their participation in the jury as examiners.

I would like to express my gratitude to all people who helped me in technical details of this work. I would thank Stephane Chambrey and Jingping Hong for their help in experimental tests, and Simon Piché for the slurry reactor data set. I also acknowledge Pascal Roussel, Christine Lancelot, Christophe Dujardin and Anne-Sophie Mamede for bringing me their expertise in XRD, STEM-EELS, IR, and XPS, respectively.

I would also thank all the laboratory members for their contribution to the warm atmosphere of the laboratory. I would thank the UCCS secretaries for their help in administrative works. I also thank the Fischer-Tropsch team members for their helpful discussions.

Finally I would like to finish this acknowledgement by expressing my deepest gratitude to my parents and my wife who have supported me during these years and I am sure I would not be able to defend this thesis if I did not have their patience, kindness, and understanding.

Abstract

Fischer-Tropsch (FT) synthesis produces ultra-clean liquid fuels from a wide range of feedstock including natural gas, coal, or biomass. Supported cobalt catalysts are the catalysts of choice for low temperature FT due to their high activity toward heavy paraffinic products. However catalyst deactivation remains a major challenge in FT synthesis; as it reduces the catalyst lifetime and leads to lower catalyst productivity.

Catalyst deactivation during low temperature FT synthesis can be attributed to certain mechanisms including sintering, active metal re-oxidation, metal-support interactions, and carbon deposition. Sintering is proposed in this thesis to be responsible for the initial deactivation whereas coking is suggested to be the main cause of long-term deactivation.

The dissertation therefore proposes some quantitative approaches to enhance our understanding about cobalt-based catalyst deactivation in low temperature FT synthesis. The final objective is to develop the mechanistic models which could predict the extent of catalyst deactivation with time in different operating conditions. In the first step, the change in the catalyst physico-chemical properties with time on stream is considered. A three-step sintering model is proposed which involves the effect of water acceleration through the formation of surface cobalt oxide layer. Such a surface oxidation is supported by the characterization tools as well as the thermodynamic studies. This mechanism allows correlating the crystallites growth with certain operating conditions especially the $\text{H}_2\text{O}/\text{H}_2$ molar ratio inside the reactor. We have also developed a mechanism for the active site poisoning by carbon deposition for the long-term deactivation. This mechanism helps to evaluate the change in the active sites coverage with time as well the Fischer-Tropsch reaction rates.

The two microscopic models are then integrated in the reactor models in order to correlate the change in the catalytic activity with the catalyst properties. We have developed the models dedicated to fixed bed and slurry reactors. The effect of operating conditions on the crystallite size, active sites fraction, and conversion is considered by the simulations. The models are then employed in the laboratory scale reactors to fit the experimental data and to optimize the deactivation constants.

Keywords: Fischer-Tropsch, catalyst, deactivation, nanoparticles, modeling

Résumé

La synthèse Fischer-Tropsch (FT) produit des carburants ultra-propres à partir de ressources fossiles et renouvelables comme le gaz naturel, le charbon et la biomasse. Les catalyseurs supportés à base de cobalt sont souvent choisis pour la synthèse FT à basse température en raison de leur haute sélectivité en paraffines. Ils présentent en revanche l'inconvénient d'une désactivation qui limite leur durée de vie, ainsi que leur productivité.

La désactivation du catalyseur lors de la synthèse Fischer-Tropsch à basse température peut être liée à différents phénomènes, par exemple, au frittage, à l'oxydation du métal actif, à l'interaction entre le métal et le support et au dépôt de carbone... Il a été démontré que le frittage pourrait être la source principale de la désactivation initiale, qui se poursuit à long terme avec le phénomène de cokage.

Cette thèse propose ainsi des outils quantitatifs pour améliorer la compréhension des phénomènes de désactivation des catalyseurs FT à base de cobalt. Le but est de développer des modèles mécanistiques capables de prédire l'évolution d'activité catalytique dans le temps. Un modèle de frittage à trois étapes est développé ; il inclut l'effet accélérateur de l'eau grâce à la formation d'une couche d'oxyde de cobalt à la surface des particules métalliques. L'analyse d'oxydation à la surface est appuyée par des méthodes de caractérisation de catalyseurs, ainsi que par des études thermodynamiques. Le mécanisme de frittage nous permet de lier l'agglomération des particules de cobalt à des conditions opératoires, notamment à des rapports molaires de H_2O/H_2 dans le milieu réactionnel. Nous avons aussi développé un mécanisme de désactivation à long-terme par dépôt de carbone. Ce mécanisme permet d'évaluer le changement de la concentration des sites actifs avec le temps, ainsi que les vitesses de réaction.

Ces deux phénomènes microscopiques (frittage et cokage) sont ensuite intégrés dans les modèles des réacteurs pour coupler les propriétés des catalyseurs et l'activité catalytique. L'effet des conditions opératoires sur la taille des cristallites, la concentration des sites actifs et la conversion est considéré par simulation. Les modèles sont ensuite confrontés aux résultats expérimentaux obtenus dans les réacteurs à lit fixe et slurry.

Mots clés: Fischer-Tropsch, catalyseur, désactivation, nanoparticules, modélisation

List of Symbols

Latin letters

a	catalyst activity (dimensionless)
a	absolute error tolerance (dimensionless)
a	surface area of cobalt crystallite (m^2)
A	surface area per mole of surface atoms (m^2/mol)
A_i	peak area detected by the TCD for component i (dimensionless)
$A_{m,\text{support}}$	specific surface area for the catalyst support (m^2/kg)
C_i	gas concentration of component i in the gas or liquid mixture (mol/m^3)
C_k	coke concentration on the catalyst surface ($\text{mol}_{\text{coke}}/\text{kg}_{\text{cat}}$)
C_n	symbol for paraffinic hydrocarbon component $\text{C}_n\text{H}_{2n+2}$
const.	proportional time-independent constant to fulfil the equality (unit depends on the equation in which it is inserted)
C_t	total concentration of the catalyst active sites (mol/m^3)
d	deactivation order (dimensionless)
d	dead fraction in RTD model (dimensionless)
\bar{d}	number-average Co crystallite diameter (nm)
\bar{D}	metal dispersion of catalyst sample (dimensionless)
d_{Co}	average cobalt crystallite diameter (nm)
d_{CoO}	average CoO crystallite diameter (nm)
d_i	cobalt crystallite diameter (nm)
D_i	diffusion coefficient for Co particle with diameter d_i within alumina support (m^2/s)
D_{ij}	relative diffusion coefficient for Co particles of diameters d_i and d_j within alumina support (m^2/s)
d_p	catalyst pellet diameter (μm)
\bar{d}_s	surface-average cobalt crystallite diameter (nm)
D_s	diffusion coefficient for metal atoms on the cobalt particle surface (m^2/s)
D_s^{CoO}	diffusion coefficient for CoO molecules on the cobalt particle surface (m^2/s)
d_t	tube diameter (m)
e	mathematical constant (2.718)
E_i	activation energy for the kinetic coefficient i (kJ/mol)
$E(t)$	residence-time distribution function at time t (dimensionless)
F_i	molar flow rate of component i (mol/hr)
$F(t)$	Cumulative residence time distribution function at instance t (dimensionless)
$f_{\text{LN}}(d_j)$	fractional number of particles in the logarithmic size interval $d\ln(d_j)$ based on LNDF (dimensionless)
G	molar flow rate of gas phase (mol/s)
G_i	Gibbs free energy of component i (J/mol)
H_2/CO	hydrogen to carbon monoxide molar ratio in the syngas (mol/mol)
ID	reactor internal diameter (mm)
k_a (k'_a , k''_a), \bar{k}_a , k_b , k_d , k_e	kinetic parameters (unit depends on the kinetic law in which they are utilized)
k_i	vapour-liquid coefficient of component i (dimensionless)
k_s	sintering constant used in SPLE, GPLe, and proposed mechanism (unit depends on each respective equation)

K_{CO}	CO adsorption equilibrium constant (m^3/mol)
K_{CoO}	reaction equilibrium constant for surface CoO formation (dimensionless)
K_1, K'_1, K_2	deactivation constants in Qin model (unit depends on the constant type)
k_d, k_r	deactivation and regeneration constants in Bremaud and Lida models ($m^3/mol.s$)
L	molar flow rate of liquid phase (mol/s)
L	reactor (catalytic bed) volume (mm)
m	sintering order used in the GPLE (dimensionless)
m_{Co}	cobalt mass in the catalyst sample (kg)
$\%mol_i$	molar percentage of component i inside the calibration cylinder (dimensionless)
n	number of carbon atoms in the FT produced hydrocarbon C_nH_{2n+2}
n	sintering order used in the SPLE and Lida model (dimensionless)
n	number of CSTRs in RTD models (dimensionless)
N	total number of Co crystallites in the catalyst sample (dimensionless)
N	mole number of tracer material injected to the RTD setup (mol)
$N/A_{support}$	total number of Co crystallites per square meter of support (m^{-2})
N_{AV}	Avogadro's number (6.022×10^{23} atoms/mol)
n_d	the number of differential variables in the problem (dimensionless)
NF	normalization factor (g_{Co}^{-1})
n_i^G	the individual gas-phase mole number of component i
n_i^L	the individual liquid-phase mole number of component i
P	pressure (bar)
r	Co-Co interatomic distance, 0.125 nm
r	relative error tolerance
R	gas constant, 8.314 J/K/mol
r_d	catalyst deactivation rate (s^{-1})
RF_i	response factor of component i for the GC-analysis (dimensionless)
r_i	production or consumption rate for component i in the FT reaction (mol/kg _{cat} .s)
$r_{k,0}$	initial coking rate (mol _{coke} /kg _{cat} .s)
r_P	chain propagation rate the FT reaction (mol/kg _{cat} .s)
r_p	FT reaction rate (mol/m ³ _{cat} .s)
r_T	chain termination rate the FT reaction (mol/kg _{cat} .s)
Re	fluid Reynolds number (dimensionless)
S	metal surface area of catalyst sample ($m^2/m^2_{support}$)
S_{SV}	entropy (J/K)
t	time (s)
t_{min}	time when the first signal of tracer is detected in the RTD output (min)
\bar{t}	mean residence time calculated from RTD analysis (min)
T	temperature (K)
T_A	adiabatic temperature (K)
T_p	the reactor wall temperature (K)
u	fluid velocity in the z-direction (m/s)
U	global heat exchange coefficient (W/m ² K)
V	volume (mL)
w_n	mass fraction of FT product with n carbon atoms (dimensionless)
x	number of surface atoms deactivated/ total number of surface atoms
x_i	molar fraction of component i in the liquid phase (dimensionless)
x_i	current value the i th differential variable (dimensionless)
X_{Co}	cobalt content in the catalyst sample (wt%)
X_{CO}	CO conversion (mol %)
y_i	molar fraction of component i in the gas phase (dimensionless)
z	axial position inside the reactor (m)

Greek letters

α	ASF probability factor (dimensionless)
β	coking deactivation constant (mol/kg _{cat} .s)
γ	specific surface energy (J/m ²)
Γ	total surface energy (J)
$\Delta(\bar{d})$	increase in the particles number-average diameter after one collision (nm)
$\Delta E_{surface}$	normalized surface energy change (J/mol)
ΔG_{rxn}	Gibbs free energy of reaction (J/mol)
ΔH	heat of adsorption for CO (kJ/mol)
ΔH_R	reaction enthalpy (J/mol)
ε	bed void fraction (dimensionless)
ε	system phase shift in Wolf and Resnick model (dimensionless)
ε_i	solver's estimate for the local error in the <i>i</i> th differential variable
η	effectiveness factor of the catalyst particle (dimensionless)
η	coefficient of exponent in Wolf and Resnick model (dimensionless)
θ	normalized time (dimensionless)
θ_{CoO}	CoO surface coverage on cobalt crystallites (dimensionless)
λ_{er}^{sf}	effective radial thermal conductivity (W/m.K)
μ	fluid dynamic viscosity (Pa.s)
μ_i	Chemical potential of component <i>I</i> (J/mol)
v	effluent volumetric flow rate (m ³ /s)
π	mathematical constant (3.14)
ρ	fluid mixture density (kg/m ³)
ρ_{cat}	bulk density of catalyst pellet (kg _{cat} /m ³)
ρ_{Co}	bulk density of metallic cobalt (kg/m ³)
σ	standard deviation of the lognormal distribution (dimensionless)
σ	variance of the residence time distribution function (min)
τ	theoretical or ideal residence time (min)
Φ	total number of particles collisions per second (s ⁻¹)
Φ_i	collision rate for a crystallite having a diameter <i>d_i</i> with all other particles (s ⁻¹)

Subscripts

<i>0</i>	initial state (at time <i>t</i> = 0)
<i>cat</i>	catalyst bed
<i>eq</i>	final steady state (at time <i>t</i> = ∞)

Table of Contents

ACKNOWLEDGEMENT.....	III
ABSTRACT.....	V
RÉSUMÉ.....	VII
LIST OF SYMBOLS.....	IX
TABLE OF CONTENTS.....	XIII
CHAPTER 1: LITERATURE REVIEW.....	1
1.1. Fischer Tropsch synthesis: The state of art.....	2
1.1.1. Thermodynamic aspects of Fischer-Tropsch synthesis.....	4
1.1.2. Kinetic aspects of Fischer-Tropsch synthesis.....	6
1.1.2.1. Kinetics and mechanisms for the CO+H ₂ reaction.....	7
1.1.2.1.1. Alkyl mechanism.....	8
1.1.3. Typical FT catalysts.....	9
1.1.4. Typical FT reactors.....	11
1.1.4.1. HTFT reactors.....	11
1.1.4.2. LTFT reactors.....	13
1.2. Causes of deactivation during Fischer Tropsch synthesis.....	14
1.2.1. Catalyst poisoning.....	15
1.2.2. Metallic re-oxidation.....	17
1.2.3. Sintering.....	31
1.2.3.1. Sintering of active metal.....	31
1.2.3.2. Support sintering.....	39
1.2.4. Carbon compounds.....	39
1.2.4.1. Bulk carbide formation.....	41
1.2.4.2. Carbon fouling.....	43
1.2.4.3. Carbon induced surface reconstruction.....	45
1.2.5. Metal-support solid-state interactions.....	46
1.3. Modeling of deactivation phenomena.....	47
1.3.1. Microscopic models.....	47
1.3.2. Empirical Macroscopic models.....	53
1.4. Objectives and aims of thesis.....	55
1.5. References.....	58
CHAPTER 2: METHODOLOGY AND TOOLS.....	69
2.1. Introduction.....	70
2.2. Choice of experimental set-up.....	70
2.2.1. Used catalyst.....	71
2.2.2. Reactor configurations.....	72
2.2.2.1. Capillary fixed bed reactor.....	72
2.2.2.2. Milli-fixed bed reactor.....	73
2.2.2.3. Slurry reactor.....	76
2.2.3. Data collection and treatment (GC-analysis).....	78
2.2.3.1. Catalytic performance estimation.....	78
2.3. Residence time distribution (RTD).....	79
2.3.1. Experimental RTD measurements in milli-fixed bed set-up.....	82

2.3.2. Proposition of a global hydrodynamic model based on the RTD analysis to improve the deactivation simulation.....	87
2.4. Modeling of experimental reactors.....	91
2.4.1. Choice of kinetic equation.....	91
2.4.2. Fixed bed reactor (FBR) model.....	95
2.4.2.1. Fixed bed reactor (FBR) model with condensers.....	96
2.4.3. Continuous stirred tank reactor (CSTR) model.....	97
2.4.3.1. Continuous stirred tank reactor (CSTR) model with condensers.....	99
2.5. Choice of numerical approaches.....	100
2.6. Conclusion.....	101
2.7. References.....	103
CHAPTER 3: DEVELOPMENT OF MICROSCOPIC DEACTIVATION MODELS.....	105
3.1. Introduction.....	106
3.2. Development of initial deactivation model (sintering).....	107
3.2.1. Study of cobalt particles oxidation during Fischer-Tropsch synthesis.....	107
3.2.1.1. Introduction.....	107
3.2.1.2. Catalyst characterizations.....	108
3.2.1.2.1. X-ray diffraction.....	109
3.2.1.2.2. X-ray photoelectron spectroscopy.....	110
3.2.1.2.3. STEM-EELS.....	111
3.2.1.3. Thermodynamic oxidation models.....	112
3.2.1.3.1. Bulk oxidation (van Steen) model.....	112
3.2.1.3.2. Surface oxidation: our conceptual model.....	114
3.2.1.3.2.1. Temperature effect.....	117
3.2.1.3.3. Thermodynamics model limitations.....	119
3.2.2. Intermediate conclusions.....	120
3.2.3. Existing model for catalyst sintering (Sehested Model).....	121
3.2.4. Proposed mechanism and model: water-accelerated sintering.....	124
3.2.4.1. Cobalt sintering: Atomic or particle migration?.....	124
3.2.4.1.1. Further information from the particle size distribution curves.....	126
3.2.4.2. Proposed sintering mechanism.....	128
3.3. Development of long-term deactivation model (coking).....	132
3.3.1. Existing models for long-term catalyst deactivation.....	133
3.3.2. Proposed mechanism and model: active site carbon poisoning.....	133
3.4. Concluding remarks.....	135
3.5. References.....	137
CHAPTER 4: DEACTIVATION IN FIXED BED REACTORS.....	141
4.1. Introduction.....	142
4.2. Effect of particle growth on catalytic activity.....	142
4.3. Effect of operating conditions on fixed bed reactor model.....	144
4.3.1. Syngas ratio.....	145
4.3.2. Syngas dilution.....	146
4.3.3. Co-fed water.....	147
4.4. Validation of existing experimental runs.....	148
4.4.1. Capillary fixed bed reactor model.....	148
4.4.1.1. Effect of further microscopic catalyst properties on the catalytic activity.....	150
4.4.2. Milli-fixed bed reactor model with hot and cold condensers.....	152
4.4.2.1. Milli-fixed bed reactor tests under different syngas ratios.....	154
4.4.2.2. Milli-fixed bed reactor tests at higher temperatures.....	158

4.4.2.2.1. Milli-fixed bed reactor model with coking.....	160
4.5. Concluding remarks.....	162
4.6. References.....	164
CHAPTER 5: DEACTIVATION IN SLURRY REACTORS.....	165
5.1. Introduction.....	166
5.2. Effect of operating conditions on slurry reactor model.....	167
5.2.1. Syngas ratio.....	169
5.2.2. Co-fed water.....	173
5.3. Intermediate conclusions.....	175
5.4. Validation of existing experimental runs.....	176
5.4.1. Continuous stirred tank (slurry) reactor.....	176
5.4.1.1. Slurry reactor tests under different syngas ratios.....	178
5.4.1.2. Slurry reactor tests at different pressures.....	181
5.4.1.3. Slurry reactor model with sintering and coking.....	183
5.5. Concluding remarks.....	184
5.6. References.....	186
CHAPTER 6: CONCLUSION AND PERSPECTIVES.....	187
6.1. Introduction.....	188
6.2. General conclusions.....	189
6.1.1. Effect of operating conditions on catalyst deactivation.....	190
6.1.2. Effect of reactor configuration on deactivation profile.....	191
6.3. Perspectives.....	192
APPENDIX A: LIST OF CATALYTIC TESTS.....	195
APPENDIX B: HISTOGRAM ANALYSIS.....	199
APPENDIX C: REACTOR GEOMETRY AND CATALYST DEACTIVATION.....	201
C.1. Effect of reacting phase within the slurry reactor.....	202
C.1.1. Constant GHSV and reactor volume.....	203
C.1.2. Constant GHSV and gas volume.....	204
C.1.3. Constant gas volume and conversion.....	205
C.2. Effect of reactor hydrodynamics.....	207
C.2.1. Constant initial conversion.....	207
C.2.2. Constant initial conversion, reactor volume, and catalyst loading.....	210
C.2.3. Normal operating conditions.....	211
C.3. References.....	211

CHAPTER

1

LITERATURE REVIEW

1.1. Fischer Tropsch synthesis: The state of art

Currently more than 80% of energy used in transportation sector comes from refined oil used either in terms of gasoline or diesel [1], [2]. Finding alternatives to fossil fuels is one of the major challenges of our society. There is many ways available to produce fuels with different industrial maturity and potential drawbacks.

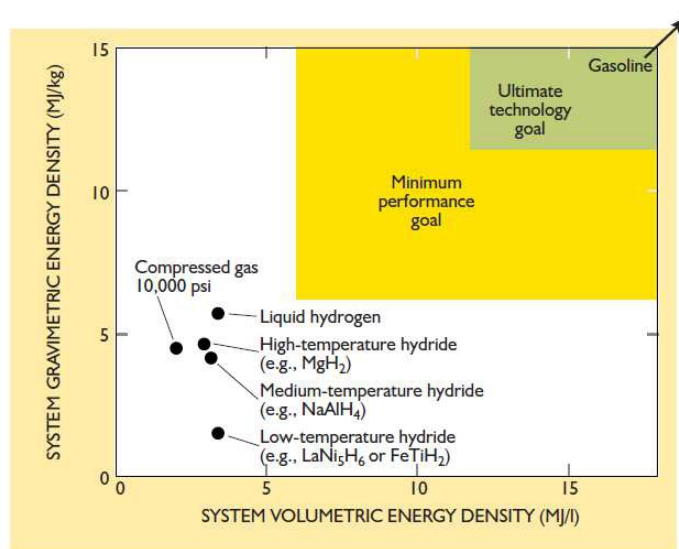


Figure 1.1 Comparison of hydrogen and gasoline energy densities – Adapted from reference [3]

Indeed high demand for energy production, as well as increased oil prices, leads to the valorization of alternative energy sources such as natural gas, coal, or biomass. As a matter of fact these valorization techniques could also utilize the natural gas resources. As of 2011 about 150 billion cubic meter of associated natural gas (equivalent to 25% of US gas consumption) is flared annually due to the problems of distance (as in offshore gas platforms) [4]. The natural gas liquefaction leading to LNG processes is generally limited due to their high costs [5].

There are generally two types of processes for valorization of alternative energy sources: (a) direct processes, and (b) indirect ones. Direct processes are mainly used for the natural gas feedstock, whereas the indirect processes could be used in the case of all alternative energy sources (natural gas, coal, or biomass). As methane molecule is not so reactive due to high bond carbon-hydrogen bond energy ($E_{C-H}=431$ kJ), direct processes frequently use reactions with other components (steam, oxygen, carbon dioxide, sulfuric components, ammonia, etc.) in order to produce a wide range of commercial products such a ethylene, methanol, etc.

An important family of indirect processes is CO hydrogenation. Since the first discovery of CO hydrogenation reaction by Sabatier and Senderens in 1902 [6], the process has been subject to several investigations [7] followed by its industrialization by the two German scientists Fischer and Tropsch in 1936 [8], [9], [10], [11].

Indirect processes or XTL (X-To-Liquids, with X= natural gas G, coal C, or biomass B) involve intermediate step of synthesis gas (syngas) production. The syngas, which is a mixture of CO and H₂, could be used to produce a wide range of end products (Fig. 1.2).

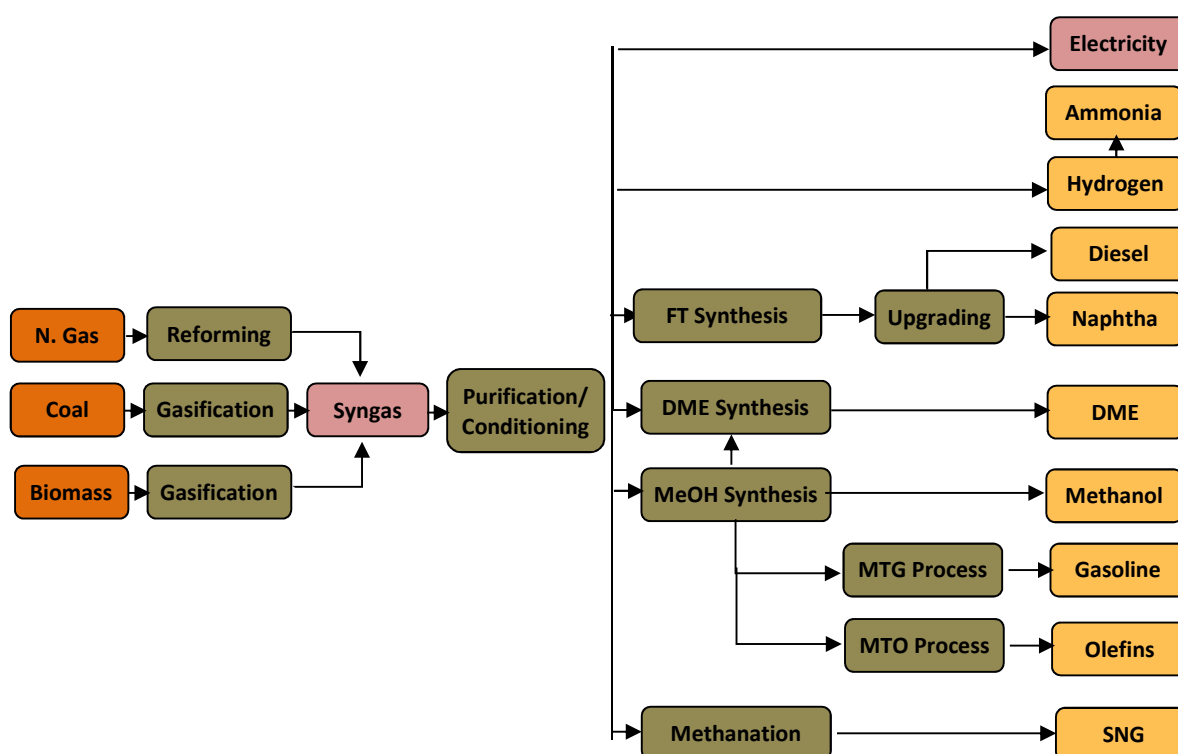


Figure 1.2 General Scheme of indirect XTL processes

Although several products could be made using syngas, the emphasis here is made on the Fischer-Tropsch synthesis leading to liquid-phase fuels including naphtha and diesel after hydrocracking of long-chain hydrocarbons. The Fischer-Tropsch synthesis is a set of catalytically-activated parallel reactions producing a wide range of paraffins, olefins, and oxygenated components as follows [12]:

Table 1.1 Principle reactions of Fischer-Tropsch synthesis [13]

Paraffin Formation	$(2n+1) \text{H}_2 + n \text{CO} \rightarrow \text{C}_n\text{H}_{2n+2} + n \text{H}_2\text{O}$ $(n+1) \text{H}_2 + 2n \text{CO} \rightarrow \text{C}_n\text{H}_{2n+2} + n \text{CO}_2$
Olefins Formation	$2n \text{H}_2 + n \text{CO} \rightarrow \text{C}_n\text{H}_{2n} + n \text{H}_2\text{O}$ $n \text{H}_2 + 2n \text{CO} \rightarrow \text{C}_n\text{H}_{2n} + n \text{CO}_2$
Alcohols Formation	$2n \text{H}_2 + n \text{CO} \rightarrow \text{C}_n\text{H}_{2n+1}\text{OH} + n \text{H}_2\text{O}$ $(n+1) \text{H}_2 + (2n-1) \text{CO} \rightarrow \text{C}_n\text{H}_{2n+1}\text{OH} + (n-1) \text{CO}_2$

1.1.1. Thermodynamic aspects of Fischer-Tropsch synthesis

The thermodynamic aspects of the Fischer-Tropsch synthesis are the key to understand how the reaction takes place on the catalyst surface. Although the FT mechanism is still the subject of several debates, it is generally accepted that it could be considered as a polymerization reaction of carbon-containing species (e.g. CH, CH₂, and CH₃) which lead to the formation of long-chain hydrocarbons and therefore lower energy levels (as the reaction is highly exothermic). Kölbel et al. [14] have proposed a polymerization mechanism based on $-(CH_2)-$ as in Table 1.2.

Table 1.2 FTS based on $-(CH_2)-$ mechanism and associated heats of reaction

(1)	$CO + H_2 \rightarrow -(CH_2)- + H_2O$	$\Delta H_R^\circ (500\text{ K}) = -165\text{ kJ/mol}$
(2)	$2\text{ CO} + H_2 \rightarrow -(CH_2)- + CO_2$	$\Delta H_R^\circ (500\text{ K}) = -205\text{ kJ/mol}$
(3)	$3\text{ CO} + H_2O \rightarrow -(CH_2)- + 2\text{ CO}_2$	$\Delta H_R^\circ (500\text{ K}) = -245\text{ kJ/mol}$
(4)	$CO_2 + 3\text{ H}_2 \rightarrow -(CH_2)- + 2\text{ H}_2O$	$\Delta H_R^\circ (500\text{ K}) = -125\text{ kJ/mol}$

However the reaction byproducts (CO₂ and H₂O) and reactants (H₂ and CO) could also react to form undesirable products based on thermodynamic reasons (Table 1.3) which could have negative effect on the selectivity of desired hydrocarbon products as they modify the H₂/CO ratio. The change in the syngas ratio could also lead to catalyst deactivation such as coke formation (Boudouard reaction) which is more probable in the case of hydrogen-deficient syngas. However at normal FT working conditions the production of undesirable products is limited. The Water-Gas-Shift (WGS) reaction occurs for example principally in Fe-catalyzed FTS and it is negligible in the case of Co-based FT catalysts. It could be also an option to produce in-situ hydrogen and increase the H₂/CO ratio.

Table 1.3 Undesirable reactions for Fischer-Tropsch synthesis

Methane formation	$CO + 3\text{ H}_2 \rightarrow CH_4 + H_2O$	$\Delta H_R^\circ (500\text{ K}) = -242\text{ kJ/mol}$
	$2\text{ CO} + 2\text{ H}_2 \rightarrow CH_4 + CO_2$	$\Delta H_R^\circ (500\text{ K}) = -254\text{ kJ/mol}$
	$CO_2 + 4\text{ H}_2 \rightarrow CH_4 + 2\text{ H}_2O$	$\Delta H_R^\circ (500\text{ K}) = -175\text{ kJ/mol}$
Coke Formation	$2\text{ CO} \rightarrow C + CO_2$	$\Delta H_R^\circ (500\text{ K}) = -134\text{ kJ/mol}$
Water Gas Shift	$CO + H_2O \rightarrow H_2 + CO_2$	$\Delta H_R^\circ (500\text{ K}) = -39\text{ kJ/mol}$

As Tables 1.2-1.3 demonstrate, all the reaction sets are exothermic in the Fischer-Tropsch synthesis with an average reaction enthalpy of -150 kJ/mol (-35.9 kcal/mol) [15]. Consequently a good control of temperature is essential in different FT reactors in order to prevent the hot spots which could affect catalytic activity and promote methane formation. Fig. 1.3 shows the evolution of average FTS enthalpy as a function of chain growth probability α .

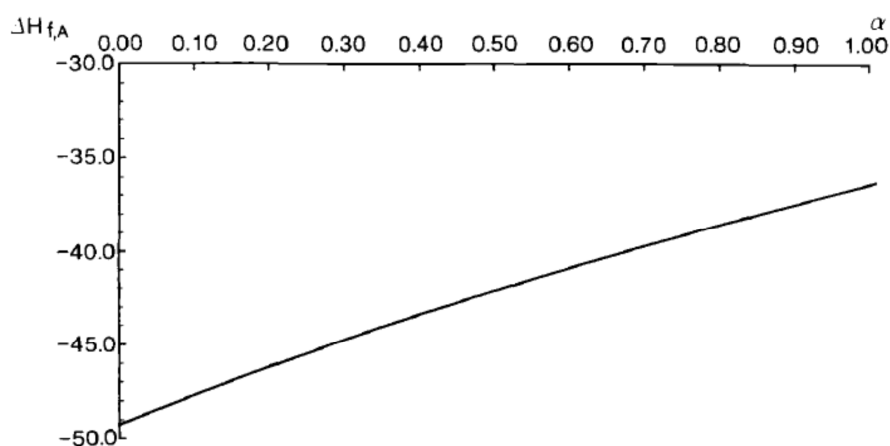


Figure 1.3 Variation of the enthalpy increment of Fischer-Tropsch synthesis (in kcal/mol) with the chain growth probability [15]

It should be noted that in the common temperature range used for Fischer-Tropsch synthesis (180-400 °C), the methane formation is always favorable from a thermodynamic point of view. In fact as shown in Fig. 1.4 at any given temperature in this range the formation probability of different species is in order: methane > paraffins > olefins > oxygenated compounds [16]. Furthermore although thermodynamics prefer methane formation than chain growth at higher temperatures, several other parameters affect the product distribution of Fischer-Tropsch synthesis notably the kinetics. For the case of cobalt catalysts for example, temperature increase leads to higher olefins and oxygenates proportion as well as lower paraffins fraction.

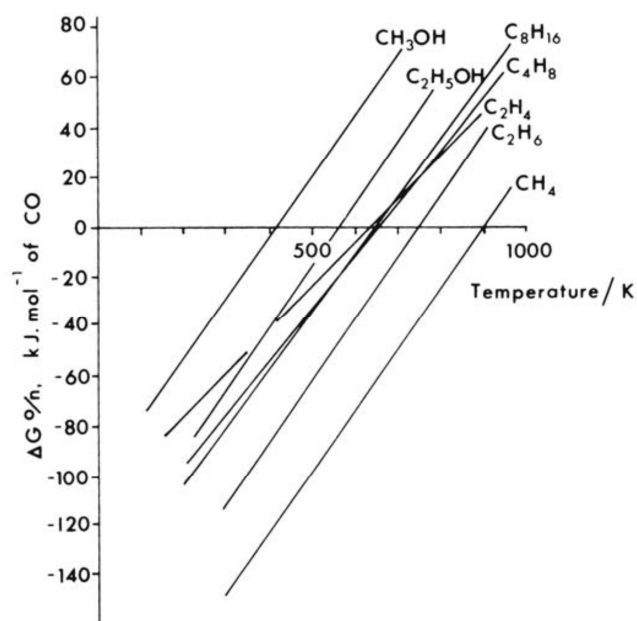


Figure 1.4 Standard free energies for the synthesis of some products from the CO+H₂ reaction [17]

1.1.2. Kinetic aspects of Fischer-Tropsch synthesis

The molar distribution of hydrocarbon products during Fischer-Tropsch synthesis was first investigated by Herington [18] and [19] in 1946 using a polymerization mechanism. Anderson et al. used the same principle in 1951 and the FTS product distribution has been since known as Anderson-Schulz-Flory (ASF) [20]. Based on the successive polymerization of monomers on the catalysts surface, ASF distribution assumes that the propagation and termination steps could affect only the terminal carbon atoms of the hydrocarbon chain. The chain growth probability α is then expressed in terms of chain propagation rate r_p and the chain termination rate r_T as:

$$\alpha = \frac{r_p}{r_p + r_T} \quad (1.1)$$

and the mass fraction w_n of each hydrocarbon components with n carbon atom is given by:

$$w_n = n\alpha^{n-1}(1-\alpha)^2 \quad (1.2)$$

Several authors have also used another form of Anderson-Schulz-Flory equation (Eq. 1.3) in order to provide a linear curve of $\log(w_n/n)$ as a function of n with a graph slope of $\log\alpha$.

$$\log\left(\frac{w_n}{n}\right) = n \log \alpha + \log\left(\frac{(1-\alpha)^2}{\alpha}\right) \quad (1.3)$$

However experimental deviations from ASF product distribution are frequently observed in the literature as shown in Fig. 1.5 [21]. These deviations include relatively high methane selectivity, a low ethane fraction, and an increase in chain growth probability with increase in carbon number. In addition the ASF model does not predict realistically formation of olefins and oxygenates.

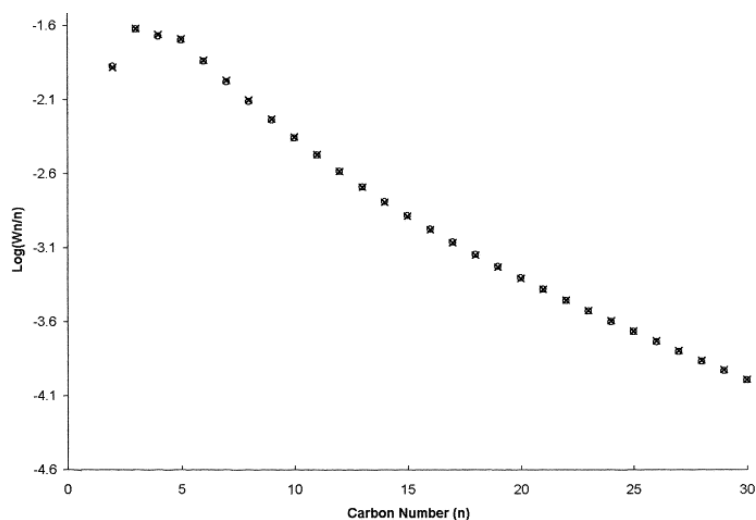


Figure 1.5 Typical experimental distribution plot of FTS products (◦) continuously changing growth factors from 0.60 to 0.90; (×) best fit two α 's ($\alpha_1=0.693$ 65%; $\alpha_2=0.866$, 35%) [21]

Therefore based on several experimental experiences, some researchers [22] and [23] have proposed that the product distribution is modified by olefin re-adsorption and other secondary reactions which result in positive C₁-C₄ product distribution deviation when compared to ASF model as well lower ethane production. Iglesia et al. [24] and [25] suggested that the longer are the olefins formed, the higher is the probability of re-adsorption and secondary reaction. The olefin re-adsorption leads to the formation of longer chains which are mainly paraffinic.

Puskas et al. [21] have shown that the chain growth probability is highly dependent on the operating conditions and it decreases once the H₂/CO ratio or temperature increase or once the syngas is diluted with an inert gas.

Finally, an experimental "trick" is still possible during kinetic study of the FTS leading to an apparent deviation due to some loss of hydrocarbons species by stripping of wax and diesel collector as mentioned in a very recent paper of Gao et al. (2012) [26].

1.1.2.1. Kinetics and mechanisms for the CO+H₂ reaction

The use of proper kinetics and mechanism for the Fischer-Tropsch synthesis has been debated in the literature [11]. The most commonly accepted kinetic expression for the two main catalyst groups are as follows:

- For Co catalysts [27]
$$-r_{CO} = \frac{k_a P_{H_2} P_{CO}}{(1 + k_b P_{CO})^2} \quad (1.4)$$

- For Fe catalysts [28]
$$-r_{CO} = \frac{k_a P_{H_2} P_{CO}}{P_{CO} + k_b P_{H_2 O}} \quad (1.5)$$

Although the use of these simple equations is generally accepted to calculate the FT reaction rate, the mechanism of the Fischer-Tropsch reaction still remains very controversial, partly due to the high complexity of reaction chemistry and the wide range of products obtained even at low CO conversion [29]. Since the first published mechanism by Fischer and Tropsch in 1926 [17], numerous researchers have tried to provide a reaction pathway which could represent the experimental data in a realistic way. Several excellent reviews are dealing with this subject [30], [17], [31], [32], [33], [34], [35].

The four main mechanistic approaches that received the most experimental support include alkyl, alkenyl, Enol (Hydroxycarbene), and CO insertion mechanisms. In general each mechanism includes several steps primarily chain initiation, chain growth, and chain termination. It should however be noted that although some mechanisms could represent the reaction in certain experimental conditions, it is generally assumed that several parallel reaction pathways may exist at the same time [30] and [17]. The alkyl mechanism is briefly described in this section as this is the mostly accepted mechanism based on experimental data.

1.1.2.1.1. Alkyl mechanism

The alkyl mechanism is currently the most widely accepted one for the formation of alkanes and alkenes during FT synthesis. Fig. 1.6 shows the three steps of alkyl mechanism.

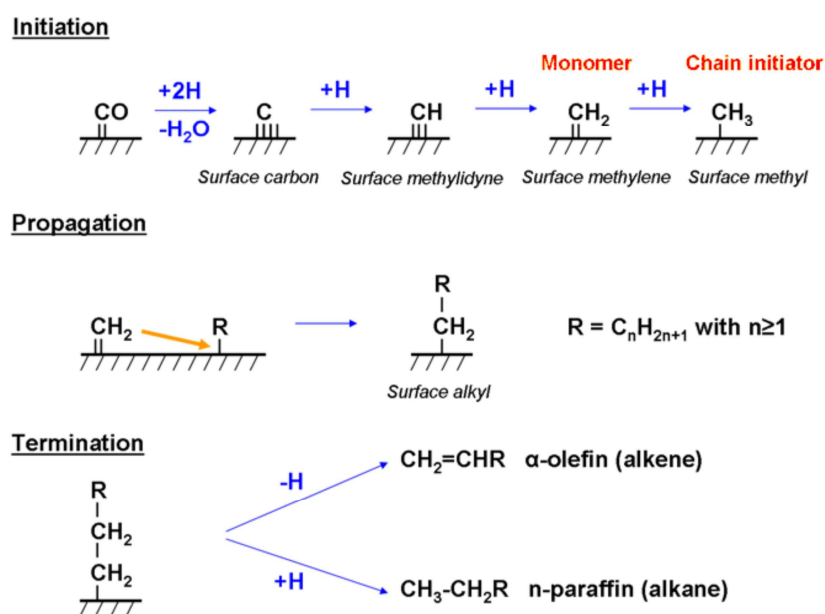


Figure 1.6 "Alkyl" mechanism for the FT reaction [36]

The initiation step starts with dissociative CO chemisorption which produces surface oxygen and surface carbon. Surface oxygen reaction with adsorbed hydrogen atoms produces

water molecules which desorb accordingly. Oxygen could also react with one CO molecule to produce CO₂ molecule which then desorbs, although the CO₂ production is negligible for Co catalysts. Surface carbon is also hydrogenated to produce in a consecutive reaction CH, CH₂ and CH₃ surface species. In this reaction scheme, the CH₂ surface species is considered as the monomer (responsible for chain lengthening) and the CH₃ surface species is the chain initiator.

Chain propagation occurs by successive addition of the CH₂ monomer to the metal-bonded growing chain. The chain could be terminated either by β-hydrogen elimination producing an α-olefin or by hydrogen addition producing a n-paraffin. However the β-H elimination is reversible and the olefin re-adsorption could lead to further chain growth. The alkyl mechanism could not explain the formation of branched hydrocarbon found in the experimental tests. In addition, it does not predict oxygenates formation (such as alcohols).

1.1.3. Typical FT catalysts

The Fischer-Tropsch synthesis is a heterogeneous catalysis process in which the catalyst properties could modify the process performance including activity and product selectivities. In general a FT catalyst mostly consists of small metallic crystallites or clusters dispersed throughout the particles of a porous refractory material [37] which is frequently called *the carrier* or *the support*. The catalyst support is mainly used to provide high surface area for the catalyst. Fig. 1.7 shows a typical metal “supported” catalyst which consists of cobalt nanoparticles (crystallites) supported over silica.

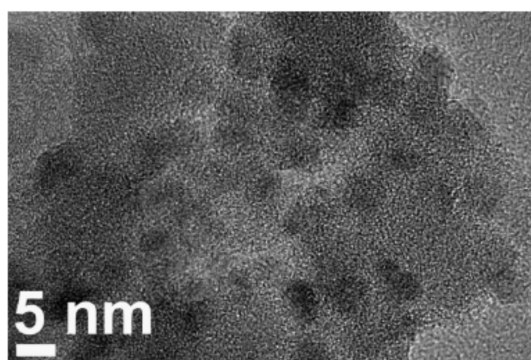


Figure 1.7 Transmission electron micrograph of Co nanoparticles supported over SiO₂ [38]

Cobalt, ruthenium, and iron are the three different transition metals typically suitable for the production of hydrocarbons using FTS as reported by several researchers [30], [39], [11], [40], [28], [31]. Although nickel could also be of interest in FTS, its high methanation property is not desirable for typical FT production. Moreover due to both high price and

limited availability of Ru, its use is not justified in commercial FT plants. Consequently cobalt and iron are used as the main metallic catalysts for a Fischer-Tropsch synthesis, whereas other metallic elements (such as Mn, Cu, Ru) could be used in small amounts to modify the catalytic properties of the main catalyst.

The element position in the periodic table seems to be crucial for the catalytic activity of metallic element for the $\text{CO} + \text{H}_2$ reaction. Indeed CO adsorption can be dissociative or associative on transition metals (Fig. 1.8). The division line is shifted to the right once the temperature is increased.

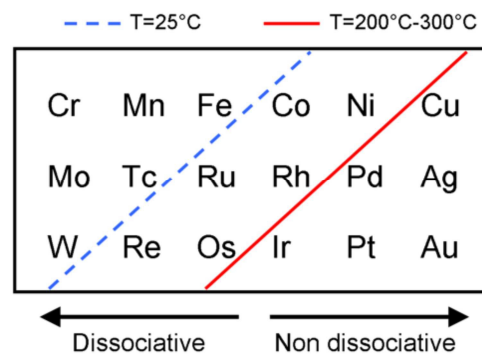


Figure 1.8 Borderline between metals on which CO adsorbs dissociatively and molecularly

On one hand, CO adsorbs dissociatively on Fe, Co and Ru at temperatures between 200°C and 300°C. On the other hand, high pressure catalytic tests have shown that the $\text{CO} + \text{H}_2$ reaction produces long chain hydrocarbons over these three metals. Accordingly, a link was established between the CO dissociation and the ability to synthesize products containing two or more carbon atoms (C_{2+} products). These metals are known as “chain lengthening” catalysts.

Table 1.4 gives a comparison between the cobalt and iron based catalysts for the Fischer-Tropsch synthesis.

Table 1.4 Comparison between Co and Fe catalysts for the FT reaction [36]

Parameter	Co	Fe
Type of FT process	LTFT*	LTFT and HTFT**
Products	Heavy paraffins	Heavy paraffins + Light olefins and Gasoline
Activity at low conversion LTFT	Comparable	Comparable
Productivity at high conversion LTFT	Higher	Lower
Maximal chain growth probability LTFT	0.94	0.95
Stability (Lifetime) LTFT	Higher	Lower
H ₂ /CO ratio	~ 2	0.5-2.5
Flexibility (T and P)	Less flexible	Flexible
WGS reaction	Not very significant	Significant
Maximal S content	< 0.1 ppm	< 0.2 ppm
Cost (relative basis)	250-1000	1

*LTFT: Low Temperature Fischer-Tropsch

**HTFT: High Temperature Fischer-Tropsch

1.1.4. Typical FT reactors

As mentioned in section 1.1.1 the reactor design is extremely important as the Fischer-Tropsch synthesis is highly exothermic, and the selected reactor should efficiently remove the heat of reaction from the catalysts particles. Otherwise the generation of local hot spot could lead to catalyst deactivation especially sintering and coking.

In order to overcome heat transfer issues, several special reactors are designed for FTS including circulating fluidized bed reactors (CFB), fixed fluidized bed reactors (FFB), multitubular fixed bed reactors and slurry phase reactors [30], [39], [41], [11], [28], [42]. The reactor selection is primarily related to the choice of temperature range used. For HTFT (300°C–350°C), only fluidized bed reactors are used (circulating or fixed bed) whereas for LTFT (200°C-240°C), only tubular and slurry reactors are being employed. The main difference is that in LTFT reactors there is no liquid product outside of catalysts particles, whereas the LTFT reactors produce liquid long chain waxes.

This section described the main reactor types used in both LTFT and HTFT processes and some industrial applications.

1.1.4.1. HTFT reactors

The two-phase (gas-solid) HTFT reactors are mainly designed to produce light alkenes and/or gasoline. The heat exchange shows high rates in these reactors due to high level of turbulence in fluidized beds and therefore the catalyst bed remains almost isothermal [36].

The circulating fluidized bed reactors (CFB), originally chosen by Sasol for the Sasolburg plant, give particularly high linear velocity to the inlet gas stream (Fig. 1.9). These

reactors were re-named Synthol reactors and were operated successfully for 30 years with a Fe catalyst at 340°C and 20 bar.

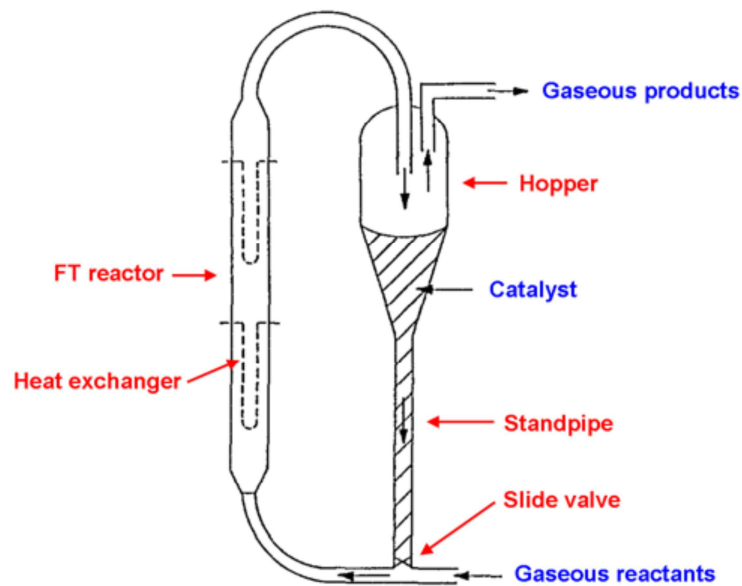


Figure 1.9 Circulating fluidized bed reactor (CFB) used by Sasol – Adapted from [43]

The CFB reactor contains two main sections i.e. the FT reactor part (with a lean phase) and the catalyst/effluents separation part (with a dense phase). The catalyst moves down in the standpipe with a controlled rate by the slide valve. It then is then carried to the reaction section by the inlet gas stream where it forms FT products. The products and catalysts particles are separated in the hopper by gravity force.

A new generation of CFB reactors was used in the Secunda Sasol plant (South Africa) and the Mossel Bay PetroSA plant (South Africa). However Secunda CFB reactors were later replaced by fixed fluidized bed reactors (FFBR), as they propose several advantages over CFB reactors including lower pressure drops, higher syngas conversions, and lower construction costs. Fig. 1.10 demonstrates a typical FFBR, commercialized by Sasol, which is then named Sasol Advanced Synthol reactor (SAS).

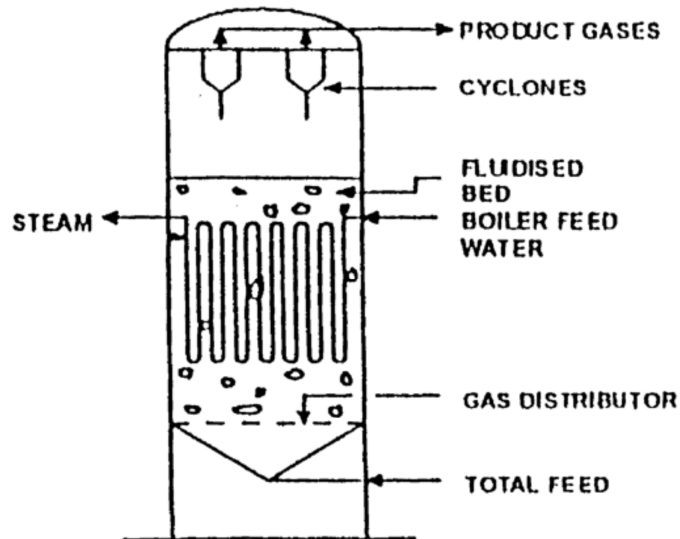


Figure 1.10 Fixed fluidized bed reactor (FFBR) used by Sasol – Adapted from [11]

1.1.4.2. LTFT reactors

The three phase (gas-liquid-solid) LTFT reactors producing mainly liquid long linear hydrocarbons are either multitubular fixed bed or slurry reactors. In the multitubular fixed bed reactors, the catalyst is placed inside the reacting tubes whereas a cooling media flows on the shell sides. Higher heat transfer rates could be established if narrow reactor tubes are used or the syngas space velocity is increased. The schematic view of multitubular fixed bed reactor is shown in Fig. 1.11.

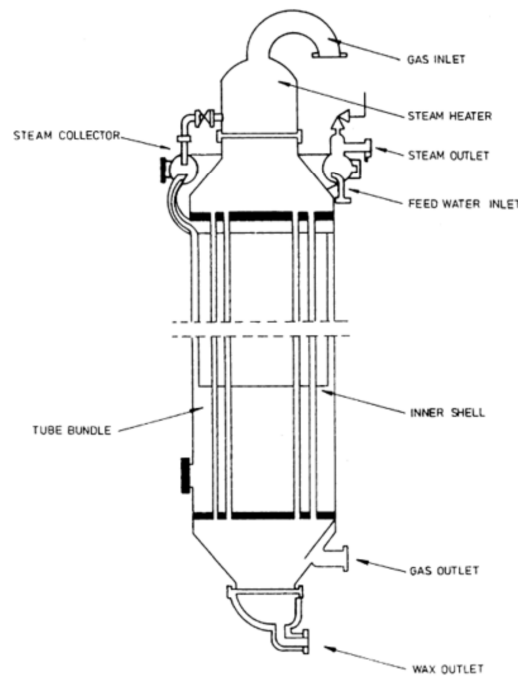


Figure 1.11 Multitubular fixed bed reactor used in FT [11]

The first commercial multitubular FBR, installed again in Sasolburg at the Sasol plant, used extruded iron-based catalysts at 230°C and 27 bar. Moreover Shell used the same reactor configuration in its plant in Bintulu (Malaysia) using cobalt-based catalyst and narrower reactor tubes. Recently the Pearl GTL plant in Qatar is developed and put in operation in 2012 using the multitubular FBR technology by Shell. Using 24 multitubular fixed bed reactors, it converts $45 \times 10^6 \text{ m}^3/\text{day}$ of natural gas into $22 \times 10^3 \text{ m}^3/\text{day}$ of petroleum liquids

The slurry reactor is also used for the LTFT processes, where a higher heat transfer could be established as the catalyst particles are suspended inside the liquid FT-produced wax. The boiler feed water flows inside the narrow tubes which are placed inside the slurry phase in order to facilitate the heat transfer. Fig. 1.12 shows a typical slurry reactor operated by Sasol.

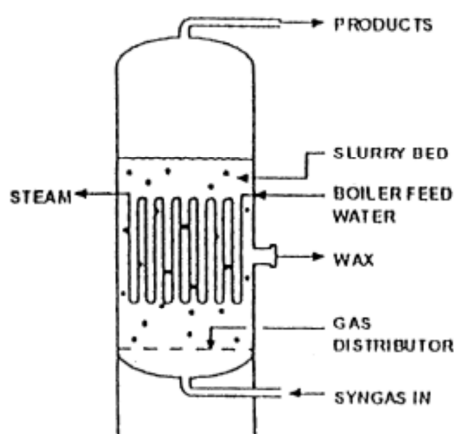


Figure 1.12 Slurry phase reactor used by Sasol for FTS [11]

Although the slurry reactor gives several advantages over fixed bed reactors (longer reactor runs, lower pressure drop, lower catalysts consumption, better temperature control, lower construction costs, etc.), it was not used before 1993 when a commercial unit is brought online by Sasol and a satisfactory way of wax/catalyst separation was found. Slurry reactors are now used by Sasol in Ras Laffan (Qatar) using Slurry Phase Distillate (SPD) process.

1.2. Causes of deactivation during Fischer Tropsch synthesis

Most of the academic and industrial studies on FTS are reporting that deactivation can occur during FTS. Deactivation leads to reduced catalytic activity and modified product selectivity. For industry, the increased cost of catalyst replacement could affect the economic margin of the process.

Deactivation is normally a complex process which depends on several parameters including the type and composition of the catalyst sample, operating conditions and reactor configuration, time-on-stream, etc.

Two-step catalysts deactivation process has been shown in demonstration plants by activity measurements (Fig. 1.13) for both cobalt and iron based catalysts [44]. The initial deactivation regime (period A in Fig. 1.13), lasting for a few hours to days, has been linked with reversible deactivation process. The second long-term deactivation regime (period B in Fig. 1.13) is suggested to be irreversible and has therefore operational significance. This combined catalysts deactivation profile with time supports the fact that deactivation is a result of several simultaneous phenomena.

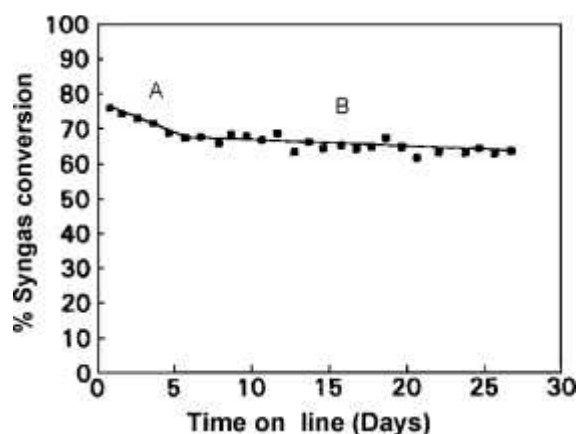


Figure 1.13 Typical deactivation profile for cobalt catalysts in FTS. Adapted from reference [44].

Deactivation is attributed to be due to several mechanisms in the literature [45] including sintering, catalyst poisoning, active metal re-oxidation, metal-support compound formation, carbidisation, among others. The comprehensive study of deactivation phenomena is therefore difficult as several mechanisms exist at the same time. The mechanistic approaches are useful as they bring about the source and the way in which the catalyst activity is reduced. In addition, the severe FTS conditions including high temperature and pressure, catalyst particles coated with a layer of wax, etc. makes the use of in-situ and operando techniques difficult and the major part of characterization tools reported could not realistically represent the catalyst behavior during FT working conditions.

This section discusses the main sources of Fischer-Tropsch catalysts deactivation.

1.2.1. Catalyst poisoning

As the Fischer-Tropsch catalysts are normally very sensitive to poisoning, the syngas purification is usually an important step of a typical Fischer-Tropsch process, mainly as the syngas is produced of either biomass or coal resources.

Most metallic catalysts are poisoned by sulphur as it is highly adsorbed on the catalytic active sites. This strong interaction leads to geometric blockage of occupied sites as well as electronic modification of neighbor active sites [46]. It has been proposed that more than two active cobalt sites are poisoned in the case of adsorption of one sulphur atom on a Co/Al₂O₃ catalyst [47] which support the hypothesis that the geometric blockage is more important for the case of cobalt poisoning.

Fig. 1.14 shows the steady-state methanation activity of Co, Fe, Ni, and Ru relative to a fresh, unpoisoned surface as a function of gas-phase H₂S concentration [46]. As the sulphur tolerance of Fischer-Tropsch catalysts is so that the sulphur concentration in feed should be less than 0.02 mg/m³ for a proper catalyst activity [11].

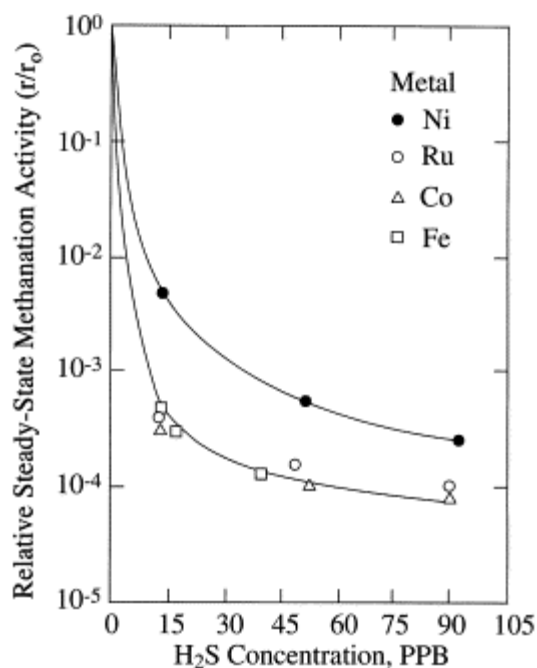


Figure 1.14 Relative steady-state methanation activity profiles for Ni (•), Co (Δ), Fe (□), and Ru (○) as a function of gas phase H₂S concentration. Reaction conditions: 100 kPa; 400°C; 1% CO/99% H₂ for CO, Fe and Ru; 4% CO/96% H₂ for Ni [48]. – Adapted from reference [46]

It is also found that even ppb levels of nitrogen-containing compounds are detrimental to catalysts activity and there is a direct correlation between the amount of such contaminants and catalyst deactivation rate. However such a deactivation is found to be reversible and

hydrogen treatment could lead to 100% activity recovery. A level of nitrogen contaminants less than 50 ppb inside the syngas is then proposed for normal FT operation [49].

In addition, small traces of alkali metals including sodium, potassium, and lithium have shown to affect the Fischer-Tropsch catalyst activity [50] and [51]. Two parallel effects are observed simultaneously once alkali metals are added in the syngas: (a) higher chain growth probability, as well as (b) lower site-time yields (Fig. 1.15). Consequently it is proposed that an optimum concentration limit exist for each specific alkali metal in order to balance the two effects [50, 52].

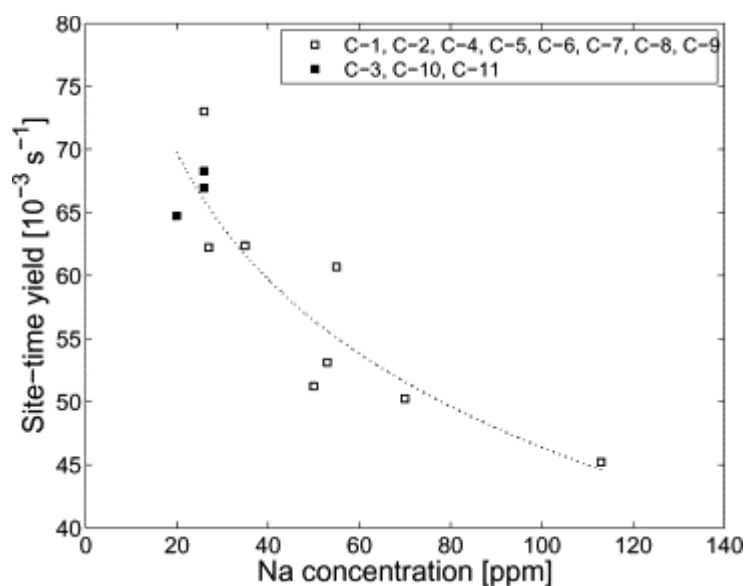


Figure 1.15 Effect of the catalyst concentration of Na on the site-time yield measured after 8 h on stream at 483 K, 20 bar, and $\text{H}_2/\text{CO}=2.1$, C-X is the catalyst sample number (cited from [53]).

1.2.2. Metallic re-oxidation

Re-oxidation of cobalt crystallites during FT synthesis has been a controversial topic in the literature. Several reviews are available on the effect of water on the catalyst activity [54], [55], and [56]. The main hypothesis is that the produced water acts as an oxidizing agent leading to surface or bulk oxidation of cobalt nanoparticles. Iglesia [57] proposed that water originates from the hydrogenation reaction of surface oxygen and hydroxyl groups formed by CO dissociation elementary steps.

Theoretical thermodynamic calculations have shown that bulk cobalt oxidation is not possible during FTS [58, 59] (Fig. 1.16a). However it is highly probably that the properties of cobalt nanoparticles differ from the properties of bulk cobalt in FT conditions. The re-oxidation of small cobalt crystallites is proposed to be possible while exposure to syngas. However, although initial thermodynamic calculations by Van Steen [59] have shown (Fig.

20b) that crystallites of 4-5 nm are unstable in typical FT conditions ($P_{H_2O}/P_{H_2} < 1.5$, which corresponds to a conversion of CO in the cobalt-based Fischer–Tropsch synthesis of ca. 75% [60]), further updated investigations [61] propose an even lower margin for catalyst oxidation, i.e. only small crystallites of about 2 nm could be oxidized in such conditions (Fig. 1.17). The calculations were based on the surface energies of cobalt crystallites that are different in size (<100 nm), morphology (e.g. spherical shape) and the initial crystal phase (e.g. β -Co (fcc)). However, support interaction and surface reconstruction at FTS conditions were not taken into consideration [45]. The respective surface energies of Co and CoO nanoparticles are calculated by Eq. 1.6-1.7:

$$\gamma_{Co} = 2.14 \left(1 + \frac{1.45}{d_{Co}} + \frac{0.55}{d_{Co}^2} \right) \quad (1.6)$$

$$\frac{\gamma_{CoO}}{\gamma_{Co}} = 0.2167 + \frac{0.011}{d_{Co}} - \frac{0.064}{d_{Co}^2} \quad (1.7)$$

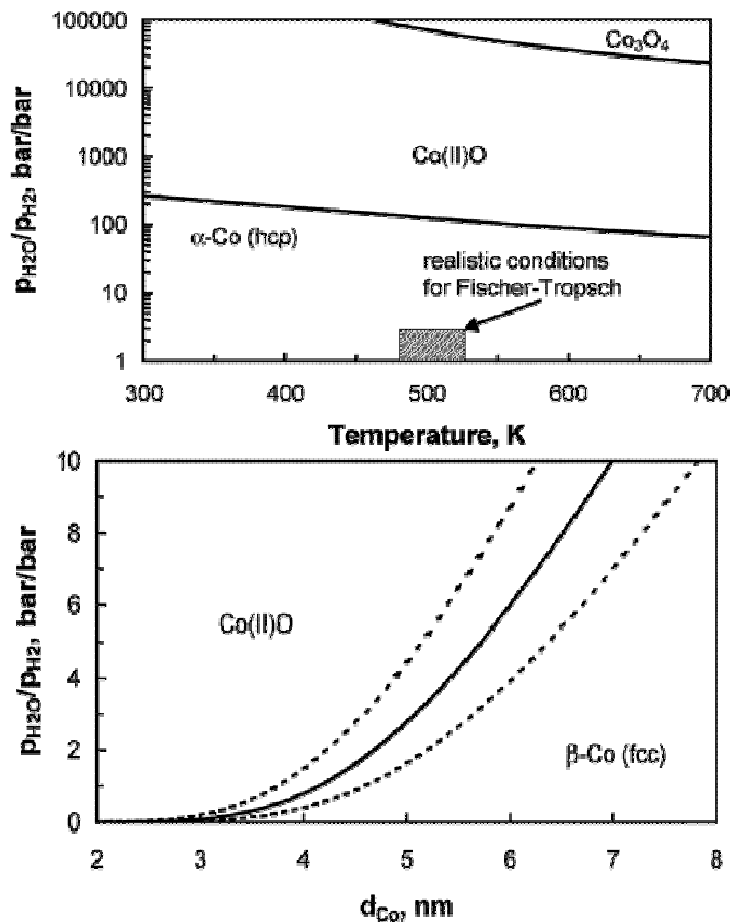


Figure 1.16 (a) Stability diagram of bulk cobalt metal and various cobalt oxide phases as a function of temperature and ratio of partial pressure of water to partial pressure of hydrogen. (b) Stability region of spherical β -Co (fcc) and $Co(II)O$ crystals in H_2O/H_2 atmospheres at 220 °C as a function of the diameter of a spherical metal Co crystallite (dotted line $\gamma_{\beta-Co} \pm 15\%$)- Adapted from [59]

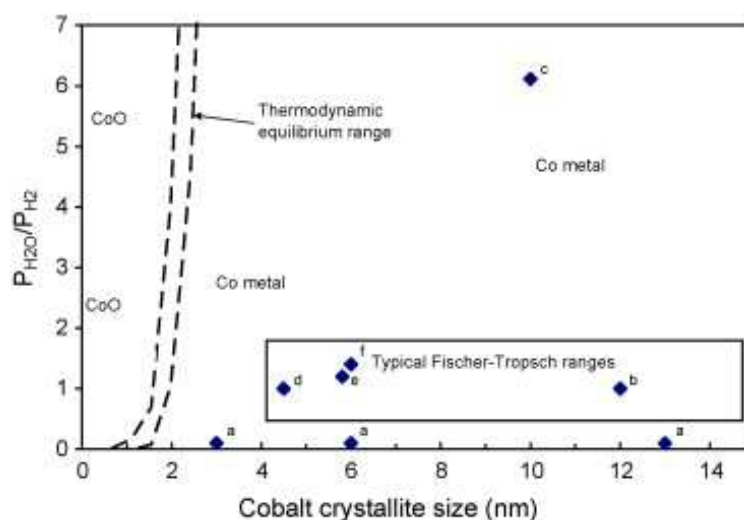


Figure 1.17 Reconciliation of the effect of the water/hydrogen reactor ratio as a function of cobalt crystallite size on the oxidation behavior of cobalt: (a) from [62]; (b) from [63]; (c) from [64]; (d) from [65]; (e) from [66]; (f) from [55]. All the data are superimposed on the thermodynamic equilibrium data range [67].

Water co-feeding in low-conversion FTS conditions is the most commonly used technique for the evaluation of water effect on catalytic activity. This is supposed to resemble high conversion FTS experiments in slurry reactor. However, long FTS experiments at low CO conversion are also employed as another technique.

In contrary to theoretical calculations, external water addition leads to surface and bulk cobalt oxidation as reported by several research groups. Schanke et al. [68] and [69] studied a rhenium promoted and an unpromoted $\text{Co}/\gamma\text{-Al}_2\text{O}_3$ catalyst using a wide range of experiments. Both water co-feeding as well as pure water-hydrogen streams were used. Cobalt re-oxidation was identified using TPR and gravimetric techniques. They proposed that surface oxidation especially in the case of highly dispersed particles could take place.

In order to study the effect of water addition on catalytic activity, they have used 17 wt% $\text{Co}/\gamma\text{-Al}_2\text{O}_3$ and 1 wt% Re-17 wt% $\text{Co}/\gamma\text{-Al}_2\text{O}_3$ catalysts at 210 °C and 13 bar [70, 71]. Water is added with the ratio of $\text{H}_2\text{O}/\text{H}_2 = 1.5$, simulating the environment of approximately 75% CO conversion. The catalyst deactivation rate was increased once the water is added in the feed (Fig. 1.18) for both promoted and unpromoted catalysts, although the promoted catalysts shows higher sensitivity to water addition. No further deactivation was observed after water had been removed from the feed. TPR and gravimetric studies showed indications of re-oxidation in the presence of steam.

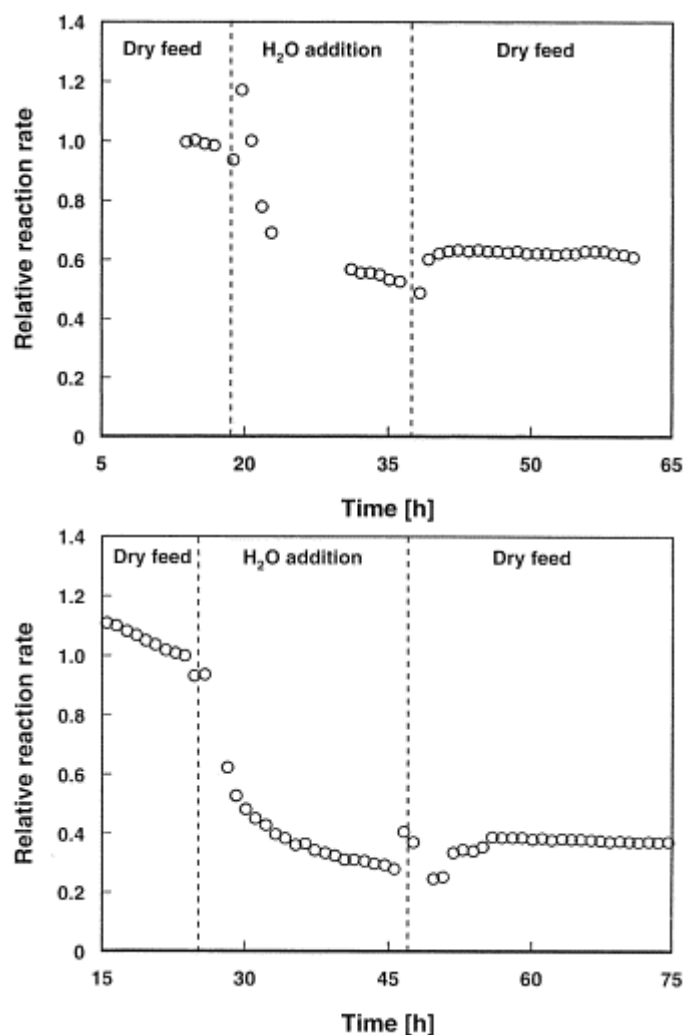


Figure 1.18 Observed reaction rate relative to the rate of CO consumption just before water addition as a function of time for (a) Co/Al₂O₃ and (b) CoRe/Al₂O₃. Feed composition: 50 mol% (H₂ + CO), H₂/CO = 2.1, balance N₂ + He or N₂ + He + H₂O, P_{tot} = 13 bar, T = 483 K. Inlet H₂O/H₂ ratio during water addition = 1.5. (Adapted from [70])

In order to evaluate the effect of catalyst morphology on the water-assisted deactivation, several catalysts with different supports and pore size distributions were analyzed [72], [73], [74], [75], [76]. Both Re-promoted and unpromoted cobalt catalysts prepared on different support including γ -Al₂O₃, SiO₂, TiO₂ were studied. It was observed that in the case of alumina supported catalysts, water addition leads to an activity reduction which increases once a promoted catalyst is used. For silica and titania supported catalysts different behaviors were obtained as depicted in Fig. 1.19. It was also observed that even a small amount of water (H₂O/H₂ = 0.4) could enhance the activity in the case of TiO₂ and SiO₂ supported catalysts. However, the effect of steam has to be discussed with respect to crystallite size, support interaction and catalysts structural characteristics (e.g. pore size) [45]. In addition, it was suggested that in the case of all catalyst supports, steam addition increases the C₅₊ selectivity.

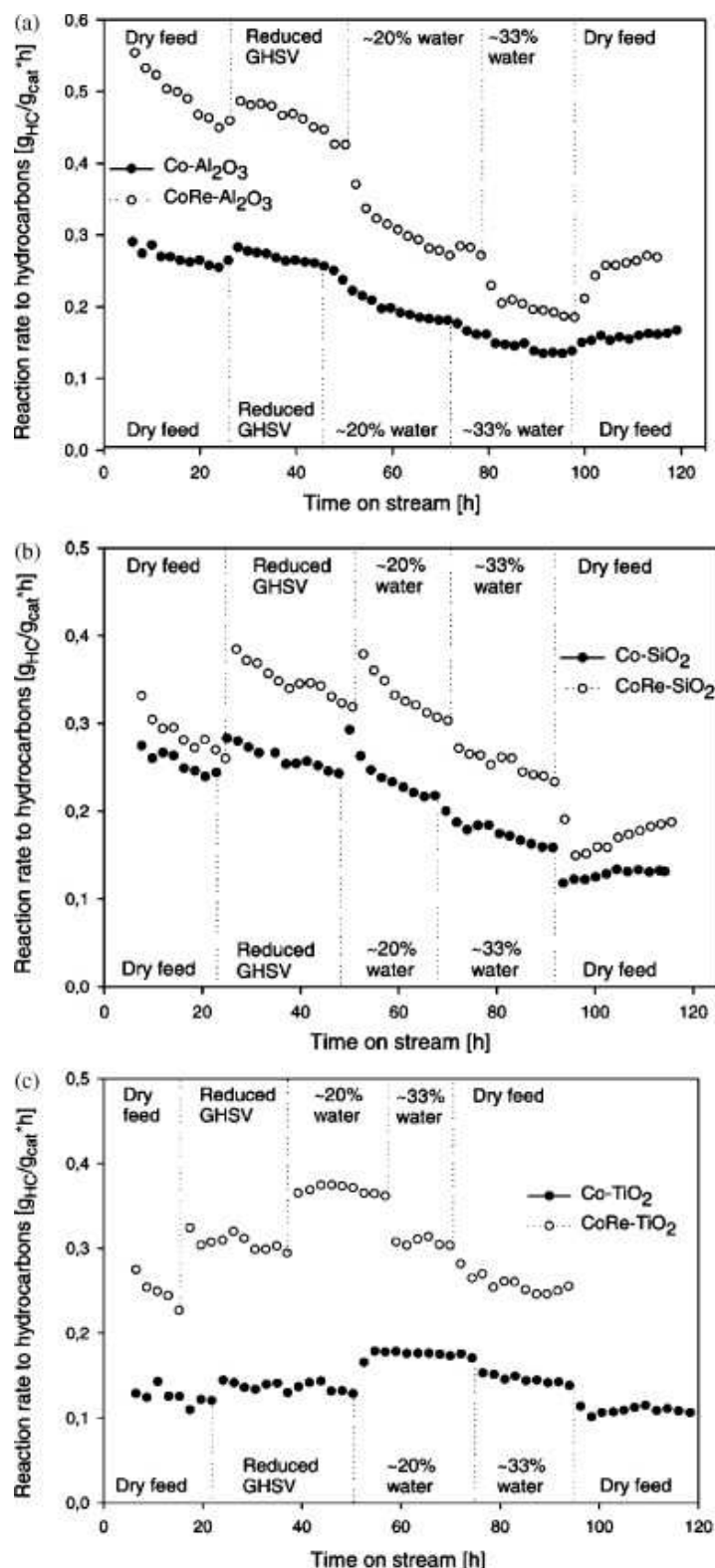


Figure 1.19 Observed reaction rate for formation of hydrocarbons as a function of time on stream 5 h after start-up for Co (●) and CoRe (○) catalysts supported on Al₂O₃ (A), SiO₂ (B), and TiO₂ (C). H₂/CO = 2.1, P_{Total} = 20 bar, T = 210 °C. Adapted from Reference [75]

The use of ex-situ characterization tools of spent catalyst allows studying the re-oxidation state of cobalt particles. Temperature-Programmed-Reduction (TPR), X-ray

photoelectron spectroscopy (XPS), Mössbauer Emission Spectroscopy (MES) and X-ray Absorption Near Edge Structure (XANES) are used. XANES appears to be the most successful technique, since it can give quantitative results on the degree of reduction (DOR) and can be applied without removing FT waxes that are covering the surface of the catalyst. However XANES technique requires synchrotron radiation although it protects the catalyst particles from exposure to air.

Van de Loosdrecht et al. [60] and [77] employed Mössbauer Emission Spectroscopy (MES) in combination with thermogravimetric analysis for the detection of changes in the oxidation state of metallic cobalt while exposure to water containing syngas. The doped catalyst prepared for MES characterization was exposed to model gaseous mixtures of H_2 , H_2O and Ar. Re-oxidation of metallic nanoparticles were observed depending on different H_2O/H_2 pressure ratio (Fig. 1.20)

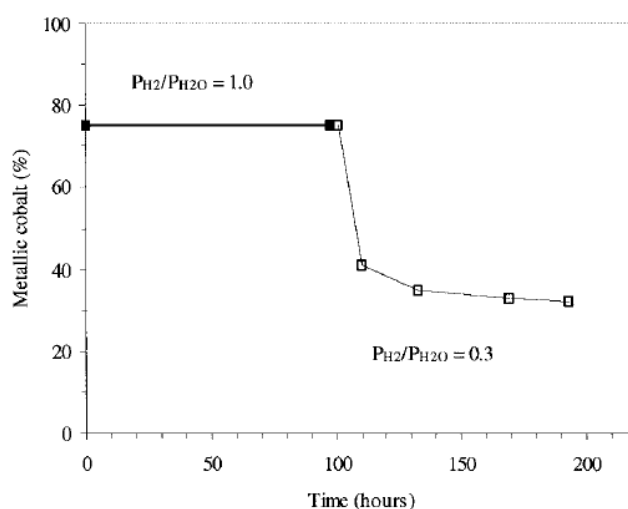


Figure 1.20 Catalyst oxidation as directly observed with MES (150°C, 1 bar, Ar/ H_2 / H_2O environment, $P_{H_2O} = 0.025$ bar). Adapted from reference [77]

The group also designed a high pressure cell [78] where the data obtained suggested a further increase in the degree of reduction while increasing the total pressure up to 10 bar ($P_{H_2O}/P_{H_2} = 1.0$, $T = 150$ °C). Consequently the effect of operating conditions on the cobalt re-oxidation should be considered.

The potential re-oxidation of industrial catalysts was also investigated by Sasol in collaboration with several research groups. Advanced characterization tools including XAS, XRD, TPR, HR-TEM as well magnetism, EXAFS, and XPS were used. FTS simulated environment ($H_2/H_2O = 1$, $P_{total} = 0.4$ mbar, $T = 150$ – 450 °C) used for a planar $Co/SiO_2/Si(100)$ model catalyst with cobalt crystallites of 4–5 nm [65] indicate no indication of cobalt re-

oxidation as the Near-edge X-ray absorption fine structure (NEXAFS) results from the Co L_{III} -edge showed (Fig. 1.21). It was then proposed that 4-5 nm crystallites do not re-oxidize in typical FT conditions.

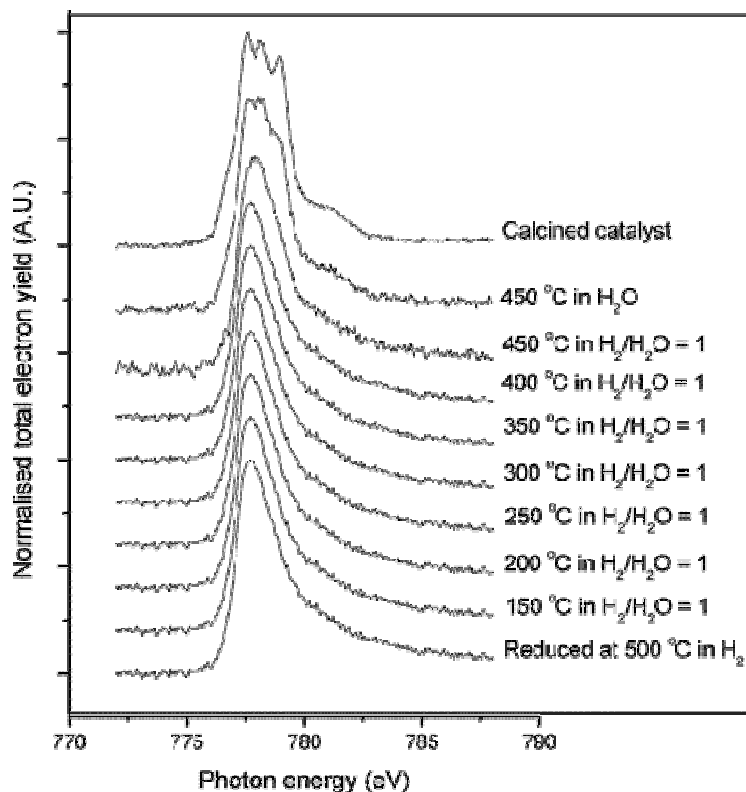


Figure 1.21 Model oxidation study of a reduced (0.2 mbar of hydrogen, 4 °C/min to 500 °C) planar Co/SiO₂/Si(100) model catalyst (2 Co atom/nm²) exposed to H₂/H₂O = 1, P_{total} = 0.4 mbar at 150 °C (10 min), 200 °C (10 min), 250 °C (60 min), 300 °C (10 min), 350 °C (60 min), 400 °C (10 min), and 450 °C (60 min). Thereafter the catalyst was exposed to 0.2 mbar of H₂O at 450 °C – Adapted from Reference [65]

In order to study the effect of particle size on Co re-oxidation state, cobalt crystallites with average size of 4, 13 and 28 nm were also examined [79] and subjected to highly oxidizing environment (H₂O/He, P_{H₂O}=0.04 bar). The 4-nm crystallites were stable even in the presence of higher amounts of co-fed water (P_{H₂O}=0.04–0.3 bar) probably due to strong metal-support interactions resulting in crystallite encapsulation by the support. This hypothesis was supported by TPR and HR-TEM (Fig. 1.22) analyses.

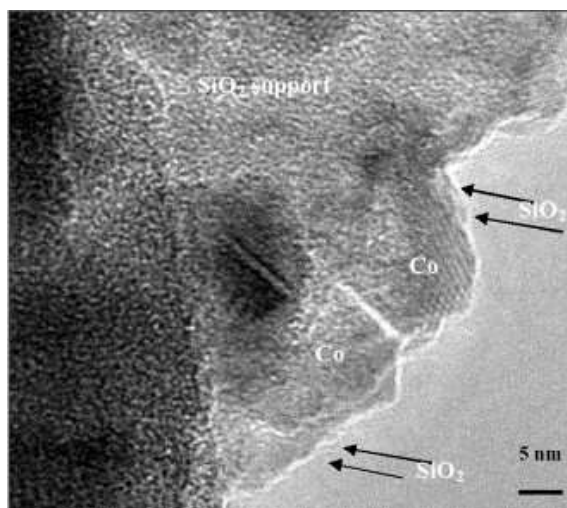


Figure 1.22 TEM analyses of the spherical 5 wt% Co/SiO₂ model catalyst with small cobalt crystallites (Co-4nm) following reduction at 700 °C in pure hydrogen (arrows indicate silica migration) – Adapted from Reference [79]

Larger cobalt nanoparticles were found to be re-oxidized when exposed to H₂O/He mixture ($P_{\text{H}_2\text{O}}=0.04$ bar) and reached a maximum of 30% oxidation at 300 °C (Fig. 1.23).

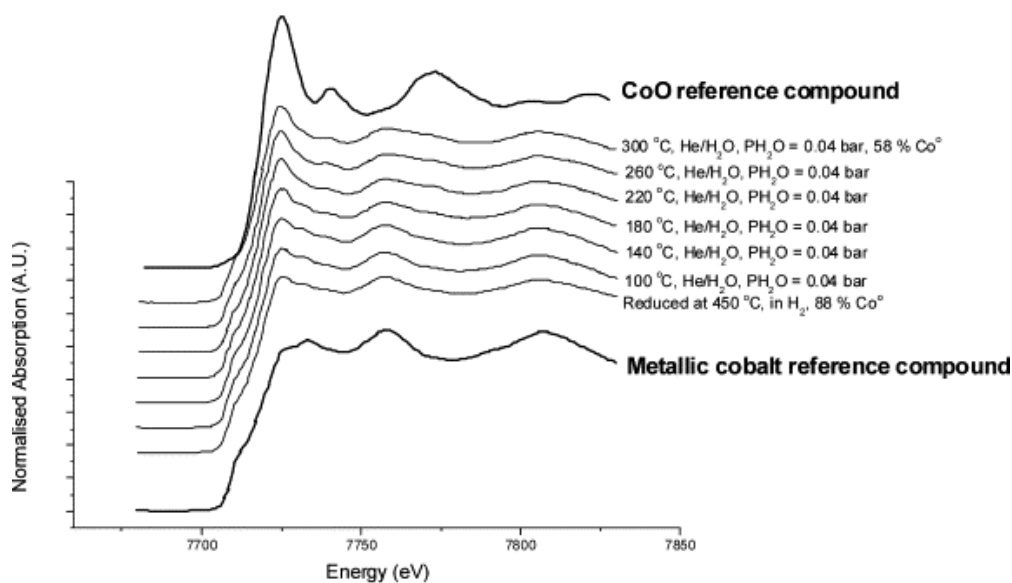


Figure 1.23 Model oxidation study of spherical Co/SiO₂ model catalyst with medium cobalt crystallites (Co-13nm), In situ model oxidation conditions: 2 °C/min to 300 °C in H₂O/He ($P_{\text{H}_2\text{O}}=0.04$ bar) with a spectrum measured every ca. 40 °C.- Adapted from Reference [79]

The same research group have continued their studies using XANES characterization of spent wax-coated catalyst samples [66]. The 20 wt% Co- 0.05 wt% Pt γ -alumina supported catalyst (with an initial reduced crystallite size of 6 nm) was unloaded from the commercial slurry column reactor (230 °C, 20 bar, 100 barrel/day, synthesis gas conversion = 50-70%) at different time on stream up to 140 days. The changes in the degree of cobalt reduction with

time were estimated using a linear combination of XANES spectra (Fig. 1.24) with standards. It was found that cobalt was further reduced from 50% to 88% during FTS (Table 1.5).

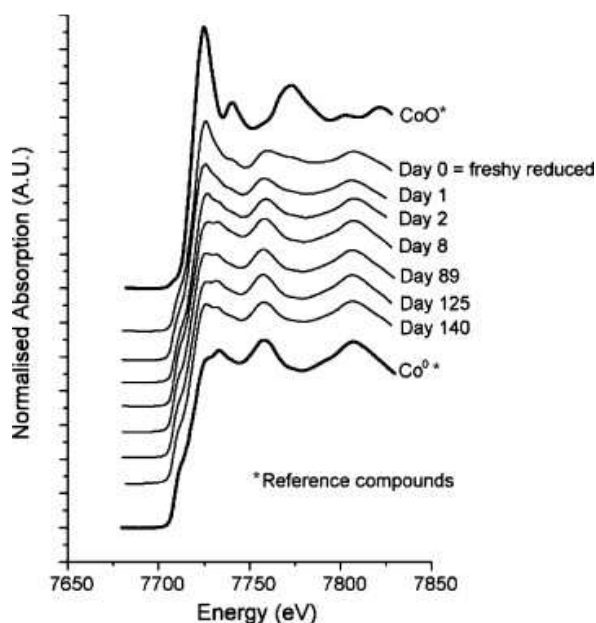


Figure 1.24 XANES analysis of a series of spent Co/Pt/Al₂O₃ catalyst samples taken from a 100-barrel/day slurry bubble column reactor operated at commercially relevant FTS conditions, i.e. 220 °C, 20 bar, (H₂ + CO) CO conversion between 50% and 70%, feed gas composition of ca. 50 vol.% H₂ and 25 vol.% CO, P_{H₂O}/P_{H₂}=1–1.5, P_{H₂O}=4–6 bar.-Adapted from reference [66].

Table 1.5 Quantification of XANES analyses of a series of spent Co/Pt/Al₂O₃ catalysts taken from a 100-barrel/day slurry bubble column reactor operated at commercially relevant FTS conditions using a linear combination of reference compounds. – Adapted from Reference [60]

Sample	Co ⁰ (%)	CoO ^a (%)
Freshly reduced	53 ^b	47
Day 1	69	31
Day 2	80	20
Day 8	85	15
Day 89	88	12
Day 125	89	11
Day 140	87	13

Error = ±2–3%.

^a The following does not rule out any minor CoAl₂O₄, which is difficult to differentiate with XANES using the current data and is most likely present at the interface of the cobalt particles with the support.

^b Although on the low side, the degree of reduction is close to that obtained from gravimetry, i.e. 63%.

In order to verify the results, the authors used XRD and magnetism techniques as well. The results were in line with XANES data, showing from the saturation magnetization the Co degree of reduction (Table 1.6). The CoO characteristic peaks were disappeared in XRD spectra after 3 days on stream. The authors then rule out oxidation as a potential deactivation

mechanism for Co crystallites of 6-nm or larger in the applied FTS conditions. They have proposed that the deactivation by oxidation could be prevented if a correct combination of water partial pressure ($P_{\text{H}_2\text{O}}/P_{\text{H}_2}$) and crystallite size is selected. However due to high cobalt loading in the catalyst, possible metal-support interaction may exist which could affect the deactivation behavior of the catalyst.

Table 1.6 Quantification of magnetic analyses of a series of spent Co/Pt/Al₂O₃ catalysts taken from FTS run – Adapted from Reference [55]

Sample	% Co ⁰
Freshly reduced	50
Day 1	58
Day 4	66
Day 10	69
Day 21	81
Day 41	71
Day 66	73
Day 90	67
Day 120	74
Day 150	88

In addition, recently Rønning et al [80] have performed a combined *in situ* XAS-XRD study at 18 bar and 210 °C and have observed a further reduction of the catalyst by XRD accompanied by sintering of the crystallites as the reaction time increased.

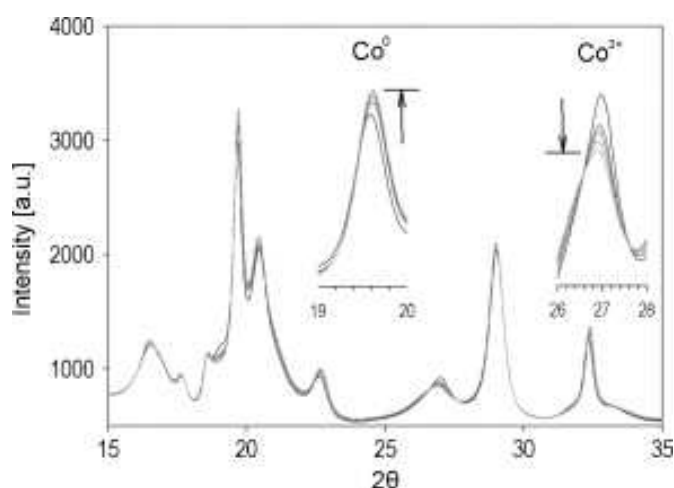


Figure 1.25 XRD patterns of a partially reduced catalyst showing a decrease in CoO peak intensity during FT synthesis (FT2) at 673 K. – Adapted from Reference [80]

In line with such these results, Botes [81] has shown that water addition has a negligible effect on the FT kinetics (Fig. 1.26), although it could lead to lower methane and higher CO₂ selectivity.

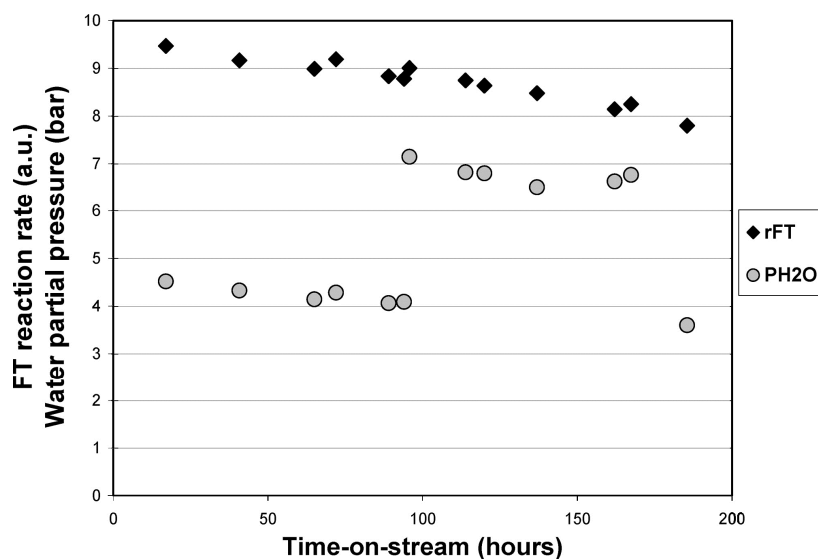


Figure 1.26 Influence of longer term exposure of the catalyst to higher water partial pressures. The experimental conditions are the following: fresh catalyst; H_2/CO ratio at the usage ratio of about 2; temperature = 230 °C. – Adapted from Reference [81]

Davis and coworkers have also studied the effect of water addition on the kinetics of FTS [82], [83], [84], [85], [86] using a wide range of silica supported catalysts. Small amounts of water added in the feed led to even higher CO conversion in the case of 12.4 wt.% Co/SiO₂ catalyst, whereas higher amounts (>20%) could lead to a gradual decrease in the activity (Fig. 1.27). Similar results were obtained once a higher cobalt content was used (20 wt.% Co/SiO₂) although the effect is less pronounced at low water contents as Fig. 1.28 demonstrates.

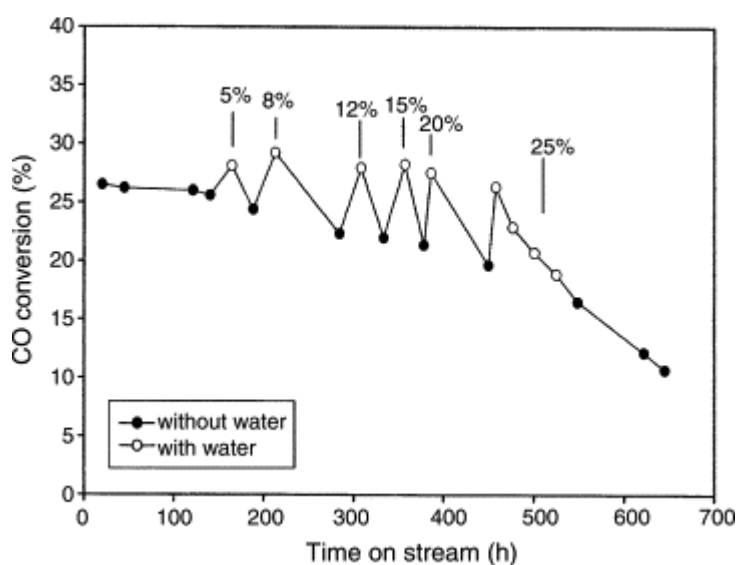


Figure 1.27 Effect of water on CO conversion for 12.4% Co on wide-pore SiO₂ support ($T = 483$ K, $P = 2$ MPa, $H_2/CO = 2.0$, $SV = 8$ SL/g cat. h, % is vol.% of total feed). – adapted from Reference [82]

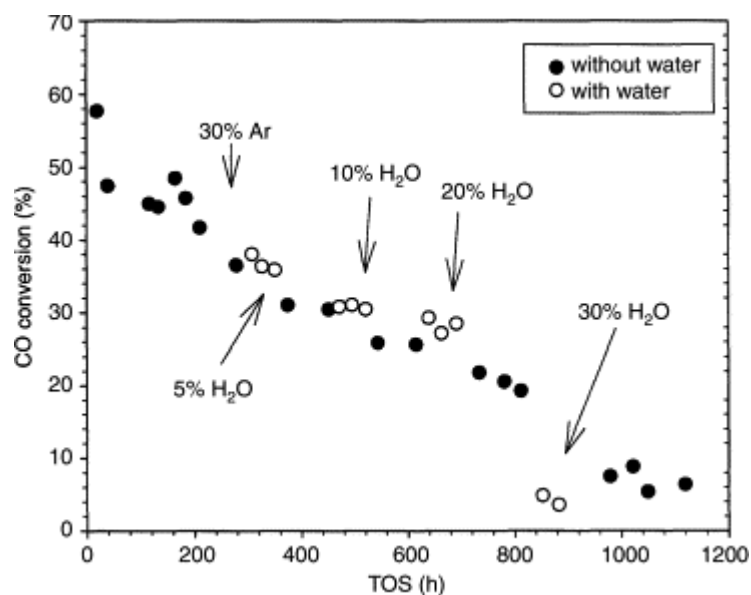


Figure 1.28 Effect of water on CO conversion for 20% Co on wide-pore SiO₂ support ($T = 483\text{ K}$, $P = 2\text{ MPa}$, $H_2/CO = 2.0$, $SV = 5\text{ SL/g cat. h}$, % H₂O is vol.% of total feed) – Adapted from Reference [82]

Iglesia et al. [87] have used an *in situ* infrared spectroscopy cell to study a 12.7 wt% Co/SiO₂ catalyst (200 °C, 5 bar and H₂/CO = 2). They have suggested that water does not affect the extent of CO adsorption on the surface. However, once subjected to simulated FTS conditions (H₂O/H₂ ratio > 0.8, $T = 200\text{ °C}$), the catalyst surface was oxidized and the oxygen islands were formed. The islands do not readily react with adsorbed hydrogen at the same rate as isolated adsorbed oxygen species formed by the CO dissociation reactions.

The effect of support on the possible cobalt oxidation was studied by the group of Li et al [88], [89], [90], [91]. Both unpromoted and promoted cobalt catalysts supported on Al₂O₃, SiO₂, and TiO₂ were tested. High steam pressures were obtained either using external water addition or changing the syngas space velocity in a continuously stirred tank reactor (210-230 °C, 20.2-29.3 bar). Low water addition in the case of both alumina and titania supported catalysts (0.5 wt% Pt-15 wt% Co/Al₂O₃ and 0.2 wt% Ru-10 wt% Co/TiO₂) resulted in a reversible deactivation, whereas higher water partial pressures ($P_{H_2O}/P_{CO}=1$) resulted in an irreversible deactivation behavior as well as an increased CO₂ selectivity (Fig. 1.29) Higher carbon dioxide selectivity was attributed to higher water-gas shift reaction extents, an indirect indication of transformation of metallic into oxidized cobalt species.

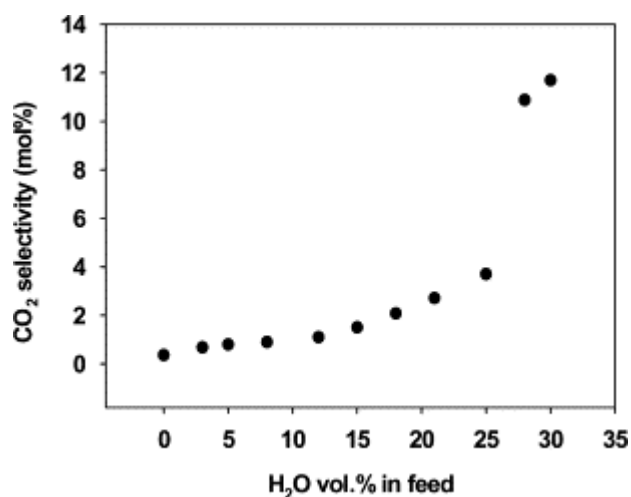


Figure 1.29 Effect of amount of water added with the syngas on the CO₂ selectivity using a Co-Pt/Al₂O₃ catalyst. – Adapted from Reference [88]

However the unpromoted silica supported catalysts (12.4 wt% Co/SiO₂) showed different behavior upon steam addition. Increased CO conversion was observed in the case of relatively small (5-25 vol%) amounts of water (Fig. 30) whilst higher water fraction led to severe catalysts deactivation. It was suggested that this difference is due to higher Co crystallites in the case of silica supported catalysts (5.6, 8.5 and 13.2 nm on alumina, titania and silica, respectively).

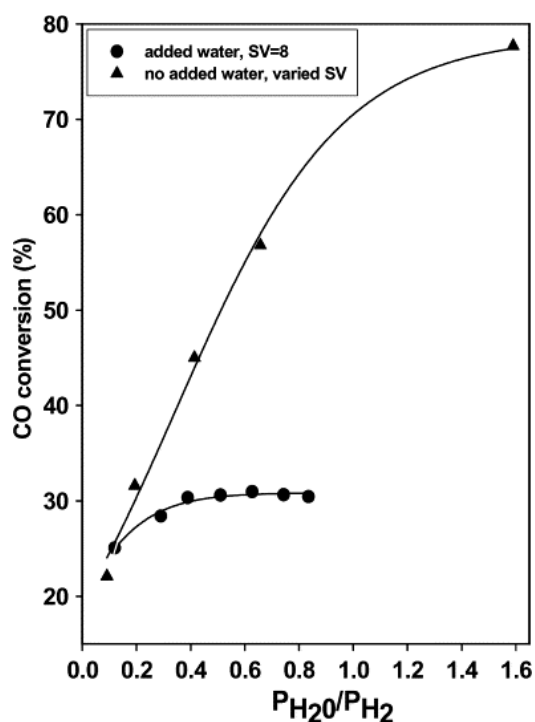


Figure 1.30 CO conversion as a function of P_{H_2O}/P_{H_2} for Co/SiO₂ catalyst (T=483 K, P=20 atm (2.02 MPa), $P_{H_2}+P_{CO}=14$ atm (1.41 MPa), H₂/CO=2.0, partial pressure is based on reactor exit). – Adapted from [90]

The impact of crystallite size on cobalt re-oxidation was also studied by Jacobs et al. [92]. They have prepared different catalysts having crystallite sizes between 5–6 and >10 nm using low and high cobalt loading respectively. The low loaded catalyst with the small crystallites increased interactions with the support once water is externally added and resulted in an irreversible deactivation after water treatment suggesting that cobalt aluminate-like species were formed according to XANES spectra. EXAFS data showed a reduced Co-Co coordination in the case of larger crystallites i.e. the formation of cobalt oxides. The re-oxidation process was reversible and a significant conversion recovery was gained once the external water is stopped suggesting that water caused a surface oxidation phenomenon.

Recently it was proposed that other oxygen containing compounds could act as mild oxidizing agents including carbon dioxide [93], methanol [94], and ethanol [95]. TPR and XRD data support the reversible formation of cobalt oxides (Fig. 1.31-1.32).

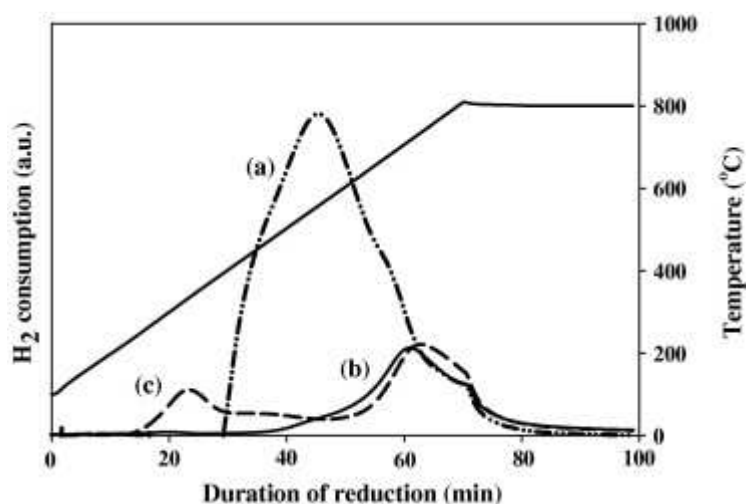


Figure 1.31 TPR profiles of Co/ γ -Al₂O₃. (a) fresh catalyst, (b) reduced catalyst, (c) CO₂ treated catalyst after reduction. – Adapted from [93]

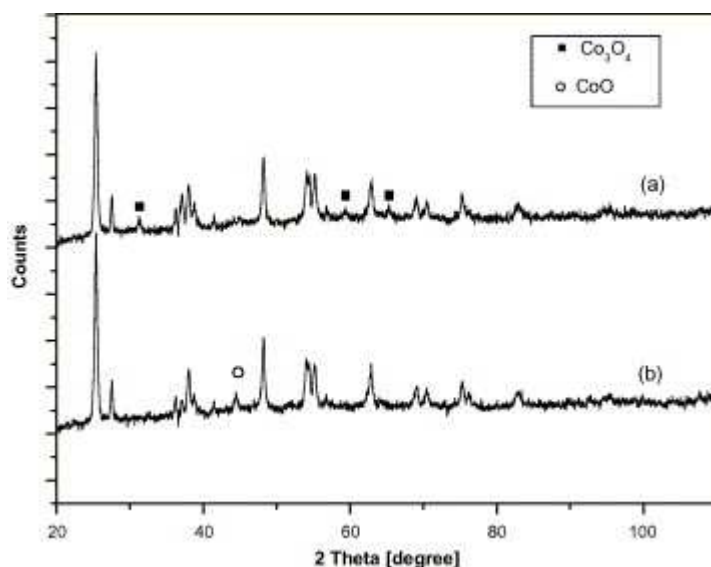


Figure 1.32 XRD patterns for 10% Co/TiO₂: (a) XRD pattern for the calcined and unreduced catalyst and (b) XRD pattern for the reduced catalyst after exposure to ethanol/nitrogen for 30 min. – Adapted from [95]

1.2.3. Sintering

1.2.3.1. Sintering of active metal

Sintering is an important route for the deactivation of Co-based Fischer Tropsch catalysts. It leads to a reduction of total active surface area and therefore a reduced activity. Sintering is thermodynamically driven from the surface energy minimization [45], as the larger crystallites have lower surface energy and therefore more thermodynamic stability (Eq. 1.7 and Fig. 1.33).

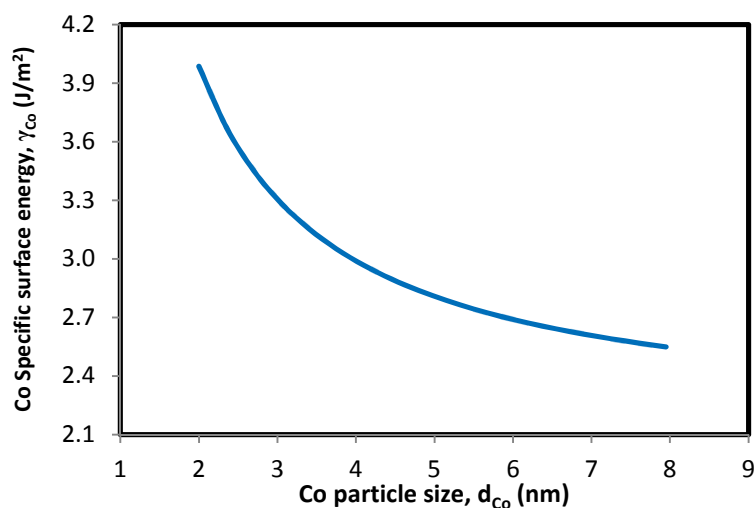


Figure 1.33 Cobalt specific surface energy as a function of crystallite size

Sintering may proceed through (a) atomic migration (Ostwald ripening, *OR*), (b) crystallite migration and coalescence (*PMC*), or (c) vapor transport between particles when the

temperature is sufficiently high. However at normal industrial application only the first two mechanisms are important as depicted in Fig. 1.34.

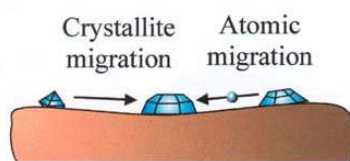


Figure 1.34 Two conceptual models for crystallite growth due to sintering by atomic or crystallite migration – Adapted from Reference [96]

The most common techniques for detecting sintering are X-ray diffraction (XRD), transmission electron microscopy (TEM) and H_2 chemisorption. Extended X-ray absorption fine structure (EXAFS) and anomalous small angle X-ray scattering (ASAXS) are gaining importance in crystallite size analysis as synchrotron based techniques with in situ capabilities are readily available [45].

Sintering is a complex process, which is influenced by several parameters including temperature, chemical environment, catalyst composition and structure, and support morphology [97]. The most important parameters are the sintering temperature and atmosphere over the catalyst [98], [99], [100], [101], [102], [103], [104]. Increasing the temperature results in a significantly faster sintering process and the presence of water greatly accelerates the sintering process [102], [46]. A number of studies related to the effect of water in the catalyst deactivation of FTS, suggest sintering of cobalt crystallites as one of the main deactivation mechanisms [45]. The water could accelerate sintering both in (a) a *direct*, or (b) an *indirect* way. Bertole et al. investigated the effect of water using a rhenium promoted unsupported cobalt catalyst [105]. They showed that the periodic addition of water at 210 °C and high partial pressures (4 and 8 bar) resulted in a permanent loss of activity (starting conditions 10 bar H_2 , 5 bar CO, 8 bar inert and ~11% CO conversion). A subsequent hydrogen treatment recovered only 80% of the activity. The CO adsorption capability of the catalyst was reduced which supports the hypothesis of loss of active surface area due to sintering of cobalt crystals. Recent studies by Kiss et al. point to sintering as an indirect deactivation mechanism [106]. It appears that crystallite growth occurs as a consequence of re-oxidation of cobalt crystallites. The authors use *ex-situ* TEM images to follow the crystallite size distribution before/after the sintering (Fig. 1.35). They have also proposed particle migration and coalescence as the predominant sintering mechanism as indicated in Fig. 1.36.

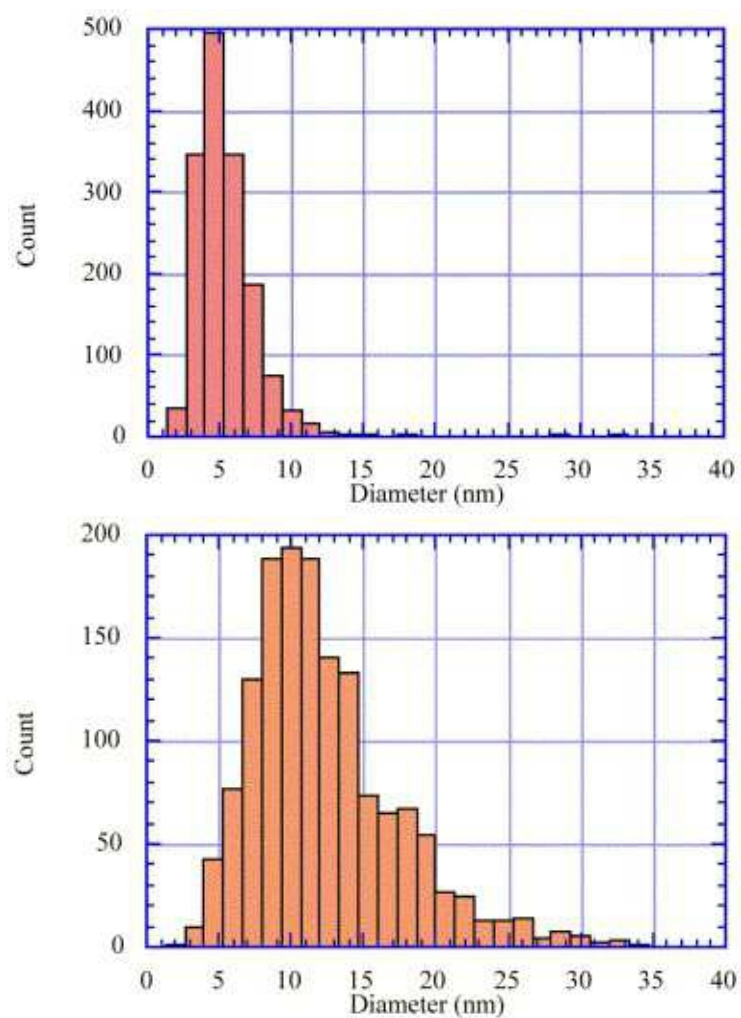


Figure 1.35 Cobalt particle size distributions in (a) the fresh reduced 700 °C vacuum-annealed Co-Re/SiO₂ and (b) the spent Co-Re/SiO₂ sample from the 3.5 MPa high CO conversion run. – Adapted from Reference [107]

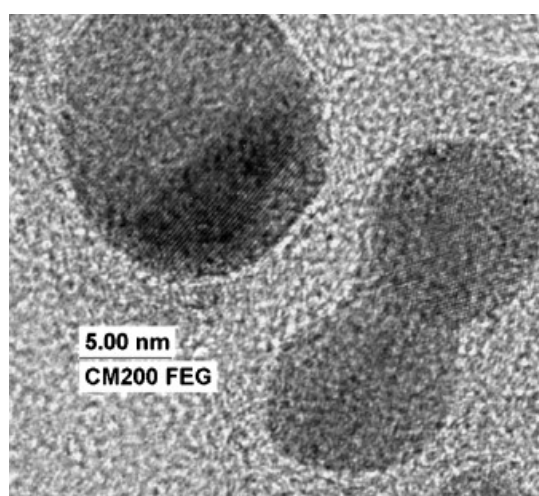


Figure 1.36 TEM image of two cobalt particles during coalescence - Adapted from reference [108]

Sun et al. [109] studied the effect of syngas ratio on the crystallite growth. 15%Co/SiO₂ catalysts was subjected to syngas in a down flow fixed bed reactor (210 °C, 20 bar). The three reactions (H₂/CO = 1, 2, 3) were all run for 800 h for comparison. Under the same syngas space velocity (1000 h⁻¹) the *ex-situ* XRD analysis showed higher crystallite size in the spent catalysts in the case of higher inlet syngas ratio (Table 1.7) Catalytic tests also indicated a higher deactivation rate in the case of H₂/CO = 3.

Table 1.7 The physico-chemical properties and deactivation rates of the spent catalysts- Adapted from reference [109]

H ₂ / CO	Particle size ^a (nm)	Deactivation Rate (h ⁻¹) – dX(CO + H ₂) / dt
1	17	0.022 %
2	19	0.043 %
3	20	0.053 %

^aThe catalyst was treated with solvent-extraction

Bian et al. [64] investigated the behavior of a calcined and an uncalcined SiO₂ catalysts exposed to syngas in a fixed bed reactor for 60 h at 10 bar, 200-240°C and CO conversion up to 90%. XRD, EXAFS and H₂ chemisorption were indicative of the crystallite size increased during FTS . As expected the uncalcined catalyst (initial crystallite size = 10.4 nm) was more sensitive to sintering whereas the calcined catalyst displayed only minor changes in crystallite size (initial particle diameter = 29.1 nm). In addition, the sintering was shown to be accelerated once the temperature is increased from 200°C to 240°C (Table 1.8).

Table 1.8 Characterization results for the used Co/SiO₂ catalysts by H₂ chemisorptions [64]

Sample	Reaction temperature (°C), CO conversion (%)	H ₂ uptake (ml/g)	D _p (nm)
uncalcined Co/SiO ₂	200, 40	2.52	11.1
uncalcined Co/SiO ₂	240, 40	1.74	16.1
uncalcined Co/SiO ₂	240, 90	1.63	17.2
calcined Co/SiO ₂	200, 40	1.01	28.8
calcined Co/SiO ₂	240, 40	0.93	31.3
calcined Co/SiO ₂	240, 90	0.9	32.3

Tavasoli et al. [110], [111] concluded that catalyst deactivation is related to sintering at low steam partial pressures where the effect of water-induced oxidation is not so severe. Cobalt re-oxidation and formation of mixed metal–support compounds were identified as the main deactivation mechanisms when P_{H₂O}/(P_{H₂} + P_{CO}) was above 0.75. Experiments were

performed in a laboratory fixed-bed reactor using a Co-Ru/ γ -Al₂O₃ catalyst. According to the authors sintering is the main cause of long-term deactivation in FTS and the change in cobalt cluster size can be modeled using a power law expression having a power order of $n = 39.7$ [110]. These results were derived from H₂ chemisorption of a fresh catalyst and catalyst subjected to 220°C, 20 bar, and a H₂/CO = 2 for a period of 850 and 1000 h. Additionally, the increase in the C₅₊ selectivity with time on stream (TOS) supports these results since larger cobalt particles are more selective to higher molecular weight products. Finally, analysis of samples from different parts of the reactor bed showed an increased particle growth towards the reactor outlet. This sintering gradient along the reactor may be due to different partial pressures of steam or temperature gradients along the reactor bed.

Commercial Sasol catalysts containing Co/Pt/Al₂O₃ used in slurry reactor were analyzed under commercial FT conditions (230 °C, 20 bar, H₂/CO~2) [112]. The samples were periodically unloaded from the reactor, treated in a procedure consisting of xylene extraction followed by hydrocracking, passivated over dry ice and characterized by means of H₂ chemisorption and high angle annular dark field-transmission electron microscopy (HAADF-TEM). Crystallite morphology changes were evident after 3 days on stream. Crystallite growth was observed up to 5-7 days reaction time (Fig. 1.37) and suggested as the main mechanism for initial catalysts deactivation. A simple deactivation model (assuming a direct correlation between cobalt metal surface area and cobalt catalyst activity [61]) proposed that 30-40% of total deactivation could be attributed to sintering.

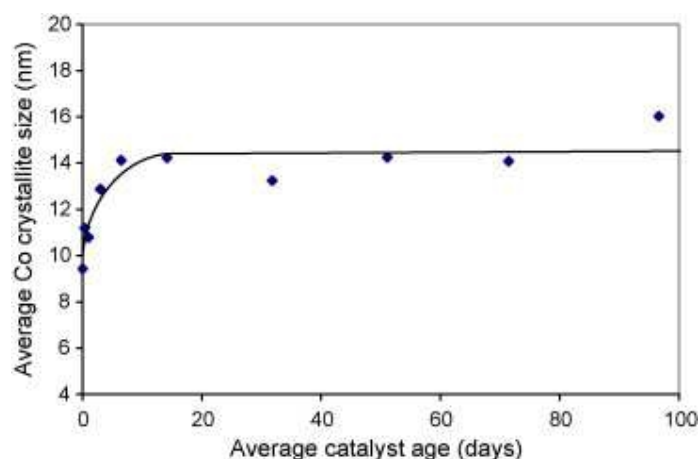


Figure 1.37 Average surface area weighted cobalt crystallite size as function of average catalyst age, as determined by means of TEM/HAADF – Adapted from Reference [112]

Recently an *in-situ* XRD-XAS study published by Rønning et al. [80] used synchrotron radiation as a tool to follow the Co crystallite size of Re-promoted Co/ γ -Al₂O₃

catalyst. Plug flow hydrodynamics can be suggested in the capillary reactor cell, initially proposed by Clausen group [113]. Line broadening analysis (LBA) of XRD spectra during FTS start-up at 210 °C suggested that no crystallite sintering took place in this phase. However further temperature increase to 400 °C accelerated sintering leading to 20% increase in the crystallite size. Catalyst exposure to syngas under typical industrial conditions ($T = 483$ K, $P = 18$ bar, $GHSV = 7.8$ $\text{NI}/(\text{g}_{\text{cat}} \text{ h})$, $\text{CO conversion} = 30\text{-}50\%$) up to 6 h showed no detectable changes in the cobalt crystallite size (Fig. 1.38).

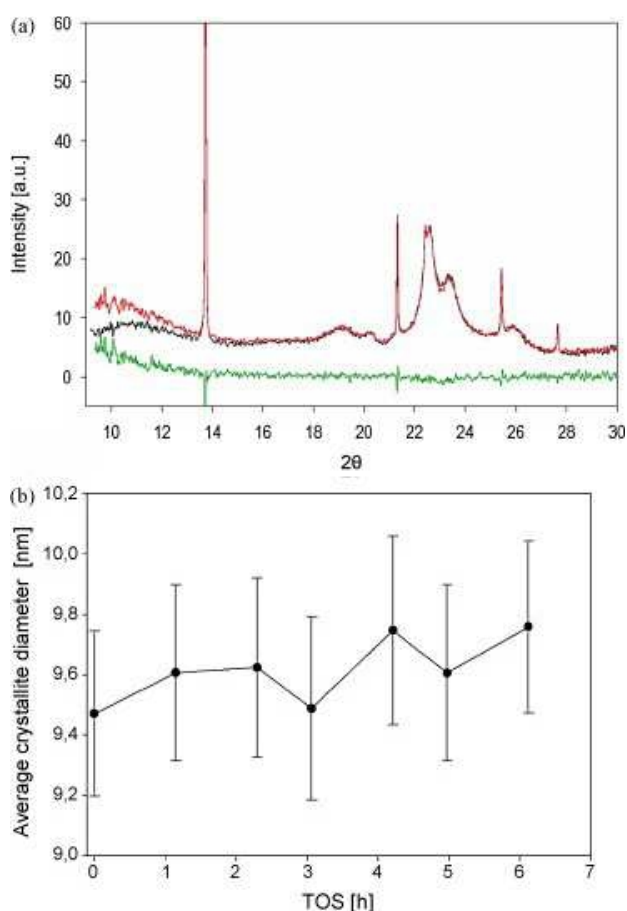


Figure 1.38 (a) The difference curve (green) of the two diffractograms collected at the start (black) and at the end of the FT experiment. (b) LBA at different stages of the reaction using the Scherrer equation, $\lambda = 0.8007$ Å. – Adapted from Reference [80]

Karaca et al. [114] used the similar reactor geometry (Fig. 1.39) to perform an *in-situ* synchrotron XRD study of crystallite size evolution during FTS. Alumina supported cobalt catalysts were tested at 210 °C, 20 bar and $\text{H}_2/\text{CO} = 2$. Cobalt-fcc phase sintering was observed during the initial stages of the reaction with a diameter increase from 6 to 7 nm in 100 min (Fig. 1.40) while the size of cobalt hcp crystallites (cobalt minor phase) remains relatively stable.

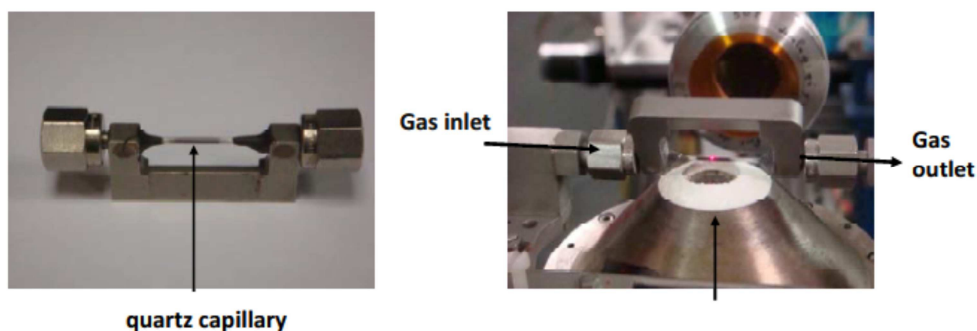


Figure 1.39 Capillary reactor used for in-situ XRD measurements.- Adapted from Reference [115]

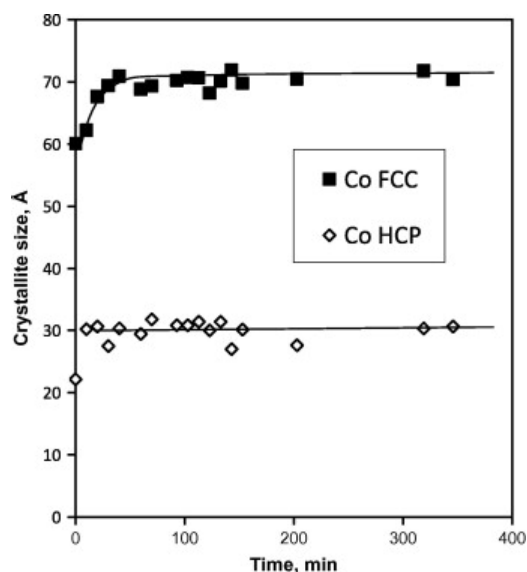


Figure 1.40 Evolution of cobalt particle sizes in CoPt/Al₂O₃-N1 during FT synthesis ($T = 493$ K, $P = 20$ bar, $H_2/CO = 2$, $GHSV = 25,000$ ml $g^{-1} h^{-1}$) calculated using full profile matching (instrument broadening was deduced using standard silicon material). – Adapted from reference [114]

The sintering could also be detected based on the catalyst activity. Bartholomew [116] and Yermakov [117] and [118] pioneered this field in 1985, and later Iglesia and co-workers studied the surface-specific activity, often referred to as turnover frequency (*TOF*) for cobalt particle size between 9-200 nm [119], [120], and [57]. Recently Bezemer et al. [62] have further extended the analysis into smaller cobalt particles using carbon nanofibers (CNF) as an inert support material as there are several evidences that support material may have masked the cobalt particle size effects [90], [60], and [121]. It was seen that larger cobalt crystallites have higher C_{5+} but constant methane selectivity with respect to normal 4-5 nm particles as Fig. 1.41 demonstrates.

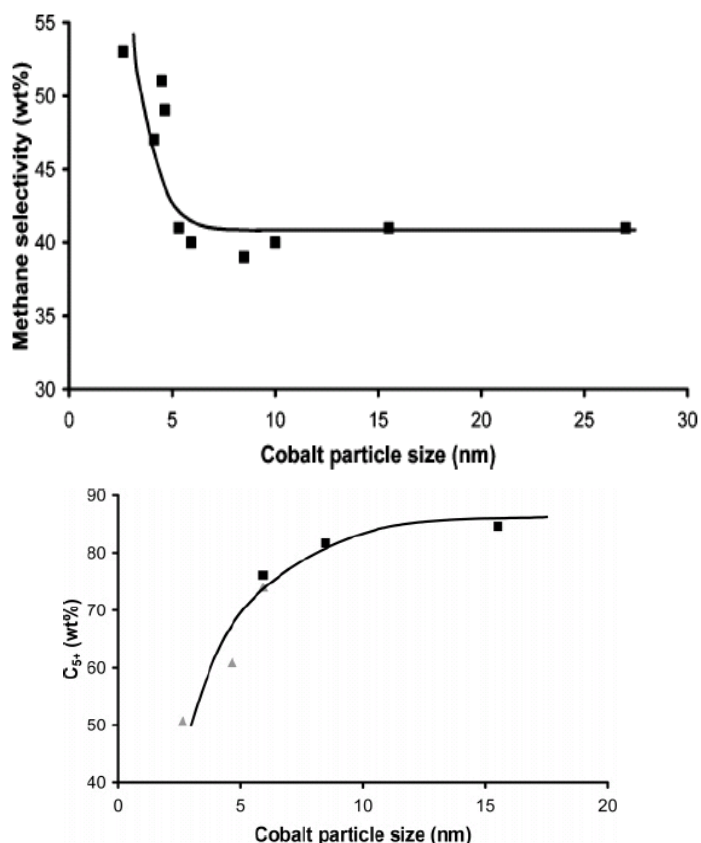


Figure 1.41 The influence of cobalt particle size on (a) methane selectivity (220°C, 1 bar, H₂/CO = 2) and (b) C₅₊ selectivity measured at 35 bar; ■ at 210 °C and ▲ at 250 °C of Co/CNT catalyst [62]

Although sintering is commonly considered to be irreversible, crystallite redispersion assisted by the Kirkendall effect [122], [123] could be used to reverse the phenomenon. The reduction-oxidation-reduction (ROR) cycles at certain conditions are suggested to help cobalt nanoparticles to regain dispersion [61]. The Kirkendall effect occurs as a result of different diffusivities of cobalt and oxygen. After the oxidation step the previously metallic particles (Fig. 1.42 (a)) are transformed into hollow Co₃O₄ particles (Fig. 1.42 (b)) as the rapid outward Co diffusion (migration) through the oxide layer occurs, creating “Kirkendall voids” [61] close to metal-oxide interface. In the reduction phase (Fig. 1.42 (c)) the hollow Co₃O₄ nanoparticles break up to smaller metallic particles. Although the ROR cycles lead to smaller crystallites with similar initial CO conversion, higher deactivation rate are usually observed for the re-dispersed catalysts [106].

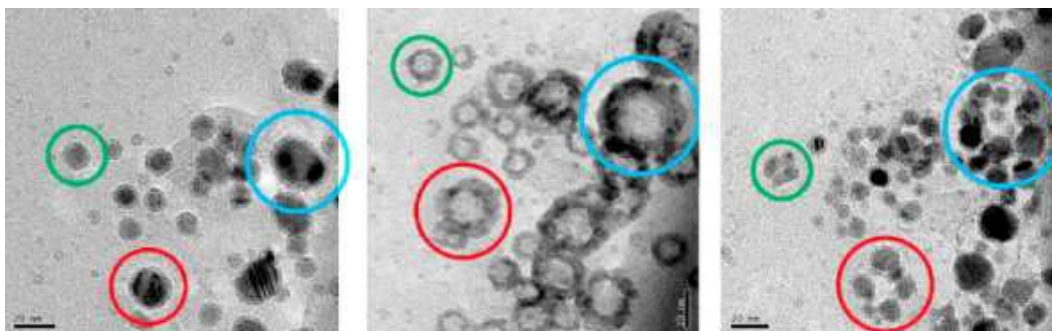


Figure 1.42 Co particles supported on a flat SiO₂ support during different stages of an oxidation reduction cycle. Model catalyst in the metallic state before oxidation (left). Hollow oxide particles, formed upon oxidation (middle). Reduction of the hollow particles, which break up into several smaller metallic particles (right). – Adapted from reference [61]

1.2.3.2. Support sintering

Sintering of the catalyst support is possible especially under extreme hydrothermal conditions. However, since FTS is usually performed at rather mild conditions, the phenomenon is rarely observed in the literature. Huber et al. [124] suggested that sintering of silica support could cause cobalt-based catalyst deactivation. High surface area silica-supported catalysts were treated by high pressure steam at 220°C resembling the typical FTS conditions. The BET surface area was reduced significantly (77-79%) and the pore size distribution was affected (Fig. 1.43). Activity measurements on the same catalysts showed activity loss during time on stream.

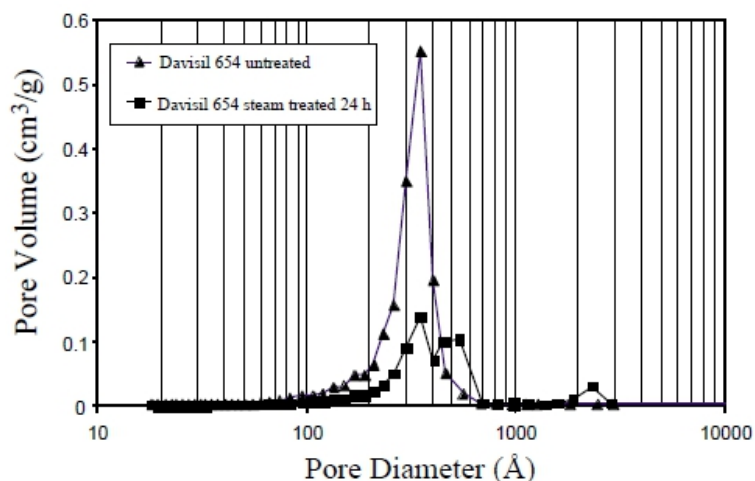


Figure 1.43 Pore size distribution measurements of silica-supported catalyst (Davisil 654) before and after steam treatments. (Average pore diameter of 250 Å for untreated and 290 Å for steam-treated sample.) – Adapted from reference [124]

1.2.4. Carbon compounds

Carbon is generally known to have both positive and negative effects on the catalysts [46], [125]. Bartholomew [126] has given a detailed list of the carbon species which could be

formed on a catalyst surface during methanation reaction. The origin of different carbon species is supposed to be the presence of carbon monoxide in the syngas, as the FTS mechanism has been proposed to proceed through different carbon-assisted mechanisms such as CO dissociation, H₂ assisted CO dissociation, and molecularly adsorbed CO. In any case the catalyst surface is covered with a wide range of carbon species, each of which could react in a different manner and lead to carbon-containing molecules formation. In addition, the CO disproportionation reaction (so-called Boudouard reaction) may enhance the carbon formation as well (Fig. 1.44). It is generally believed that the carbon deposition on the surface is more pronounced in the case of hydrogen-deficient environments and therefore the typical syngas ratio of H₂/CO = 2 may limit carbon formation on the surface. Indeed it is generally accepted that Fischer-Tropsch reaction is carbon insensitive [125], however several authors pointed to FT catalysts deactivation due to the formation of several carbon-containing molecules.

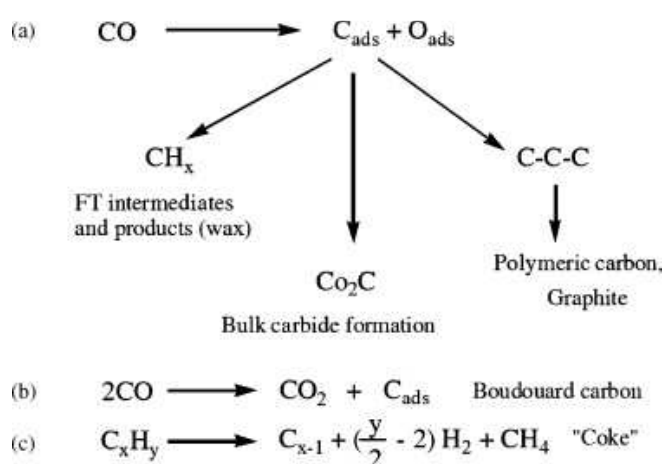


Figure 1.44 Possible carbon formation routes on cobalt based catalysts during Fischer-Tropsch synthesis. - Adapted from reference [127].

Temperature programmed techniques are among the most common techniques to detect the carbon formation in the literature [128], [129] and [130]. The deactivated catalyst is usually exposed to high temperature hydrogen in order to follow the evolution of methane and higher hydrocarbons. The carbon species are evaluated according to their hydrogenation resistance. However recently further advanced techniques including energy filtered-transmission electron microscopy (EF-TEM), high sensitivity-low energy ion scattering (HS-LEIS) [129], Auger electron spectroscopy (AES), X-ray photoelectron spectroscopy (XPS), and X-ray diffraction (XRD) [131], [132] were also used.

1.2.4.1. Bulk carbide formation

The formation of bulk carbides is less likely in the cobalt crystallites than iron counterparts [133]. In fact thermodynamic calculations showed that bulk cobalt carbides (Co_2C and Co_3C) are stable only between 500–800 °C [134]. The UBI-QEP method also yielded a lower calculated value for the chemisorption heat of atomic carbon on cobalt (162 kcal/mol) than on iron (200 kcal/mol), suggesting that the possibility of bulk carbide formation is lower in the case of cobalt catalysts [135] and [136].

However Karaca et al [115] have recently observed small peaks of Co_2C species under long exposure of FT catalysts to syngas ($\text{H}_2/\text{CO} = 2$, $T = 220^\circ\text{C}$, $P = 20$ bar) or sharper peaks upon exposure to pure CO stream using *in-situ* XRD technique.

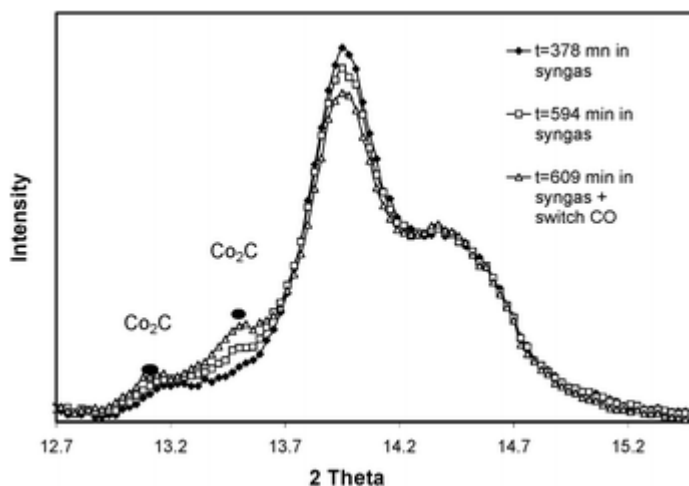


Figure 1.45 Evolution of in situ XRD patterns ($\lambda = 0.5 \text{ \AA}$) of $\text{CoPt}/\text{Al}_2\text{O}_3$ -773 catalyst at longer time-on-stream in syngas and under the flow of pure CO ($T = 493 \text{ K}$, $P = 20$ bar). – Adapted from reference [115]

The authors have also shown that the bulk cobalt carbide could be decomposed once treated with hydrogen. The hydrogen treatment creates primarily a hexagonal close packed (*hcp*) cobalt structure which apparently is more active in FTS than traditional *fcc* structure as reported by Ducreux and coworkers [137]. Fig. 1.46 shows the structural representation of different Co metallic phases as well as Co_2C .

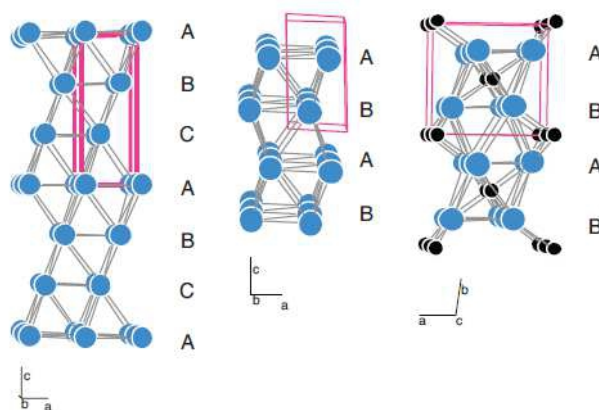


Figure 1.46 Structural representation of fcc Co (left), hcp Co (center) and Co_2C (right). – Adapted from reference [137]

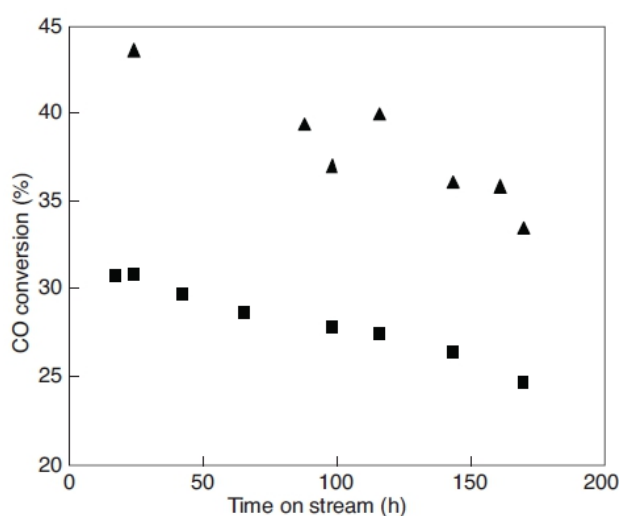


Figure 1.47 Activity of the $\text{Co}/\text{Al}_2\text{O}_3$ catalyst, activated by reduction (fcc structure, squares) and by carbide formation and decomposition (hcp structure, triangles). – Adapted from reference [137]

They [137] have also proposed a direct link between the bulk cobalt carbide formation and catalysts deactivation. They have studied cobalt-based catalysts supported on Al_2O_3 , SiO_2 , and TiO_2 at $230\text{ }^\circ\text{C}$, 3 bar, $\text{H}_2/\text{CO} = 9$ and CO conversion $\sim 20\%$. Although the activity decline was different for the different supports, it was simultaneous with the appearance of Co_2C peaks in the XRD spectra. The TiO_2 -supported catalysts however did not show any Co_2C peak during the analysis.

The formation of bulk cobalt carbide was also reported by Jacobs et al. [138], Gruver and coworkers [139], Xiong et al. [140] using XRD and XPS, and Pennline et al. [141] and [142] using a bifunctional catalyst.

1.2.4.2. Carbon fouling

The long hydrocarbon products of FT reaction, accumulated on the catalyst surface, could limit the reactants diffusion rates and therefore slow down FT reaction rate [143]. Carbon fouling refers to accumulation and blocking of catalyst micropores (and hence catalytically active sites) by long hydrocarbons, or so-called polymeric amorphous carbon, that are produced during either main or side reactions including condensation, oligomerizations, cracking, etc. Furthermore, physical blocking and poisoning of surface active sites by more stable carbon compound with less hydrogen content, e.g. graphite-like species may result in direct catalyst deactivation as reported by Bartholomew [46] and [126]. Fig. 1.48 shows different types of carbon fouling.

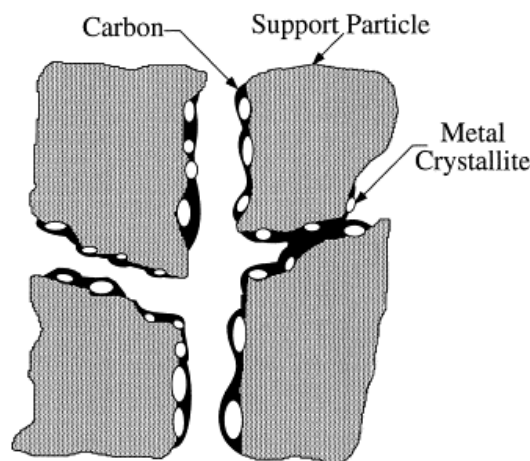


Figure 1.48 Conceptual model of fouling, crystallite encapsulation and pore plugging of a supported metal catalyst due to carbon deposition [46]

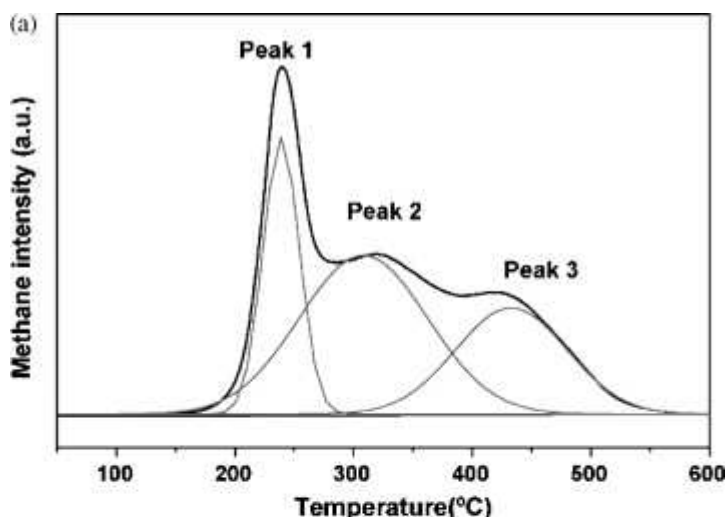
Thermogravimetric-temperature programmed reduction and Auger electron spectroscopy were used by Lee et al. [128] to distinguish different forms of produced CO on a reduced Co/Al₂O₃ sample at different temperatures. Both atomic and polymeric carbons were suggested to be formed. AES results showed that the total carbon deposition was increased with a reduced atomic carbon fraction, once the temperature is increased. Consequently the remaining sample was more resistant to reduction. It was then suggested that the graphitic and/or polymeric carbon have more a diffusion inhibition effect than an electronic modification of surface sites. Activity tests also showed a higher deactivation rate in higher temperatures as well as a shifted product distribution toward unsaturated hydrocarbons.

Niemelä and Krause [144] proposed that selective blockage of catalyst micropores by heavy hydrocarbon compounds and or/coke is responsible for initial Co/SiO₂ catalyst deactivation as the probability of chain growth increased during the reaction.

Catalyst samples obtained from large demonstration units were studied for carbon fouling [129]. 0.05 wt% Pt-20 wt% Co/ γ -Al₂O₃ catalyst samples were unloaded from a 100-barrel/day slurry bubble column reactor operated for 6 months, and dewaxed under inert conditions before characterization by temperature programmed techniques, EF-TEM and HS-LEIS. Catalysts were then gone through temperature programmed hydrogenation (TPH) followed by temperature programmed oxidation (TPO) processes. It was evident that there are at least three major types of carbonaceous species based on their reactivity to H₂ (Fig. 1.49a). The methane peaks are compared to literature TPH values in an attempt to assign them to different types of carbon species (Table 1.9). Subsequent temperature programmed oxidation (TPO) gave a quantitative approximation of the amount of hydrogen resistant carbon accumulating on the surface (Fig. 1.49b).

Table 1.9 Possible species observed in the TPH profile of the wax-extracted catalysts in Fig. 58, based on the literature values reported for TPH of cobalt-based FTS catalysts [129].

Peak	T_{hyd} (°C)	Possible carbon species based on T_{hyd}	Refs.
1	250	Surface carbidic species (atomic carbon)	[128]
		Residual wax/hydrocarbons	[145]
		Bulk cobalt carbide	[139] and [146]
2	330	Residual wax (probably contained in small pores)	[145]
3	445	Polymeric (amorphous) carbon on cobalt or the support	[128]



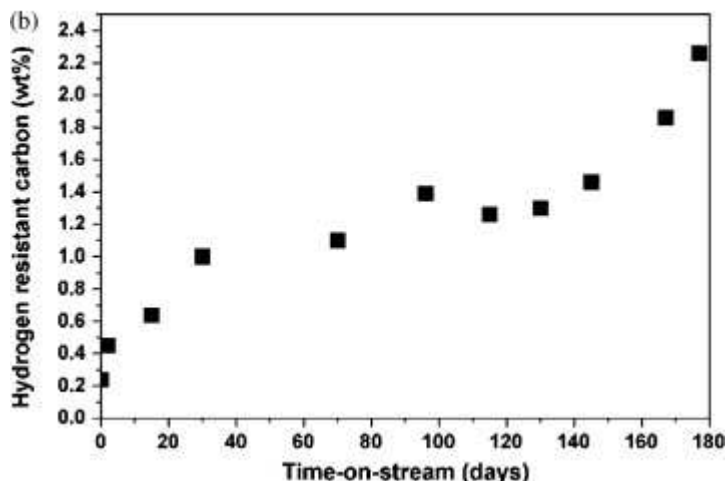


Figure 1.49 (a) Peak deconvolution of a methane profile for TPH of a wax-extracted Co/Pt/Al₂O₃ catalysts from the FTS run in the slurry bubble column. (b) Carbon amounts obtained from TPO experiments following TPH which represents carbon resistant to hydrogen at 350 °C. – Adapted from reference [129]

High resolution-transmission electron microscopy (HR-TEM) confirmed the presence and the nature of carbon species and carbon mapping using EF-TEM images gave the topography of polymeric carbon. The authors concluded that long-term catalyst deactivation could be attributed to polymeric carbon accumulation [129]. Such a conclusion was also made by Font Freide et al. [147] based on the results from laboratory and demonstration pilot plant reactors.

1.2.4.3. Carbon induced surface reconstruction

Cobalt-based catalyst behavior may change once the catalyst surface undergoes a reconstruction as this process alters the nature of active sites and hence the catalytic activity.

Reconstruction may also render the surface more sensitive to events which may deactivate the catalyst. Thus, an indirect contribution of surface reconstruction to activity loss should not be neglected. [45]. However the detection of surface reconstruction is not easy as sophisticated techniques are required basically as it is a dynamic phenomenon and the use of ex-situ tools is not possible. Therefore most researchers used either probe microscopic methods of model compounds or computational approaches [45].

de Groot and Wilson [148] reported that a model flat Co(0001) surface reconstruct into triangular shaped cobalt islands (Fig. 1.50) once exposed to a typical syngas stream (250 °C, 4 bar and constant flow 1 ml/min of H₂/CO = 2). Surface reconstruction in similar model catalysts was further confirmed by polarization modulation-reflection absorption infrared spectroscopy (PM-RAIRS) [149] and [150].

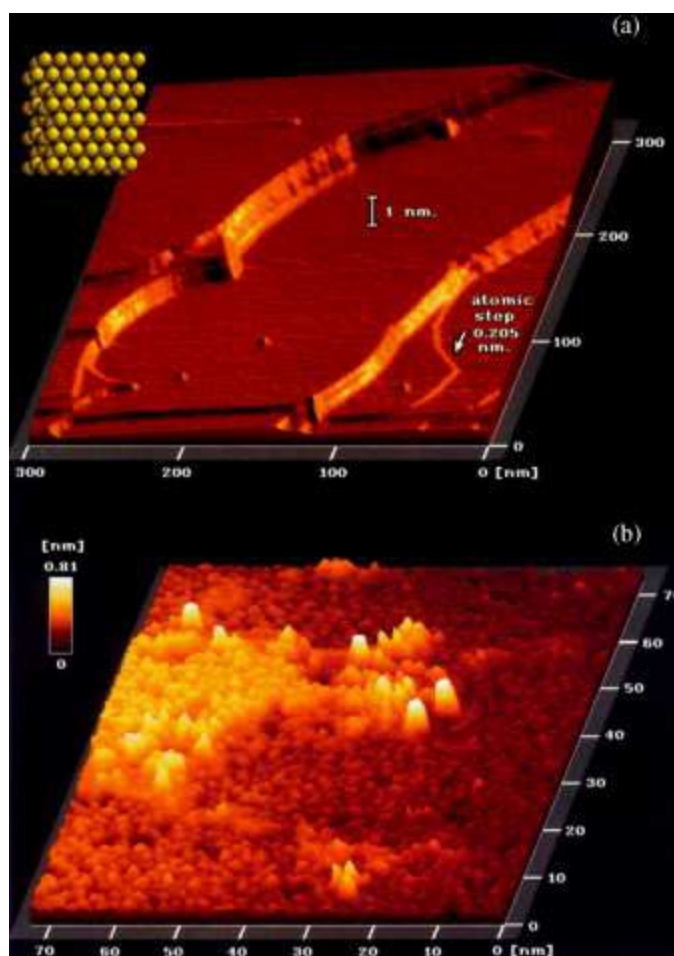


Figure 1.50 (a) STM image of the clean Co (0 0 0 1) surface (prior to reaction) showing atomically flat terraces 150 nm (ca. 600 atoms) in width (tunneling current $I_t = 2$ nA, sample bias $V = 0.05$ V). The smallest step visible is monatomic in height, 0.205 nm being the expected single atom step height on Co (0 0 0 1). (b) STM image of the Co (0 0 0 1) surface after 1 h exposure to high-pressure CO hydrogenation conditions ($I_t = 0.5$ nA, $V = 0.5$ V). Inset: hard-sphere model of the bulk-terminated Co (0 0 0 1) surface [148].

1.2.5. Metal-support solid-state interactions

The cobalt-support mixed compounds formations were frequently observed in the literature especially in the case of alumina-supported catalysts [121]. Although these mixed-oxide compounds are hardly reducible, it has been reported that they could enhance the crystallite resistance to sintering [151] even in high temperatures. The mixed metal-support compounds are known to be formed principally during catalysts preparation steps including calcination and reduction [152], [153], [154], [155], [156] and [157]. These steps enhance the migration/diffusion of cobalt cations (e.g. Co^{2+} , Co^{3+}) into the support crystal structure and the support cations (e.g. Al^{3+}) toward the surface [158], [159] and [160].

The effect of mixed oxide formation on the catalytic activity has been investigated by several researchers. Davis group [88] and [161] have used platinum promoted 15wt% Co/ γ - Al_2O_3 catalysts exposed to syngas inside a CSTR (210 °C, 20 and 29.3 bar, $\text{H}_2/\text{CO} = 2$, 750

rpm and 30% Ar in the feed). Both different space velocities and the external water addition are examined to see the effect of different steam concentrations. The catalyst samples before, during, and after water treatment were analyzed by XAS. The spectra were normalized and derivatives were obtained. XAS results strongly suggested that the irreversible loss in activity after the external introduction of steam at high concentrations led to the reaction of the cobalt clusters with the support, forming cobalt aluminate-like species. A sharp peak rise ~ 5 eV after the edge was observed in XANES results resembling the sharp feature of cobalt aluminate, but absent in CoO. Activity measurement showed a low CO conversion which increased linearly at higher syngas conversion. This was attributed to increase in water-gas-shift reaction with higher water partial pressures. Therefore it was suggested that another cobalt species such as cobalt aluminate enhances the catalyst WGS activity. This is in line with the XAS data for the formation of mixed oxide compounds.

Formation of hydrated cobalt silicates was observed by Chen et al. [162] and [163] on a Co/ZrO₂/SiO₂ catalyst (20 bar, 500 h⁻¹, H₂/CO = 2 in the temperature range from 186 to 191 °C) by XRD, FT-IR, TPR and TGA. It was proposed that the catalyst deactivation is mainly attributed to the hydrated cobalt silicates and their formation is accelerated at high water partial pressures.

1.3. Modeling of deactivation phenomena

Although several experimental works exist in the literature, the FT catalyst deactivation suffers from a comprehensive quantitative approach which could explain the catalyst behavior under different deactivation conditions, and the effect of operating parameters including temperature, pressure, syngas ratio, etc.

The deactivation models could be generally divided into two main categories: (a) the microscopic models which study the effect of operating conditions on the microscopic properties of catalyst sample during deactivation including crystallite size, dispersion, surface area, and (b) macroscopic models which study the catalytic performance with time in a given reactor environment.

1.3.1. Microscopic models

The microscopic models are mainly concerned with the evolution of catalyst physico-chemical properties with time during deactivation process. Both empirical and mechanistic approaches are proposed in the literature.

The microscopic models are basically developed for catalyst sintering. Fuentes [164] and Bartholomew [165], [166], [167] provided description of sintering in terms of variation in metal dispersion. The change in catalyst dispersion with time was studied using an empiric correlation proposed as early as in 1975, where the reduction in dispersion \bar{D} with time t was correlated in a simple power law expression (*SPLE*):

$$\frac{-d(\bar{D}/\bar{D}_0)}{dt} = k_s \left(\frac{\bar{D}}{\bar{D}_0} \right)^n \quad (1.8)$$

where k_s is the temperature-dependent sintering constant, \bar{D}_0 the initial dispersion, and n the sintering order, which may vary from 3 to 15 [165] and [168].

However, this simple rate expression is very limited in its ability to represent and more importantly, to predict experimental data. Indeed it is found that even for the same catalyst sintering order may vary as a function of time, temperature and atmosphere. Further progress was then done through the application of the general power law expression (*GPLE*) originally developed by Fuentes [169] and co-workers in 1987.

$$\frac{-d(\bar{D}/\bar{D}_0)}{dt} = k_s \left(\frac{\bar{D}}{\bar{D}_0} - \frac{\bar{D}_{eq}}{\bar{D}_0} \right)^m \quad (1.9)$$

which adds a term $-\bar{D}_{eq}/\bar{D}_0$ to correct for the experimental asymptotic trend of the typical dispersion versus time toward a limiting dispersion \bar{D}_{eq} at time $t=\infty$. It was suggested that all sintering data could be fitted to GPLE with either $m = 1$ or 2.

Bartholomew [165] found that for a wide range of supported metallic catalysts, sintering behavior could be well represented using GPLE. For most of catalysts, the sintering order is 2, and it is independent of the operating parameters. It is believed that sintering order of 2 suggests Particle Migration and Coalescence as the main process for the sintering. The order $m = 1$ would be more indicative of Ostwald ripening. The sintering constant (k_s) could be usually fitted into an Arrhenius-type expression with activation energies in the range of 60-80 kJ/mol [170].

The work done by the team of Holmen [171] on de activation of Ni (11 wt%)/(CaO) α -Al₂O₃ tested in methane reforming conditions (T = 500-650°C, P = 1-5 bar, gas flow = 0.36 m³/h), proposed that the decrease in catalyst surface area with time could be expressed using

an equation similar to second-order GPLE (Eq. 1.10). The authors attributed the surface area changes to the particle sintering and carbon deposition on catalyst surface.

$$\frac{-d(S/S_0)}{dt} = k_s \left(\frac{S}{S_0} - \frac{S_{eq}}{S_0} \right)^2 \quad (1.10)$$

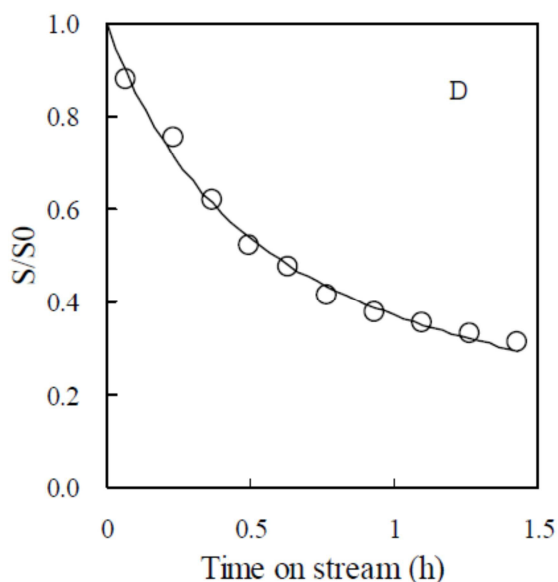


Figure 1.51 (A) Calculated (line) and experimental changes in relative surface area. Line simulated by Eq 10. Reaction conditions: $T = 650\text{ }^{\circ}\text{C}$; $W/F_{\text{CH}_4} = 0.15\text{ g.h/mol}$, $\text{CH}_4/\text{CO}_2/\text{N}_2+\text{Ar} = 1/1/1.89$, $P_{\text{tot}} = 0.5\text{ MPa}$ [171].

Several researchers used particle size distribution to distinguish between different sintering mechanisms (i.e. Ostwald Ripening, Particle Migration and Coalescence, etc.). According to Datye et al [172], Ostwald Ripening follows Lifshitz–Slyozov–Wagner theory [173] which results in an asymmetric particle size distribution shape skewed to the smaller particle sizes and a cut off in the size distribution at a diameter which is twice smaller than the mean particle diameter (Fig. 1.52). The size distribution produced by Particle Migration and Coalescence is very different. It is skewed to the larger sizes (Fig. 61) as shown by Granqvist and Buhrmann [174]. Although such direct reasoning has been challenged by Wanke [175] mainly because of TEM limitations, the appearance of several major developments such as availability of high angle annular dark field (HAADF) imaging in a 200 kV scanning transmission electron microscope (STEM) which increases the reliability of detection of heavy metal particles below 1 nm in diameter could overcome the experimental imaging constraints .

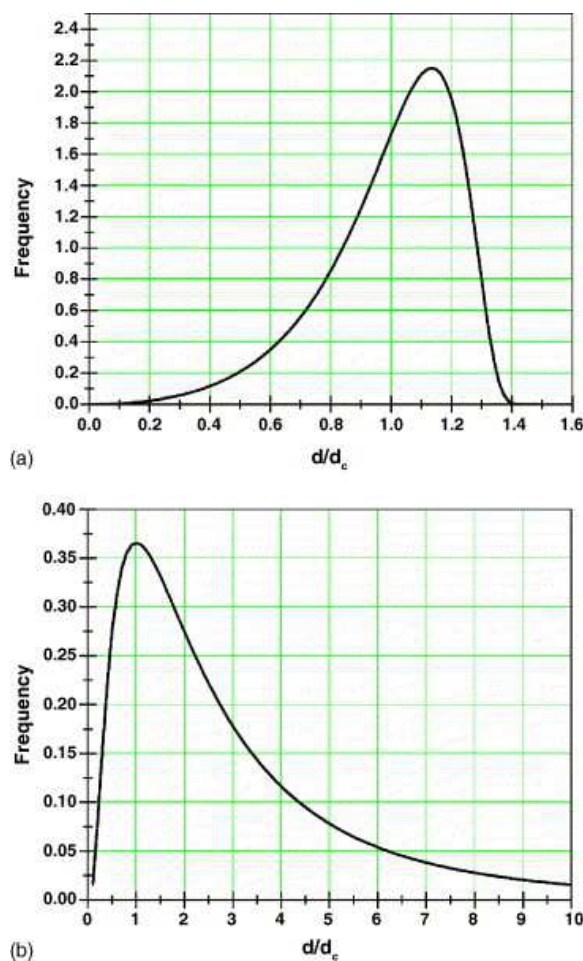


Figure 1.52 Proposed particle size distributions for: (a) Ostwald ripening [173] and (b) log normal distribution [174]

Datye et al. [172] have analyzed the particle size distribution of Pd-based catalysts under an atmosphere of 10% H_2O in flowing N_2 at 900 °C and atmospheric pressure to accelerate sintering. The mean particle size increased from 20 nm to 500 nm as detected by TEM images. The results indicated that at all reaction instances, the particle size distribution could be fitted using a LNDF curve (Fig. 1.53) and therefore they have suggested that particle coalescence and migration could be dominant for Pd-based catalysts.

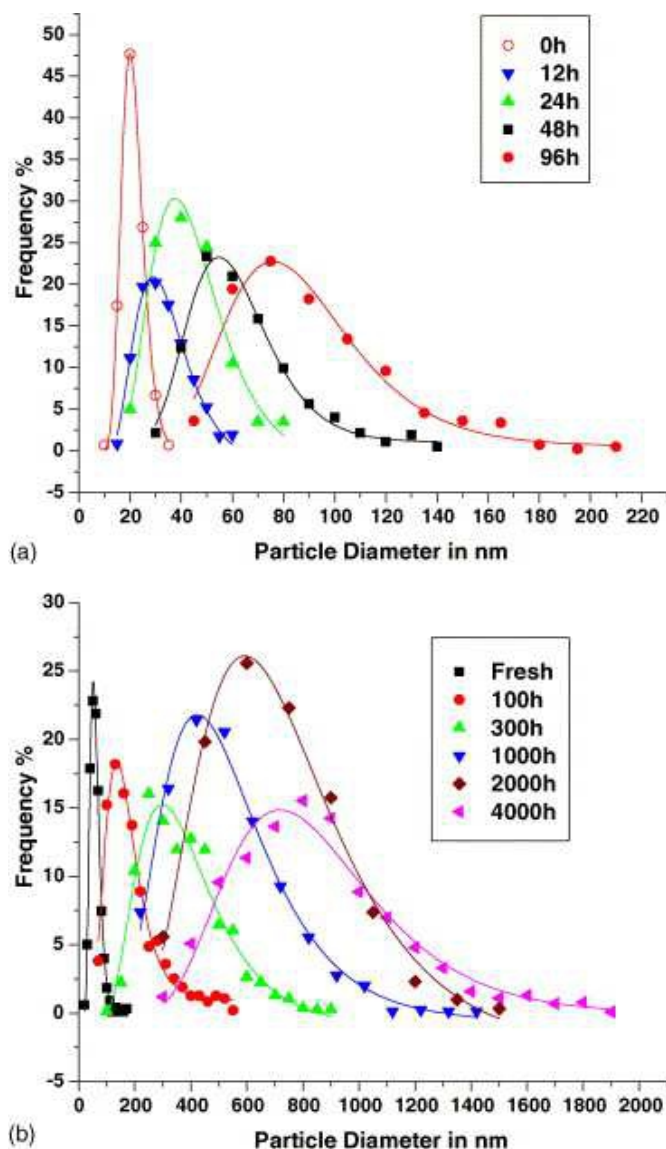


Figure 1.53 Particle size distributions after sintering at 900 °C for differing lengths of time. All data have been fitted using a log normal distribution: (a) 7 wt.% Pd/alumina and (b) 15 wt.% Pd/silica–alumina [172].

Zhu et al. [176] have studied the coke formation in activated carbon catalysts. Novel micro-balance was used to follow the weight change of catalyst sample with time during coke formation. Results showed that coke formation occurs rapidly at first times on stream and becomes increasingly slower as coke piles up. Consequently a logarithmic correlation was proposed to predict the coke accumulation rate (Fig. 1.54):

$$C_k = \beta \ln \left(1 + \frac{r_{k,0} t}{\beta} \right) \quad (1.11)$$

where C_k is the coke concentration, β the deactivation constant, and $r_{k,0}$ the initial coking rate.

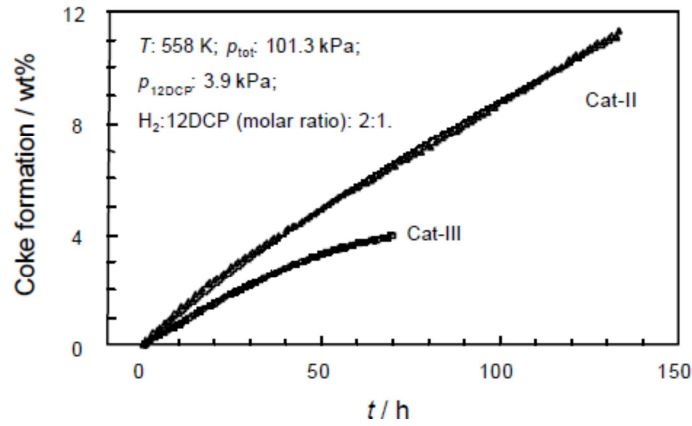


Figure 1.54 Coke formation on Cat-II (0.5 wt% Pt) and Cat-III (0.9 wt% Cu) catalysts for hydrodechlorination of 1,2-dichloropropane. The solid lines are fitted by Eq. 1.11 [176].

Qin et al. [177] have investigated sintering and re-dispersion of cobalt-based FTS catalysts by a mathematical microscopic approach. They have found considering the loss of metal by formation of aluminates species (interaction cobalt-support) that the catalyst deactivation rate could be expressed by:

$$r_d(x,s) = \frac{dx}{dt} = \frac{K_1}{1 + K'_1 \frac{P_{H_2}}{P_{H_2O}}} \varepsilon \left(1 - \frac{x}{\varepsilon}\right)^2 - K_2 P_{H_2}^{1/2} x \left(1 - \frac{x}{\varepsilon}\right) \quad (1.12)$$

with x as number of surface atoms deactivated/ total number of surface atoms, $\varepsilon = 3.1088/d_{Co}(nm)$ for Co/Al₂O₃ catalysts, and $K_1 = 0.0036 \text{ h}^{-1}$, $K'_1 = 0.423$, $K_2 = 1.13 \times 10^{-7} \text{ bar}^{-1/2} \text{ h}^{-1}$ are deactivation constants. However such a mathematical model was not validated with experimental data and it only predicts the catalyst behavior in typical FT conditions.

Bremaud et al. [178] have suggested that for moderate levels of water in a FTS slurry reactor ($C_{H_2O}^L/C_{H_2}^L < 4$ corresponding to $P_{H_2O}/P_{H_2} < 0.4$), a simple kinetic model assuming a reversible oxidation of cobalt active sites by water in competition with their reduction by hydrogen seems to represent satisfactorily the initial behavior of the catalyst.



Consequently assuming the total number of sites (reduced and oxidized) to remain constant during the run and reaction R1.1 is a pseudo-elementary step, the mass balance for the active sites and FT rate equations were suggested as:

$$-\frac{d[*]}{dt} = k_d [*] C_{H_2O}^L - k_r (1 - [*]) C_{H_2}^L \quad (1.13)$$

$$-r_{CO} = -r_{CO}^0 [*] = [*] \times \frac{k_a C_{CO}^L C_{H_2}^L}{(1 + k_b C_{CO}^L)^2} \quad (1.14)$$

The model was shown to be able to represent the experimental data in typical FT conditions as depicted in Fig. 1.55.

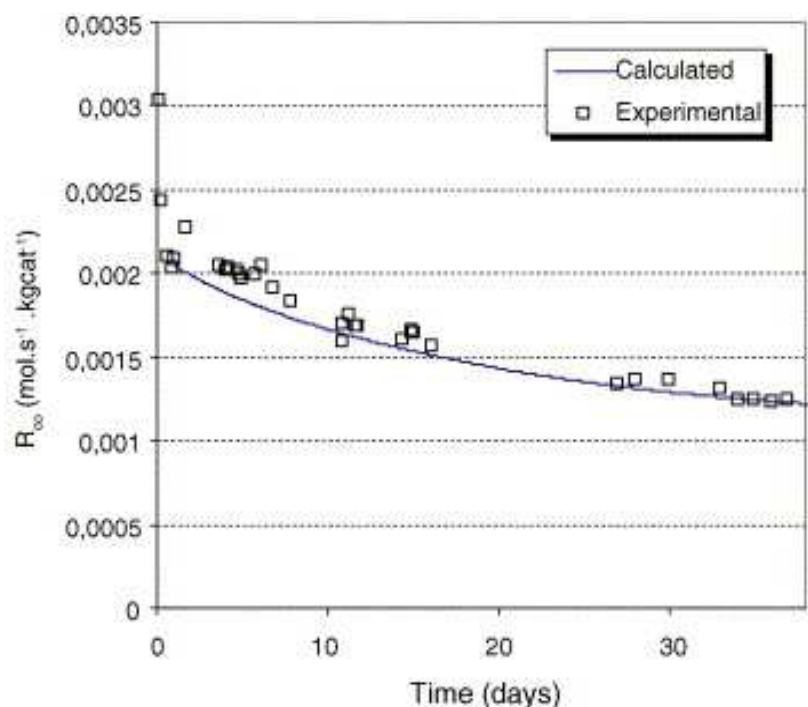


Figure 1.55 Evolution of liquid phase concentration of CO, H₂, H₂O and R_{CO} for the RUN03 (inlet H₂/CO = 3.35) [178].

1.3.2. Empirical macroscopic models

Although the microscopic models are useful in establishing the relationships on how the catalyst particles evolve with time, the macroscopic models are indeed required to express how the catalytic activity is modified during deactivation. The macroscopic models use a modified unsteady state rate equation in line with governing equations (for heat, mass, and momentum balances) for different reactor configurations in order to represent observed deactivation results in laboratory and industrial reactors.

One of the most accepted approaches in macroscopic deactivation modeling, is that one can propose that the kinetic and deactivation terms could be decoupled as suggested by Levenspiel [179], Butt [180], [181],[182], and Froment [183]:

$$\text{rate of reaction}(t) = \text{rate of reaction}(t=0) \times \text{activity}(t) \quad (1.15)$$

where the activity function, $a(t)$, has a fractional value between 0 and 1.

Bartholomew and Farrauto [170] used the same concept to study the catalyst deactivation during a wide range of catalytic reactions. They have proposed that the reaction rate at any instant could be expressed by:

$$-r_m = k(T)f(C)\eta a \quad (1.16)$$

where r_m is the rate of main reaction, $k(T)$ is the rate constant, $f(C)$ is the function of reactants and product concentrations, η is the effectiveness factor (pore diffusional resistance), and a the activity function = reaction rate / fresh catalyst reaction rate.

The decrease in activity with time or deactivation rate was given by:

$$-r_d = -\frac{da}{dt} = k_d g(C)\eta_d a^d \quad (1.17)$$

with k_d the deactivation constant, η_d is the effectiveness factor for deactivation, and d the deactivation order, typically in the range of 0 and 1.

As in the case of *SPLE*, Eq. 1.14 is valid only if the catalyst activity approaches zero at steady state. However there are many deactivation processes (e.g. reversible poisoning or sintering) in which the steady state activity is not zero and thus the application of equation (14) is not correct. Based on Fuentes [164], the use of General Power Law Expression (GPLE) is more appropriate in these cases:

$$-r_d = -\frac{da}{dt} = k_d g(C)\eta_d (a - a_{eq})^d \quad (1.18)$$

where a_s stands for the steady state activity.

Eq. 1.15 was found to fit many experimentally observed catalytic results. Bowman and Bartholomew [184] have used the GPLE to follow the activity function during CO hydrogenation of Ru-based catalyst in a mixed reactor (CSTR) in different temperatures (Fig. 1.56).

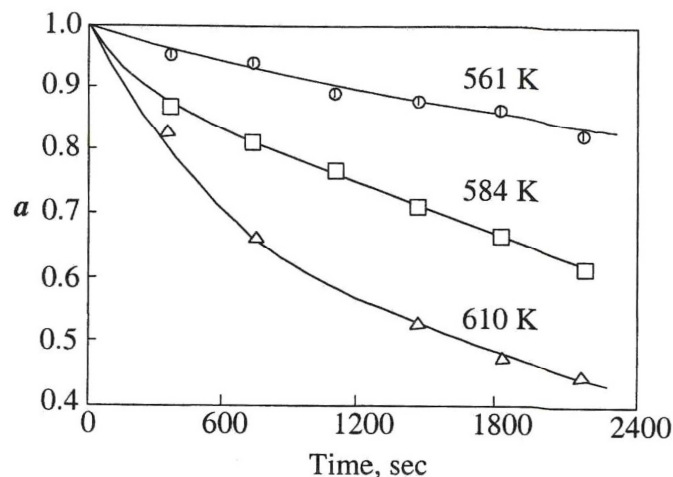


Figure 1.56 Activity versus time during CO hydrogenation on Ru/Al₂O₃ [184]

Lida et al. [185] have used similar equations to evaluate the catalytic performance of Water-Gas-Shift catalysts. Zinc oxide supported copper catalysts (Cu/ZnO) were tested at

200-350°C for 250 h where the change in the reaction r was correlated using initial Cu surface area S_0 , deactivation constant k_d , and deactivation order n :

$$r_t = r_0 a = r_0 \left[(n-1) S_0^{n-1} k_d t + 1 \right]^{-\frac{1}{n-1}} \quad (1.19)$$

Tavasoli et al. [110] have suggested an empirical form for deactivation of ruthenium promoted Co/Al₂O₃ catalyst used in FTS (Fig. 1.57). The initial CO conversion was proposed to decrease by Eq. 1.17 for the first 250 h on stream in a tubular fixed-bed micro-reactor:

$$X_{\text{CO}} = -0.035t_{(\text{h})} + 79.655 \quad (1.20)$$

whereas it was given by

$$X_{\text{CO}} = 85.685t_{(\text{h})}^{-0.0258} \quad (1.21)$$

For $t > 250$ h.

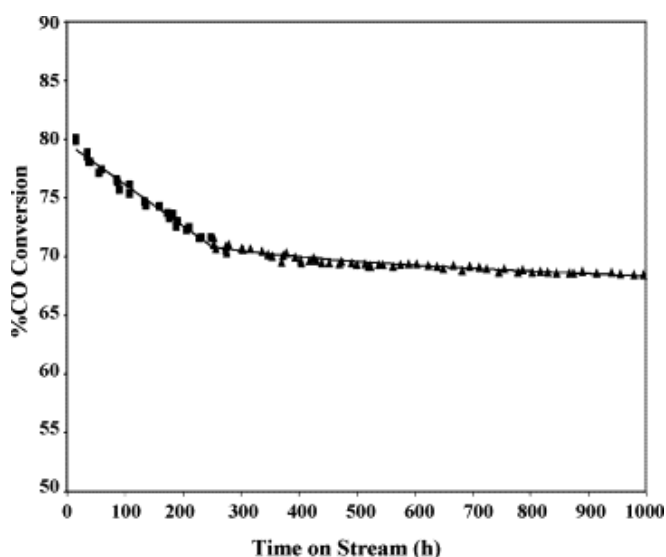


Figure 1.57 %CO conversion with time-on-stream ($T = 220$ °C, $P = 20$ bar, $H_2/CO = 2$) [110].

1.4. Objectives and aims of thesis

The previous sections provided the basic understanding about different aspects of the principles of Fischer-Tropsch synthesis (FTS). The different causes of the catalyst deactivation are described in details as this is the main subject of the current dissertation. Catalyst poisoning, oxidation, sintering, carbon deposition, and mixed oxide formation are discussed as the principle sources of catalyst decay in typical low-temperature Fischer-Tropsch (LTFT) synthesis. Unfortunately no mechanistic quantitative model for deactivation of FT catalysts has been available in the literature.

The goal of this thesis is to provide a quantitative description of the deactivation of cobalt catalysts in fixed bed and slurry FT reactors. The modeling results are compared with the results of catalysts characterization and kinetic measurements.

Sintering seems to be the main responsible phenomenon for the initial catalyst deactivation. The in-situ characterization tools suggest that the activity decline could be related to the crystallite growth during the first period of time on stream. However the long-term deactivation is proposed to be mainly due to the carbon deposition both using the characterization techniques and theoretical analyzes. Consequently these two mechanisms are considered for modeling and interpretation of the experimental results.

The deactivation phenomena are studied in both fixed bed and slurry reactors. The deactivation phenomena are studied using a mechanistic approach. Sintering mechanism involves the effect of water in accelerating the rate of crystallite growth and helps to establish a correlation which could predict the crystallite sizes in different operating conditions. The crystallite size is then included in a modified form of FT rate reaction in order to account for the sintering and to allow to study deactivation in different experimental laboratory-scale reactors. Carbon monoxide dissociation is considered as the main source of carbon deposition in coking modeling.

Once a mechanistic model could be built using the experimental data, the effect of operating conditions on the initial deactivation rate is investigated. Syngas ratio, water and inert co-feeding, and the syngas flow rate are considered.

The laboratory scale millimetric fixed bed reactor then permits to optimize and improve the model and study the effect of temperature on the deactivation apparent activation energy. The effect of crystallite size on the intrinsic rate constants are considered as there are certain evidences that the turn-over-frequency (TOF) rates depend on the cobalt particle diameter. In addition, the long-term deactivation mechanism is developed with carbon deposition as the main phenomena. The rate of surface coverage change of active catalytic sites is correlated to that of carbon-poisoned sites which in turn depends on the operating conditions. Such a mechanism is included in the reactor modeling and it is adjusted based on the experimental data. The effect of hot and cold condensers on the apparent CO conversion is investigated. This experimental artifact could infer in the data validation and model applications.

FT synthesis and catalyst deactivation are then modeled in the slurry reactor under transient conditions. The effect of different operating conditions on the rate of activity decline

is investigated. The model limitations are discussed. The relative comparison of fixed bed and slurry reactor behavior to catalyst deactivation is then followed in order to explain different catalytic observations in different reactors.

A set of theoretical thermodynamic calculations, catalyst characterization tools, and experimental catalytic tests are performed in order to support and validate the modeling results. The methodology and tools employed in this thesis are described in detail in Chapter 2.

1.5. References

- [1] B. Bensaïd, Alternative Motor Fuels Today and Tomorrow, in, IFP Panorama, 2005.
- [2] A.G. Douaud, C. , Les nouvelles Technologies de moteurs et de carburants pour les transports routiers. , in, www.worldenergy.org.
- [3] B.G.W. Frederick E. Pinkerton, Bottling the Hydrogen Genie, *The Industrial Physicist*, 10 (2004) 20-23.
- [4] T.W. Bank, Global Gas Flaring Reduction Partnership (GGFR), in, 2011.
- [5] A. Lecarpentier, Short-term trends in the gas industry, in: Panorama, IFP Energies nouvelles, 2011.
- [6] J.B.S. P. Sabatier, New methane synthesis, *Compt. Rend. Acad. Sci.*, 134 (1902) 514.
- [7] Fischer-Tropsch Archive, in.
- [8] H.T. F. Fischer, in, 1922.
- [9] H.T. F. Fischer, *Brennst. Chem.*, 4 (1923) 276.
- [10] R.B. Anderson, *The Fischer-Tropsch synthesis*, Academic Press, New York, 1984.
- [11] M.E. Dry, The Fischer–Tropsch process: 1950–2000, *Catalysis Today*, 71 (2002) 227-241.
- [12] S. Sun, N. Tsubaki, K. Fujimoto, The reaction performances and characterization of Fischer–Tropsch synthesis Co/SiO₂ catalysts prepared from mixed cobalt salts, *Applied Catalysis A: General*, 202 (2000) 121-131.
- [13] H. Karaca, Propriétés catalytiques et versatilité des catalyseurs à base de cobalt lors du procédé Fischer-Tropsch, in: *Sciences de la Matière, du Rayonnement et de l'Environnement*, University of Lille, Lille, France, 2010.
- [14] M. Röper, *Adv. Catal, Catal. Rev.*, 41 (1984).
- [15] P. Chaumette, C. Verdon, P. Boucot, Influence of the hydrocarbons distribution on the heat produced during Fischer-Tropsch synthesis, *Topics in Catalysis*, 2 (1995) 301-311.
- [16] A.A. Adesina, Hydrocarbon synthesis via Fischer-Tropsch reaction: travaux and triumphs, *Applied Catalysis A: General*, 138 (1996) 345-367.
- [17] J.P. Hindermann, G.J. Hutchings, A. Kiennemann, Mechanistic Aspects of the Formation of Hydrocarbons and Alcohols from CO Hydrogenation, *Catalysis Reviews*, 35 (1993) 1-127.
- [18] G.P. Van Der Laan, A.A.C.M. Beenackers, Kinetics and Selectivity of the Fischer–Tropsch Synthesis: A Literature Review, *Catalysis Reviews*, 41 (1999) 255-318.
- [19] J. Yang, Y. Liu, J. Chang, Y.-N. Wang, L. Bai, Y.-Y. Xu, H.-W. Xiang, Y.-W. Li, B. Zhong, Detailed Kinetics of Fischer–Tropsch Synthesis on an Industrial Fe–Mn Catalyst, *Industrial & Engineering Chemistry Research*, 42 (2003) 5066-5090.
- [20] G. Henrici-Olivé, S. Olivé, The Fischer-Tropsch Synthesis: Molecular Weight Distribution of Primary Products and Reaction Mechanism, *Angewandte Chemie International Edition in English*, 15 (1976) 136-141.
- [21] I. Puskas, R.S. Hurlbut, Comments about the causes of deviations from the Anderson–Schulz–Flory distribution of the Fischer–Tropsch reaction products, *Catalysis Today*, 84 (2003) 99-109.
- [22] E. Iglesia, S.C. Reyes, R.J. Madon, S.L. Soled, Selectivity Control and Catalyst Design in the Fischer-Tropsch Synthesis: Sites, Pellets, and Reactors, in: H.P. D.D. Eley, B.W. Paul (Eds.) *Advances in Catalysis*, Academic Press, 1993, pp. 221-302.
- [23] E.W. Kuipers, I.H. Vinkenburg, H. Oosterbeek, Chain Length Dependence of α -Olefin Readsorption in Fischer-Tropsch Synthesis, *Journal of Catalysis*, 152 (1995) 137-146.
- [24] E. Iglesia, S.C. Reyes, R.J. Madon, Transport-enhanced α -olefin readsorption pathways in Ru-catalyzed hydrocarbon synthesis, *Journal of Catalysis*, 129 (1991) 238-256.

- [25] R.J. Madon, E. Iglesia, The Importance of Olefin Readsorption and H₂/CO Reactant Ratio for Hydrocarbon Chain Growth on Ruthenium Catalysts, *Journal of Catalysis*, 139 (1993) 576-590.
- [26] J. Gao, B. Wu, L. Zhou, Y. Yang, X. Hao, J. Xu, Y. Xu, Y. Li, Irregularities in Product Distribution of Fischer–Tropsch Synthesis Due to Experimental Artifact, *Industrial & Engineering Chemistry Research*, 51 (2012) 11618-11628.
- [27] I.C. Yates, C.N. Satterfield, Intrinsic kinetics of the Fischer-Tropsch synthesis on a cobalt catalyst, *Energy & Fuels*, 5 (1991) 168-173.
- [28] M.E. Dry, Practical and theoretical aspects of the catalytic Fischer-Tropsch process, *Applied Catalysis A: General*, 138 (1996) 319-344.
- [29] X. Dupain, R.A. Krul, C.J. Schaverien, M. Makkee, J.A. Moulijn, Production of clean transportation fuels and lower olefins from Fischer-Tropsch Synthesis waxes under fluid catalytic cracking conditions: The potential of highly paraffinic feedstocks for FCC, *Applied Catalysis B: Environmental*, 63 (2006) 277-295.
- [30] A.P.D. Steynberg, M. E., Fischer-Tropsch Technology, *Studies in Surface Science and Catalysis*, 152 (2004).
- [31] H. Schulz, Short history and present trends of Fischer–Tropsch synthesis, *Applied Catalysis A: General*, 186 (1999) 3-12.
- [32] B.H. Davis, Fischer–Tropsch synthesis: current mechanism and futuristic needs, *Fuel Processing Technology*, 71 (2001) 157-166.
- [33] H. Schulz, Major and Minor Reactions in Fischer–Tropsch Synthesis on Cobalt Catalysts, *Topics in Catalysis*, 26 (2003) 73-85.
- [34] B.H. Davis, Fischer–Tropsch Synthesis: Reaction mechanisms for iron catalysts, *Catalysis Today*, 141 (2009) 25-33.
- [35] M.J. Overett, R.O. Hill, J.R. Moss, Organometallic chemistry and surface science: mechanistic models for the Fischer–Tropsch synthesis, *Coordination Chemistry Reviews*, 206–207 (2000) 581-605.
- [36] J. SCHWEICHER, Kinetic and Mechanistic Studies of CO Hydrogenation over Cobalt-based Catalysts, in: Faculty of Applied Sciences Université Libre de Bruxelles, Brussels, Belgium, 2010.
- [37] M. Bowker, *The Basis and Applications of Heterogeneous Catalysis*, Oxford University Press, Oxford, UK, 1998.
- [38] T. Herranz, X. Deng, A. Cabot, J. Guo, M. Salmeron, Influence of the Cobalt Particle Size in the CO Hydrogenation Reaction Studied by In Situ X-Ray Absorption Spectroscopy, *The Journal of Physical Chemistry B*, 113 (2009) 10721-10727.
- [39] J.M.T. Thomas, W. J. , *Principles and Practice of Heterogeneous Catalysis*, VCH, 1997.
- [40] M.E. Dry, Present and future applications of the Fischer–Tropsch process, *Applied Catalysis A: General*, 276 (2004) 1-3.
- [41] B.H. Davis, Fischer–Tropsch Synthesis: Comparison of Performances of Iron and Cobalt Catalysts, *Industrial & Engineering Chemistry Research*, 46 (2007) 8938-8945.
- [42] S.T. Sie, R. Krishna, Fundamentals and selection of advanced Fischer–Tropsch reactors, *Applied Catalysis A: General*, 186 (1999) 55-70.
- [43] M.E. Dry, Fischer-Tropsch synthesis over iron catalysts, *Catalysis Letters*, 7 (1990) 241-251.
- [44] P.J. van Berge, R.C. Everson, Cobalt as an alternative Fischer-Tropsch catalyst to iron for the production of middle distillates, in: R.L.E.C.P.N.J.H.S. M. de Pontes, M.S. Scurrill (Eds.) *Studies in Surface Science and Catalysis*, Elsevier, 1997, pp. 207-212.
- [45] N.E. Tsakoumis, M. Rønning, Ø. Borg, E. Rytter, A. Holmen, Deactivation of cobalt based Fischer–Tropsch catalysts: A review, *Catalysis Today*, 154 (2010) 162-182.

- [46] C.H. Bartholomew, Mechanisms of catalyst deactivation, *Applied Catalysis A: General*, 212 (2001) 17-60.
- [47] P.K. Agrawal, J.R. Katzer, W.H. Manogue, Methanation over transition metal catalysts: III. CoAl_2O_3 in sulfur-poisoning studies, *Journal of Catalysis*, 69 (1981) 327-344.
- [48] C.H. Bartholomew, P.K. Agrawal, J.R. Katzer, Sulfur Poisoning of Metals, in: H.P. D.D. Eley, B.W. Paul (Eds.) *Advances in Catalysis*, Academic Press, 1982, pp. 135-242.
- [49] C.J.M. S.C. LeVignes, W.C. Behrman, S.J. Hsia, D.R. Neskora, in, assigned to Exxon research and engineering company, 1998.
- [50] J.G.G.J. S. Eri, G. Marcelin, T. Riis., in, assigned to Statoil, 1989.
- [51] J. Gaube, H.F. Klein, The promoter effect of alkali in Fischer-Tropsch iron and cobalt catalysts, *Applied Catalysis A: General*, 350 (2008) 126-132.
- [52] S.E. E. Rytter, in, assigned to Statoil ASA and Petroleum Oil & Gas Corporation of South Africa PTY., 2006.
- [53] Ø. Borg, S. Eri, E.A. Blekkan, S. Storsæter, H. Wigum, E. Rytter, A. Holmen, Fischer-Tropsch synthesis over γ -alumina-supported cobalt catalysts: Effect of support variables, *Journal of Catalysis*, 248 (2007) 89-100.
- [54] E. Anders Blekkan, O. Borg, V. Froseth, A. Holmen, Fischer-Tropsch synthesis on cobalt catalysts: the effect of water, in: *Catalysis*, The Royal Society of Chemistry, 2007, pp. 13-32.
- [55] J. van de Loosdrecht, B. Balzhinimaev, J.A. Dalmon, J.W. Niemantsverdriet, S.V. Tsybulya, A.M. Saib, P.J. van Berge, J.L. Visagie, Cobalt Fischer-Tropsch synthesis: Deactivation by oxidation?, *Catalysis Today*, 123 (2007) 293-302.
- [56] A.K. Dalai, B.H. Davis, Fischer-Tropsch synthesis: A review of water effects on the performances of unsupported and supported Co catalysts, *Applied Catalysis A: General*, 348 (2008) 1-15.
- [57] E. Iglesia, Design, synthesis, and use of cobalt-based Fischer-Tropsch synthesis catalysts, *Applied Catalysis A: General*, 161 (1997) 59-78.
- [58] *Catalysis Science and Technology*, Springer-Verlag, New York, 1981.
- [59] E. Van Steen, M. Claeys, M.E. Dry, J. Van De Loosdrecht, E.L. Viljoen, J.L. Visagie, Stability of nanocrystals: Thermodynamic analysis of oxidation and re-reduction of cobalt in water/hydrogen mixtures, *Journal of Physical Chemistry B*, 109 (2005) 3575-3577.
- [60] P.J. van Berge, J. van de Loosdrecht, S. Barradas, A.M. van der Kraan, Oxidation of cobalt based Fischer-Tropsch catalysts as a deactivation mechanism, *Catalysis Today*, 58 (2000) 321-334.
- [61] A.M. Saib, D.J. Moodley, I.M. Ciobîcă, M.M. Hauman, B.H. Sigwebela, C.J. Weststrate, J.W. Niemantsverdriet, J. van de Loosdrecht, Fundamental understanding of deactivation and regeneration of cobalt Fischer-Tropsch synthesis catalysts, *Catalysis Today*, 154 (2010) 271-282.
- [62] G.L. Bezemer, J.H. Bitter, H.P.C.E. Kuipers, H. Oosterbeek, J.E. Holewijn, X. Xu, F. Kapteijn, A.J. van Dillen, K.P. de Jong, Cobalt Particle Size Effects in the Fischer-Tropsch Reaction Studied with Carbon Nanofiber Supported Catalysts, *Journal of the American Chemical Society*, 128 (2006) 3956-3964.
- [63] N.O. Elbashir, P. Dutta, A. Manivannan, M.S. Seehra, C.B. Roberts, Impact of cobalt-based catalyst characteristics on the performance of conventional gas-phase and supercritical-phase Fischer-Tropsch synthesis, *Applied Catalysis A: General*, 285 (2005) 169-180.
- [64] G.-Z. Bian, N. Fujishita, T. Mochizuki, W.-S. Ning, M. Yamada, Investigations on the structural changes of two Co/SiO_2 catalysts by performing Fischer-Tropsch synthesis, *Applied Catalysis A: General*, 252 (2003) 251-260.
- [65] A.M. Saib, A. Borgna, J. van de Loosdrecht, P.J. van Berge, J.W. Niemantsverdriet, In Situ Surface Oxidation Study of a Planar $\text{Co/SiO}_2/\text{Si}(100)$ Model Catalyst with Nanosized

Cobalt Crystallites under Model Fischer–Tropsch Synthesis Conditions, *The Journal of Physical Chemistry B*, 110 (2006) 8657-8664.

[66] A.M. Saib, A. Borgna, J. van de Loosdrecht, P.J. van Berge, J.W. Niemantsverdriet, XANES study of the susceptibility of nano-sized cobalt crystallites to oxidation during realistic Fischer–Tropsch synthesis, *Applied Catalysis A: General*, 312 (2006) 12-19.

[67] J. Swart, PhD thesis, in, UCT, Cape Town, South Africa, 2008.

[68] D. Schanke, A.M. Hilmen, E. Bergene, K. Kinnari, E. Rytter, E. Ådnanes, A. Holmen, Study of the deactivation mechanism of Al₂O₃-supported cobalt Fischer-Tropsch catalysts, *Catalysis Letters*, 34 (1995) 269-284.

[69] D. Schanke, A.M. Hilmen, E. Bergene, K. Kinnari, E. Rytter, E. Ådnanes, A. Holmen, Reoxidation and Deactivation of Supported Cobalt Fischer–Tropsch Catalysts, *Energy & Fuels*, 10 (1996) 867-872.

[70] A.M. Hilmen, D. Schanke, K.F. Hanssen, A. Holmen, Study of the effect of water on alumina supported cobalt Fischer–Tropsch catalysts, *Applied Catalysis A: General*, 186 (1999) 169-188.

[71] A.M. Hilmen, D. Schanke, A. Holmen, Reoxidation of supported cobalt Fischer-Tropsch catalysts, in: R.L.E.C.P.N.J.H.S. M. de Pontes, M.S. Scurrall (Eds.) *Studies in Surface Science and Catalysis*, Elsevier, 1997, pp. 237-242.

[72] A.M. Hilmen, O.A. Lindvåg, E. Bergene, D. Schanke, S. Eri, A. Holmen, Selectivity and activity changes upon water addition during Fischer-Tropsch synthesis, in, 2001, pp. 295-300.

[73] S. Storsæter, B. Tøtdal, J.C. Walmsley, B.S. Tanem, A. Holmen, Characterization of alumina-, silica-, and titania-supported cobalt Fischer–Tropsch catalysts, *Journal of Catalysis*, 236 (2005) 139-152.

[74] S. Storsæter, Ø. Borg, E.A. Blekkan, B. Tøtdal, A. Holmen, Fischer–Tropsch synthesis over Re-promoted Co supported on Al₂O₃, SiO₂ and TiO₂: Effect of water, *Catalysis Today*, 100 (2005) 343-347.

[75] S. Storsæter, Ø. Borg, E.A. Blekkan, A. Holmen, Study of the effect of water on Fischer–Tropsch synthesis over supported cobalt catalysts, *Journal of Catalysis*, 231 (2005) 405-419.

[76] Ø. Borg, S. Storsæter, S. Eri, H. Wigum, E. Rytter, A. Holmen, The Effect of Water on the Activity and Selectivity for γ -Alumina Supported Cobalt Fischer–Tropsch Catalysts with Different Pore Sizes, *Catalysis Letters*, 107 (2006) 95-102.

[77] J. van de Loosdrecht, P.J. van Berge, M.W.J. Crajé, A.M. van der Kraan, The Application of Mössbauer Emission Spectroscopy to Industrial Cobalt Based Fischer–Tropsch Catalysts, *Hyperfine Interactions*, 139-140 (2002) 3-18.

[78] M.W.J. Crajé, A.M. van der Kraan, J. van de Loosdrecht, P.J. van Berge, The application of Mössbauer emission spectroscopy to industrial cobalt based Fischer–Tropsch catalysts, *Catalysis Today*, 71 (2002) 369-379.

[79] A.M. Saib, A. Borgna, J. van de Loosdrecht, P.J. van Berge, J.W. Geus, J.W. Niemantsverdriet, Preparation and characterisation of spherical Co/SiO₂ model catalysts with well-defined nano-sized cobalt crystallites and a comparison of their stability against oxidation with water, *Journal of Catalysis*, 239 (2006) 326-339.

[80] M. Rønning, N.E. Tsakoumis, A. Voronov, R.E. Johnsen, P. Norby, W. van Beek, Ø. Borg, E. Rytter, A. Holmen, Combined XRD and XANES studies of a Re-promoted Co/ γ -Al₂O₃ catalyst at Fischer–Tropsch synthesis conditions, *Catalysis Today*, 155 (2010) 289-295.

[81] F.G. Botes, Influences of Water and Syngas Partial Pressure on the Kinetics of a Commercial Alumina-Supported Cobalt Fischer–Tropsch Catalyst, *Industrial & Engineering Chemistry Research*, 48 (2009) 1859-1865.

[82] A.K. Dalai, T.K. Das, K.V. Chaudhari, G. Jacobs, B.H. Davis, Fischer–Tropsch synthesis: Water effects on Co supported on narrow and wide-pore silica, *Applied Catalysis A: General*, 289 (2005) 135-142.

- [83] T.K. Das, X. Zhan, J. Li, G. Jacobs, M.E. Dry, B.H. Davis, Fischer-Tropsch synthesis: Kinetics and effect of water for a Co/Al₂O₃ catalyst, in: B.H. Davis, M.L. Occelli (Eds.) *Studies in Surface Science and Catalysis*, Elsevier, 2007, pp. 289-314.
- [84] T.K. Das, W. Conner, G. Jacobs, J. Li, K. Chaudhari, B.H. Davis, Fischer-Tropsch synthesis: effect of water on activity and selectivity for a cobalt catalyst, in: B. Xinhe, X. Yide (Eds.) *Studies in Surface Science and Catalysis*, Elsevier, 2004, pp. 331-336.
- [85] T.K. Das, W.A. Conner, J. Li, G. Jacobs, M.E. Dry, B.H. Davis, Fischer-Tropsch Synthesis: Kinetics and Effect of Water for a Co/SiO₂ Catalyst, *Energy & Fuels*, 19 (2005) 1430-1439.
- [86] G. Jacobs, T.K. Das, J. Li, M. Luo, P.M. Patterson, B.H. Davis, Fischer-Tropsch synthesis: influence of support on the impact of co-fed water for cobalt-based catalysts, in: B.H. Davis, M.L. Occelli (Eds.) *Studies in Surface Science and Catalysis*, Elsevier, 2007, pp. 217-253.
- [87] S. Krishnamoorthy, M. Tu, M.P. Ojeda, D. Pinna, E. Iglesia, An Investigation of the Effects of Water on Rate and Selectivity for the Fischer-Tropsch Synthesis on Cobalt-Based Catalysts, *Journal of Catalysis*, 211 (2002) 422-433.
- [88] J. Li, X. Zhan, Y. Zhang, G. Jacobs, T. Das, B.H. Davis, Fischer-Tropsch synthesis: effect of water on the deactivation of Pt promoted Co/Al₂O₃ catalysts, *Applied Catalysis A: General*, 228 (2002) 203-212.
- [89] J. Li, G. Jacobs, T. Das, B.H. Davis, Fischer-Tropsch synthesis: effect of water on the catalytic properties of a ruthenium promoted Co/TiO₂ catalyst, *Applied Catalysis A: General*, 233 (2002) 255-262.
- [90] J. Li, G. Jacobs, T. Das, Y. Zhang, B. Davis, Fischer-Tropsch synthesis: effect of water on the catalytic properties of a Co/SiO₂ catalyst, *Applied Catalysis A: General*, 236 (2002) 67-76.
- [91] J. Li, B.H. Davis, Effect of water on the catalytic properties of supported cobalt Fischer-Tropsch catalysts, in: B. Xinhe, X. Yide (Eds.) *Studies in Surface Science and Catalysis*, Elsevier, 2004, pp. 307-312.
- [92] G. Jacobs, P.M. Patterson, T.K. Das, M. Luo, B.H. Davis, Fischer-Tropsch synthesis: effect of water on Co/Al₂O₃ catalysts and XAFS characterization of reoxidation phenomena, *Applied Catalysis A: General*, 270 (2004) 65-76.
- [93] S.-M. Kim, J.W. Bae, Y.-J. Lee, K.-W. Jun, Effect of CO₂ in the feed stream on the deactivation of Co/ γ -Al₂O₃ Fischer-Tropsch catalyst, *Catalysis Communications*, 9 (2008) 2269-2273.
- [94] W. Zhou, Z. Ma, K. Fang, J.-g. Chen, Y.-h. Sun, Effects of methanol co-feeding in F-T synthesis on a silica supported Co-catalyst, *Fuel Processing Technology*, 89 (2008) 1113-1120.
- [95] K. Jalama, N.J. Coville, D. Hildebrandt, D. Glasser, L.L. Jewell, Fischer-Tröpsch synthesis over Co/TiO₂: Effect of ethanol addition, *Fuel*, 86 (2007) 73-80.
- [96] U. Lassi, Deactivation Correlations of Pd/Rh Three-way Catalysts Designed for Euro IV Emission Limits, in: Faculty of Technology Oulu University, Finland, 2003.
- [97] J. Sehested, A. Carlsson, T.V.W. Janssens, P.L. Hansen, A.K. Datye, Sintering of Nickel Steam-Reforming Catalysts on MgAl₂O₄ Spinel Supports, *Journal of Catalysis*, 197 (2001) 200-209.
- [98] J.R. Rostrup-Nielsen, in: J.R.A.a.M. Boudart (Ed.) *Catalysis, Science and Technology*, Springer-Verlag, Berlin, 1984.
- [99] J.T. Richardson, J.G. Crump, Crystallite size distributions of sintered nickel catalysts, *Journal of Catalysis*, 57 (1979) 417-425.
- [100] A.C.S.C. Teixeira, R. Giudici, Deactivation of steam reforming catalysts by sintering: experiments and simulation, *Chemical Engineering Science*, 54 (1999) 3609-3618.

- [101] H.K. Kuo, P. Ganesan, R.J. De Angelis, The sintering of a silica-supported nickel catalyst, *Journal of Catalysis*, 64 (1980) 303-319.
- [102] C.H. Bartholomew, W.L. Sorensen, Sintering kinetics of silica- and alumina-supported nickel in hydrogen atmosphere, *Journal of Catalysis*, 81 (1983) 131-141.
- [103] D.J. Young, P. Udaja, D.L. Trimm, Deactivation Due to Metal-Catalysed Phase Transformations in Λ - Al_2O_3 Supports, in: B. Delmon, G.F. Froment (Eds.) *Studies in Surface Science and Catalysis*, Elsevier, 1980, pp. 331-340.
- [104] M.S. Borisova, Fenelov, V. B., Dzisko, V. A., and Simonova, L. G, *Kinetika i Kataliz (Kinetics and Catalysis)*, 17 (1976) 653.
- [105] C.J. Bertole, C.A. Mims, G. Kiss, The Effect of Water on the Cobalt-Catalyzed Fischer–Tropsch Synthesis, *Journal of Catalysis*, 210 (2002) 84-96.
- [106] S.S. G. Kiss, C. Kliewer, in: *International Symposium on Catalyst Deactivation*, Delft, The Netherlands, 2009.
- [107] G. Kiss, C.E. Kliewer, G.J. DeMartin, C.C. Culross, J.E. Baumgartner, Hydrothermal deactivation of silica-supported cobalt catalysts in Fischer–Tropsch synthesis, *Journal of Catalysis*, 217 (2003) 127-140.
- [108] C.K. S. Soled, G. Kiss, J. Baumgartner, in: N.A.C.S. (NAM-NACS) (Ed.) 11th Int. Symp. 21st North American Meeting, San Francisco, USA, 2009.
- [109] W. Zhou, J.-G. Chen, K.-G. Fang, Y.-H. Sun, The deactivation of Co/SiO_2 catalyst for Fischer–Tropsch synthesis at different ratios of H_2 to CO , *Fuel Processing Technology*, 87 (2006) 609-616.
- [110] A. Tavasoli, R.M. Malek Abbaslou, A.K. Dalai, Deactivation behavior of ruthenium promoted $\text{Co}/\gamma\text{-Al}_2\text{O}_3$ catalysts in Fischer–Tropsch synthesis, *Applied Catalysis A: General*, 346 (2008) 58-64.
- [111] A. Tavasoli, M. Irani, R.M.M. Abbaslou, M. Trépanier, A.K. Dalai, Morphology and deactivation behaviour of $\text{Co-Ru}/\gamma\text{-Al}_2\text{O}_3$ Fischer–Tropsch synthesis catalyst, *The Canadian Journal of Chemical Engineering*, 86 (2008) 1070-1080.
- [112] B.B. M.J. Overett, E. du Plessis, W. Erasmus, J. van de Loosdrecht, *Prepr. Pap.-Am. Chem. Soc., Div. Petr. Chem.*, 53 (2008) 126–128.
- [113] J.-D. Grunwaldt, B.S. Clausen, Combining XRD and EXAFS with on-Line Catalytic Studies for in situ Characterization of Catalysts, *Topics in Catalysis*, 18 (2002) 37-43.
- [114] H. Karaca, O.V. Safonova, S. Chambrey, P. Fongarland, P. Roussel, A. Griboval-Constant, M. Lacroix, A.Y. Khodakov, Structure and catalytic performance of Pt-promoted alumina-supported cobalt catalysts under realistic conditions of Fischer–Tropsch synthesis, *Journal of Catalysis*, 277 (2011) 14-26.
- [115] H. Karaca, J. Hong, P. Fongarland, P. Roussel, A. Griboval-Constant, M. Lacroix, K. Hortmann, O.V. Safonova, A.Y. Khodakov, In situ XRD investigation of the evolution of alumina-supported cobalt catalysts under realistic conditions of Fischer-Tropsch synthesis, *Chemical Communications*, 46 (2010) 788-790.
- [116] R.C. Reuel, C.H. Bartholomew, Effects of support and dispersion on the CO hydrogenation activity/selectivity properties of cobalt, *Journal of Catalysis*, 85 (1984) 78-88.
- [117] A.S. Lisitsyn, A.V. Golovin, V.L. Kuznetsov, Y.I. Yermakov, *C1 Mol. Chem.*, 1 (1984) 115-135.
- [118] A.S. Lisitsyn, A.V. Golovin, V.L. Kuznetsov, Y.I. Yermakov, Properties of catalysts prepared by pyrolysis of $\text{Co}_2(\text{CO})_8$ on silica containing surface Ti ions, *Journal of Catalysis*, 95 (1985) 527-538.
- [119] E. Iglesia, S.L. Soled, R.A. Fiato, Fischer-Tropsch synthesis on cobalt and ruthenium. Metal dispersion and support effects on reaction rate and selectivity, *Journal of Catalysis*, 137 (1992) 212-224.

- [120] E. Iglesia, S.L. Soled, R.A. Fiato, G.H. Via, Dispersion, support, and bimetallic effects in Fischer-Tropsch synthesis on cobalt catalysts, in: H.E. Curry-Hyde, R.F. Howe (Eds.) *Studies in Surface Science and Catalysis*, Elsevier, 1994, pp. 433-442.
- [121] G. Jacobs, T.K. Das, Y. Zhang, J. Li, G. Racoillet, B.H. Davis, Fischer-Tropsch synthesis: Support, loading, and promoter effects on the reducibility of cobalt catalysts, *Applied Catalysis A: General*, 233 (2002) 263-281.
- [122] Y. Yin, R.M. Rioux, C.K. Erdonmez, S. Hughes, G.A. Somorjai, A.P. Alivisatos, Formation of Hollow Nanocrystals Through the Nanoscale Kirkendall Effect, *Science*, 304 (2004) 711-714.
- [123] P.A. Chernavskii, G.V. Pankina, V.I. Zaikovskii, N.V. Peskov, P. Afanasiev, Formation of Hollow Spheres upon Oxidation of Supported Cobalt Nanoparticles, *The Journal of Physical Chemistry C*, 112 (2008) 9573-9578.
- [124] G.W. Huber, C.G. Guymon, T.L. Conrad, B.C. Stephenson, C.H. Bartholomew, Hydrothermal stability of Co/SiO₂ fischer-tropsch synthesis catalysts, in: G.W.R. J.J. Spivey, B.H. Davis (Eds.) *Studies in Surface Science and Catalysis*, Elsevier, 2001, pp. 423-430.
- [125] P.G. Menon, Coke on catalysts-harmful, harmless, invisible and beneficial types, *Journal of Molecular Catalysis*, 59 (1990) 207-220.
- [126] C.H. Bartholomew, CARBON DEPOSITION IN STEAM REFORMING AND METHANATION, *Catalysis Reviews*, 24 (1982) 67-112.
- [127] J.v.d.L. D.J. Moodley, A.M. Saib, J.W. Niemantsverdriet, *Prepr. Pap.-Am. Chem. Soc., Div. Petr. Chem.*, 53 (2008) 122-125.
- [128] D.-K. Lee, J.-H. Lee, S.-K. Ihm, Effect of Carbon Deposits on Carbon Monoxide Hydrogenation over Alumina-Supported Cobalt Catalyst, *Applied Catalysis*, 36 (1988) 199-207.
- [129] D.J. Moodley, J. van de Loosdrecht, A.M. Saib, M.J. Overett, A.K. Datye, J.W. Niemantsverdriet, Carbon deposition as a deactivation mechanism of cobalt-based Fischer-Tropsch synthesis catalysts under realistic conditions, *Applied Catalysis A: General*, 354 (2009) 102-110.
- [130] A. Barbier, A. Tuel, I. Arcon, A. Kodre, G.A. Martin, Characterization and Catalytic Behavior of Co/SiO₂ Catalysts: Influence of Dispersion in the Fischer-Tropsch Reaction, *Journal of Catalysis*, 200 (2001) 106-116.
- [131] L.J.E. Hofer, W.C. Peebles, Preparation and X-Ray Diffraction Studies of a New Cobalt Carbide₁, *Journal of the American Chemical Society*, 69 (1947) 893-899.
- [132] O. Ducreux, J. Lynch, B. Rebours, M. Roy, P. Chaumette, In situ characterisation of cobalt based Fischer-Tropsch catalysts: A new approach to the active phase, in, 1998, pp. 125-130.
- [133] E. de Smit, B.M. Weckhuysen, The renaissance of iron-based Fischer-Tropsch synthesis: on the multifaceted catalyst deactivation behaviour, *Chemical Society Reviews*, 37 (2008) 2758-2781.
- [134] S.R. Shatynski, The thermochemistry of transition metal carbides, *Oxidation of Metals*, 13 (1979) 105-118.
- [135] S. Storsæter, D. Chen, A. Holmen, Microkinetic modelling of the formation of C₁ and C₂ products in the Fischer-Tropsch synthesis over cobalt catalysts, *Surface Science*, 600 (2006) 2051-2063.
- [136] E. Shustorovich, A.T. Bell, An analysis of Fischer-Tropsch synthesis by the bond-order-conservation-Morse-potential approach, *Surface Science*, 248 (1991) 359-368.
- [137] O. Ducreux, B. Rebours, J. Lynch, M. Roy-Auberger, D. Bazin, Microstructure de catalyseurs Fischer-Tropsch à base de cobalt supporté, *Oil & Gas Science and Technology - Rev. IFP*, 64 (2009) 49-62.

- [138] G. Jacobs, P.M. Patterson, Y. Zhang, T. Das, J. Li, B.H. Davis, Fischer–Tropsch synthesis: deactivation of noble metal-promoted Co/Al₂O₃ catalysts, *Applied Catalysis A: General*, 233 (2002) 215-226.
- [139] V. Gruver, X. Zhan, J. Engman, H.J. Rabota, S.L. Suib, M. Polverejan, Deactivation of a Fischer-Tropsch catalyst through the formation of cobalt carbide under laboratory slurry reactor conditions, *American Chemical Society, Division of Petroleum Chemistry, Preprints*, 49 (2004) 192-194.
- [140] J. Xiong, Y. Ding, T. Wang, L. Yan, W. Chen, H. Zhu, Y. Lu, The formation of Co₂C species in activated carbon supported cobalt-based catalysts and its impact on Fischer–Tropsch reaction, *Catalysis Letters*, 102 (2005) 265-269.
- [141] S.S.P. H.W. Pennline, *Ind. Eng. Chem. Prod. Res. Dev.*, 25 (1980) 11-14.
- [142] R.J.G. H.W. Pennline, R.R. Schehl, *Ind. Eng. Chem. Prod. Res. Dev.*, 23 (1984) 393–404.
- [143] M.E. Dry, in: M.B. J.R. Anderson (Ed.) *Catalysis Science and Technology*, vol. 1, Springer-Verlag, New York, 1981, pp. 195.
- [144] M.K. Niemelä, A.O.I. Krause, The long-term performance of Co/SiO₂ catalysts in CO hydrogenation, *Catalysis Letters*, 42 (1996) 161-166.
- [145] V. Gruver, R. Young, J. Engman, H.J. Robota, The role of accumulated carbon in deactivating cobalt catalysts during FT synthesis in a slurry-bubble-column reactor, *American Chemical Society, Division of Petroleum Chemistry, Preprints*, 50 (2005) 164-166.
- [146] G.V. Pankina, P.A. Chernavskii, A.S. Lermontov, V.V. Lunin, The study of carbon deposits formed on the surface of supported cobalt catalysts during the Fischer-Tropsch process, *Petroleum Chemistry*, 42 (2002) 217-220.
- [147] J.J.H.M. Font Freide, T.D. Gamlin, J.R. Hensman, B. Nay, C. Sharp, Development of a CO₂ Tolerant Fischer-Tropsch Catalyst: From Laboratory to Commercial-Scale Demonstration in Alaska, *Journal of Natural Gas Chemistry*, 13 (2004) 1-9.
- [148] J. Wilson, C. de Groot, Atomic-Scale Restructuring in High-Pressure Catalysis, *The Journal of Physical Chemistry*, 99 (1995) 7860-7866.
- [149] G.A. Beitel, A. Laskov, H. Oosterbeek, E.W. Kuipers, Polarization modulation infrared reflection absorption spectroscopy of CO adsorption on Co(0001) under a high-pressure regime, *Journal of Physical Chemistry*, 100 (1996) 12494-12502.
- [150] G.A. Beitel, C.P.M. de Groot, H. Oosterbeek, J.H. Wilson, A Combined in-Situ PM-RAIRS and Kinetic Study of Single-Crystal Cobalt Catalysts under Synthesis Gas at Pressures up to 300 mbar, *The Journal of Physical Chemistry B*, 101 (1997) 4035-4043.
- [151] L.B. Backman, A. Rautiainen, A.O.I. Krause, M. Lindblad, A novel Co/SiO₂ catalyst for hydrogenation, *Catalysis Today*, 43 (1998) 11-19.
- [152] J.T. Richardson, L.W. Vernon, The Magnetic Properties of the Cobalt Oxide–Alumina System, *The Journal of Physical Chemistry*, 62 (1958) 1153-1157.
- [153] R.L. Chin, D.M. Hercules, Surface spectroscopic characterization of cobalt-alumina catalysts, *The Journal of Physical Chemistry*, 86 (1982) 360-367.
- [154] R.B. Gregor, F.W. Lytle, R.L. Chin, D.M. Hercules, Investigation of supported cobalt and nickel catalysts by x-ray absorption spectroscopy, *The Journal of Physical Chemistry*, 85 (1981) 1232-1235.
- [155] J.M. Jabłoński, M. Wołczyr, L. Krajczyk, On Cobalt Silicate Formation during High-Temperature Calcination of Impregnated Cobalt/Silica Catalysts, *Journal of Catalysis*, 173 (1998) 530-534.
- [156] B. Ernst, S. Libs, P. Chaumette, A. Kiennemann, Preparation and characterization of Fischer–Tropsch active Co/SiO₂ catalysts, *Applied Catalysis A: General*, 186 (1999) 145-168.
- [157] P. Arnoldy, J.A. Moulijn, Temperature-programmed reduction of CoO/Al₂O₃ catalysts, *Journal of Catalysis*, 93 (1985) 38-54.

- [158] K.E. Coulter, A.G. Sault, Effects of Activation on the Surface Properties of Silica-Supported Cobalt Catalysts, *Journal of Catalysis*, 154 (1995) 56-64.
- [159] P.H. Bolt, F.H.P.M. Habraken, J.W. Geus, Formation of Nickel, Cobalt, Copper, and Iron Aluminates from α - and γ -Alumina-Supported Oxides: A Comparative Study, *Journal of Solid State Chemistry*, 135 (1998) 59-69.
- [160] W. Chu, P.A. Chernavskii, L. Gengembre, G.A. Pankina, P. Fongarland, A.Y. Khodakov, Cobalt species in promoted cobalt alumina-supported Fischer-Tropsch catalysts, *Journal of Catalysis*, 252 (2007) 215-230.
- [161] G. Jacobs, T.K. Das, P.M. Patterson, J. Li, L. Sanchez, B.H. Davis, Fischer-Tropsch synthesis XAFS: XAFS studies of the effect of water on a Pt-promoted Co/Al₂O₃ catalyst, *Applied Catalysis A: General*, 247 (2003) 335-343.
- [162] J.G. Chen, X.Z. Wang, H.W. Xiang, Y.H. Sun, Study on stability of Co/ZrO₂/SiO₂ catalyst for F-T synthesis, in: J.J.S. E. Iglesia, T.H. Fleisch (Eds.) *Studies in Surface Science and Catalysis*, Elsevier, 2001, pp. 525-529.
- [163] J.G. Chen, H.-W. Xiang, H.-Y. Gao, Y.-H. Sun, Study on Deactivation of Co/ZrO₂/SiO₂ Catalyst For Fischer-Tropsch Synthesis, *Reaction Kinetics and Catalysis Letters*, 73 (2001) 169-177.
- [164] G.A. Fuentes, Catalyst deactivation and steady-state activity: A generalized power-law equation model, *Applied Catalysis*, 15 (1985) 33-40.
- [165] C.H. Bartholomew, Sintering kinetics of supported metals: new perspectives from a unifying GPLE treatment, *Applied Catalysis A: General*, 107 (1993) 1-57.
- [166] C.H. Bartholomew, *Catalysis, Specialist Periodical Report*, in: Royal Society of Chemistry, 1992.
- [167] C.H. Bartholomew, Sintering Kinetics of Supported Metals: Perspectives from a Generalized Power Law Approach, in: B. Delmon, G.F. Froment (Eds.) *Studies in Surface Science and Catalysis*, Elsevier, 1994, pp. 1-18.
- [168] S.E. Wanke, P.C. Flynn, The Sintering of Supported Metal Catalysts, *Catalysis Reviews*, 12 (1975) 93-135.
- [169] G.A. Fuentes, E.D. Gamas, Towards A Better Understanding of Sintering Phenomena in Catalysis, in: H.B. Calvin, B.B. John (Eds.) *Studies in Surface Science and Catalysis*, Elsevier, 1991, pp. 637-644.
- [170] C.H.F. Bartholomew, R.J. , *Fundamentals of Industrial Catalytic Processes*, 2nd Ed. ed., Wiley, New York, 2005.
- [171] R.L. De Chen, Kjersti Omdahl, Arne Anundskås, Ola Olsvik, Anders Holmen, A Model for Reforming on Ni Catalyst with Carbon Formation and Deactivation, in: 9th International Symposium on Catalyst Deactivation, Lexington, KY, 2001.
- [172] A.K. Datye, Q. Xu, K.C. Kharas, J.M. McCarty, Particle size distributions in heterogeneous catalysts: What do they tell us about the sintering mechanism?, *Catalysis Today*, 111 (2006) 59-67.
- [173] R. Finsky, On the critical radius in Ostwald ripening, *Langmuir*, 20 (2004) 2975-2976.
- [174] C.G. Granqvist, R.A. Buhrman, Size distributions for supported metal catalysts: Coalescence growth versus ostwald ripening, *Journal of Catalysis*, 42 (1976) 477-479.
- [175] S.E. Wanke, Comments on the sintering mechanism of supported metal catalysts, *Journal of Catalysis*, 46 (1977) 234-237.
- [176] W. Zhu, J. Zhang, F. Kapteijn, M. Makkee, J.A. Moulijn, Hydrodechlorination of 1,2-dichloropropane over Pt-Cu/C catalysts: Coke formation determined by a novel technique-TEOM, in: G.W.R. J.J. Spivey, B.H. Davis (Eds.) *Studies in Surface Science and Catalysis*, Elsevier, 2001, pp. 21-28.

- [177] Q. Qin, D. Ramkrishna, Modeling of Surface Structure of Supported Catalysts. Application to Deactivation of FT Reactors, *Industrial & Engineering Chemistry Research*, 43 (2004) 2912-2921.
- [178] M. Bremaud, P. Fongarland, J. Anfray, S. Jallais, D. Schweich, A.Y. Khodakov, Influence of syngas composition on the transient behavior of a Fischer–Tropsch continuous slurry reactor, *Catalysis Today*, 106 (2005) 137-142.
- [179] O. Levenspiel, *Chemical Reaction Engineering*, 3rd Edition ed., Wiley, New York, 1999.
- [180] J.B. Butt, Catalyst Poisoning and Chemical Process Dynamics, in: B. Delmon, G.F. Froment (Eds.) *Studies in Surface Science and Catalysis*, Elsevier, 1980, pp. 21-41.
- [181] J.B. Butt, Catalyst poisoning and chemical process dynamics, in: J.L. Figueiredo (Ed.) *Progress in Catalyst Deactivation*, Nijhoff, Boston, 1982, pp. 153-208.
- [182] J.B. Butt, Catalyst deactivation: How we cannot yet subvert nature, in: C.H. Bartholomew, G.A. Fuentes (Eds.) *Studies in Surface Science and Catalysis*, Elsevier, 1997, pp. 69-86.
- [183] G.F. Froment, A Quantitative Approach of Catalyst Deactivation by Coke Formation, in: B. Delmon, G.F. Froment (Eds.) *Studies in Surface Science and Catalysis*, Elsevier, 1980, pp. 1-19.
- [184] R.M. Bowman, C.H. Bartholomew, Deactivation by carbon of Ru/Al₂O₃ during CO hydrogenation, *Applied Catalysis*, 7 (1983) 179-187.
- [185] H. Iida, T. Yamamoto, M. Inagaki, A. Igarashi, Derivation of Initial Rate Equations for Low-temperature Water Gas Shift Reaction over Pt-Re/ZrO₂ Catalysts, *Chemistry Letters*, 39 (2010) 144-145.

CHAPTER

2

METHODOLOGY AND TOOLS

2.1. Introduction

In order to study the kinetics and deactivation behavior of Fischer-Tropsch catalysts, a set of experimental and modeling tools are required.

The FT reaction tests were conducted in different laboratory reactors. As several data points are already collected internally before the current thesis using fixed bed and slurry reactors, the work is limited to these reactor types. In the first step, the details of each experimental reactor are explained. Next, the condenser problems frequently encountered in the case of milli-fixed bed are discussed and some solutions are proposed in order to decouple the physical (condensers) and reactive (FT reactor) setup responses. The methodology then continues with several approaches to model different reactors with/without condensers. The choice of kinetics (CO consumption rate, and hydrocarbon production rates) is discussed and the governing equations are developed for each specific reactor. The deactivation mechanisms developed in chapter 3 are then added to the reactor models. The details of programming packages used are given. The reactor models are then applied to the collected experimental data to view the model suitability. Further adjustment and optimization are conducted in order to validate and yield realistic deactivation models.

2.2. Choice of experimental set-up

Experimental catalytic tests have been performed in the Catalysis and Solid State Chemistry Lab (Unité de Catalyse et Chimie du Solide, UCCS) and European Synchrotron Research Facility (ESRF, Swiss-Norwegian Beam Lines SNBL). Recent experimental data obtained in capillary fixed bed reactor as well as slurry reactor were also used to build and validate the reactor models.

Table 2.1 gives a summary of the setups used in this study along with the motivation for each reactor. The final objective of the study is to develop a universal model for deactivation which could be applied for all the reactor types.

Table 2.1 List of reactors used in this study

Reactor Set-up	Typical Dimensions	Typical Catalyst	Advantages
Capillary fixed-bed reactor	ID = 0.96 mm L = 9.1 mm 10 mg catalyst	Reference Catalyst	- Crystallite size follow-up by in-situ XRD -Direct correlation between micro and macro models -No condenser (only reactive part)
Milli-fixed bed reactor with condensers	ID = 1.4-1.7 mm L = 40 - 180 mm 50-500 mg catalyst	Reference Catalyst	- Wider window of operating conditions - Plug flow (concentration and size profile along reactor) - Study the effect of condenser on overall performance -Effect of reactor size on deactivation
Slurry reactor with condenser	ID = 46 mm V = 300 mL 5 g catalyst	Süd-Chemie Catalyst	- Effect of reactor geometry on FTS performance -Uniform concentration and crystallite size within reactor - Effect of catalyst type

2.2.1. Used catalysts

Two sets of cobalt-based alumina supported FT catalysts are used in the experimental tests, one for the fixed bed reactors tests and a second one for the slurry test.

- A 25%Co0.1%Pt/ γ -Al₂O₃ catalyst has been defined as a reference since it has been intensively studied in terms of characterization and catalytic activity in the PhD work of Heline Karaca [1]. It has been prepared using two-step impregnation procedure with cobalt nitrate (Co(NO₃)₂·6H₂O) and tetramine platinum nitrate (Pt(NH₃)₄(NO₃)₂) [1]. After impregnation, the catalysts were dried in air flow at 100°C and then calcined at 300°C or 500°C for 5 h with a temperature ramp of 1 °C/min. Table 2.2 gives the basic properties of reference catalyst.

This catalyst has been used mainly for the fixed bed reactors.

Table 2.2 Adsorption properties of the reference catalyst

Catalyst	Cobalt loading, %	Platinum loading, %	support	S _{BET} , m ² /g	TPV, mL/g	BJH pore diameter, nm
Reference-- 25CoPt/ γ - h Al ₂ O ₃	25	0.1	Puralox SCCA- 5/170 γ -alumina	165	0.48	8.3

- Data collected in the slurry reactor configuration used 5 grams of industrial catalyst supplied by Süd-Chemie (15% Co/Al₂O₃, FTCB20-B, 2 kg du lot # 095 H/04) [2]. The Co metal crystallite size is calculated as 9 nm in the fresh catalyst (with 12 nm for Co₃O₄). The catalyst samples were sieved before use in the reactor in order to obtain a particle size larger than 40 μ m with a median of 75 μ m (Fig. 2.1).

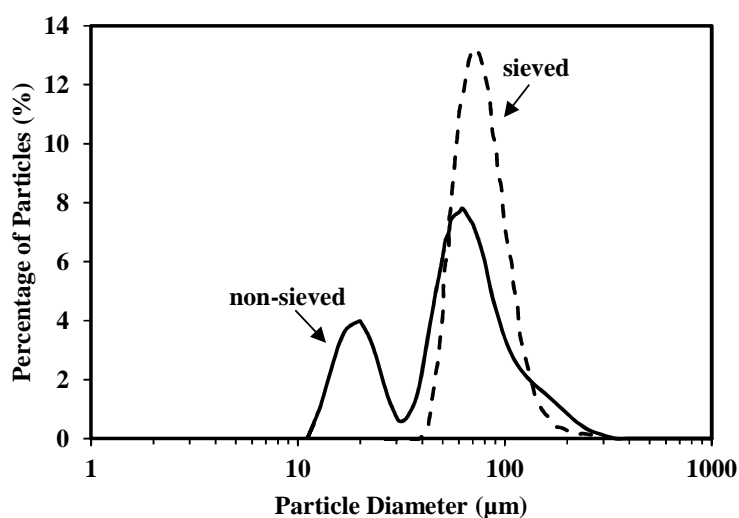


Figure 2.1 Particle size distribution of Süd-Chemie catalyst before/after sieving – Adapted from reference [2]

2.2.2. Reactor configurations

Fischer-Tropsch synthesis was carried out in two main reactor types i.e. fixed bed and slurry reactors as they impose different hydrodynamic regimes on the reactants. Two different fixed bed reactor (FBR) scales are used: a capillary fixed bed and millimetric fixed bed reactors. The use of slurry reactor is justified by the fact that there is large experimental dataset already obtained [2] which could be used in line with previously-developed kinetic models to improve our understanding about the catalyst behavior in the most promising reactor type.

2.2.2.1. Capillary fixed bed reactor

The *in-situ* catalytic activity as well as time-resolved XRD data were measured at the BM01B-SNBL beamline (ESRF, France) using a high resolution diffractometer, a gas manifold system and a capillary cell reactor (Figures. 2.2-2.3), the detailed information is provided by H. Karaca [1]. The known amount of catalyst was loaded in the quartz capillary ($ID = 1$ mm, wall thickness = 0.02 mm) and pressed from both sides with quartz wool. The capillary was attached to the stainless steel holder using high temperature epoxy glue. Before the FT tests, the catalysts were reduced in hydrogen flow at 350°C at atmospheric pressure (temperature ramp of 3 °C /min) and cooled down to room temperature in H₂ flow. After reduction, the catalyst was heated to 160 °C using a Cyberstar gas blower and exposed to the syngas (H₂/CO = 2) at atmospheric pressure. Then, the reactors were pressurized up to 20 bar, and temperature of the catalyst was risen up to 220 °C under syngas flow with temperature ramp of 2 °C/min. The time-resolved XRD patterns were recorded *in-situ* under gas flows at desired temperatures and pressures.

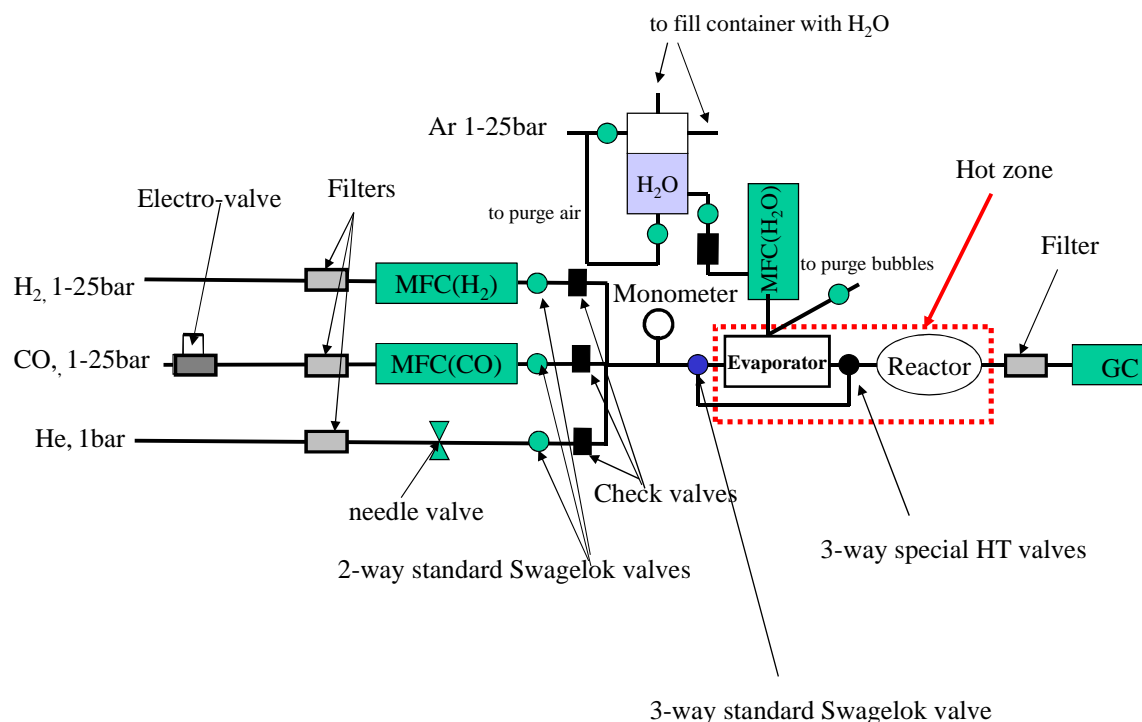


Figure 2.2 Schematic view of operando set-up used in ESRF

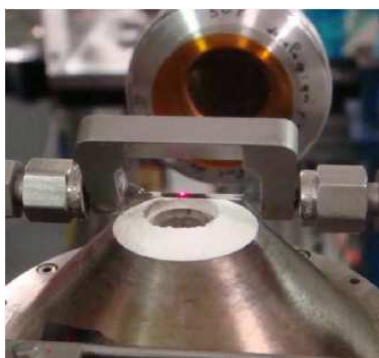


Figure 2.3 Photo of capillary fixed bed reactor [1]

The details of the FT catalyst test performed in the capillary reactor are given in Appendix A.

2.2.2.2. Milli-fixed bed reactor

The Fischer-Tropsch synthesis was carried out in a milli-fixed bed stainless-steel tubular reactor ($d_{\text{int}} = 1.4 \text{ mm}$ or 1.75 mm) operating at 20 bar [3]. The scheme of the reaction setup is shown in Figures 2.4-2.5. The reference catalyst was crushed and sieved to obtain catalyst grains of 66-160 μm in diameter. The catalyst loading was between 50 and 500 mg. It is diluted with SiC for the sake of temperature control as the FT reaction is highly exothermic. However some experiments conducted at high temperature use non-diluted catalyst samples as the reaction is highly exothermic. Non-diluted tests have been also performed in order to

study how dilution could affect the hydrodynamic behavior of inlet syngas. Fig. 2.6 shows the both configurations used. The thermocouple was set in direct contact with the catalyst before the test, so that the thermocouple measurements could reflect the real temperature inside the reactor. It was found that the temperature was homogeneous along the catalyst bed. No temperature spike and temperature swings were observed during the whole catalytic testing at atmospheric pressure.

Before reaction, the samples were reduced in hydrogen flow at 1 bar and 350 °C (with a temperature ramp of 10°C/min) for 10 h. The reactor was then cooled down to ambient temperature. The premixed syngas with a stable H₂/CO ratio was then injected into the reactor at 160 °C, and the pressure is gradually increased to 20 bar. The temperature is then increased with a ramp of 10 °C/min to reach 220°C and to start the FT synthesis.

The FT effluents are separated with the help of two condensers, the first of which is operated at 150°C and removes the so-called “wax” fraction. The second condenser is maintained at 10°C by water circulation and separates the lighter “diesel” fraction. The non-condensable remaining gas is then expands into atmospheric pressure through a back-pressure regulator and is then injected into the GC Varian 3800. The outlet gas can also be directed into an Agilent AMD 2000 mass flow meter in order to measure its flow rate.

The syngas conversion was calculated from the gas chromatographs and the FT reaction rates were obtained from carbon monoxide conversions and gas hourly space velocities and normalized by the number of cobalt atoms loaded in the reactor.

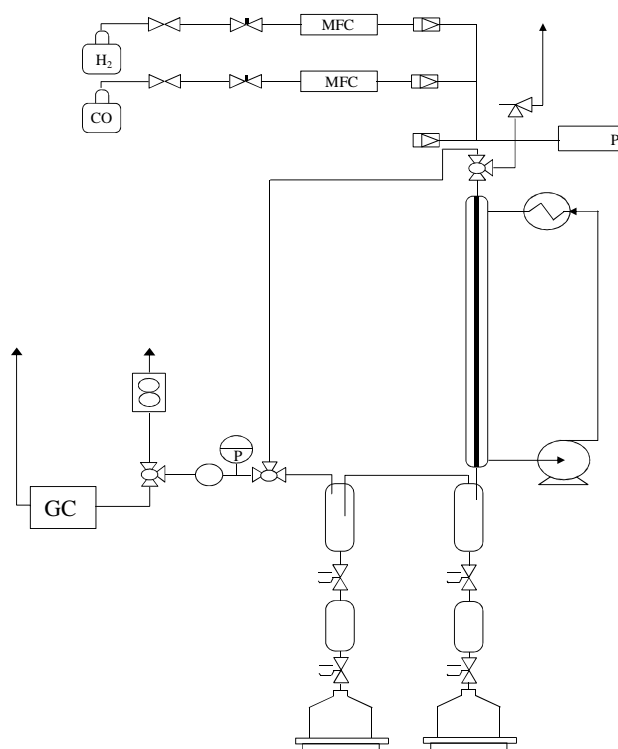


Figure 2.4 Scheme of experimental setup for FT synthesis in milli-fixed bed reactor (MFC = Mass flow controller; GC = gas chromatography; P = Pressure regulator)

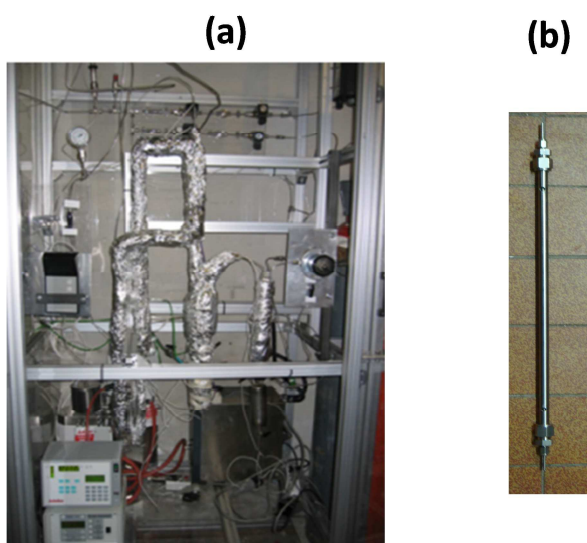


Figure 2.5 Overview of milli-fixed bed pilot (a) and milli-fixed bed reactor (b) used for FT synthesis.

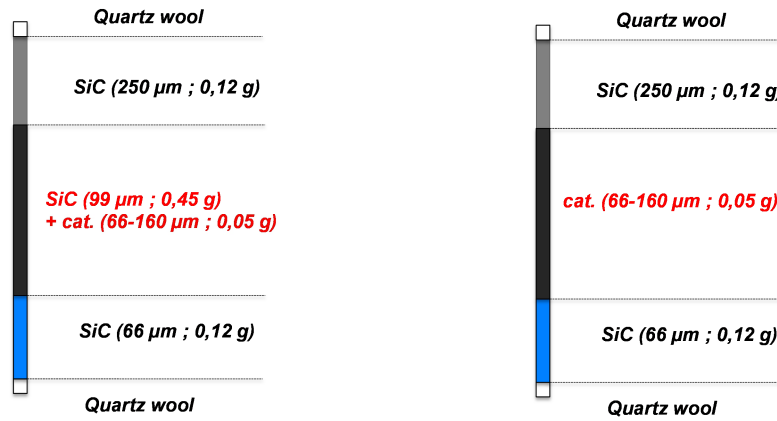


Figure 2.6 Scheme of two catalyst configuration used in milli-fixed bed reactor: diluted (left-hand side) and non-diluted (right-hand side) configurations

The Mears criterion was used to verify the isothermal regime in the milli-fixed bed reactor [4] and [5]. When this criterion is fulfilled, the radial temperature profile could be neglected, while the presence of heat spots along the bed cannot be excluded:

$$(1 - \varepsilon) r_p \left| \Delta H_R \right| \frac{T_A d_t^2}{4 \lambda_{er}^{sf} T_p^2} \left(1 + \frac{8 \lambda_{er}^{sf}}{U d_t} \right) < 0.4 \quad (2.1)$$

with ε as the void fraction of the catalyst, r_p the rate of reaction, ΔH_R the reaction enthalpy, T_A the adiabatic temperature, d_t the tube diameter, λ_{er}^{sf} the effective radial thermal conductivity, T_p the reactor wall temperature, and U the global heat exchange coefficient.

Calculation gives the Mears criteria of 1.46 assuming 60% carbon monoxide conversion as well as a radial temperature gradient of about 0.5 K in milli-fixed bed reactor. The absence of external and internal mass transfer limitation is also verified. Further details could be found in [3].

The list of experimental FT runs performed in the milli-fixed reactor is given in Appendix A.

2.2.2.3. Slurry reactor

The experimental slurry runs [2] were utilized during this thesis. 300 mL continuous slurry stirred tank reactor has been used. A commercial catalyst (15% w/w Co on Al_2O_3 , 50 μm , 5 g) was reduced in situ by hydrogen, and the Shell SX70 wax was used as the initial solvent. Samples of gaseous and liquid products (aqueous phase and two organic condensates) were periodically analyzed by gas chromatography and outlet flow rates were measured. The chemical regime has been checked in the reactor by studying the effect of the impeller rotation rate and computing the Weisz criteria for the internal mass transfer coupling. Temporal evolution of carbon monoxide conversion and hydrocarbon selectivities were

followed until a steady state was reached (from 10 to 45 days). The effect of inlet ratio H_2/CO (from 1.6 to 3.35), gas space velocity ($0.15-0.57\text{ h}^{-1}$), total syngas pressure (15-30 bar), and operating temperature ($210-230^\circ\text{C}$) was studied. CO conversions from 17% to 100% were obtained. More details on the experimental set-up and design, and analyses can be found in [6]. Fig. 2.7 shows the schematic view of the slurry configuration used.

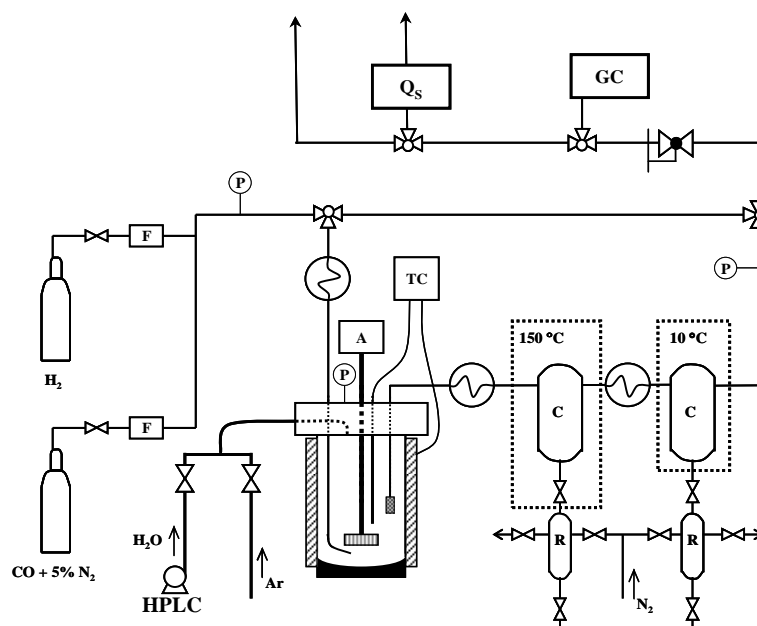


Figure 2.7 Scheme of experimental setup for FT synthesis in slurry reactor (F = Mass flow controller; GC = gas chromatography; P = Pressure regulator; TC = Temperature controller; C = Condenser; R = Collector; A = Agitation; HPLC = High-performance liquid chromatography)



Figure 2.8 Overview of slurry reactor pilot used for FT synthesis.

The details of experimental runs performed in the slurry reactor are given in Appendix A.

2.2.3. Data collection and treatment (GC-analysis)

The gaseous reaction products were analyzed on-line at atmospheric pressure by gas chromatography (GC Varian 3800) in the milli-fixed bed and slurry pilots. Analysis of H₂, CO, CO₂, CH₄ and N₂ was performed several times per day using a CTR-1 column and a thermal conductivity detector. Hydrocarbons (C₁-C₇) were separated in a capillary CP-Plot column and analyzed by a flame ionization detector. Carbon monoxide contained 5% nitrogen which was used as an internal standard for calculating carbon monoxide conversion. Detailed operating parameters of the GC Varian 3800 are given elsewhere [1].

For simultaneous analysis of the reaction products in the capillary fixed bed reactor an Agilent micro gas chromatograph was used. 5% of argon was used as an internal standard. Carbon monoxide conversion and methane selectivity were calculated from carbon monoxide, methane and argon chromatographic peaks.

2.2.3.1. Catalytic performance estimation

The catalytic performance is estimated based on the CO conversion and the selectivity of the hydrocarbon products.

The CO conversion is based on the carbon monoxide flow rate reacted during the FT reaction. The initial calibration using a premixed gas cylinder containing CO, CH₄, and N₂ gives the response factor of these components:

$$RF_i = \frac{\%mol_i}{A_i} \quad (2.2)$$

where RF_{*i*}, %mol_{*i*}, and A_{*i*} are the component response factor, the molar percentage inside the calibration cylinder, and the peak area detected by the TCD, respectively.

The use of internal calibration gas i.e. N₂ (which is inert during FTS) inside the reacting CO cylinder permits to calculate the CO and CH₄ outlet flow rate ($F_{CO,out}$, and $F_{CH_4,out}$ in mol/hr) by the inlet N₂ flow rate ($F_{N_2,in}$) as well as the respective response factor RF_i and GC peak areas A_i .

$$F_{i,out} = \frac{RF_i}{RF_{N_2}} \times \frac{A_i}{A_{N_2}} \times F_{N_2,in} \quad (i = CO \text{ or } CH_4) \quad (2.3)$$

Once the CO outlet flow rate is determined, the conversion could be calculated using Eq. 2.4.

$$X_{CO} = \left(1 - \frac{F_{CO,in}}{F_{CO,out}} \right) \times 100\% \quad (2.4)$$

The methane selectivity is also calculated by Eq. 2.5:

$$F_{CH_4} = \left(\frac{F_{CH_4,out}}{F_{CO,in} - F_{CO,out}} \right) \times 100\% \quad (2.5)$$

Similar relationships are used to find the selectivity of other hydrocarbons based on their respective GC area peaks.

2.3. Residence time distribution (RTD)

Although the experimental data obtained through the GC-analysis are useful in developing unsteady-state deactivation models, the problem of residence time distribution needs to be investigated, especially in the case of milli-fixed bed reactor.

More precisely, the use of two condensers (hot and cold ones) downstream of the FT reactor causes modification of concentration transient response curves. Fig. 2.9 shows a typical CO conversion as obtained by the GC data treatment. Surprisingly, the initial conversion is very low and it rises during the first 3-22 hr (depending on the gas flow rate) on stream to the maximum point, after which the “apparent” deactivation begins. However such a phenomenon is not in line with the results obtained in the capillary reactor where the conversion curve starts immediately from its maximum initial value.

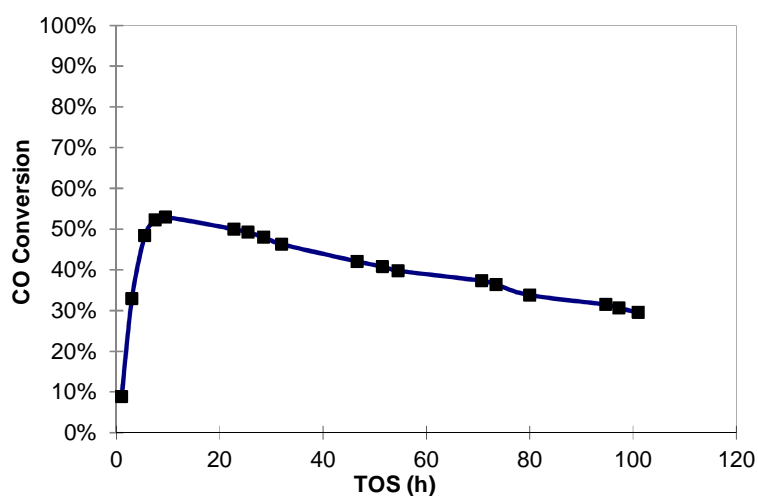


Figure 2.9 Typical conversion curve obtained by GC data treatment in milli-fixed bed setup ($H_2/CO = 2$, $GHSV = 3.11 \times 10^6 \text{ Nm}^3/\text{mol}_{CO}\cdot\text{h}$, $T = 220^\circ\text{C}$, $P = 20 \text{ bar}$)

As the reactor geometry is similar in both capillary and milli-fixed bed reactor, we speculate that modification of transient concentrations in milli-fixed bed setup is due to the presence of condensers. Consequently, a comprehensive study is conducted in order to confirm such a hypothesis with an objective to decouple the effect of the condenser hydrodynamics and the intrinsic catalytic activity. The final objective is to be able to construct the real conversion curve at the outlet of the reactor from the experimental signals obtained through the GC at the outlet of the cold condenser.

The study begins with a qualitative analysis of the FT tests in milli-fixed bed reactor setup. As already stated in the section 2.2.2.2, prior to direct injection of syngas to FT reactor, the syngas ratio is adjusted using GC. This is clearly shown in Fig. 2.10 where the bypassed syngas is directed into the GC for 4-5 hours in order to stabilize the H₂/CO ratio. This clearly shows how the condensers are completely filled with a H₂+CO mixture prior to reaction.

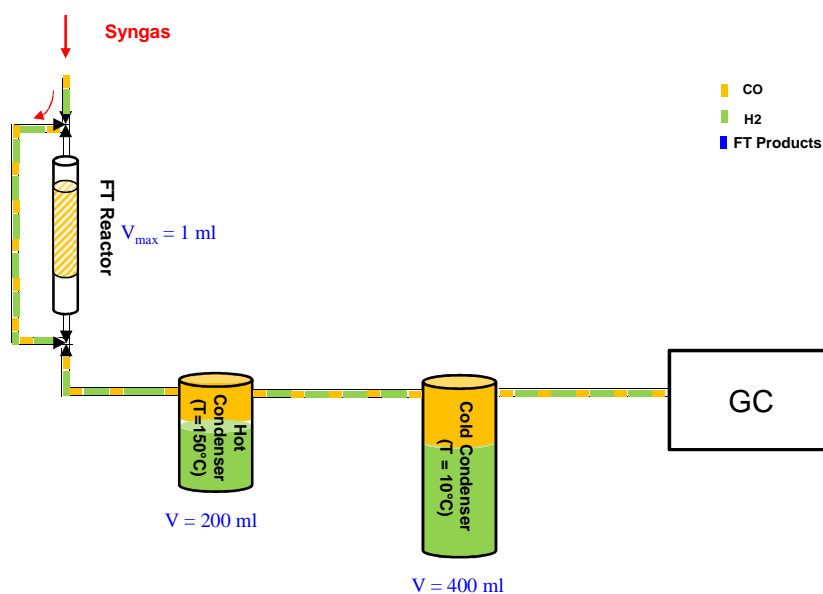


Figure 2.10 Graphical representation of vessels' filling during H₂/CO ratio stabilization period

Once the syngas ratio is stabilized, the syngas is directed into the catalytic reactor where the FT synthesis begins, leading to a mixture of FT products and unreacted syngas as effluent. Such a mixture flows through the tube lines as well as hot and cold condensers (Fig. 2.11). However due to the relative large volume of condensers as well as low syngas flow rate, a sufficiently long time is required to replace the initially filled syngas inside the condensers. Consequently the effluent composition is modified during the first hours on stream and the catalytic activity is not the same at the reactor outlet and as seen by the GC.

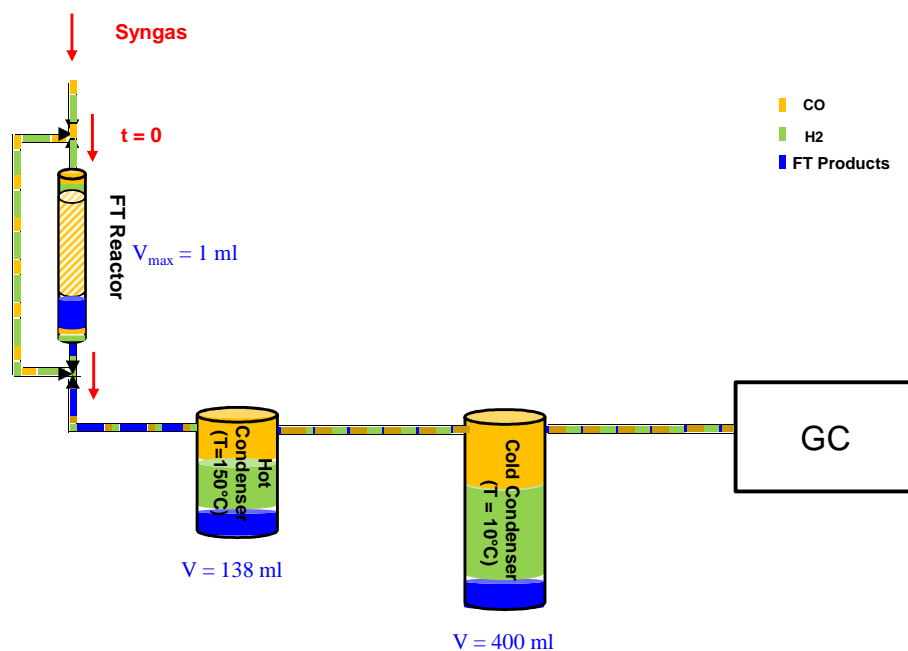


Figure 2.11 Graphical representation of FT effluent composition change during the first hours on stream

Consequently the role of hot and cold condensers should be also included in both experimental runs and modeling tools if a realistic picture of catalytic activity and deactivation is sought.

Note that, the milli-fixed bed reactor set-up is found to be the one the most affected, as the reactor is 200-400 times smaller than the condensers. By the same reason the catalytic activity is not much affected by the condensers in slurry set-up as the reactor/condenser volumes are close. The change in the activity profile is a strong function of operating conditions including temperature, pressure, and gas flow rate (Fig. 2.12).

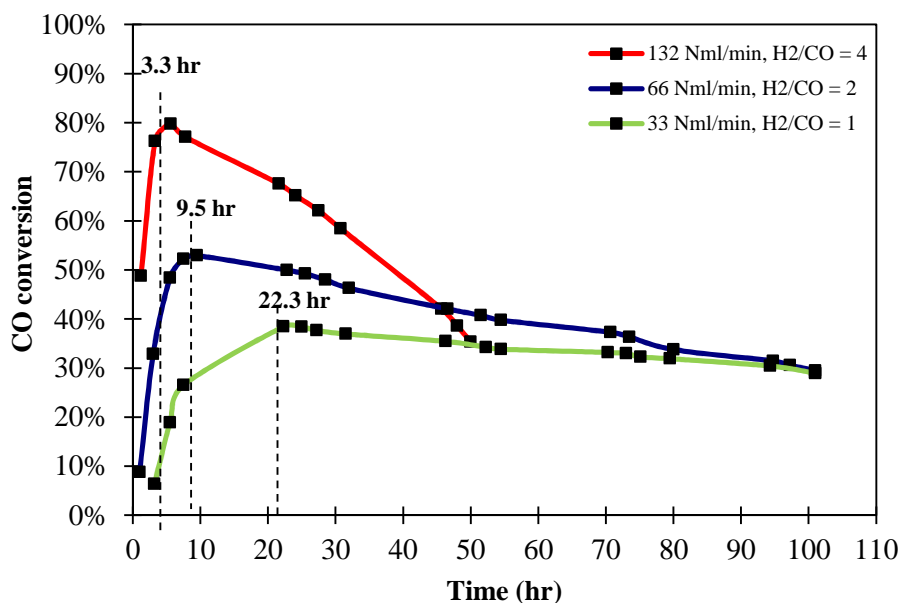


Figure 2.12 Effect of syngas flow rate on the initial apparent conversion increase period in the milli-fixed bed reactor set-up ($T = 220^{\circ}\text{C}$, $P = 20$ bar): (a) 33 Nml/min $\text{H}_2/\text{CO} = 1$, (b) 66 Nml/min $\text{H}_2/\text{CO} = 2$, (c) 132 Nml/min $\text{H}_2/\text{CO} = 4$

2.3.1. Experimental RTD measurements in milli-fixed bed set-up

Residence time distribution (RTD) measurements have been performed in milli-fixed bed set-up in order to characterize the hydrodynamics of both reactor and condensers.

Residence time distribution (RTD) is a model for characterizing the hydrodynamics of a chemical reactor. The two major uses of the residence time distribution to characterize non-ideal reactors are [7]:

- To diagnose problems of reactors in operation
- To predict conversion or effluent concentration in existing/available reactors when a new reaction is used in the reactors

The residence time distribution (RTD) of a reactor is a characteristic of the mixing that occurs in the chemical reactor. It is determined experimentally by injecting an inert chemical, molecule, or atom, called a tracer, into the reactor at some time $t = 0$ and then measuring the tracer concentration, C , in the effluent stream as a function of time. We have used nitrogen as tracer in this study, as this is easily detectable by the gas chromatography and it has physical properties similar to those of the reacting mixture i.e. $\text{H}_2 + \text{CO}$.

In an ideal plug-flow reactor, all the atoms of the tracer leaving the reactor have been inside it for exactly the same amount of time. However in the real milli-fixed bed setup, where the tracer molecules need to flow through the condensers as well, they exhibit different

residence times in the whole setup before being detected by the GC. One can therefore establish a residence time distribution, most often represented by a frequency distribution.

On an experimental point of view, we have used the pulse input experiment, where a known amount of tracer (1.6 ml N₂ kept in a reservoir that bypasses the reactor) is suddenly injected into the feedstream (pure H₂ stream) entering the reactor in as short a time as possible (4.5 s at 1 bar and 25°C). The milli-fixed bed reactor contains 50 mg reference catalyst in addition to 120 mg SiC of 62µm size and 120 mg of SiC with 250 µm average diameter. Note that although the hot and cold condensers are kept at constant temperatures of 150°C and 10°C respectively, the experiment is repeated at several different reactor temperatures and pressures in order to identify the sensible parameters on RTD. The experiment is performed for reactor + condenser assembly, reactor only, and condensers only geometries to measure the RTD in different configurations.

The outlet concentration is then measured through gas chromatography analysis at the reactor and/or condensers output as a function of time. The concentration-time curves, also referred to C-curves are then obtained.

However in order to make a comprehensive RTD analysis, the C-curves should be transformed into frequency curves. This is performed as follows. First, we choose an increment of time Δt sufficiently small that the concentration of the tracer, $C(t)$, exiting between time t and $t + \Delta t$ is essentially the same. The amount of tracer material, ΔN , leaving the reactor (or condensers or the whole setup) between time t and $t + \Delta t$ is then:

$$\Delta N = C(t)v\Delta t \quad (2.6)$$

where v is the effluent volumetric flow rate. In other words, ΔN is the amount of material exiting the reactor (or the setup) that has spent an amount of time between t and $t + \Delta t$ in the reactor (or the setup). If we now divide by the total amount of material that was injected into the reactor, N_0 , we obtain:

$$\frac{\Delta N}{N_0} = \frac{C(t)v}{N_0} \Delta t \quad (2.7)$$

which represents the fraction of material that has a residence time in the reactor (or the setup) between t and $t + \Delta t$.

For pulse injection we define:

$$E(t) = \frac{C(t)v}{N_0} \quad (2.8)$$

So that

$$\frac{\Delta N}{N_0} = E(t) \Delta t \quad (2.9)$$

The quantity $E(t)$ is called the *residence-time distribution function*. It is the function that describes in a quantitative manner how much time different fluid elements have spent in the reactor (or the set-up). The quantity $E(t)dt$ is the fraction of fluid exiting the reactor (or the set-up) that has spent between the time t and $t + dt$ inside the reactor (or the set-up).

As N_0 is not known directly, it can be obtained from the outlet concentration measurement by summing up the amounts of materials, ΔN , between time equal to zero and infinity.

$$N_0 = \int_0^{\infty} vC(t)dt \quad (2.10)$$

The volumetric flow rate v is usually constant from $t = 0$ to ∞ as the tracer (i.e. nitrogen) amount is negligible in the carrier gas (i.e. hydrogen), so we can define $E(t)$ as:

$$E(t) = \frac{C(t)}{\int_0^{\infty} C(t)dt} \quad (2.11)$$

The integral in the denominator is the area under the C-curve.

Eq. 2.11 allows therefore constructing $E(t)$ curve from the experimental $C(t)$ curve. Fig. 2.13-2.14 show the $E(t)$ curves for the reactor + condensers assembly in different temperatures and pressures.

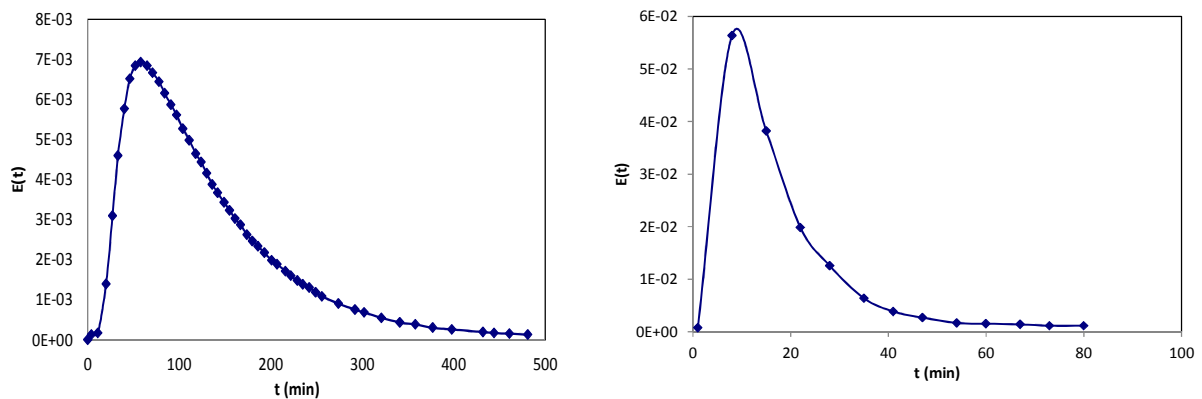


Figure 2.13 Residence time distribution determination for milli-fixed bed reactor and condensers (left: $T = 20$ °C, $P = 20$ bar; right: $T = 20$ °C, $P = 2.7$ bar).

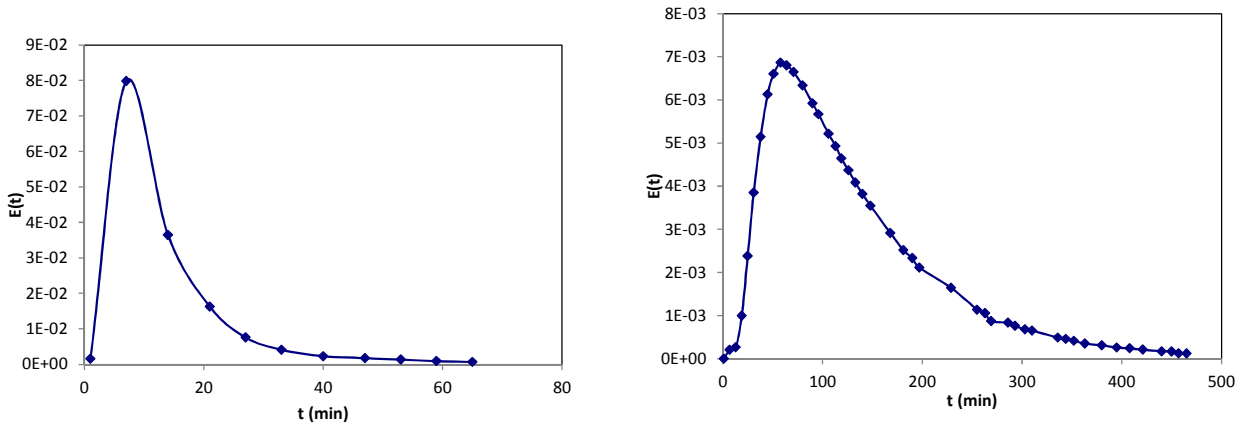


Figure 2.14 Residence time distribution determination for milli-fixed bed reactor and condensers (left: T = 260 °C, P = 2.7 bar; right: T = 260 °C, P = 20 bar).

Additionally, the RTD distribution $E(t)$ curves in both millifixed bed reactor only and condensers only configuration is depicted in Fig. 2.15, in order to identify the mixing characteristics of both geometries. The curves suggest a plug flow regime for the fixed bed reactor whereas condensers can be viewed as continuous stirred tank reactors without reaction, as they possess a decreasing exponential $E(t)$ curve.

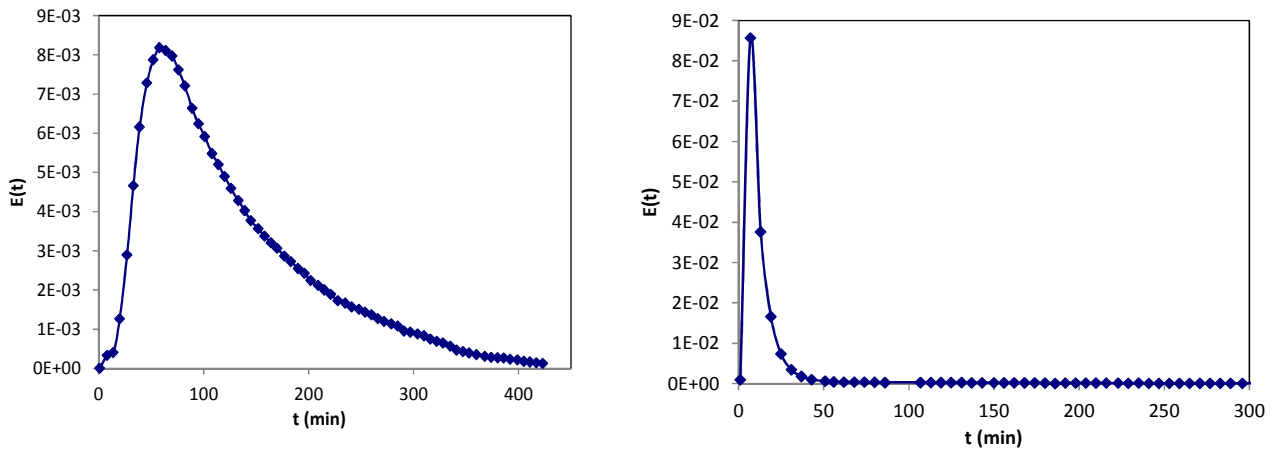


Figure 2.15 Residence time distribution determination for milli-fixed bed reactor (right) and condensers (left) at T = 260 °C and P = 20 bar.

In addition to the residence-time distribution function, the first moment of the RTD function, defined as the mean residence time is used in order to compare with the ideal residence time $\tau = V/v$ where V is the reactor (or setup) volume:

$$\bar{t} = \frac{\int_0^{\infty} t \cdot E(t) dt}{\int_0^{\infty} E(t) dt} = \int_0^{\infty} t \cdot E(t) dt \quad (2.12)$$

The average residence time for the different configurations and operating conditions are summarized in Table 2.3, along with the theoretical residence time. Note that in the case of theoretical residence time calculation, the flow rate should be corrected as the temperature is not the same in different parts of the set-up, i.e. the reactor, the hot and cold condensers, as well the tubes. Note that the average residence time \bar{t} calculated from Eq. 2.12 and theoretical residence time τ are in the same order of magnitude in most cases.

Table 2.3 Average and theoretical residence time for milli-fixed bed reactor and condensers under different temperatures and pressures.

System	T (°C)	P (bar)	\bar{t} (min)	σ (min)	τ (min)
Milli-fixed bed + condensers	20	2.7	18	23	23
Milli-fixed bed + condensers	20	20	130	87	124
Milli-fixed bed + condensers	260	2.7	14	16	23
Milli-fixed bed + condensers	260	20	131	86	125
Milli-fixed bed only	260	20	21	13	12
Condensers only	260	20	120	66	122

Table 2.5 allows identifying the parameters that modify the residence time distribution as well. As can be seen, temperature does not affect the RTD significantly as the RTD curves at 20 °C and 260 °C show only a slight difference (Fig. 2.14-2.15) . The average residence time reduces from 18 min to 14 min when the temperature is increased from 20°C to 260°C (Table 2.5). This is reasonable as the temperature increase occurs only in the reactor (with a volume of 1 mL) which is only a small part of the whole setup (with a total volume of ~550 mL).

However, the pressure effect is much more pronounced. A pressure increase from 2.7 bar to 20 bar causes a significant rise in the mean residence time, which increases from 14 min to 131 min at 260 °C (Fig. 2.14 -2.15 and Table 2.3). High pressure reduces the superficial velocity of the Hydrogen/nitrogen mixture in the whole reactor + condenser assembly as the backpressure regulator is placed after the cold condenser.

In addition to the first moment of RTD function $E(t)$, the second moment is also commonly calculated and it is called the variance, or square of the standard deviation. It is defined by:

$$\sigma^2 = \int_0^{\infty} (t - \bar{t})^2 \cdot E(t) dt \quad (2.13)$$

The magnitude of this moment is an indication of the “spread” of the distribution; the greater the value of this moment is, the greater a distribution’s spread will be. The list of variances in different configurations tested in this study is also provided in Table 2.5.

In addition to the first and second moment of the RTD distribution function, the cumulative RTD function $F(t)$ is also sometimes used to represent the fraction of the exit stream that has resided in the reactor (or the set-up) for a period of time shorter than a given value t :

$$F(t) = \int_0^t E(t) dt \quad (2.14)$$

We can calculate $F(t)$ at various times t from the area under the curve of an $E(t)$ versus t plot. However for the experimental part of this work this does not bring significant information.

The next section proposes a global hydrodynamic model for the whole milli-fixed bed reactor setup in order to account for the presence of the condensers and to use the correct information for deactivation modeling.

2.3.2. Proposition of a global hydrodynamic model based on the RTD analysis to improve the deactivation simulation

In order to correct the effect of condensers on the concentration measured at the exit of the set-up and estimate the values at the exit of the reactor, a hydrodynamic model has been selected for milli-fixed bed reactor based on the experimental RTD data. The model consists of a plug flow reactor (as the reactive part i.e. the milli-fixed bed) with a finite number of CSTRs having dead volume fractions in series (as the condensers partially mixed). Such a model is referred to as a “complete RTD model” and is depicted in Fig. 2.16.

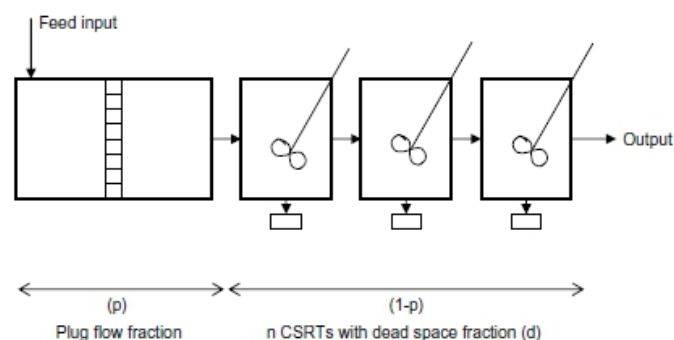


Figure 2.16 Graphical representation of the “full model” used for RTD modeling

D. Wolf and W. Resnick [8] were among the first to analyze the RTD behavior of real systems in 1963. They have found that the residence time distribution for most real systems can be represented by a cumulative RTD function (*F-function*) of the form:

$$F(t) = 1 - \exp\left[-\eta\left(\frac{t-\varepsilon}{\theta}\right)\right] \quad \text{for } t > \varepsilon \quad (2.15)$$

$$F(t) = 0 \quad \text{for } t < \varepsilon \quad (2.16)$$

with η the coefficient of exponent, ε the system phase shift, and θ the normalized time $\theta = t/\bar{t}$.

This equation results for a number of plausible flow models that include the additional possibilities of dead space, short-circuiting, error in average residence time determination, and lag in response and any combination of these models. This equation can be used to describe the experimental results obtained for single as well as multistage systems.

The characteristic parameters (η and ε/θ) were calculated for a set of frequent experimental configurations as Table 2.4 shows.

Table 2.4 Derived Values of η and ε/θ and Derived Flow Models from Some Experimental Data [8]

Flow System	Derived Flow Model						
	Derived Values		<i>a</i> , Perfect mixing of effective volume	<i>p</i> , plug flow of effective volume	<i>d</i> , Dead space of total volume,	<i>F</i> , Short circuiting of flow rate,	<i>L</i> , Lag of θ , %
	η	ε/θ	%	%	%	%	
Turbulent oil in pipe	0	1	0	100
Laminar in pipe	2.56	0.5	44	56	11
Gas fluidized bed	1.74	0.42	58	42
Gas fluidized bed	1.3	0.3	77	23	7
Gas fluidized bed	1.2	0.16	84	16
Gas fluidized bed	1.1	0.08	92	8
Gas fixed bed	7.95	0.84	13	87	3
Gas in pipe	13.4	0.92	8	92
Gas fluidized bed	1.15	0.17	87	13	4
Gas spherical stirred reactor	1.0	0	100
Gas fluidized bed	2.12	0.34	58	42	19	..	Indefinable
Gas fluidized bed	1.5	0.29	70	30	4
Gas fluidized bed	2.05	0.25	58	42	20	5	9
Liquid Denver flotation cell	1.05	-0.05	100	..	9	5	...
Liquid Mat flotation cell	1.15	0.06	94	6	7
Liquid Fagergren flotation cell	1.01	0	100
Liquid MacKintosh flotation cell	1.19	0	100	..	16
Liquid fixed bed	3.15	0.7	32	68	2
Gas fluidized bed	2.2	0.55	45	55
Gas fluidized bed	0.70	-0.25	100	30	25
Gas fluidized bed	0.74	-0.3	100	26	10
Gas fluidized bed	0.68	-0.2	100	32	36
Solid fluidized bed	1.23	0.1	89	11	9

The “complete RTD model” proposed by Kumar et al [9] is an extension of the model originally developed by Levenspiel in 1972 [10] for a CSRT cascade (the tank-in-series model). The following equation was developed for plug flow reactor with finite number of CSTRs with dead volume in series

$$E(t) = \frac{b [b(\theta - p)]^{n-1}}{(n-1)!} \exp[-b(\theta - p)] \quad (2.17)$$

where

$$b = \frac{n}{(1-p)(1-d)} \quad (2.18)$$

Hence, the four parameters that fully represent this model are \bar{t} , p , n and d .

Average residence time \bar{t} is given by experimental RTD data as well as the fraction of plug flow (p):

$$\bar{t} = \int_0^{\infty} tE(t)dt \quad (2.19)$$

$$p = \frac{t_{\min}}{t} \quad (2.20)$$

with t_{\min} the time when the first signal of tracer is detected in the output.

The dead fraction (d) and the number of CSTR (n) are therefore estimated based on the least sum of squares of error (between experimental and calculated $E(t)$ curves). In the first time both parameters are subject to optimizations. A theoretical number of condensers of 1.82 is obtained with an ideal dead volume of 9.5%. In the second step, the CSTR number is set to $n = 2$ due to the geometry of the problem (two condensers), which helps to optimize the dead volume fraction only. The results of both models are given in Table 2.5. As the least sum of squares of error is comparable for both configurations, the second complete RTD model is used in the deactivation modeling as it conveys a better image of the setup geometry.

Table 2.5 Complete RTD model with different optimization methods for the case of milli fixed bed reactor in series with hot and cold condenser (P = 20 bar, T = 260°C)

System	n	d	$\sum (E_{\text{exp}}(t) - E_{\text{mod}}(t))^2$
Model 1	1.82	0.095	2.8×10^{-6}
Model 2	2	0.107	4.5×10^{-6}

Fig. 2.17 shows the experimental and modeled $E(t)$ curves in high temperature and pressure conditions. The experimental parameters for the both “complete RTD model” in these conditions are: $\bar{t} = 131$ min, $p = 0.137$ ($t_{min} = 13$ min).

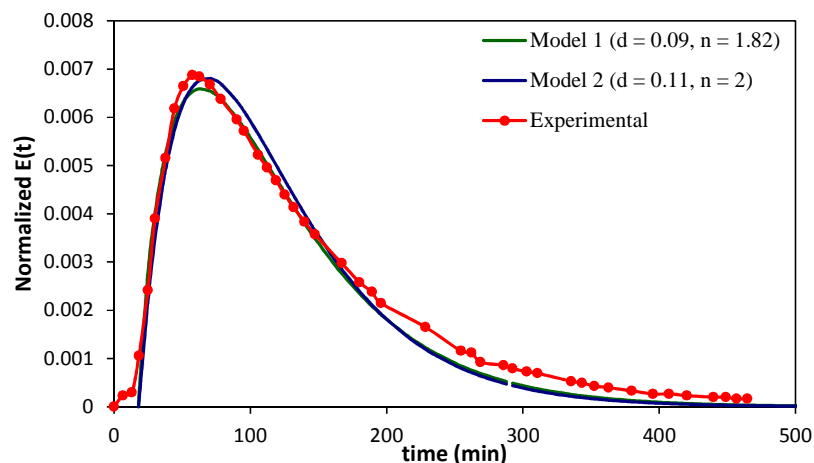


Figure 2.17 Experimental and modeling RTD profile for milli-fixed bed reactors and condensers at $P = 20$ bar, $T = 260$ °C

The results of the “complete RTD model” are used in the deactivation modeling of reactors where the proper interpretation of experimental data should be made. A paper is also in preparation to present the information the model could bring about. A typical example of such a method is depicted in Fig. 2.18 where the “complete RTD model” is taken into account in order to construct the CO conversion not only at the reactor outlet but also at the whole setup exit (also known as full profile prediction). Such an approach enables us to compare the experimental and model findings and to fit the corresponding kinetic/deactivation constant. Further details are given in Chapter 4.

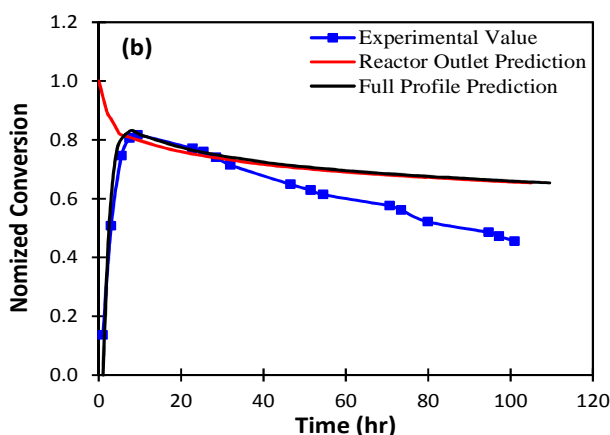


Figure 2.18 Experimental and calculated CO conversion profile of reference catalyst during FT synthesis using the improved model: milli-fixed bed reactor, reference catalyst, $T = 493$ K, $P = 20$ bar, $H_2/CO = 2$, $GHSV = 3.1 \times 10^6$ $Nml/(mol_{Cobalt} \cdot h^{-1})$

2.4. Modeling of experimental reactors

Although the experimental data are required to study the catalyst behavior, modeling tools could predict the deactivation phenomena in a quantitative way.

Two general groups of chemical reactors are modeled in this thesis: tubular Fixed Bed Reactors and Continuous Stirred Tank Reactors. This section gives the details of both reactor models.

Fig. 2.19 shows all the information required to model the deactivation in experimental reactors. All the different steps are then describes in the following sections.

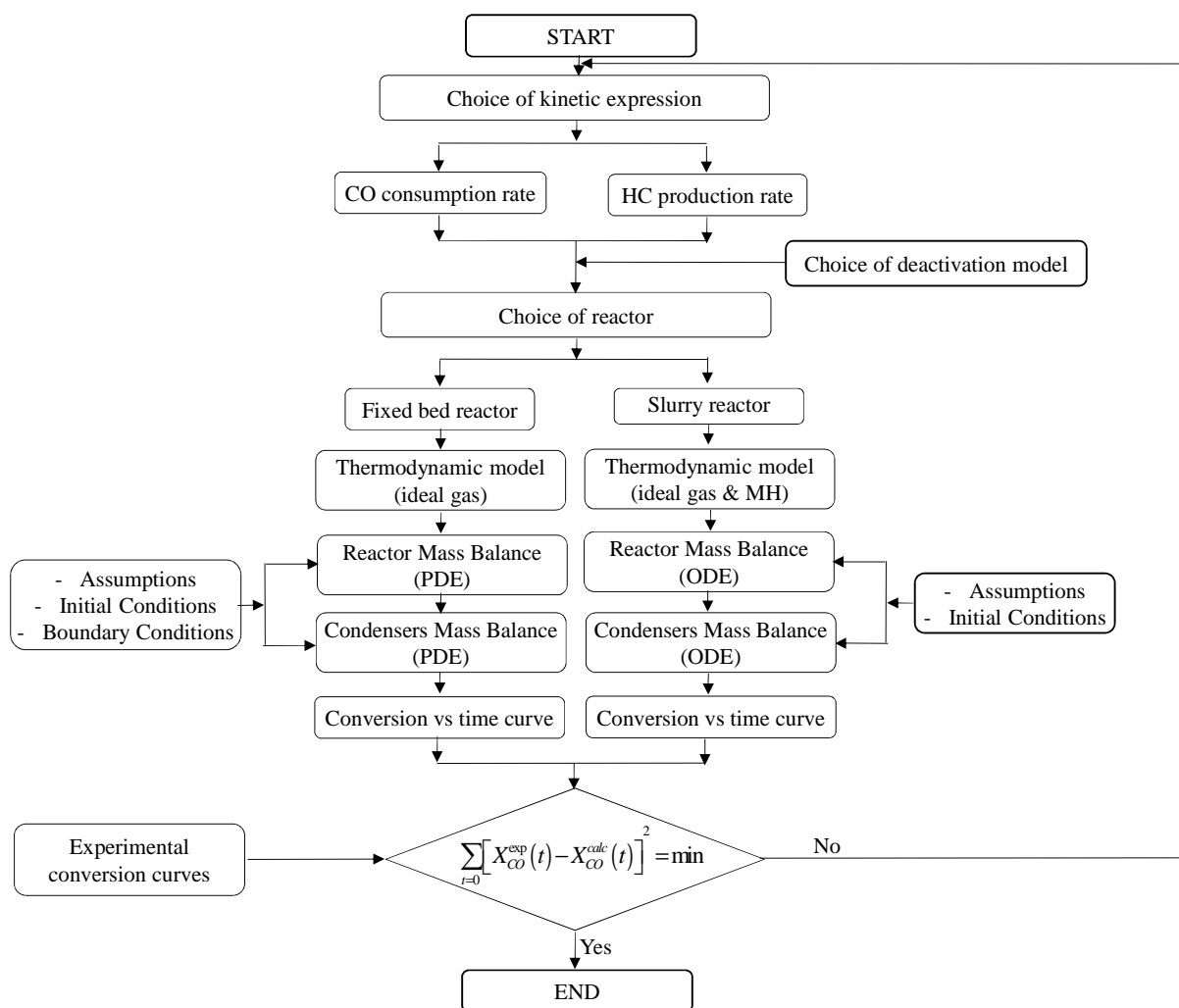


Figure 2.19 Flowchart of developing unsteady state deactivation models for experimental reactors

2.4.1. Choice of kinetic equation

Modeling the FTS reactor requires a rate equation for the intrinsic kinetics from the consumption of CO to the formation of the hydrocarbons.

A. CO consumption rate

There are several empirical and mechanistic kinetic expressions in the literature (Table 2.6) for the steady-state CO consumption rate. However the rate expression suggested by Yates and Satterfield shows a good fit with the experimental data especially in the previous works performed in UCCS [6], [2], [11].

The experimental work of Yates and Satterfield has led to the following expression:

$$-r_{CO} = \frac{k_a P_{H_2} P_{CO}}{[1 + k_b P_{CO}]^2} \quad (2.21)$$

which is based on a mechanistic approach including a non-dissociative CO adsorption step. Further details and improvements are given by J. Anfray [6] and L. Silva [11].

It should be noted that although the Yates-Satterfield expression is initially given in terms of partial pressures of reactants, we have used the liquid concentrations for the slurry reactor as this reaction can be limited by the external mass transfer in industrial reactors. We have then corrected the expression using a liquid-gas repartition according to the Henry's law. The Yates-Satterfield equation expressed by gas concentration is used for the fixed bed reactors to simplify the modeling. It is expected that in the reality the catalyst can be dry in the first part of the bed and fully wetted in the last part of the bed. However, we do not provide in this work any tools to compute the wetting efficiency along the bed in a FTS fixed-bed reactor.

Table 2.6 Bibliography review of CO consumption rate expressions [6]

Reference	Catalyst	Reactor type	T (°C)	P (MPa)	CO conversion	Inlet H ₂ /CO ratio	Kinetic Expression
Brötz (1949) [12]	Co/MgO/ThO ₂ /kieselguhr	Fixed-bed (gas-solid)	185-200	0.1		2	$-r_{CO} = \frac{k_a P_{H_2}^2}{P_{CO}}$
Anderson (1956) [13]	Co/ThO ₂ /kieselguhr	Fixed-bed (gas-solid)	186-207	0.1		0.9-3.5	$-r_{CO} = \frac{k_a P_{H_2}^2 P_{CO}}{1 + k_b P_{H_2}^2 P_{CO}}$
Yang et al. (1979) [14]	Co/CuO/Al ₂ O ₃	Fixed-bed (gas-solid)	235-270	0.17-5.5		1.0-3.0	$-r_{CO} = k_a P_{H_2}^2 P_{CO}^{-0.5}$
Rautavuoma et Van der Baan (1981) [15]	Co/ Al ₂ O ₃	Fixed-bed (gas-solid)	250	0.1	< 2 %	0.2-4.0	$-r_{CO} = \frac{k_a P_{H_2} P_{CO}^{1/2}}{[1 + k_b P_{CO}]^3}$
Sarup et Wojciechowski (1989) [16]	Co/ kieselguhr	Berty (gas-solid)	190	0.2-1.5		0.5-8.3	$-r_{CO} = \frac{k_a P_{H_2}^{1/2} P_{CO}}{[1 + k_b P_{CO} + k_c P_{H_2}^{1/2}]^2}$
Yates/Satterfield (1989) [17]	Co/MgO/SiO₂	Slurry (three-phasic)	220-240	0.5-1.5	6-68 %	1.5-3.5	$-r_{CO} = \frac{k_a P_{H_2} P_{CO}}{[1 + k_b P_{CO}]^2}$
Iglesia/Reyes/Soled/Becker (1993) [18]	Co/SiO ₂	Fixed-bed (gas-solid)	200-210	0.1-3	< 15 %	1-10	$-r_{CO} = \frac{k_a P_{H_2}^{0.6} P_{CO}^{0.65}}{[1 + k_b P_{CO}]^2}$
E. Van Steen, Schulz (1999) [19]	Co/MgO/ThO ₂ /SiO ₂ Co/SiO ₂	Slurry (three-phasic)	190-210	0.5-2.5			$-r_{CO} = \frac{k_a P_{H_2}^{3/2} P_{CO} / P_{H_2O}}{[1 + k_b P_{H_2} P_{CO} / P_{H_2O}]^2}$
Zennaro et al (2000) [20]	Co/TiO ₂	Fixed-bed (gas-solid)	200	0.8-1.6	< 5 %	1-4	$-r_{CO} = \frac{k_a P_{H_2}^{0.74} P_{CO}}{[1 + k_b P_{CO}]^2}$
Zennaro et al (2000) [20]	Co/TiO ₂	Fixed-bed (gas-solid)	200	0.8-1.6	< 5 %	1-4	$-r_{CO} = k_a P_{H_2}^{0.74} P_{CO}^{-0.24}$

B. Hydrocarbons production rate

The individual reaction rates, r_i of different components are also defined based on the work of Philippe et al [5] as follows:

$$r_{H_2O} = -r_{CO} = +r_{FT} \quad (2.22)$$

$$r_{H_2} = \sum_{i=1}^N [(2i+1) \cdot r_{C_i}] \quad (2.23)$$

$$r_{C_1} = k_d \cdot r_{FT} \quad (2.24)$$

$$r_{C_2} = k_e \cdot r_{FT} \quad (2.25)$$

$$\text{For } n \geq 3: r_{C_n} = \alpha \cdot r_{C_{n-1}} \quad (2.26)$$

where we assume Anderson-Schulz-Flory distribution for C_{3+} hydrocarbons with chain growth probability ($\alpha = 0.9$) typical for low temperature FT synthesis. Methane and ethane production rates are given by separate expressions. For the sake of simplicity, olefins and oxygenates are not taken into account as well as Water-Gas-Shift (WGS) reaction. The number of considered hydrocarbons is also limited to $n_{max} = 100$ for slurry and $n_{max} = 20$ for fixed bed reactors. These assumptions are then checked by the experimental data, and adjusted if required.

The activation energies for the three kinetic parameters (k_a , k_d , and k_e) as well as the CO heat of adsorption for k_b are taken from the literature data [5], [21], [22]. The pre-factors are however optimized for each specific reactor. Table 2.7 summarizes the kinetic parameters used for different reactor configurations used in this study. The difference in the kinetic values between the fixed bed and slurry reactors could be attributed to several factors including the difference in the catalyst used, reduction protocol employed, flow regime, etc.

Table 2.7 List of kinetic parameters used in different reactor configurations

Reactor Type		$k_{a,0}$ ($m^7/[kg_{cat} \cdot mol \cdot hr]$)	E_a (kJ/mol)	$k_{b,0}$ (m^3/mol)	ΔH_b (kJ/mol)	$k_{d,0}$ (-)	E_d (kJ/mol)	$k_{e,0}$ (-)	E_e (kJ/mol)
Capillary fixed bed reactor		4.62×10^{-8}	100	0.342	20	0.1	81	1.3×10^{-2}	49
Milli-fixed bed reactor		4.62×10^{-8}	100	0.342	20	0.1	81	1.3×10^{-2}	49
Slurry reactor	Pure simulation runs	1.10×10^{-7}	100	1.475	20	0.1	81	1.3×10^{-2}	49
	Model validation	3.46×10^{-7}	100	0.14185	20	0.1	81	1.3×10^{-2}	49

* The subscript 0 refers to the parameter value at 493.15 K

The next section described the dedicated kinetic models for each specific reactor type.

2.4.2. Fixed bed reactor (FBR) model

The reactor geometry selected for the modeling fixed bed reactor consists of a one-dimensional plug flow reactor through which a gas mixture (including the reactants as well as the products) flow. This helps to validate the model using two available reactors: the operando capillary-fixed bed reactor as well as the laboratory milli-fixed bed reactor. The catalyst distribution is considered uniform throughout the reactor (Fig. 2.20).

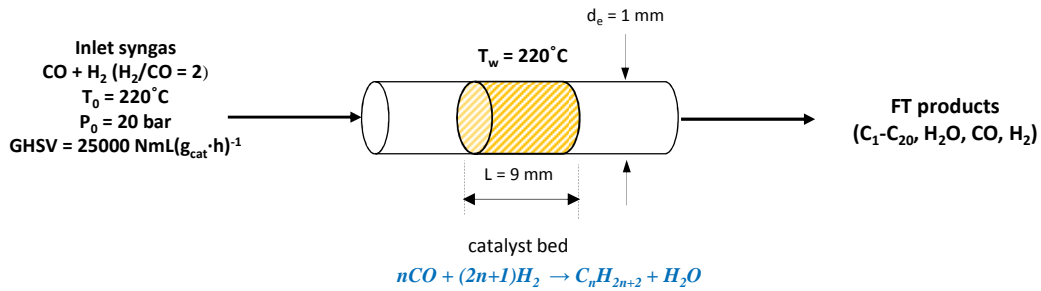


Figure 2.20 Typical representation of the reactor configuration used for FBR modeling

Thermodynamic calculations using PRO/II software showed that more than 85% of molar flow rate is in the gas phase under typical low temperature FT condition (20 bar, 220°C). Thus a pseudo-homogenous gas-phase system can be assumed for the model development. Ideal gas law is used as the equation of state. Mass transfer limitations are assumed to be negligible under these conditions. The unsteady-state model is made of the mass balance equations (partial differential). The parameters can be then calculated as functions of time (t) and position in the reactor (z). The model assumes isothermal conditions. The heat balance expressions are not necessary in this case. The mass-balance equation however is applied which contains accumulation, convection and reaction terms. The continuity equation yields volume change for the gas mixture. The classical Ergun law is applied for the momentum balance:

$$\varepsilon \frac{\partial C_i}{\partial t} + \frac{\partial (C_i u)}{\partial z} - (1 - \varepsilon) \eta r_i \rho_{cat} = 0 \quad (2.27)$$

$$\varepsilon \frac{\partial \rho}{\partial t} + \frac{\partial (\rho u)}{\partial z} = 0 \quad (2.28)$$

$$\frac{\partial P}{\partial z} + \frac{1 - \varepsilon}{\varepsilon} \left(1.75 + 150 \frac{1 - \varepsilon}{\text{Re}} \right) \frac{\rho u^2}{d_p} = 0 \quad (2.29)$$

where P is the total pressure, ε is the bed void fraction, η represents the catalyst effectiveness factor, Re is the fluid Reynolds number and d_p and ρ_{cat} show the catalyst pellet diameter the catalyst density, respectively.

The partial differential set of equations is solved in conjunction with the kinetic and deactivation expressions. The following set of boundary and initial conditions is applied:

$$\left. \begin{aligned} P(z=0, t=0) &= P_{syngas} \\ u(0,0) &= u_{syngas} \\ C_i(0,0) &= C_{i,syngas} \end{aligned} \right\} \text{boundary conditions} \quad (2.30)$$

$$\left. \begin{aligned} \frac{\partial C_i}{\partial t}(z,0) &= 0 \\ \frac{\partial \rho}{\partial t}(z,0) &= 0 \\ \bar{d}_s(z,0) &= \bar{d}_{s,0} \end{aligned} \right\} \text{initial conditions} \quad (2.31)$$

For the individual components, physicochemical properties (ρ , μ) are determined from classical correlations as functions of temperature. A typical Co-based reference catalyst is considered for the simulations. The catalyst characteristics are listed in Table 2.8.

Table 2.8 Main characteristics of the reference catalyst

Mean catalyst diameter (μm)	Initial particle diameter (nm)	Bulk density, ρ (kg/m^3)	Cobalt content, X_{Co} (%)	Cobalt density, ρ_{Co} (kg/m^3)	Bed void fraction ε (-)	Effectiveness factor η (-)
90	6.0	2030	25	8900	0.4	1

2.4.2.1. Fixed bed reactor (FBR) model with condensers

Based on the results of the RTD measurements and modeling, the contribution of condensers to the catalytic activity of the whole FBR set-up is included in the modeling where the condensers are assumed to be Continuous Stirred Tank Reactors (CSTR) without any reaction. The actual condenser volume is adjusted by the dead volume fraction (namely 10%) in the calculations.

Similar to the reactor, the condensers are assumed to contain only a gas mixture as the thermodynamic flash calculations show a small fraction of liquid produced in most cases. Ordinary differential equations (ODE) are then used to follow the change in the condensers compositions with time only. The condensers are assumed to work under isothermal regime. The overall mass balance equations (Eq. 2.32) as well as geometrical limitation (Eq. 2.33) enable us to solve the $n+1$ equations with $n+1$ unknowns (the outlet gas flow rate G , as well individual components molar fractions y_i).

$$\frac{dn_i^G}{dt} = G_{inlet} y_{i,inlet} - G y_i \quad (2.32)$$

$$V_G = V_{condenser} \quad (2.33)$$

where V represents the volume and n_i^G the individual gas-phase mole number of component i .

The ordinary differential set of equations is solved in line with a set of initial conditions and inlet compositions.

$$\left. \begin{aligned} G_{inlet} &= G_{reactor,outlet} \\ y_{i,inlet} &= y_{i,reactor,outlet} \\ y_i(0) &= y_{i,syngas} \end{aligned} \right\} \text{Hot Condenser} \quad (2.34)$$

$$\left. \begin{aligned} G_{inlet} &= G_{hot\ condenser,outlet} \\ y_{i,inlet} &= y_{i,hot\ condenser,outlet} \\ y_i(0) &= y_{i,syngas} \end{aligned} \right\} \text{Cold Condenser} \quad (2.35)$$

2.4.3. Continuous stirred tank reactor (CSTR) model

Several approaches (including Ahon et al. [23] and Pinna and coworkers [24]) are available in the literature for the slurry reactor modeling. J. Anfray [6] has developed a complex model which includes the liquid-mass transfer limitation as well as sophisticated vapor liquid equilibria. The model developed by Philippe et al [5] for the FT reaction over Co/SiC simplifies the kinetics as it does not take the production of olefins and alcohols into account.

In the present study both models are combined in order to develop a new hybrid model which is simpler in some aspects but still capable of representing the reactor realistically.

This model uses a continuous stirred tank reactor (CSTR) geometry (with an inner diameter of 46 mm and a total volume of 300 mL) initially filled with 40 g of synthetic heavy paraffinic solvent of SX70 with a molecular weight of 464 g/mol. The reactor is then closed and exposed to the syngas stream. The FT produced wax replaces the initial solvent with time. Fig. 2.21 shows a graphical representation of the geometry used for slurry reactor modeling.

In addition to previously described kinetic assumptions, a set of thermodynamic and geometric assumptions are also used in order to simplify the model:

1. The outlet filter is placed on the top of the initial paraffinic wax (~100 mL). In other words, the level of suspended mixture is constant inside the reactor. This assumption reduces the simulation time and allows studying deactivation in a more comprehensive way.

2. Pseudo-components (cuts) are defined starting from $n = 6$ in order to limit the number of products and the calculation time, while still maintaining accuracy of results. It is reasonable to assume that the properties of each cut are the same as the properties of the average carbon-number component, which is the ‘model’ component, in the cut.

3. The reactor is assumed to work under chemical regime and the liquid phase in equilibrium with the gas phase.

4. The components’ fugacity in the liquid phase is calculated using Henry’s coefficients for the light components (CO , N_2 , H_2 , CH_4 , C_2H_6 , and C_3H_8). For heavier condensable hydrocarbons (C_{3+}) the Rault’s law has been used [6]. The gas phase is assumed to be ideal. This is in line with Anfray [6] where has demonstrated in his work that PRSV model leads to a fugacity coefficient close to 1 in gas phase, i.e. ideality.

5. Isothermal and isobaric conditions are assumed.

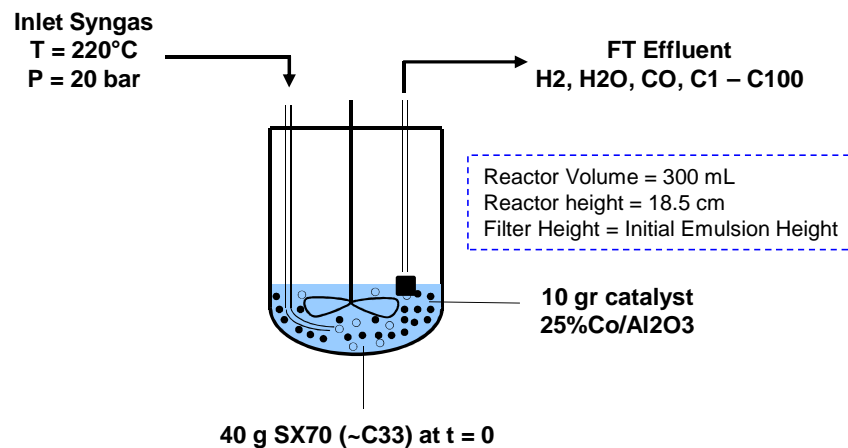


Figure 2.21 Schematic View of the slurry reactor configuration used in the current study

The reactor model is then composed of Ordinary differential equations (ODE) that give the change in the reactor composition with time only. The mass balances are written for the whole system, i.e. for each component both the liquid and gas phase contributions are considered at the same time. This is in line with the methodology developed by Ahon et al [23] as the vapor-liquid equilibria exist between both phases.

The overall mass balance equations are written as follows:

$$\frac{d}{dt}(n_i^L + n_i^G) = G_{inlet} y_{i,inlet} - G y_i - L x_i + R_i m_{Co} \quad (2.36)$$

where G and L are the gas and liquid molar flow rate, n_i^L and n_i^G are the number of moles of the component i within liquid and gas phases inside the reactor, x_i and y_i are the component molar fractions inside liquid and gas phases, R_i is the reaction rate for each component, and m_{Co} is the cobalt mass loaded into the reactor.

The calculation of hydrodynamic properties is made according to the method used by Anfray [6]. The liquid-vapor equilibria relate the compositions in the liquid and gas phases:

$$y_i = k_i x_i \quad (2.37)$$

The system of $2n+2$ unknowns (n_i^L , n_i^G , L , and G) requires $2n+2$ equations. In combination with Eq. 2.36 (n equations) and Eq. 2.37 (n equation) the following two equations are used to solve the equation system.

$$\text{Geometrical Limitation } V_L + V_G + V_S = V_{reactor} \quad (2.38)$$

$$V_{em} = \text{cons. therefore } \frac{dn_L}{dt} = 0 \quad (2.39)$$

2.4.3.1. Continuous stirred tank reactor (CSTR) model with condensers

A methodology similar to the one developed for the FBR condensers are used for the CSTR condensers. However both the liquid and gas phases are included. The set of overall mass balances (Eq. 2.40), vapor-liquid equilibria (Eq. 2.41), and geometric condition (Eq. 2.42) allows to find then set of $2n+1$ unknowns (the outlet gas flow rate G , as well individual components molar fractions x_i and y_i). It should be noted that the liquid flow rate is set to zero as it was assumed that the liquid-phase products accumulate inside the condensers with time. The condensers are then emptied at the end of each catalytic run.

$$\frac{d}{dt}(n_i^L + n_i^G) = G_{inlet} y_{i,inlet} - G y_i \quad (2.40)$$

$$y_i = k_i x_i \quad (2.41)$$

$$V_G = V_{condenser} \quad (2.42)$$

The set of initial conditions and inlet compositions are as follows:

$$\left. \begin{aligned} G_{inlet} &= G_{reactor,outlet} \\ y_{i,inlet} &= y_{i,reactor,outlet} \\ y_i(0) &= y_{i,syngas} \\ x_i(0) &= 0 \end{aligned} \right\} \text{Hot Condenser} \quad (2.43)$$

$$\left. \begin{aligned} G_{inlet} &= G_{hot\ condenser,outlet} \\ y_{i,inlet} &= y_{i,hot\ condenser,outlet} \\ y_i(0) &= y_{i,syngas} \\ x_i(0) &= 0 \end{aligned} \right\} \text{Cold Condenser} \quad (2.44)$$

2.5. Choice of numerical approaches

As the governing equations in deactivation modeling are partial differential equations (PDEs), appropriate software should be used which could handle such equations. The related concerns such as convergence and tolerance limit and the calculations stability need to be considered.

A set of relevant software were therefore utilized during this thesis. MATLAB® was used initially to develop the steady state equations in fixed bed reactors where the accumulation terms are set to zero. This gave an initial image of the FT process in different operating conditions. The use of MATLAB® is also justified by the fact that it provides strong solver which could lead to more stable results. Parameters adjustments are obtained using multi-parameter regression (Levenberg-Marquardt method). The MATLAB® data output were then used as initial order of magnitude in other programming software.

Once the initial steady state results are obtained, the algebraic equations, ODEs and PDEs are solved simultaneously within gPROMS® ModelBuilder 3.3.1.

Models are constructed in the gPROMS® ModelBuilder by writing down the fundamental chemistry, physics, chemical engineering, operating procedures and other relationships that govern the FT synthesis process.

There are two standard mathematical solvers for the solution of mixed sets of differential and algebraic equations in gPROMS, namely DASOLV and SRADA. DASOLV is based on variable time step/variable order Backward Differentiation Formulae (BDF), whereas SRADAU implements a variable time step, fully-implicit Runge-Kutta method. We have used the DASOLVE in this thesis as it has been proved to be efficient for a wide range of problems. Both of the above solvers are designed to deal with large, sparse systems of equations in which the variable values are restricted to lie within specified lower and upper

bounds. Moreover, they can handle situations in which some of the partial derivatives of the equations with respect to the variables are available analytically while the rest have to be approximated. Efficient finite difference approximations are used for the latter purpose. Both solvers automatically adjust each time step taken so that the following criterion is satisfied:

$$\sqrt{\frac{1}{n_d} \sum_{i=1}^{n_d} \left(\frac{\varepsilon_i}{a + r|x_i|} \right)^2} < 1 \quad (2.45)$$

where n_d is the number of differential variables in the problem; ε_i is the solver's estimate for the local error in the i th differential variable; x_i is the current value the i th differential variable; a is an absolute error tolerance; and r is a relative error tolerance. The maximum values used for the absolute and relative error tolerance are 7×10^{-4} and 3×10^{-2} respectively.

The resulting model is then validated against the observed laboratory data to adjust model parameters to match reality as closely as possible.

For slurry reactor, initial codes written [6] within FORTRAN® were initially used which evaluate the wax replacement time. The calculation codes are written in FORTRAN® 90 and compiled under Microsoft Visual Studio platform for the PC version. However as they do not take the deactivation terms, gPROMS® was again employed to obtain more precise results about the catalyst deactivation behavior in different operating conditions as well to fit the experimentally observed data.

Thermodynamic properties as well as physical and chemical parameters were calculated using PRO/II® 8.0.

2.6. Conclusion

The previous sections described the methodology used in the current work to study the catalyst deactivation in experimental FTS reactors. The choice of experimental set-ups is discussed along with the catalyst used. The experimental artifact that the hydrodynamics of hot and cold condensers could interfere on the data analysis of milli-fixed bed reactor is investigated and a complete set of residence time distribution experiments is conducted in order to understand the hydrodynamic behavior of the whole system. The results of such experiments are further used in the RTD modeling where a coherent model is developed which could fit the experimental findings. The model is used in the deactivation model of experimental reactor to yield both the real CO conversion at the reactor outlet as well as apparent CO conversion at the setup outlet.

The methodology used for the reactor modeling of the FT reactor is also described in detail. The choice of proper kinetic expression is discussed. The set of mass balance equations for both fixed bed and slurry reactor is provided along with the assumptions, initial and boundary conditions used for model development. The mass balance equations for condensers are also presented. The numerical approaches used for simulations are detailed.

2.7. References

- [1] H. Karaca, Propriétés catalytiques et versatilité des catalyseurs à base de cobalt lors du procédé Fischer-Tropsch, in: Sciences de la Matière, du Rayonnement et de l'Environnement, University of Lille, Lille, France, 2010.
- [2] S. Piché, P. Fongarland, Etude expérimentale de la réaction Fischer-Tropsch en réacteur slurry et modélisation (catalyseur cobalt et conditions WGS), in, Université de Lille, 2008.
- [3] S. Chambrey, P. Fongarland, H. Karaca, S. Piché, A. Griboval-Constant, D. Schweich, F. Luck, S. Savin, A.Y. Khodakov, Fischer-Tropsch synthesis in milli-fixed bed reactor: Comparison with centimetric fixed bed and slurry stirred tank reactors, *Catalysis Today*, 171 (2011) 201-206.
- [4] D.E. Mears, Diagnostic criteria for heat transport limitations in fixed bed reactors, *Journal of Catalysis*, 20 (1971) 127-131.
- [5] R. Philippe, M. Lacroix, L. Dreibine, C. Pham-Huu, D. Edouard, S. Savin, F. Luck, D. Schweich, Effect of structure and thermal properties of a Fischer-Tropsch catalyst in a fixed bed, *Catalysis Today*, 147, Supplement (2009) S305-S312.
- [6] J. Anfray, Acquisition de données pour la modélisation d'une colonne à bulles Fischer-Tropsch, in, University of Lyon, 2005.
- [7] H.S. Fogler, Elements of chemical reaction engineering, Foruth Edition ed., Prentice Hall, 2006.
- [8] D. Wolf, W. Resnick, Residence Time Distribution in Real Systems, *Industrial & Engineering Chemistry Fundamentals*, 2 (1963) 287-293.
- [9] A. Kumar, G.M. Ganjyal, D.D. Jones, M.A. Hanna, Modeling residence time distribution in a twin-screw extruder as a series of ideal steady-state flow reactors, *Journal of Food Engineering*, 84 (2008) 441-448.
- [10] O. Levenspiel, Chemical reaction engineering, Wiley, New York, 1972.
- [11] L. Silva, Kinetic modelling of alcohol production and Water Gas Shift reaction in a Fischer-Tropsch synthesis over a Co/Al₂O₃ catalyst, in: Master Catalyse et Procédés, Ecole Centrale de Lille, Lille, France, 2008.
- [12] W. Brötz, *Elektrochem*, 5 (1949) 301-306.
- [13] R.B. Anderson, Catalysts for the Fischer-Tropsch synthesis, Van Nostrand Reinhold, New York, 1956.
- [14] C.-H. Yang, E. Massoth F, G. Oblad A, Kinetics of CO + H₂ Reaction over Co-Cu-Al₂O₃ Catalyst, in: Hydrocarbon Synthesis from Carbon Monoxide and Hydrogen, AMERICAN CHEMICAL SOCIETY, 1979, pp. 35-46.
- [15] A. Outi, I. Rautavuoma, H.S. van der Baan, Kinetics and mechanism of the fischer tropsch hydrocarbon synthesis on a cobalt on alumina catalyst, *Applied Catalysis*, 1 (1981) 247-272.
- [16] B. Sarup, B.W. Wojciechowski, Studies of the fischer-tropsch synthesis on a cobalt catalyst II. Kinetics of carbon monoxide conversion to methane and to higher hydrocarbons, *The Canadian Journal of Chemical Engineering*, 67 (1989) 62-74.
- [17] I.C. Yates, C.N. Satterfield, Intrinsic kinetics of the Fischer-Tropsch synthesis on a cobalt catalyst, *Energy & Fuels*, 5 (1991) 168-173.
- [18] E. Iglesia, Reyes, S.C., Soled, S.L., in: C.J.P. E.R. Becker (Ed.) Computer-Aided Design of Catalysts, Dekker, New York, 1993.
- [19] E. van Steen, H. Schulz, Polymerisation kinetics of the Fischer-Tropsch CO hydrogenation using iron and cobalt based catalysts, *Applied Catalysis A: General*, 186 (1999) 309-320.
- [20] R. Zennaro, M. Tagliabue, C.H. Bartholomew, Kinetics of Fischer-Tropsch synthesis on titania-supported cobalt, *Catalysis Today*, 58 (2000) 309-319.

- [21] M.J. Keyser, R.C. Everson, R.L. Espinoza, Fischer–Tropsch Kinetic Studies with Cobalt–Manganese Oxide Catalysts, *Industrial & Engineering Chemistry Research*, 39 (1999) 48-54.
- [22] S. Storsæter, D. Chen, A. Holmen, Microkinetic modelling of the formation of C1 and C2 products in the Fischer–Tropsch synthesis over cobalt catalysts, *Surface Science*, 600 (2006) 2051-2063.
- [23] V.R. Ahón, E.F. Costa Jr, J.E.P. Monteagudo, C.E. Fontes, E.C. Biscaia Jr, P.L.C. Lage, A comprehensive mathematical model for the Fischer–Tropsch synthesis in well-mixed slurry reactors, *Chemical Engineering Science*, 60 (2005) 677-694.
- [24] D. Pinna, E. Tronconi, L. Lietti, R. Zennaro, P. Forzatti, Wax composition transients during Fischer–Tropsch synthesis, *Journal of Catalysis*, 214 (2003) 251-260.

CHAPTER

3

**DEVELOPMENT OF MICROSCOPIC
DEACTIVATION MODELS**

3.1. Introduction

In this thesis, the deactivation phenomena are investigated in both catalyst (microscopic and reactor (macroscopic) scale. Once the processes that lead to deactivation are studied at the catalyst surface level, the modification in the catalyst physico-chemical properties with time are correlated by mathematical equations. Such equations are then used in macroscopic modeling to find the catalytic activity change (i.e. deactivation) at the reactor scale with time.

To study the changes that lead to deactivation at the catalyst particles level, we have decided to divide the full deactivation profile into two parts: (a) an initial deactivation step as well as (b) a second long-term deactivation period. This is in line with the works already cited in Chapter 1 where a two-step deactivation profile is observed by several authors.

Although several deactivation mechanisms may be present simultaneously in the both steps, one can assume that a single deactivation mechanism is responsible for each step in order to simplify the calculations and the correlations found. The choice of this deactivation mechanism is based on catalyst characterization tools as well as literature works. Further addition of other deactivation mechanisms could be sought if the single-mechanism correlations are not able to fit the experimentally-observed deactivation profile.

In order to model the initial deactivation period, catalyst sintering is selected as the main mechanism whereas coking is chosen to be responsible for the long-term deactivation step.

The first part of this chapter addresses the initial deactivation mechanism; i.e. sintering. The possibility of cobalt oxidation at the catalyst surface is investigated through the help of characterization tools and thermodynamic models. The existing sintering model for nickel-based catalysts is then reviewed which is accelerated by oxygen-containing species at the surface. Based on the similarity of nickel and cobalt catalysts, the proposed model for the cobalt sintering in Fischer-Tropsch conditions is then developed which includes the accelerated effect of water through the formation of surface oxide layer. Such a mechanism leads to a unique correlation for the evolution of cobalt crystallite diameter with time as well as other operating conditions.

The second part of this chapter deals with the long-term deactivation mechanism; i.e. coking. After a short study of the existing models, the developed model for the active site poisoning by coke formation is developed and the correlation for the evolution of the active site fraction with time as well as other operating conditions is proposed.

The chapter then ends with the conclusion of the both catalyst deactivation models.

3.2. Development of initial deactivation model (sintering)

Sintering was shown to occur during the initial periods of Fischer-Tropsch synthesis [1, 2]. The thermodynamic reasons are the main driving force for the sintering as larger cobalt crystallites have lower surface energy and higher thermodynamic stability when compared to smaller counterparts (Fig. 3.1).

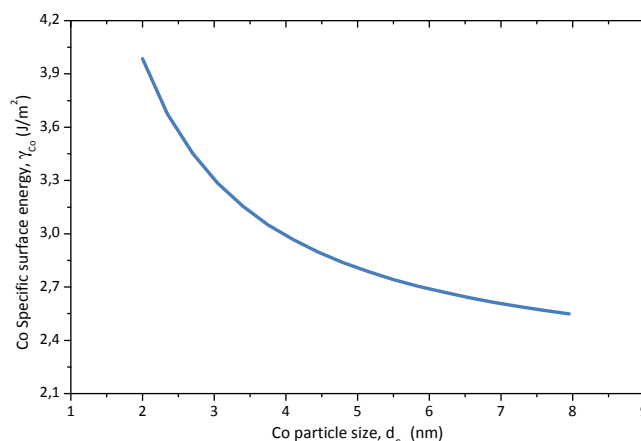


Figure 3.1 Evolution of specific surface energy with cobalt particle size – constructed from the formula provided in [1]

In the first part of this section we explain how the surface oxidation of cobalt particles is thermodynamically possible under typical Fischer-Tropsch operating conditions. This is suggested by a range of catalyst characterization tools as well as thermodynamic models. Later the surface oxidation step is considered as an important step in the sintering of cobalt crystallites as sintering is not observed under inert conditions. The derivation of such a model is inspired by the mechanistic model recently developed by Sehested et al. [1] for sintering of nickel steam reforming catalysts. The similarity between the nickel and cobalt catalysts suggests that a common approach could be employed for the description of sintering in Co-based particles.

3.2.1. Study of cobalt particles oxidation during Fischer-Tropsch synthesis

3.2.1.1. Introduction

Oxidation by water produced within FT reaction ($nCO + (2n + 1)H_2 \rightleftharpoons C_nH_{2n+2} + nH_2O$) has been considered for many years as possible cause of catalyst deactivation [2].

Although oxidation of bulk cobalt is not favorable, oxidation of nano-sized cobalt crystallites could be thermodynamically possible under the realistic conditions of FT synthesis [2]. This is due to the significant contribution of surface energy of nano-sized cobalt crystallites to the overall oxidation process. Assuming spherical morphology of nanoparticles, under realistic conditions of FT synthesis ($P_{\text{H}_2\text{O}}/P_{\text{H}_2} < 1.5$) metallic cobalt crystallites smaller than 4–5 nm were expected to be unstable and could be re-oxidized to CoO. Several papers reported cobalt oxidation during FT reaction on the basis of *ex-situ* characterization. Davis and co-workers [3], [4], [5], [6], [7], [8], [9] have performed XAS analysis of supported cobalt catalysts withdrawn from the liquid phase of the laboratory slurry reactor. Inside the reactor and during the analysis, the catalyst samples were suspended in FT wax. The authors believe that coating in wax prevents cobalt catalysts from oxidation. Analysis of XANES derivatives was indicative of partial re-oxidation of cobalt metal particles during FT synthesis.

It is often suggested that cobalt oxidation is caused by water. It seems, however, that oxidation by water could only involve surface and subsurface layers of cobalt metal particles. According to Sasol [9] and [10] researchers who conducted extensive *ex-situ* studies of both used cobalt catalysts and *in-situ* characterization with model $\text{H}_2\text{O}/\text{H}_2$ gas mixtures [10] and [11], cobalt bulk re-oxidation is not a significant deactivation mechanism of cobalt catalyst under commercially relevant FT conditions. According to Khodakov et al. [12] cobalt oxidation cannot be a dominant mechanism of catalyst deactivation at moderate level of carbon monoxide conversion in cobalt catalysts containing either larger or smaller cobalt particles.

3.2.1.2. Catalyst characterizations

In order to investigate the oxidation state of cobalt crystallite during exposure to syngas, the catalysts were characterized *ex-situ* using X-ray diffraction, X-ray photoelectron spectroscopy, and scanning transmission electron microscopy (STEM) combined with electron energy loss spectroscopy (EELS).

In addition to *ex-situ* characterization, the reference 25%Co0.1%Pt/ γ - Al_2O_3 catalyst was loaded into a laboratory millimetric fixed bed reactor (reactor diameter = 0.14 cm, reactor

length = 32 cm, catalyst loading = 0.5 g). Conventional operating conditions ($T = 220^{\circ}\text{C}$, $P = 20$ bar) are used except for a run made at high temperature of 340°C to study the effect of temperature on the oxidation.

3.2.1.2.1. X-ray diffraction

Ex-situ X-ray powder diffraction experiments were conducted using a Bruker AXS D8 diffractometer using $\text{Cu}(\text{K}\alpha)$ radiation for crystalline phase detection. The XRD spectra of $\gamma\text{-Al}_2\text{O}_3$ support, fresh calcined, as well as the used catalysts (exposed to different H_2/CO ratios) are shown in Fig. 3.2.

The catalyst samples after each run were removed from the reactors and directly sent for XRD characterization. XRD results suggest that the catalysts are protected by a thin layer of FT wax produced during the reaction, even after they are exposed to air for a short time. This is deduced from Fig. 3.2 where there is no characteristic peak for cobalt oxide species (including CoO or Co_3O_4). This suggests that Co particles remain almost metallic even after long time on stream. However as the XRD is a volumetric method, it could not well represent the surface state of cobalt particles after the reaction.

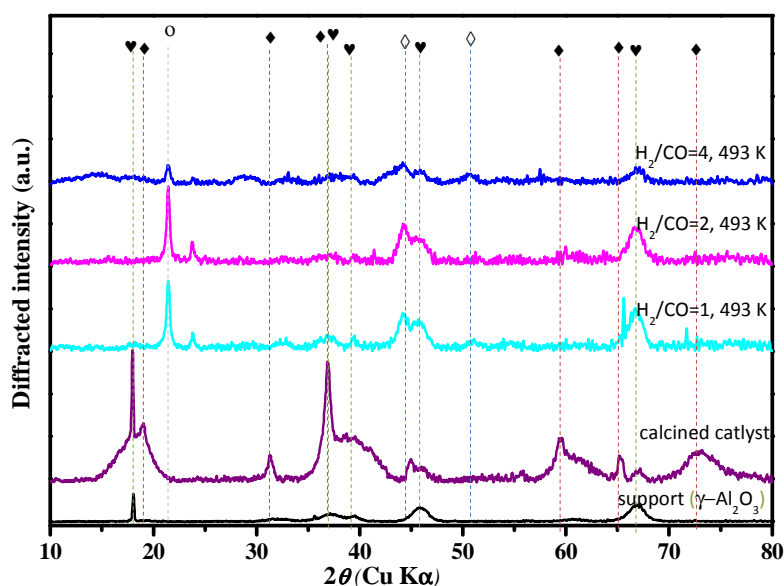


Figure 3.2 Diffraction patterns for $\gamma\text{-Al}_2\text{O}_3$, fresh calcined, and sintered catalyst samples in the milli-fixed bed FT reactor (\blacklozenge Co_3O_4 , \diamond Co, \heartsuit $\gamma\text{-Al}_2\text{O}_3$, \circ wax - offset for clarity)

3.2.1.2.2. X-ray photoelectron spectroscopy

Ex-situ XPS analyses were performed using a Kratos Analytical AXIS UltraDLD spectrometer. A monochromated aluminum source (Al K α = 1486.6 eV) was used for excitation. The X-ray beam diameter was approximately 1 mm. The analyzer was operated at constant pass energy of 40 eV using an analysis area of approximately 700 μm \times 300 μm . Charge compensation was applied to compensate for the charging effects that occurred during the analysis. The C 1s (285.0 eV) binding energy (BE) was used as internal reference. The spectrometer BE scale was initially calibrated against the Ag 3d $_{5/2}$ (368.2 eV) level. Pressure was in the 1 $^{-10}$ torr range during the experiments. Simulation of the experimental XPS peaks was carried out using CasaXPS software.

The catalyst was exposed to a syngas stream of H $_2$ /CO = 2 (T = 220°C, P = 20 bar) for about 100 hrs. The sample was then directly sent for the XPS analysis without any elementary pretreatment. Although, as already mentioned, the XRD data show the bulk of cobalt particles is remained metallic, XPS data suggest that the surface is oxidized even it is protected by the FT wax. The Co2p $_{3/2}$ 2+ signal at 781.5 eV as well as Co2p $_{3/2}$ 0 signal at 778.5 eV indicate 7% of Co(0) as well as 93% Co $^{2+}$ on the surface.

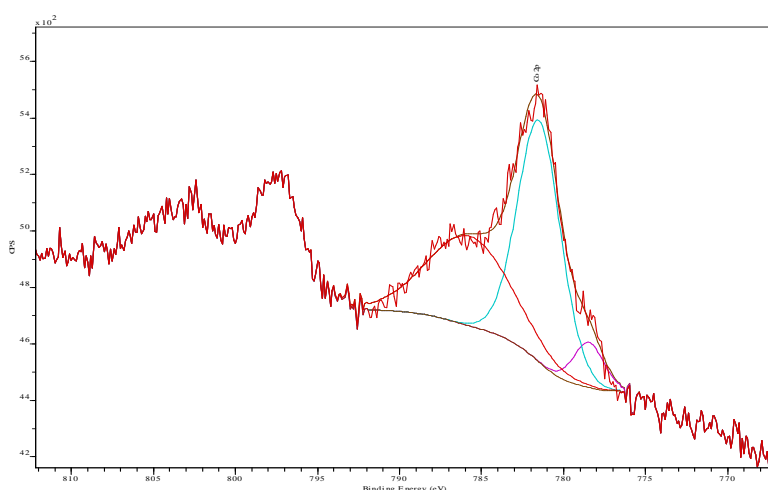


Fig 3.3 XPS spectra for the Co/Al $_2$ O $_3$ reference catalysts used in the FT reaction (T = 220°C; P = 20 bar, H $_2$ /CO = 2, TOS = 100 hr)

3.2.1.2.3. STEM-EELS

Scanning transmission electron microscopy- Electron energy loss spectroscopy (STEM-EELS) measurements were performed on a 100-keV STEM instrument (VG HB 501) equipped with a field emission source and a parallel Gatan 666 EELS spectrometer. The instrument was in operation in Orsay and produced EELS spectra with 0.5-eV energy resolution and subnanometer spatial resolution within a typical acquisition time of less than a second per pixel. A TECNAI electron microscope operating at an accelerating voltage of 200 kV was equipped with a LaB₆ filament. The catalyst sample in wax was pretreated under severe conditions of FT synthesis (T=340°C) and then ground under an inert atmosphere.

Similar to the results provided by XPS and XRD, the microscopy data demonstrate that although the bulk cobalt atoms remain metallic during FT conditions, the surface is readily oxidized at higher temperatures although no oxidation is evidenced at typical FT conditions. The elemental mappings of cobalt and oxygen demonstrate that even first few layers (3-4 nm) are replaced by oxidized cobalt. Sub-surface oxidation happens as the temperature is sufficiently high where the oxygen diffusion rates are increased.

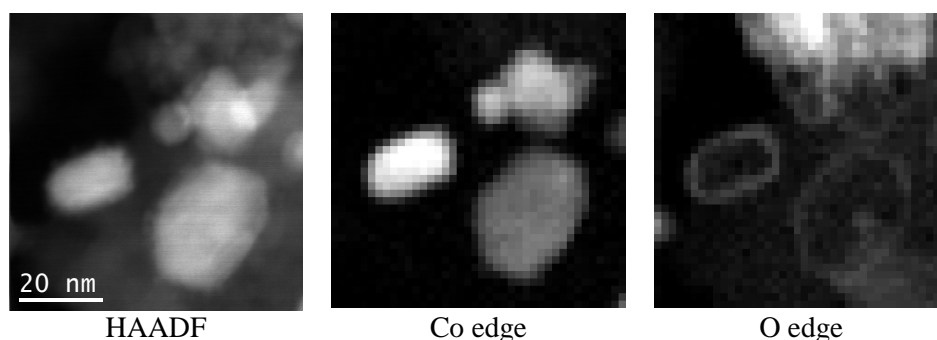


Figure 3.4 HAADF images for the Co/Al₂O₃ catalyst after FT reaction at high temperature together with the spatially resolved EELS intensities for cobalt and oxygen [in collaboration with Christine Lancelot]

Note that we have to be careful with these experimental observations since an oxidation due to the exposure to the air cannot be excluded even when the cobalt particles are coated with wax.

3.2.1.3. Thermodynamic oxidation models

A theoretical study has been performed to evaluate the oxidation phenomenon in a better way which could explain the driving force, the extent of oxidation, as well as the important factors which could affect the process. We have developed several models for the oxidation process and the most relevant models are presented in the following sections.

2.1.3.1. Bulk oxidation (van Steen) model

In order to study the oxidation phenomena in a comprehensive way, one can start with the process of total particle oxidation. Although several models are proposed for bulk cobalt oxidation, the model developed by van Steen et al [1] is the one more frequently used to study the thermodynamics of such a process.

The model deals with a complete transformation of a pure metallic particle into a new formed particle made 100% of cobalt oxide (CoO). Fig. 3.5 gives the schematic of such a process.

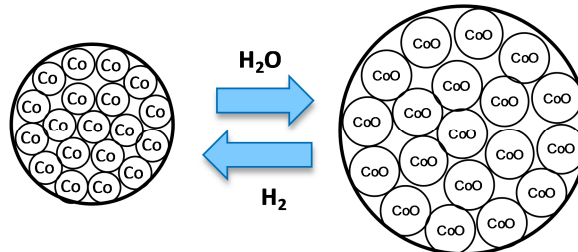


Figure 3.5 Schematic view of the bulk oxidation of spherical cobalt crystallites

The new oxidized particle has however a larger diameter as the CoO molar density is lower than that of pure metallic cobalt:

$$d_{CoO} = \left[\frac{\rho_{Co}}{\rho_{CoO}} \right]^{1/3} d_{Co} \quad (3.1)$$

where ρ is the molar density (at $T = 220^\circ\text{C}$: $\rho_{Co} = 1.51 \times 10^5 \text{ mol/m}^3$; $\rho_{CoO} = 8.59 \times 10^4 \text{ mol/m}^3$).

In order to study the thermodynamics of such a process a precisely defined system should be defined. We have defined our system as a spherical particle placed in a gas atmosphere composed of both H_2O and H_2 . The relative number of moles of H_2O and H_2 is

given by their respective partial pressures. The spherical particle has an initial state of 100% metallic Co and a final state of 100% CoO. The chemical reaction is written as follows:



The number of moles of H₂O used as well as H₂ produced during the reaction is equal to the number of moles of metallic Co being oxidized which is equal to:

$$n_{\text{Co}} = \frac{\rho_{\text{Co}} \pi d_{\text{Co}}^3}{6} \quad (3.2)$$

The total energy change due to this reaction is composed of three main terms: (a) the change in the chemical potentials, (b) the change the particle's surface energy, and (c) the change in gas fugacities. The total surface energy term of either a completely oxidized particle or a metallic one is equal to their corresponding specific surface energy multiplied by their surface area.

$$\Gamma_{\text{CoO}} = \gamma_{\text{CoO}} \left[\pi d_{\text{CoO}}^2 \right] = \gamma_{\text{CoO}} \pi d_{\text{Co}}^2 \left(\frac{\rho_{\text{Co}}}{\rho_{\text{CoO}}} \right)^{1/3} \quad (3.3)$$

$$\Gamma_{\text{Co}} = \gamma_{\text{Co}} \left[\pi d_{\text{Co}}^2 \right] \quad (3.4)$$

However as the particle is completely oxidized, the contribution of surface energy to the total energy is calculated by dividing the total surface energy per number of moles of Co in a particle. This gives a normalized surface energy $\Delta E_{\text{surface}}$ (in J/mol) which could be added with other two terms resulting in the total change in the Gibbs free energy of the system, ΔG_{system} :

$$\Delta E_{\text{surface}} = \frac{\Gamma_{\text{CoO}} - \Gamma_{\text{Co}}}{\rho_{\text{Co}} \pi d_{\text{Co}}^3 / 6} = \frac{6\gamma_{\text{Co}}}{\rho_{\text{Co}} d_{\text{Co}}} \left[\frac{\gamma_{\text{CoO}}}{\gamma_{\text{Co}}} \left(\frac{\rho_{\text{Co}}}{\rho_{\text{CoO}}} \right)^{2/3} - 1 \right] \quad (3.5)$$

$$\Delta G_{\text{system}} = \mu_{\text{CoO}(s)}^{\circ} + \mu_{\text{H}_2(g)}^{\circ} - \mu_{\text{Co}(s)}^{\circ} - \mu_{\text{H}_2\text{O}(g)}^{\circ} + RT \ln \left[\frac{P_{\text{H}_2}}{P_{\text{H}_2\text{O}}} \right] + \Delta E_{\text{surface}} \quad (3.6)$$

The bulk oxidation is thermodynamically feasible once the ΔG_{system} becomes negative; the case which is dependent only on the relative water to hydrogen partial pressure once the temperature is constant. Fig. 3.6 shows the stability region calculated for bulk CoO as a function of $P_{\text{H}_2\text{O}}/P_{\text{H}_2}$. The result is in line with the one reported by van Steen[1].

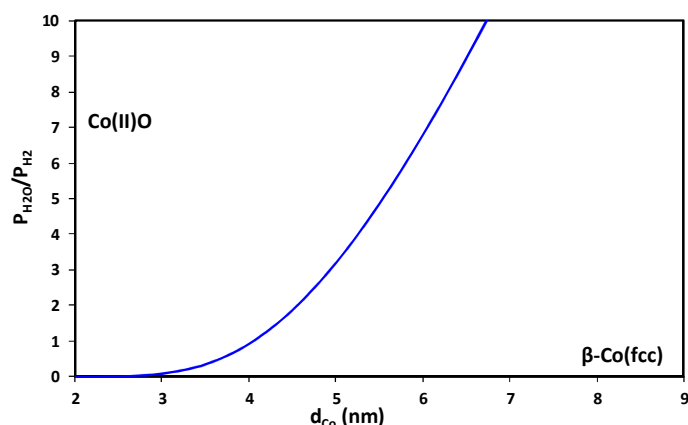


Figure 3.6 Stability region of spherical β -Co (fcc) and CoO particles in $\text{H}_2\text{O}/\text{H}_2$ atmospheres at 493 K as a function of the diameter of a spherical metal Co crystallite

Although Fig. 3.6 suggests that spherical cobalt crystallites with a diameter less than 4.4 nm will be rapidly oxidized when exposed to relevant Fischer-Tropsch conditions ($P_{\text{H}_2\text{O}}/P_{\text{H}_2} < 1.5$), *in situ* XRD data obtained at moderate carbon monoxide conversions did not show any oxidation of both larger and smaller cobalt metal particles [12]. In addition to the thermodynamics, the formation of bulk CoO is not kinetically favored as it requires diffusion of oxygen in the subsurface Co layers which is not possible according to Huo et al. [13].

3.2.1.3.2. Surface oxidation: our conceptual model

Surface oxidation is a rather kinetically simple process which involves direct interaction of water molecules in the gas phase with surface cobalt atoms, and therefore no diffusion limitations are present for a perfect surface. However the thermodynamics of such a reaction should be investigated to verify if the formed surface oxides are thermodynamically stable.

Similar to the approach taken for the bulk oxidation reaction, a pre-defined system should be considered for the thermodynamic calculations of surface oxidation. As we assume that the interior part of Co particles remains metallic during such a process, the system takes only the surface Co atoms (both metallic and oxidized) into consideration as well as gas atmosphere composed of only H_2 and H_2O . Such a system is depicted in Fig. 3.7.

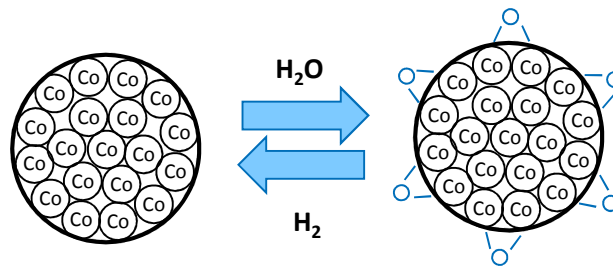


Figure 3.7 Schematic view of the surface oxidation of spherical cobalt crystallites

In order to quantify the fraction of surface which is oxidized, cobalt oxide coverage is defined in the following way:

$$\theta_{CoO} = \frac{n_{CoO,surf}}{n_{CoO,surf} + n_{Co,surf}} \quad (3.7)$$

Cobalt oxide coverage for a specific metallic particle is calculated by using the classical definition of equilibrium constant. In other words, surface oxidation proceeds until a minimum is achieved for the total Gibbs energy of the system, G^t (Fig. 3.8).

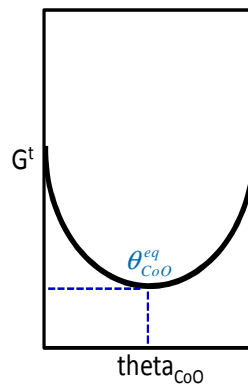


Figure 3.8 Graphical view of the methodology used for the equilibrium CoO surface coverage calculation

Consequently the total energy of the system is calculated as a function of θ_{CoO} . However, certain assumptions are required:

1. The cobalt particle is assumed to be completely spherical and defect-free.
2. The catalyst particles do not contain any trace of promoter.
3. There is no interaction between the cobalt crystallites and support.
4. The equations suggested by van Steen (Eq. 1.6 and 1.7) realistically represent the specific surface energy of both metallic and oxidized Co.

5. The surface formed CoO atoms have the same thermodynamic properties as those of bulk CoO.

The total energy of the heterogeneous system already defined is equal to the sum of contributions of all different components (i.e. Co, CoO, H₂O and H₂).

$$G^t = G_{Co} + G_{CoO} + G_{H_2} + G_{H_2O} \quad (3.8)$$

or alternatively:

$$G^t = n_{Co(s)} \left[\mu^\circ_{Co(s)} + RT \ln(1 - \theta_{CoO}) \right] + n_{CoO(s)} \left[\mu^\circ_{CoO(s)} + RT \ln(\theta_{CoO}) \right] \\ + n_{H_2O,rxn} \left[\mu^\circ_{H_2O} + RT \ln P_{H_2O} \right] + n_{H_2,rxn} \left[\mu^\circ_{H_2} + RT \ln P_{H_2} \right] \quad (3.9)$$

where the standard states are defined as 25°C and 1 atm.

The standard chemical potential of each surface species is the sum of the chemical potential of the bulk form and the surface energy term [14], i.e.

$$G^t = n_{Co(s)} \left[\mu^\circ_{Co} + \gamma_{Co} a + RT \ln(1 - \theta_{CoO}) \right] + n_{CoO(s)} \left[\mu^\circ_{CoO} + \gamma_{CoO} a + RT \ln(\theta_{CoO}) \right] \\ + n_{H_2O,rxn} \left[\mu^\circ_{H_2O} + RT \ln P_{H_2O} \right] + n_{H_2,rxn} \left[\mu^\circ_{H_2} + RT \ln P_{H_2} \right] \quad (3.10)$$

where a , the specific surface area (area per moles of surface cobalt atoms) depends only on the cobalt density and therefore has a constant value ($a = 4.14 \times 10^4 \text{ m}^2/\text{mol}_{\text{surface}}$).

The standard chemical potential of elements (Co and H₂ here) is set as zero. In addition the number of Co atoms in the surface is related to the dispersion as well as CoO surface coverage. This is similar for $n_{CoO(s)}$, n_{H_2} , and n_{H_2O} . Therefore Eq. 3.10 is transformed into:

$$G^t = n_{total} D (1 - \theta_{CoO}) \left[\gamma_{Co} a + RT \ln(1 - \theta_{CoO}) \right] + n_{total} D \theta_{CoO} \left[\mu^\circ_{CoO} + \gamma_{CoO} a + RT \ln(\theta_{CoO}) \right] \\ + n_{total} D (1 - \theta_{CoO}) \left[\mu^\circ_{H_2O} + RT \ln P_{H_2O} \right] + n_{total} D \theta_{CoO} \left[RT \ln P_{H_2} \right] \quad (3.11)$$

where n_{total} is the total number of moles of cobalt in the particle.

For calculation of equilibrium θ_{CoO} , one can use:

$$\frac{\partial G^t}{\partial \theta_{CoO}} = 0 \quad \Rightarrow \quad \frac{\partial (G^t / n_{total} D)}{\partial \theta_{CoO}} = 0 \quad (3.12)$$

which gives the surface coverage is implicitly by solving Eq. 3.13:

$$\frac{(\gamma_{CoO} - \gamma_{Co})a}{RT} + \frac{\mu^{\circ}_{CoO} - \mu^{\circ}_{H_2O}}{RT} + \ln \frac{\theta_{CoO} P_{H_2}}{(1 - \theta_{CoO}) P_{H_2O}} = 0 \quad (3.13)$$

Using van Steen equations for the surface energy terms, one can notice that that in Eq. 3.13 the main contribution is due to the surface energy difference between metallic and oxidized cobalt states.

As an example, the particles of 6 nm diameter need only a trace of water (partial pressure ratio of $P_{H_2O}/P_{H_2} = 1.145 \times 10^{-7}$) in order to be oxidized by $\theta_{CoO} = 30\%$ at 220°C . The corresponding values for the first and second terms (in Eq. 3.13) are -21.27 and 4.14 (dimensionless) respectively.

In other words, although it might seem surprising, the formation of cobalt oxide monolayer is much more favorable than what was assumed before.

However as already mentioned this conclusion directly depends on the choice of surface energy terms as they determine equilibrium state of surface oxidation.

We have also studied the effect of temperature on the extent of surface oxidation as follows.

3.2.1.3.2.1. Temperature effect

As shown in section 3.2.1.2.3, microscopy data suggests that surface (and even subsurface) oxidation is accelerated at high temperature. Both the chemical potentials and surface energy terms change with temperature. The term $(\mu^{\circ}_{CoO} - \mu^{\circ}_{H_2O})/RT$ however remains almost constant as the temperature is raised. Table 3.1 gives $\Delta\mu^{\circ}/RT$ at five different temperatures.

Table 3.1 Effect of temperature on the chemical potential difference for cobalt surface oxidation

Temperature ($^{\circ}\text{C}$)	$\Delta\mu^{\circ}/RT$ (dimensionless)
220	4.89
260	4.77
300	4.67
340	4.57
1000	3.86

Temperature also reduces the surface energy of bulk solid metals up to their melting point.

Tyson [15] has proposed that the surface energy changes according to:

$$\gamma_{SV} - \gamma_{SV}(T_m) = \int_T^{T_m} \frac{S_{SV}}{A} dT \quad (3.14)$$

where γ_{SV} is the specific surface energy at any given temperature T , S_{SV} is the entropy at temperature T (given by Fig. 3.9) and A is the surface area per mole of surface atoms.

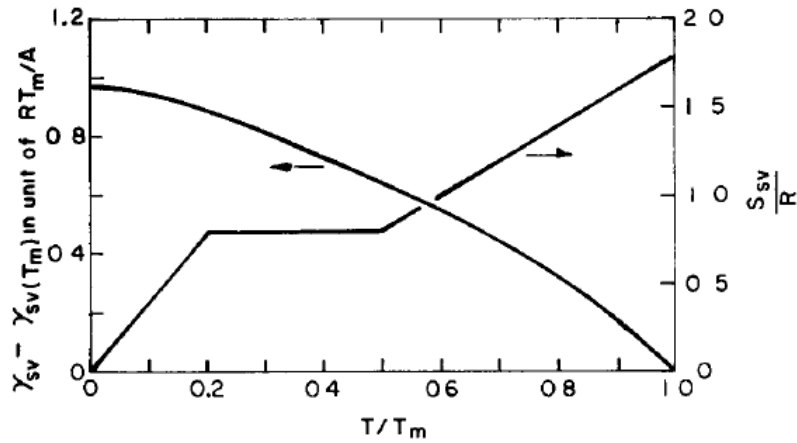


Figure 3.9 Variation of surface free energy and entropy with homologous temperature T/T_m [15]

For the temperature region $0.2 < T/T_m < 0.5$ ($80^\circ\text{C} < T < 610^\circ\text{C}$ for Co) where the term S_{SV}/R has a constant value of 0.75 (further details and reasoning given by Tyson [15]), the integration is made easily and the specific surface energy for bulk cobalt species is given with temperature as:

$$\gamma_{Co} (J/m^2) = 2.448 + 1.299 \times 10^{-4} T (K) \quad (3.15)$$

Recombination with the van Steen formula for the size dependent surface energy gives:

$$\gamma_{Co} = \left[1 + \frac{1.45}{d_{Co}} + \frac{0.55}{d_{Co}^2} \right] (2.198 - 1.166 \times 10^{-4} T) \quad (3.16)$$

Table 3.2 shows how the specific surface energy changes with a temperature for metallic cobalt particles of 6 nm.

Table 3.2 Effect of temperature on the specific surface energy of metallic Co crystallites of 6 nm

Temperature (°C)	γ_{Co} (J/m ²)
220	2.690
260	2.684
300	2.678
340	2.672
600	2.634

As the γ_{Co} is shown not to be very sensitive to the temperature in typical FT conditions, the specific surface energy ratio γ_{CoO}/γ_{Co} is assumed to be temperature independent.

This study suggests that the extent of the surface oxidation will not be much affected by the temperature increase according to the thermodynamic model as the change in the surface energy term is negligible in the range 220-600°C.

3.2.1.3.3. Thermodynamics model limitations

Although the model predicts that a large surface fraction will be oxidized once a trace of water is present, the calculations are based on several simplifications, some of which might not be realistic.

First of all, the properties of surface CoO layer (including chemical potential and specific surface energy) were assumed to be identical to those of bulk CoO. This is generally not true, as the atomic interactions between metallic and oxidized cobalt lead to some differences in the properties.

Secondly, the effect of promoter is neglected in this study. Increased metallic stability is expected once the promoter is added. The properties of the adsorbed hydrogen are not the same as that of gas phase hydrogen. In the similar way the interactions with the catalysts supports were ignored.

The surface energy terms are also approximated by van Steen correlations [1]. As Eq. 3.13 proposes the most significant reason for the surface oxidation is the difference in the specific surface energy of metallic cobalt and that of CoO. An 80% difference in surface energy leads to complete surface oxidation at the presence of water trace amounts, whereas lower difference could reduce the extent of surface oxidation. A sensibility analysis performed for

γ_{Co} shows that $\pm 15\%$ in the calculated surface energy results in a change in surface oxidation threshold from 4 nm to 6 nm.

In addition, the formation of CoO layers will itself create new interfaces for which the surface energy terms apply. As shown by Fig. 3.10, the surface CoO leads to the formation of 4 interfaces: (1) CoO-gas mixture, (2) Co-gas mixture, (3) Co-CoO, and (4) CoO-Co surfaces.

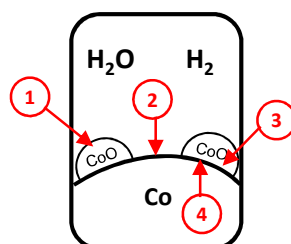


Figure 3.10 New interfaces created during surface oxidation process

These limitations among some others give us an overestimation of the equilibrium CoO surface coverage. Classical thermodynamics calculations should be thus improved once a more realistic look of surface oxidation is required.

3.2.2. Intermediate conclusions

The previous section provides experimental and theoretical data about cobalt oxidation in typical FTS conditions.

The ex-situ characterization tools could provide some evidences about the bulk and surface properties of the Co crystallites although the use of in-situ techniques could be more reliable. The X-ray diffraction (XRD) spectra of catalysts exposed to different syngas ratios ($\text{H}_2/\text{CO} = 1.5-4$) at typical FTS temperature and pressure shows no bulk oxidation even after exposure to air for a short period of time. The use of XPS and STEM-EELS proposes a surface oxidation of cobalt crystallites. These ex-situ analyses have to be taken with caution since a passivation of the metallic particles is still possible during the storage of the sample or during their transfer in the analysis chamber.

The thermodynamic models suggest that the bulk cobalt oxidation is only possible for small crystallites of < 4 nm size under typical $P_{\text{H}_2\text{O}}/P_{\text{H}_2}$ ratios. However as the 80% decrease in the surface energy of CoO compared to that of metallic cobalt plays the most significant role in the surface oxidation process, the particles' surface could be fully covered with a layer

of cobalt oxide even at very low pressure of water. The CoO surface coverage could be calculated for different crystallite diameters and water partial pressures using Eq. 3.13. Temperature was found not to affect the surface oxidation process. The limits of applying a pure thermodynamic model are discussed in section 3.2.1.3.3.

Once the cobalt surface is found to be prone to the oxidation by the help of water produced during the Fischer-Tropsch synthesis, a mechanistic model was proposed that involves the surface oxidation as an intermediate step in the process of crystallite growth. The mechanism is similar to the one developed by Sehested for the nickel-based catalysts where the surface oxygenated species could facilitate sintering.

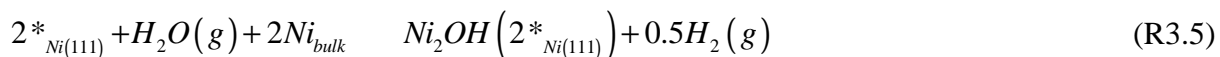
3.2.3. Existing model for catalyst sintering (Sehested Model)

As in the case of FTS catalysts, sintering is the reason for loss of activity for many industrial catalyst systems. Steam reforming over nickel catalyst is among the industrial processes mostly affected by sintering:



Sehested et al. [16] studied the mechanism for sintering of nickel steam-reforming catalysts at 500 °C, 30 bar, H₂O/H₂ = 10/1 and concluded on the basis of the particle size distributions that sintering occurred via the crystallite migration mechanism. For this sintering mechanism mass transport by diffusion of nickel atoms on the nickel crystallite surfaces is necessarily an important step, so the diffusivity and concentration of single metal atoms and small clusters are central parameters in the understanding of the sintering phenomenon.

They have then shown that on Ni(111) a nickel-dimer bonded to an OH radical is a very stable adspecies. Indeed the energy associated with formation of a Ni₂(OH) complex is ca. 58 kJ mol⁻¹ lower than that of a nickel adatom and consequently once exposed to water the catalyst surface is more probably covered with Ni₂(OH) species than with nickel adatoms:



where ^{*}Ni₍₁₁₁₎ is a surface (111) Ni site whereas Ni_{bulk} represents the bulk Ni atoms.

The equilibrium constant associated with the formation of Ni₂(OH) species is given by:

$$K_{Ni_2(OH)} = \frac{\theta_{Ni_2(OH)}}{(1 - 2\theta_{Ni_2(OH)})^2} \frac{P_{H_2}^{0.5}}{P_{H_2O}} \quad (3.17)$$

where $\theta_{Ni_2(OH)}$ and $1 - 2\theta_{Ni_2(OH)}$ are the coverages of $Ni_2(OH)$ species and of free sites at the surface of the nickel particles, respectively, neglecting the presence of other species on the catalyst surface. The authors also assumed that $\theta_{Ni_2(OH)}$ is small, so that Eq. 3.17 may be rewritten:

$$\theta_{Ni_2(OH)} \approx K_{Ni_2(OH)} \frac{P_{H_2O}}{P_{H_2}^{0.5}} \quad (3.18)$$

The authors then proposed that under steam-reforming conditions, an equilibrium among water vapor, hydrogen, and OH-bonded nickel dimers at the nickel surface is most likely established. This is line with the results of Aparicio [17] which suggest a total isotopic scrambling in H_2O/D_2 mixtures at a temperature of 200 °C while a temperature of 450 °C is required before total isotopic scrambling in CD_4/H_2 mixtures. In addition, as shown by Bengaard et al. [18], the lowest energy barrier for ethane dehydrogenation over nickel is 39 kJ mol⁻¹ higher than for the lowest barrier for abstraction of a hydrogen atom from a water molecule.

The authors then used the expression derived by Gruber [19] for the diffusion of gas bubbles in metals which could be also used for describing the diffusivity of metallic spherical nanoparticles on a planar noninteracting ceramic carrier, $D_{particle}$ as suggested by Wynblatt and Gjostein [20]:

$$D_{particle} = 0.301D_{atom} \left(\frac{a_0}{r} \right)^4 \quad (3.19)$$

where D_{atom} is the diffusion constant for metal Ni atoms (estimated as 3.3×10^{-8} m²/s at 773 K), a_0 is the interatomic Ni-Ni distance and r is the particle radius (2.3 Å for nickel).

However, the rate of the mass transport due to $Ni_2(OH)$ was calculated to be approximately 700 times higher than that due to nickel adatoms. Hence, the rate of sintering was proposed to be dominated by the $Ni_2(OH)$ species. The authors then calculated the diffusion coefficient for the nickel particles when OH-bonded nickel dimers dominate nickel surface transport as:

$$D_{particle} = 0.602D_{Ni_2OH} \left(\frac{a_0}{r} \right)^4 \theta_{Ni_2OH} = 0.602D_{Ni_2OH} \left(\frac{a_0}{r} \right)^4 K_{Ni_2(OH)} \frac{P_{H_2O}}{P_{H_2}^{0.5}} \quad (3.20)$$

They have then used Eq. 3.20 to derive to expression for the time-dependent average nickel particle \bar{d}_{Ni}^7 diameter using a particle migration and coalescence mechanism as follows:

$$\bar{d}_{Ni} = \left(\text{const} \frac{K_{Ni_2OH} D_{Ni_2OH} X_{Ni} t \left(\frac{P_{H_2O}}{P_{H_2}^{0.5}} \right)}{(1 - X_{Ni}) A_{car}} + \bar{d}_{Ni,0}^7 \right)^{1/7} \quad (3.21)$$

where X_{Ni} is the nickel weight fraction in the catalyst, A_{car} is the surface area of the carrier per gram of carrier, t is the sintering time, $\bar{d}_{Ni,0}^7$ is the average nickel particle diameter of the fresh sample, K_{Ni_2OH} is defined by Eq. 3.17, and “const” is an arbitrary constant.

The effect of water presence in the increased rate of sintering is clearly represented in Eq. 3.21 and it was found to be in line with the experimentally observed crystallite growth as shown in Fig. 3.11.

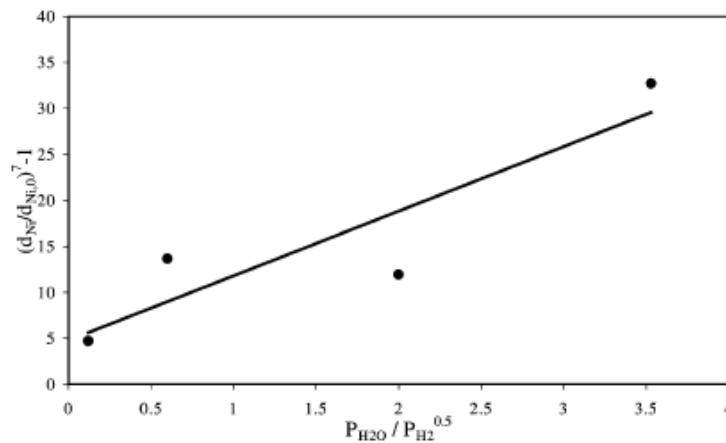


Figure 3.11 $\left(\left(\bar{d}_{Ni} / \bar{d}_{Ni,0} \right)^7 - 1 \right)$ for catalyst samples with 19.4 wt% nickel supported on an Al_2O_3 carrier (plotted as a function of $P_{H_2O} / P_{H_2}^{0.5}$. The catalyst was sintered for 50 h at 550 °C and 1 bar total pressure with the steam to hydrogen ratio varied by two orders of magnitude. The line is a linear least-squares fit to the data.- Adapted from reference [21]

The developed model seemed to give a good quantitative description of the observed data at low temperatures where the sintering is dominated by particle migration and coalescence. Higher temperature (>600°C) found to accelerate sintering through Ostwald ripening (atomic migration). In addition, according to the model, there will be a threshold value of the $P_{H_2O} / P_{H_2}^{0.5}$ ratio where mass transport at the nickel particles due to OH-bonded nickel dimers and free nickel adatoms will be equally important. It is also interesting to note that the highest values of the $P_{H_2O} / P_{H_2}^{0.5}$ ratio are found at the entrance of a prereformer or a fired reformer; hence this factor speeds up the sintering at the entrance of the reforming unit.

Sintering is also more severe at the outer shell of a catalyst in the case where the effectiveness factor for a catalyzed reaction is less than one, which is normally the case for reforming.

The similarity of nickel and cobalt catalyst suggests that a similar approach could be used for the cobalt-based catalysts that could explain the experimentally-observed water-accelerated sintering.

3.2.4. Proposed mechanism and model: water-accelerated sintering

As presented in Chapter 1, the effect of water on the sintering of cobalt-based FTS catalysts is discussed by several researchers in the literature. In this section we propose a mechanistic model for the sintering of Co-based catalysts under different conditions of FT synthesis. The sintering proceeds via surface oxidation and diffusion of cobalt nanoparticles. An attempt has been made to quantitatively explain the experimentally observed initial catalyst deactivation under realistic conditions of FT synthesis which could be attributed to cobalt sintering.

3.2.4.1. Cobalt sintering: Atomic or particle migration?

The way in which the catalyst particles grow, is essentially important for establishing the mechanism of sintering. Sintering of cobalt nanoparticles through intermediate formation of surface oxide layer is studied in this work. The possibility of surface oxide formation is already proposed by both characterization and thermodynamic data.

Chapter 1 has already presented some evidences that sintering of cobalt-based particles is dominated by Particle Migration and Coalescence (PMC) mechanism. As already stated there particle size distribution in spent catalysts can provide an efficient way to distinguish between different sintering mechanisms. The TEM images of a sufficiently large number of cobalt particles within sintering process of Co-Re/SiO₂ catalysts during FT reaction provided by Kiss et al. [22] could be used as another way to distinguish the sintering mechanism. The catalyst was subject to high CO conversion regime which was supposed to result in important cobalt sintering. The particle size distribution after the experiment could be fitted using a log normal distribution function (LNDF), proposing again a Particle Migration and Coalescence sintering mechanism, as seen in Fig. 3.12.

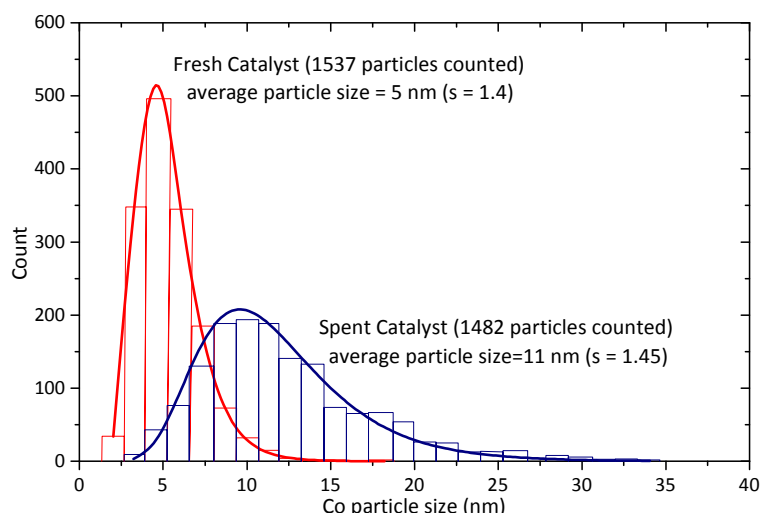


Figure 3.12 Log-normal fit for cobalt particle size distributions of the fresh reduced 973 K vacuum-annealed Co–Re/SiO₂ and the spent Co–Re/SiO₂ catalyst sample from the 35 bar high CO conversion run (raw experimental data cited from [22]).

The particle size distribution change before/after sintering could reveal further facts. As an example, our calculations uncovered that sintering in this case resulted in 57% surface area reduction as well as 62% total surface energy decrease when compared to the fresh catalyst. Further details of such calculations are given in section 3.2.2.2.1

We have also used the general power law expression (GPLe) to find the sintering order and consequently the principle sintering mechanism. The works reported by Karaca et al. [12] and [23] uncovered cobalt sintering, which coincided with catalyst deactivation in alumina supported cobalt catalysts at $P = 20$ bar, $H_2/CO = 2$ and $T = 493$ K using synchrotron based operando XRD. We have found that the observed sintering [12] could be also satisfactorily fitted using second order GPLe, proposing a Particle Migration and Coalescence mechanism (Fig. 3.13). Only fits of poor quality were obtained with the first order GPLe. This seems to be additional evidence in favor of Particle Migration and Coalescence as a dominant mechanism of sintering of supported cobalt FT catalysts.

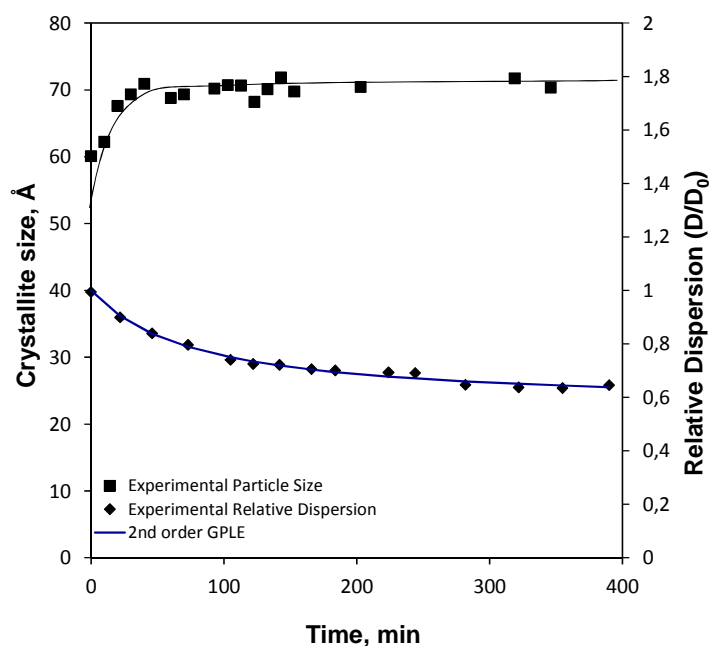


Figure 3.13 Evolution of cobalt particle size (reprinted from [3]) and cobalt dispersion of Co-Pt/Al₂O₃ catalyst sample during FT synthesis (T = 493 K, P = 20 bar, H₂/CO = 2, GHSV = 25000 Nml g⁻¹ h⁻¹) in a capillary-fixed bed reactor

3.2.4.1.1. Further information from the particle size distribution curves

Based on the method suggested by den Breejen et al. [24], one can find how sintering could affect the cobalt catalytic properties during Fischer-Tropsch synthesis, if considerably a large number of particles has been investigated in the TEM analysis. We have used such a large TEM image dataset, provided by Kiss et al. [22] (for both a fresh and sintered cobalt catalyst under high CO conversion regimes) to evaluate the influence of the catalyst sintering on the surface concentration of the active phase and therefore on the catalytic activity.

A histogram analysis was performed on different cobalt particle sizes. The particles with diameters close enough are placed in so-called “bins” with a maximum size difference of 1.35 nm for fresh and 1.34 nm for spent catalyst samples. An overview of the bins used in this study is given in Appendix B.

Experimental TEM histograms were then fitted with a lognormal distribution function, (*LNDF*) [25] to find the approximate number (N_i) of Co crystallites in each specific bin i . The surface-average Co crystallite diameter (d_i) of each sample as well the standard deviation (s) are also calculated as depicted in Fig. 12. The broad particle size distribution after sintering is clearly identified.

The total volume of particles in the catalyst sample (V_{total} , m³) is the calculated assuming spherical particles:

$$V_{total} = \sum_{i=1}^m N_i V_i = \sum_{i=1}^m N_i \frac{\pi d_i^3}{6} \quad (3.22)$$

As the fresh and spent catalyst samples represented by TEM images do not show the same catalyst mass and particle number, a normalization factor (NF , $\text{g}_{\text{Co}}^{-1}$) is required to compare both samples on a weight basis:

$$NF = \frac{1}{V_{total} \cdot \rho_{\text{Co}}} \quad (3.23)$$

where ρ_{Co} is the cobalt mass density at room temperature (8900 kg/m^3).

In the next step, the surface area per gram of cobalt (A_i , $\text{m}^2 \cdot \text{g}_{\text{Co}}^{-1}$) was calculated for each bin by multiplying the number of particles by the surface area of one particle and the normalization factor.

$$A_i = N_i \pi d_i^2 NF \quad (3.24)$$

The weight based surface area could be then converted into the number of Co atoms ($n_{S,i}$, $\text{mol}_{\text{SurfCo}} \cdot \text{g}_{\text{Co}}^{-1}$) at the surface, assuming one Co atom per 0.0628 nm^2 ($4r^2$, $r = \frac{1}{2}$ Co-Co bond length) of surface area.

$$n_{S,i} = \frac{A_i}{4r_{\text{Co,atomic}}^2 N_{AV}} \quad (3.25)$$

in which N_{AV} stands for the Avogadro's number.

The total number of cobalt atoms at the surface (n_S , $\text{mol}_{\text{SurfCo}} \cdot \text{g}_{\text{Co}}^{-1}$) is the sum of $n_{S,i}$.

$$n_S = \sum_{i=1}^m n_{S,i} \quad (3.26)$$

The actual dispersion (\bar{D} , $\text{mol}_{\text{SurfCo}} \cdot \text{mol}_{\text{Co}}^{-1}$) is determined by multiplying the total number of cobalt atoms at the surface and the cobalt molecular weight (MW_{Co} , $\text{g}_{\text{Co}} \cdot \text{mol}_{\text{Co}}^{-1}$).

$$\bar{D} = n_S MW_{\text{Co}} \quad (3.27)$$

The sintering process minimizes the total surface area energy. To find out how the surface energy is decreased during sintering, van Steen surface energy correlations [1] were used.

$$\Gamma_{\text{Co},i} = \gamma_{\text{Co},i} A_i \quad (3.28)$$

The total weighted surface energy of the catalyst sample (Γ_{Co} , $\text{J} \cdot \text{g}_{\text{Co}}^{-1}$) is derived by adding-up all the contributions:

$$\Gamma_{\text{Co}} = \sum_{i=1}^m \Gamma_{\text{Co},i} \quad (3.29)$$

Table 3.3 shows the summary of the results obtained.

Table 3.3 Detailed PSD analysis of Co-Re/SiO₂ catalyst [22] before/after sintering in high CO conversion regime

Property	Fresh Catalyst	Sintered Catalyst	Variation (%)
Calc. Cobalt Time Yield $\frac{(\text{mol}_{\text{CO}}/[\text{g}_{\text{CoS}}])}{(\text{mol}_{\text{CO}}/[\text{mol}_{\text{CoS}}])}$	4.27×10^{-5}	2.80×10^{-5}	-34 %
Dispersion ($\text{mol}_{\text{SurfCo}}/\text{ol}_{\text{Co}}$)	0.16	0.07	-56 %
Particles Surface area ($\text{m}^2/\text{gr}_{\text{Co}}$)	101.8	44.1	-57%
Total Surface Energy ($\text{J}/\text{g}_{\text{Co}}$)	275.1	104.8	-62%

3.2.4.2. Proposed sintering mechanism

Thus, previous reports are indicative of Particle Migration and Coalescence (PMC) mechanism for sintering of cobalt nanoparticles during FT synthesis. In that mechanism, sintering kinetics is governed by three successive steps: diffusion, collision, and agglomeration. Cobalt particles diffuse within the support pores before reaching each other and forming larger agglomerates. Diffusion coefficient for Co nanoparticles within the alumina support is proposed by the similar equation [16] given previously for nickel particles:

$$D_i = 4.818D_s \left(\frac{2r}{d_i} \right)^4 \quad (3.30)$$

where r is the atomic radius (for Co 0.125 nm) and D_s is the surface diffusion coefficient, which is estimated as $3.3 \times 10^{-18} \text{ m}^2/\text{s}$ at 773 K [16].

The proposed water-assisted sintering mechanism is shown in Fig. 3.14. The sintering is driven by minimization of particle surface energy and therefore it results in more thermodynamically stable particles. The experimental data suggest a very significant effect of water on the sintering rate [23] and [26]. We suggest here that water facilitates sintering by both reducing the particles surface energy via oxidation of particle surface and increasing their mobility. This suggestion is consistent with previous results of van Steen et al. [2] who showed that bulk cobalt oxide (CoO) particles have about 80% smaller surface energy than metallic cobalt particles with the same size. The results of van Steen et al. [1] are also consistent with more recent calculations which are also indicative of lower surface energy of oxide nanoparticles relative to the metallic species [2].

In the work of Sehested [27] focused on nickel catalysts, higher diffusivity of oxide nanoparticles was attributed to higher surface diffusivity (up to hundred times) of surface species (Eq. 3.32). Therefore because of both thermodynamic and kinetic reasons, sintering of cobalt nanoparticles should be accelerated after surface oxidation. Although the formation of bulk cobalt oxide is not possible during FT reaction according to Saib and van Steen [2] and

[1], formation of the surface oxides could probably occur under typical FT conditions as previously discussed. Indeed, metallic particles partially covered with a surface layer of CoO have lower surface energy and therefore total energy would be lower. Thus it can be suggested that the first step of cobalt sintering in the presence of water could possibly involve reversible surface oxidation of cobalt nanoparticles:

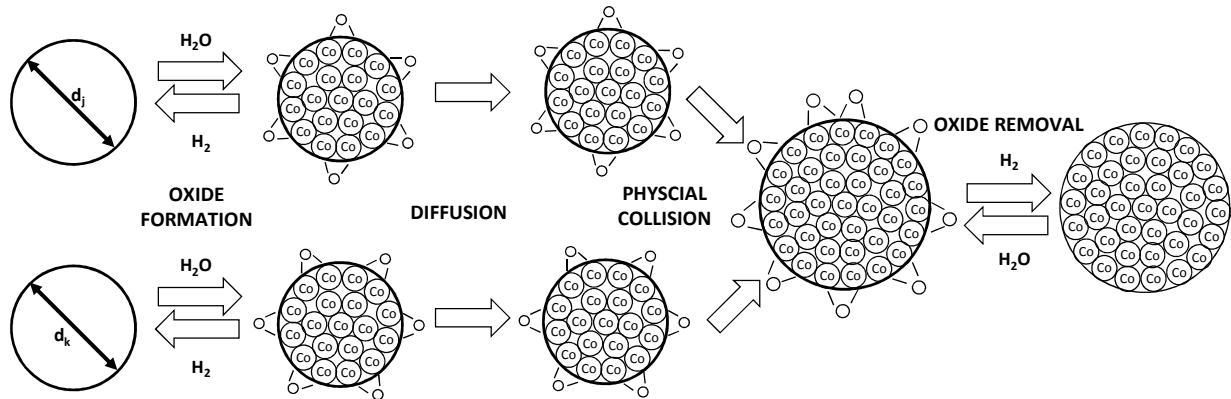


Figure 3.14 Proposed water-assisted mechanism for Co particles sintering during FT synthesis

The surface coverage by CoO in this case would be dependent on H_2O and H_2 pressures (in the case of fixed bed reactors). The assumption that cobalt sintering is accelerated via particle surface oxidation would also explain why the sintering does not take place in the presence of either inert or reducing atmospheres, as they would inhibit the formation of surface CoO species. Eq. 3.31 allows calculation of CoO surface coverage θ_{CoO} as a function of operating conditions:

$$K_{\text{CoO}} = \frac{\theta_{\text{CoO}}}{1 - \theta_{\text{CoO}}} \left(\frac{P_{\text{H}_2}}{P_{\text{H}_2\text{O}}} \right)^{(\theta_{\text{CoO}} - 1)} \approx \theta_{\text{CoO}} \frac{P_{\text{H}_2}}{P_{\text{H}_2\text{O}}} \Rightarrow \theta_{\text{CoO}} = K_{\text{CoO}} \frac{P_{\text{H}_2\text{O}}}{P_{\text{H}_2}} \quad (3.31)$$

where for the sake of simplicity, the particle surface is assumed to be covered by either metallic or oxidized cobalt species.

Because of higher diffusivity of CoO relative to metallic cobalt we assume that particle diffusion is due to the presence of superficially oxidized cobalt particles [21].

$$D_i = 4.818 D_S^{\text{CoO}} \theta_{\text{CoO}} \left(\frac{2r}{d_i} \right)^4 = 4.818 D_S^{\text{CoO}} \left(\frac{2r}{d_i} \right)^4 K_{\text{CoO}} \frac{P_{\text{H}_2}}{P_{\text{H}_2\text{O}}} \quad (3.32)$$

where D_S^{CoO} is CoO surface diffusivity (estimated as 3.3×10^{-8} m²/s at 773 K as in the case of nickel particles).

Once the particle surface is partially covered with cobalt oxide species, the particle growth occurs. Particle Migration and Coalescence occurs via a three-step (particle diffusion, collision, and coagulation) process. As already mentioned, the particles repartition measured during sintering [28] follows a *log normal distribution function (LNDF)*. Consequently the rate of collision, $d\Phi_i$ (s^{-1}) for a particle i (with a diameter d_i) with *all* particles j (which have an average diameter d_j in the logarithmic size interval $d\ln(d_j)$) is calculated [29] by:

$$d\Phi_i = const \cdot D_{ij} \cdot \frac{N}{A_{support}} \cdot f_{LN}(d_j) \cdot d\ln(d_j) \quad (3.33)$$

where *const.* is a time-independent constant, D_{ij} is the relative diffusion constant for particles of diameters d_i and d_j through the porous structure:

$$D_{ij} = D_i + D_j = 77.088r^4 D_S^{CoO} K_{CoO} \frac{P_{H_2}}{P_{H_2O}} \left(\frac{1}{d_i^4} + \frac{1}{d_j^4} \right) \quad (3.34)$$

$f_{LN}(d_j)$ gives the fractional number of particles in the logarithmic size interval $d\ln(d_j)$, based on the *LNDF* while $N/A_{support}$ gives the total number of Co particles per square meter of support:

$$\frac{N}{A_{support}} = \frac{6X_{Co}}{\rho_{Co}(1-X_{Co})A_{m,support}\pi\bar{d}^3} \quad (3.35)$$

where ρ_{Co} is the cobalt mass density, X_{Co} is the cobalt loading in the catalyst, and $A_{m,support}$ is the specific support surface area. Therefore Φ_i the rate of collision of a particle j having a diameter d_i with all other particles is given by [27]:

$$\Phi_i = const \cdot \frac{N}{A_{support}} \int_{-\infty}^{+\infty} D_{ij} f_{LN}(d_j) d\ln\left(\frac{d_j}{d}\right) = const \cdot \frac{N}{A_{support}} D_S^{CoO} K_{CoO} \frac{P_{H_2}}{P_{H_2O}} \left(\frac{1}{d_i^4} + \frac{e^{4\ln^2 \sigma}}{\bar{d}^4} \right) \quad (3.36)$$

The total number of collisions per second Φ is calculated by:

$$\Phi = N \int_{-\infty}^{+\infty} \Phi_i f_{LN}(d_i) d\ln\left(\frac{d_i}{d}\right) = const \cdot \frac{N^2}{A_{support}} D_S^{CoO} K_{CoO} \frac{P_{H_2}}{P_{H_2O}} \bar{d}^4 \quad (3.37)$$

The collision of two particles of diameters d_i and d_j results in a larger particle of diameter $(d_i^3 + d_j^3)^{1/3}$. The number of particles N is also reduced by one. The average increase in number-average diameter for the entire catalyst sample for one collision $\Delta(\bar{d})$ is then obtained from [21]:

$$\Delta(\bar{d}) = \int_{-\infty}^{+\infty} \int_{-\infty}^{+\infty} \left(\frac{N\bar{d} - d_i - d_j + (d_i^3 + d_j^3)^{1/3}}{N-1} - \bar{d} \right) f_{LN}(d_i) d \ln\left(\frac{d_i}{\bar{d}}\right) f_{LN}(d_j) d \ln\left(\frac{d_j}{\bar{d}}\right) \quad (3.38)$$

Numerical integration gives:

$$\Delta(\bar{d}) = f(\sigma) \frac{\bar{d}}{N-1} \approx f(\sigma) \frac{\bar{d}}{N} \quad (N \gg 1) \quad (3.39)$$

where $f(\sigma) = 1.36\ln^2\sigma - 0.13\ln\sigma + 0.28$ is a function of standard deviation of the lognormal distribution, σ .

The rate of increase in particle average diameter is then calculated by:

$$\frac{\partial(\bar{d})}{\partial t} = \Phi\Delta(\bar{d}) = \text{const.} \cdot f(\sigma) \frac{1.91D_s^{CoO} X_{Co} K_{CoO}}{\rho_{Co} (1 - X_{Co}) A_{sup\ port} \bar{d}^6} \cdot \frac{P_{H_2O}}{P_{H_2}} \quad (3.40)$$

Reformulation yields the evolution of number-average Co particle diameter as a function of time and H_2O/H_2 partial pressure ratio during sintering:

$$\frac{\partial\bar{d}}{\partial t} = k_s \frac{P_{H_2O}}{P_{H_2}} \cdot \frac{1}{\bar{d}^6} \quad (3.41)$$

where sintering constant k_s , is the combination of all the parameters which are kept constant during sintering:

$$k_s = \text{const.} \cdot f(\sigma) \frac{13.38D_s^{CoO} K_{CoO} X_{Co}}{(1 - X_{Co}) \rho_{Co} A_{sup\ port}} \quad (3.42)$$

In accordance with experimental data, a value of $29.68 \text{ nm}^7/\text{s}$ was used for k_s in the case of reference Co-based catalyst. An Arrhenius type of expression could be then employed for the sintering constant (k_s) to account for the variation with temperature [27]. As the XRD technique gives the surface-average diameter, Eq. 3.41 should be changed correspondingly. This is conducted using the correlation developed by Sehested [27]:

$$\bar{d}_s = e^{\frac{5}{2}\ln^2\sigma} \bar{d} \quad (3.43)$$

Fig. 3.12 suggests that the change in the standard deviation is small during sintering ($\sigma = 1.4$ for fresh catalyst, $\sigma = 1.45$ for sintered catalyst). Therefore one can neglect the change in the standard derivation for the particle diameters during sintering to convert the number-average diameter into surface-average diameter:

$$\frac{\partial \bar{d}_s}{\partial t} = k_s \frac{P_{H_2O}}{P_{H_2}} \cdot \frac{1}{\bar{d}_s^6} \quad (3.44)$$

Note that, Eq. 3.44 represent the evolution of surface-average particle diameter in the case of (capillary and millimetric) fixed bed reactors in which the surface oxidation reaction occurs at the solid-gas interface and consequently the relative water partial pressure governs the CoO coverage on the surface. In addition, as all the parameters including P_{H_2O}/P_{H_2} change with the axial position as well as time, partial difference form of equations should be applied.

In the case of slurry reactor, a similar methodology could be applied including the surface oxidation reaction at the liquid-catalyst interface. Therefore the surface coverage of cobalt oxide is expressed in this case as a function of relative water-to-hydrogen concentration in the liquid phase, which is assumed to be the constant in the whole liquid mixture at any given time. Consequently, the expression for the surface-average particle diameter evolution with time is given in this case in terms of ordinary partial differential equation of the form:

$$\frac{d\bar{d}_s}{dt} = k_s^L \frac{C_{H_2O}^L}{C_{H_2}^L} \cdot \frac{1}{\bar{d}_s^6} \quad (3.45)$$

where $C_{H_2O}^L$ and $C_{H_2}^L$ represent the water and hydrogen liquid concentration respectively.

However one should note that the sintering constant k_s^L is different for the slurry than the value used for fixed bed reactors k_s , as the former includes the vapor-liquid equilibrium coefficients for both hydrogen and water species.

Once the microscopic correlations are proposed for the initial deactivation of cobalt-based catalyst, they are used in the macroscopic models dedicatedly developed for each type of reactor so that a realistic correlation between the crystallite growth and the activity reduction could be obtained as detailed in Chapter 4.

3.3. Development of long-term deactivation model (coking)

As already stated in Chapter 1, most FT catalysts demonstrate a two-step deactivation profile including an initial and a long-term activity reduction period. Although the initial deactivation period is easier to model as the catalyst properties before start-up are available for fresh catalyst samples, the long-term deactivation involves a complex process for modeling. The difficulty of characterizing catalysts before/during this period as well as the

possibility of several simultaneous deactivation mechanisms are the factor to be considered. Consequently this section gives only an initial general model for the long-term Co-based catalyst deactivation in typical FT conditions that could represent the long term deactivation profile under typical FT conditions.

Although several mechanisms could be considered for long-term catalyst deactivation in Fischer-Tropsch conditions, several researchers have proposed coking (carbon deposition) as the main source of long-term deactivation as shown in Chapter 1. Coking has been detected by temperature programmed techniques in the literature [30], [31], [32]. Moodley et al. [31] used high resolution-transmission electron microscopy (HR-TEM) to confirm the presence and the nature of carbon species and carbon mapping using EF-TEM images gave the topography of polymeric carbon.

Consequently the main long-term deactivation mechanism considered in this study is catalyst coking, also referred to as active site poisoning by active carbons. The existing models for the coking are studied and a mechanistic mechanism is proposed for the active site positioning in the case of cobalt-based FT catalysts.

3.3.1. Existing models for long-term catalyst deactivation

As already mentioned, due to the complexity of modeling coking phenomenon, the number of long-term deactivation models which could realistically represent the experimental data is limited. Some models are already presented in Chapter 1 including the one developed by Zhu et al. [33] for coke formation in activated carbon catalysts. Note that as the catalyst characterization properties could not still be followed in a long-term in-situ basis, most authors proposed an empirical approach for the long-term deactivation. The suitability of the developed models is analyzed based on the acceptable fit with the experimental activity versus time profile

3.3.2. Proposed mechanism and model: active site carbon poisoning

Based on the experiments performed at high temperature ($T = 260^{\circ}\text{C}$), the long-term deactivation phenomena were found to dominant at high temperature as a complete catalyst deactivation was observed in several reproducible high temperature runs. Consequently it is proposed that catalyst surface coking is accelerated at higher temperatures. In addition, in line with the mechanism proposed for sintering, we suggest here that the initial reversible

oxidation reaction turns into a partially irreversible process in long-term as the adsorption-desorption properties are modified as the catalyst surface is deactivated.

Carbon is assumed to poison the surface through the dissociative carbon monoxide adsorption in a reaction which leads to atomic carbon and oxygen species on the surface. The reaction could be written in the case of fixed bed reactors as:



The changing rate of carbon-poisoned sites with time is then given by:

$$\frac{d\theta_{*-C}}{dt} = k_{CF} P_{CO} \theta_*^2 - k_{CR} \theta_{*-C} \theta_{*-O} \quad (3.46)$$

where k_{CF} and k_{CR} are the coke formation and regeneration constants respectively, whereas θ_* , θ_{*-O} and θ_{*-C} give the surface coverage of free active, carbon-poisoned, and oxygen-poisoned sites respectively.

The presence of hydrogen in the Fischer-Tropsch reacting media tends to reduce the oxygen-poisoned sites by an equilibrium reaction:



Consequently the fraction of oxygen-poisoned sites is given by:

$$\theta_{*-O} = \frac{P_{H_2O}}{P_{H_2} K_O} \theta_* \quad (3.47)$$

where K_O stands for oxidation equilibrium constant.

Eq. 3.49 helps to rewrite the production rate of carbon-poisoned sites as a function of free sites fraction:

$$\frac{\partial \theta_{*-C}}{\partial t} = \left(k_{CF} P_{CO} \theta_* - k_{CR} \theta_{*-C} \frac{P_{H_2O}}{P_{H_2} K_O} \right) \theta_* \quad (3.48)$$

Neglecting the other species on the catalyst surface, one can assume that the surface is only covered by free active, carbon-poisoned, and oxygen-poisoned sites:

$$\theta_{*-C} = 1 - \theta_* - \theta_{*-O} = 1 - \left(1 + \frac{P_{H_2O}}{P_{H_2} K_O} \right) \theta_* \quad (3.49)$$

Recombining Eq. 3.48 and 3.49 and assuming an irreversible coke formation reaction ($k_{CR} = 0$), the change in the surface coverage of free catalytic sites is given as a function of relative carbon monoxide, water, and hydrogen partial pressures:

$$-\frac{1}{\theta_*^2} \frac{\partial \theta_*}{\partial t} = k_{app,CF} \frac{P_{H_2} P_{CO}}{P_{H_2O}} \quad (3.50)$$

where $k_{app,CF}$ is the apparent coke formation constant $k_{app,CF} = k_{CF} K_O$.

Similarly to the fixed bed reactors, the coke formation in the slurry reactor could also lead to catalyst deactivation. The production rate of carbon-poisoned sites in the slurry reactor is expressed in terms of liquid concentration of CO, H₂O, and H₂ species:

$$-\frac{1}{\theta_*^2} \frac{d\theta_*}{dt} = k'_{app,CF} \frac{C_{H_2}^L C_{CO}^L}{C_{H_2O}^L} \quad (3.51)$$

where the apparent coke formation constant $k'_{app,CF}$ is adjusted by the vapor-liquid equilibrium coefficients of relevant species.

3.4. Concluding remarks

This chapter presented the developed models for initial and long-term deactivation of cobalt-based catalysts in typical Fischer-Tropsch conditions.

The possibility of surface oxidation for cobalt particles by the FT-produced water is investigated. Both the catalysts characterization tools and thermodynamic calculations suggest that the catalyst surface could be covered by the cobalt oxide species under typical FT conditions. The CoO species, formed in a reversible manner, help to accelerate sintering by both lowering the surface energy and increasing the particle mobility. Thus an increased rate of Co crystallite growth could be obtained. The operando XRD tools as well the particle size distribution of fresh/spent catalyst samples propose that sintering of cobalt crystallites proceeds through particle migration and coalescence (PMC). The sintering mechanism therefore considers PMC growth type in establishing how the crystallites grow in size. The proposed mechanism, accelerated by water, could therefore predict the rate of crystallite growth as a function of operating conditions. The relative water partial pressure is found to have the dominant effect in such a correlation and consequently any condition which increases the water relative pressure inside the reactor could lead to a higher sintering rate.

Although the sintering model is basically a mechanistic approach to explain the activity reduction profile observed during the first hours on stream, the carbon poisoning model is an empirical one to describe how deactivation leads to further decrease in catalytic activity. The reason for applying such different methodologies is already mentioned in the text where adequate characterization tools are required to study the deactivation in a comprehensive way. The use of such tools is easier in short terms and consequently the use of a mechanistic approach for the initial deactivation phenomena is more relevant. In long terms,

several side effects take place at the same time resulting in an increased complexity of studying deactivation at the catalyst surface.

The long-term deactivation model is compatible with the initial one, as it involves the surface coking and oxidation, although it is proposed that irreversible reactions occur in the long-term. The long-term deactivation mechanism is also believed to be activated by the temperature, based on experimental results.

Note that, the developed models deal with the phenomena occurring at the catalyst scale. Consequently they should be incorporated in the reactor models once a realistic picture of catalyst deactivation is desired. The developed reactor models for fixed bed and slurry reactor in the next chapter deal with such a subject.

3.5. References

- [1] E. van Steen, M. Claeys, M.E. Dry, J. van de Loosdrecht, E.L. Viljoen, J.L. Visagie, Stability of Nanocrystals: Thermodynamic Analysis of Oxidation and Re-reduction of Cobalt in Water/Hydrogen Mixtures, *The Journal of Physical Chemistry B*, 109 (2005) 3575-3577.
- [2] A.M. Saib, D.J. Moodley, I.M. Ciobîcă, M.M. Hauman, B.H. Sigwebela, C.J. Weststrate, J.W. Niemantsverdriet, J. van de Loosdrecht, Fundamental understanding of deactivation and regeneration of cobalt Fischer–Tropsch synthesis catalysts, *Catalysis Today*, 154 (2010) 271-282.
- [3] G. Jacobs, T.K. Das, P.M. Patterson, J. Li, L. Sanchez, B.H. Davis, Fischer–Tropsch synthesis XAFS: XAFS studies of the effect of water on a Pt-promoted Co/Al₂O₃ catalyst, *Applied Catalysis A: General*, 247 (2003) 335-343.
- [4] G. Jacobs, P.M. Patterson, T.K. Das, M. Luo, B.H. Davis, Fischer–Tropsch synthesis: effect of water on Co/Al₂O₃ catalysts and XAFS characterization of reoxidation phenomena, *Applied Catalysis A: General*, 270 (2004) 65-76.
- [5] G. Jacobs, Y. Zhang, T.K. Das, J. Li, P.M. Patterson, B.H. Davis, Deactivation of a Ru promoted Co/Al₂O₃ catalyst for FT synthesis, in: G.W.R. J.J. Spivey, B.H. Davis (Eds.) *Studies in Surface Science and Catalysis*, Elsevier, 2001, pp. 415-422.
- [6] G. Jacobs, P.M. Patterson, Y. Zhang, T. Das, J. Li, B.H. Davis, Fischer–Tropsch synthesis: deactivation of noble metal-promoted Co/Al₂O₃ catalysts, *Applied Catalysis A: General*, 233 (2002) 215-226.
- [7] T.K. Das, G. Jacobs, P.M. Patterson, W.A. Conner, J. Li, B.H. Davis, Fischer–Tropsch synthesis: characterization and catalytic properties of rhenium promoted cobalt alumina catalysts☆, *Fuel*, 82 (2003) 805-815.
- [8] J. Li, X. Zhan, Y. Zhang, G. Jacobs, T. Das, B.H. Davis, Fischer–Tropsch synthesis: effect of water on the deactivation of Pt promoted Co/Al₂O₃ catalysts, *Applied Catalysis A: General*, 228 (2002) 203-212.
- [9] J. Li, G. Jacobs, T. Das, Y. Zhang, B. Davis, Fischer–Tropsch synthesis: effect of water on the catalytic properties of a Co/SiO₂ catalyst, *Applied Catalysis A: General*, 236 (2002) 67-76.
- [10] A.M. Saib, A. Borgna, J. van de Loosdrecht, P.J. van Berge, J.W. Niemantsverdriet, In Situ Surface Oxidation Study of a Planar Co/SiO₂/Si(100) Model Catalyst with Nanosized Cobalt Crystallites under Model Fischer–Tropsch Synthesis Conditions, *The Journal of Physical Chemistry B*, 110 (2006) 8657-8664.
- [11] M.W.J. Crajé, A.M. van der Kraan, J. van de Loosdrecht, P.J. van Berge, The application of Mössbauer emission spectroscopy to industrial cobalt based Fischer–Tropsch catalysts, *Catalysis Today*, 71 (2002) 369-379.
- [12] H. Karaca, O.V. Safonova, S. Chambrey, P. Fongarland, P. Roussel, A. Griboval-Constant, M. Lacroix, A.Y. Khodakov, Structure and catalytic performance of Pt-promoted alumina-supported cobalt catalysts under realistic conditions of Fischer–Tropsch synthesis, *Journal of Catalysis*, 277 (2011) 14-26.
- [13] C.-F. Huo, Y.-W. Li, J. Wang, H. Jiao, Adsorption and Dissociation of CO as Well as CH_x Coupling and Hydrogenation on the Clean and Oxygen Pre-covered Co(0001) Surfaces, *The Journal of Physical Chemistry C*, 112 (2008) 3840-3848.
- [14] S.H. Overbury, P.A. Bertrand, G.A. Somorjai, Surface composition of binary systems. Prediction of surface phase diagrams of solid solutions, *Chemical Reviews*, 75 (1975) 547-560.
- [15] W.R. Tyson, W.A. Miller, Surface free energies of solid metals: Estimation from liquid surface tension measurements, *Surface Science*, 62 (1977) 267-276.

- [16] J. Sehested, A. Carlsson, T.V.W. Janssens, P.L. Hansen, A.K. Datye, Sintering of Nickel Steam-Reforming Catalysts on MgAl_2O_4 Spinel Supports, *Journal of Catalysis*, 197 (2001) 200-209.
- [17] L.M. Aparicio, Transient Isotopic Studies and Microkinetic Modeling of Methane Reforming over Nickel Catalysts, *Journal of Catalysis*, 165 (1997) 262-274.
- [18] H.S. Bengaard, J.K. Nørskov, J. Sehested, B.S. Clausen, L.P. Nielsen, A.M. Molenbroek, J.R. Rostrup-Nielsen, Steam Reforming and Graphite Formation on Ni Catalysts, *Journal of Catalysis*, 209 (2002) 365-384.
- [19] E.E. Gruber, Calculated size distributions for gas bubble migration and coalescence in solids, *Journal of Applied Physics*, 38 (1967) 243-250.
- [20] P. Wynblatt, N.A. Gjostein, Supported metal crystallites, *Progress in Solid State Chemistry*, 9 (1975) 21-58.
- [21] J. Sehested, J.A.P. Gelten, I.N. Remediakis, H. Bengaard, J.K. Nørskov, Sintering of nickel steam-reforming catalysts: effects of temperature and steam and hydrogen pressures, *Journal of Catalysis*, 223 (2004) 432-443.
- [22] G. Kiss, C.E. Klierer, G.J. DeMartin, C.C. Culross, J.E. Baumgartner, Hydrothermal deactivation of silica-supported cobalt catalysts in Fischer–Tropsch synthesis, *Journal of Catalysis*, 217 (2003) 127-140.
- [23] H. Karaca, J. Hong, P. Fongarland, P. Roussel, A. Griboval-Constant, M. Lacroix, K. Hortmann, O.V. Safonova, A.Y. Khodakov, In situ XRD investigation of the evolution of alumina-supported cobalt catalysts under realistic conditions of Fischer-Tropsch synthesis, *Chemical Communications*, 46 (2010) 788-790.
- [24] J.P. den Breejen, J.R.A. Sietsma, H. Friedrich, J.H. Bitter, K.P. de Jong, Design of supported cobalt catalysts with maximum activity for the Fischer–Tropsch synthesis, *Journal of Catalysis*, 270 (2010) 146-152.
- [25] C.G. Granqvist, R.A. Buhrman, Size distributions for supported metal catalysts: Coalescence growth versus ostwald ripening, *Journal of Catalysis*, 42 (1976) 477-479.
- [26] G.L. Bezemer, T.J. Remans, A.P. van Bavel, A.I. Dugulan, Direct Evidence of Water-Assisted Sintering of Cobalt on Carbon Nanofiber Catalysts during Simulated Fischer–Tropsch Conditions Revealed with in Situ Mössbauer Spectroscopy, *Journal of the American Chemical Society*, 132 (2010) 8540-8541.
- [27] J. Sehested, Sintering of nickel steam-reforming catalysts, *Journal of Catalysis*, 217 (2003) 417-426.
- [28] S.S. G. Kiss, C. Klierer, in: *International Symposium on Catalyst Deactivation*, Delft, The Netherlands, 2009.
- [29] E. Ruckenstein, B. Pulvermacher, Kinetics of crystallite sintering during heat treatment of supported metal catalysts, *AIChE Journal*, 19 (1973) 356-364.
- [30] D.-K. Lee, J.-H. Lee, S.-K. Ihm, Effect of Carbon Deposits on Carbon Monoxide Hydrogenation over Alumina-Supported Cobalt Catalyst, *Applied Catalysis*, 36 (1988) 199-207.
- [31] D.J. Moodley, J. van de Loosdrecht, A.M. Saib, M.J. Overett, A.K. Datye, J.W. Niemantsverdriet, Carbon deposition as a deactivation mechanism of cobalt-based Fischer–Tropsch synthesis catalysts under realistic conditions, *Applied Catalysis A: General*, 354 (2009) 102-110.
- [32] A. Barbier, A. Tuel, I. Arcon, A. Kodre, G.A. Martin, Characterization and Catalytic Behavior of Co/SiO_2 Catalysts: Influence of Dispersion in the Fischer–Tropsch Reaction, *Journal of Catalysis*, 200 (2001) 106-116.
- [33] W. Zhu, J. Zhang, F. Kapteijn, M. Makkee, J.A. Moulijn, Hydrodechlorination of 1,2-dichloropropane over Pt–Cu/C catalysts: Coke formation determined by a novel technique-

TEOM, in: G.W.R. J.J. Spivey, B.H. Davis (Eds.) *Studies in Surface Science and Catalysis*, Elsevier, 2001, pp. 21-28.

CHAPTER

4

DEACTIVATION IN FIXED BED REACTORS

4.1. Introduction

The previous chapter described the microscopic models for the catalyst sintering and coking during typical Fischer-Tropsch conditions. FT synthesis involves catalytic reactors. Thus a correlation between the catalyst properties and the catalytic activity is investigated through the application of “reactor models”. The reactor models enable us to follow how the microscopic phenomena (crystallite growth and carbon deposition) lead to the modification in carbon monoxide conversion.

Both fixed bed and slurry reactor are used for FT synthesis. Fixed bed reactors (FBR) are studied in this chapter whereas the slurry reactor is considered in Chapter 5. Although both sintering and coke deposition are analyzed by the reactor model, the main emphasis is based on the crystallite growth.

First the effect of different operating conditions on the model predictions is studied. This helps to analyze the sensible parameters and to investigate how carbon monoxide profile changes with time. The effect of syngas ratio and co-feeding by an inert gas or water are studied. The FBR model is then validated using the experimental data obtained in both a capillary-fixed bed and a laboratory millimetric fixed bed reactor. The validation step helps to fit the model prediction and the experimental finding and tune the kinetic constants.

4.2. Effect of particle growth on catalytic activity

As already stated the main emphasis here is on the initial catalyst deactivation due to sintering. The basic equations for modeling the fixed bed reactor are already given in Chapter 2.

The particle growth during the sintering leads to a decrease in the number of active sites and catalyst deactivation. Thus, for description of the evaluation of catalytic activity, FT rate expression should be modified to include both activity and deactivation terms.

As already stated in Chapter 2, we have used the kinetic expression of the type Yates-Satterfield for the consumption rate of carbon monoxide in a Co-based Fischer-Tropsch synthesis. FT reaction rate r_{FT} is described as a function of the reactants concentrations in the gas phase C_{CO} and C_{H_2} as:

$$r_{FT} = \frac{k_a'' C_{CO} C_{H_2}}{(1 + k_b C_{CO})^2} \quad (4.1)$$

where the inhibition term k_b is equal to the CO adsorption equilibrium constant K_{CO} and the adsorption term k_a'' contains the total concentration of the catalyst active sites C_t as well as a

combination of kinetic and equilibrium constants of elementary reactions denoted here by k'_a (as proposed by J. Anfray [1]).

$$k''_a = C_t \cdot k'_a \quad (4.2)$$

$$k_b = K_{CO} \quad (4.3)$$

It has been assumed that the equilibrium constant K_{CO} is only temperature-dependent, and consequently the inhibition term is kept constant during isothermal sintering. Note that in addition to the concentration of active sites, the kinetic term k''_a depends also on reaction temperature.

It is assumed that the total concentration of active sites is directly proportional to the number of Co surface atoms on the particle surface. Therefore the rate expression becomes:

$$r_{FT} = n_s \frac{\bar{k}_a C_{CO} C_{H_2}}{(1 + k_b C_{CO})^2} \quad (4.4)$$

where n_s is the total number of surface atoms. The total number of cobalt surface sites is calculated from the number of cobalt surface sites per cobalt nanoparticle multiplied by the number of cobalt nanoparticles. The total number of Co nanoparticles can be calculated from average cobalt particle diameter and Co mass in the catalyst.

$$n_s = \frac{\pi \bar{d}_s^2}{4r^2 N_{AV}} \cdot \frac{N}{m_{Co}} = \frac{3}{2r^2 N_{AV} \rho_{Co} \bar{d}_s} \quad (4.5)$$

where N_{AV} is Avogadro number.

The expression n_s is then inserted in Eq. 4.4 to obtain a new form of FT rate expression as:

$$r_{FT} = \frac{1}{\bar{d}_s} \times \frac{k_a C_{CO} C_{H_2}}{(1 + k_b C_{CO})^2} \quad (4.6)$$

where:

$$k_a = \left(\frac{3}{2r^2 N_{AV} \rho_{Co}} \right) \cdot \bar{k}_a \quad (4.7)$$

is assumed to be only temperature-dependent.

Eq. 4.6 is in line with the previous findings [2], [3], [4], [5], [6] suggesting that the kinetic-deactivation terms could be decoupled. In fact although the first term on the right had

side ($\frac{1}{d_s}$) represents the unsteady state deactivation term which changes with time, the second term is a kinetic one which does not depend on the crystallite size. Eq. 4.6 is solved in conjunction with Eq. 2.17-2.26 to calculate evolution of most common catalytic parameters such as conversion and selectivity during the reaction. The model calculates the value for each parameter at every reaction time and at all locations inside the reactor. For appropriate comparisons with experimental findings however, the dependency with time is given here for the catalytic parameters at the reactor outlet and for cobalt particle sizes in the middle of catalyst bed (for easier comparison with in-situ characterization data).

4.3. Effect of operating conditions on fixed bed reactor model

Catalytic performance data were calculated under different operating conditions using the reactor model involving FT reaction and cobalt sintering. Surface-average diameters for cobalt nanoparticles and CO consumption rates are considered. The model calculates the value for each parameter at every reaction time and at all locations inside the reactor. For appropriate comparisons with experimental findings however, the dependency with time is given here for the catalytic parameters at the reactor outlet and for cobalt particle sizes in the middle of catalyst bed (for easier comparison with in-situ characterization data).

The reactor geometry considered for this study is similar to the capillary fixed bed reactor. The reactor has an inner diameter of 1 mm as well as a reactor length of 9 mm. The amount of FT catalyst loaded into the reactor is about 8 mg. The catalyst distribution is considered uniform throughout the reactor. There is no hot or cold condenser at the reactor downstream.

In agreement with experimental data, the model suggests that cobalt sintering principally occurs during the initial reaction period. The first 400 min on stream are the most significant for cobalt sintering. It was found that sintering could reduce FT reaction rate to even half of its initial value in the most severe cases, while the Co nanoparticles grow by about 33%. Simulations showed that the rate of sintering is strongly dependent on the P_{H_2O}/P_{H_2} ratio within the reactor. The effects of the operating conditions such as H_2/CO ratio in the feed, gas-space velocity, syngas dilution and co-feeding with water on catalytic performance, cobalt sintering and deactivation rate are discussed in paragraphs below in a greater detail.

4.3.1. Syngas ratio

Syngas ratio in the feed was found to have the highest impact on sintering rate and kinetics of catalyst deactivation. The effect of the syngas ratio on the rate of sintering is considered at either constant initial conversion or space velocity as this could be found to lead to opposite findings. Consequently both references are considered for a better comparison of the results.

Fig 1-2 show variations of both particle average size and CO consumption rate with time at three different syngas ratios ($H_2/CO = 1.5, 2$ and 4) either at the same gas-space velocity or at the same conversion. The reaction rate depends on H_2/CO ratio (Eq. 4.6). An increase in this ratio results in a higher reaction rate. Fig. 1 shows that cobalt sintering proceeds much faster at higher $H_2/CO = 4$ and the same gas space velocity. These conditions correspond to higher carbon monoxide conversion. This H_2/CO ratio also corresponds to much more significant catalyst deactivation. In agreement with the model, the kinetics of sintering is driven by higher P_{H_2O}/P_{H_2} ratio which is principally due to higher carbon monoxide conversion with $H_2/CO = 4$ ratio (Fig. 4.1).

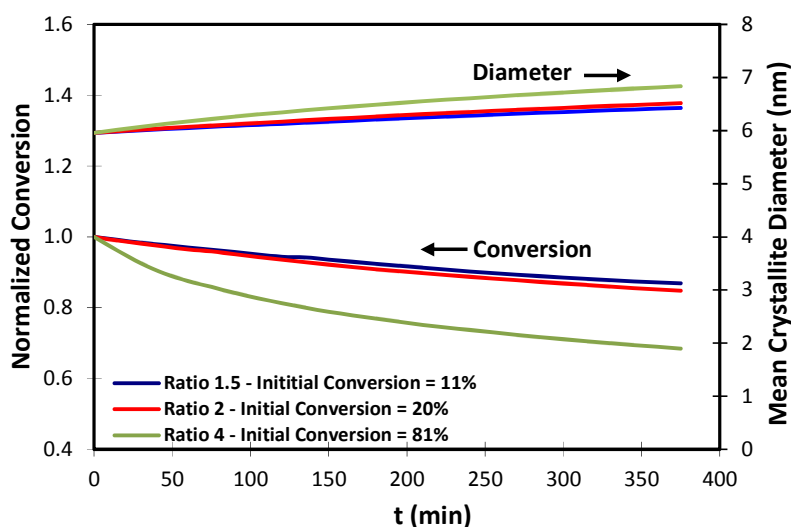


Figure 4.1 Effect of H_2/CO syngas ratio on the evolution of surface-average particle diameter [in the middle of catalyst bed] as well as relative CO conversion [at the reactor outlet] with time in a capillary-fixed bed reactor at iso-GHSV (reference catalyst, $T = 493$ K, $P = 20$ bar, initial $P_{H_2O} = 1.1, 1.5,$ and 5.0 bar for $H_2/CO = 1.5, 2,$ and 4 respectively, initial $P_{H_2O}/P_{H_2} = 0.09, 0.12,$ and 0.37 respectively, $GHSV = 75000$ $Nm^3 gcat^{-1} h^{-1}$)

The situation is different when the deactivation rates are compared at the same carbon monoxide conversion ($\sim 60\%$) but at different gas space velocities. At the same carbon monoxide conversion, lower H_2/CO ratio results in higher sintering rates and more rapid catalyst deactivation (Fig. 2). Cobalt particle size increases from 6 to 8 nm after 300 min under reaction conditions with $H_2/CO = 1.5$ in syngas, while the sintering rate is less

significant with syngas with higher H_2/CO ratios ($H_2/CO = 2$ or 4). Accordingly, a more rapid deactivation at the same conversion level ($X_{CO} = 60\%$) was also observed with syngas with lower H_2/CO ratio. Higher sintering and deactivation rates at the conversion of 60% in the case of CO-rich syngas are attributed to the higher P_{H_2O}/P_{H_2} ratio in the reactor which has a direct effect on the particle size and consequently a reverse effect on the catalytic activity.

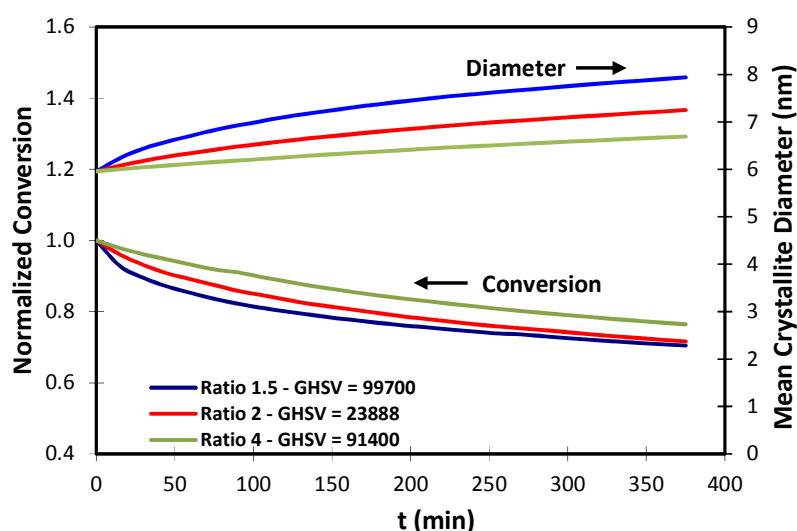


Figure 4.2 Effect of H_2/CO syngas ratio on the evolution of surface-average particle diameter [in the middle of catalyst bed] as well as relative CO conversion [at the reactor outlet] with time at iso-conversion in a capillary-fixed bed reactor (reference catalyst, $T = 493$ K, $P = 20$ bar, initial CO conversion = 58 %, initial $P_{H_2O} = 9.4, 6.5,$ and 3.3 bar for $H_2/CO = 1.5, 2,$ and 4 respectively, initial $P_{H_2O}/P_{H_2} = 2.58, 0.79,$ and 0.22 respectively, GHSV in: $Nml\ g_{cat}^{-1}\ h^{-1}$)

4.3.2. Syngas dilution

Effect of syngas dilution with inert gas on cobalt sintering rate, catalytic performance and catalyst deactivation was also studied. Dilution of syngas (Inert/ $H_2/CO = 6/2/1, 3.3/2/1$ or $1/2/1$) while keeping H_2/CO ratio constant reduces both partial pressures of carbon monoxide and hydrogen. Interestingly, it does not have any major effect on FT reaction rate (Fig. 4.3). This leads to the fact that the same carbon monoxide conversion are obtained at higher gas space velocities with diluted syngas. Note that while syngas dilution reduces the absolute water pressure in the reactor, P_{H_2O}/P_{H_2} ratio is not much affected.

Simulations did not show any significant influence of syngas dilution on cobalt sintering (Fig. 3). The cobalt particles grow with similar rate with diluted and non-diluted gas. In agreement with the model, the rate of catalyst deactivation is also not affected by syngas dilution.

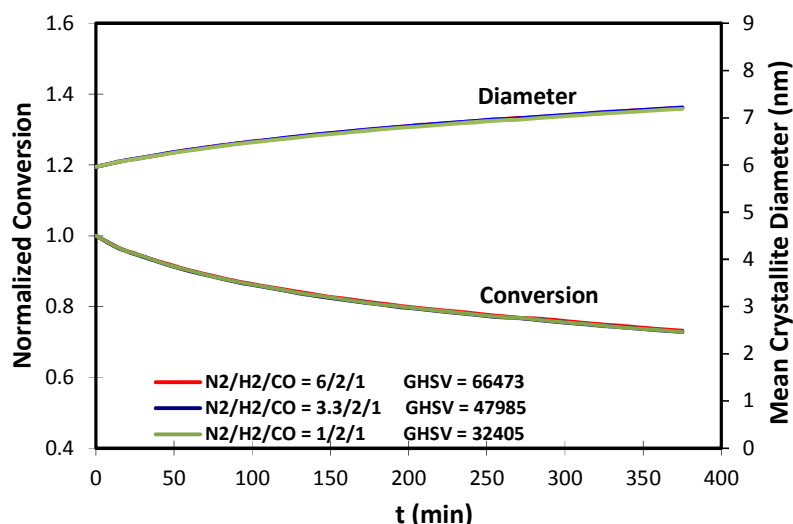


Figure 4.3 Effect of syngas dilution with inert gas on the evolution of surface-average particle diameter [in the middle of catalyst bed] as well as relative CO conversion [at the reactor outlet] with time at iso-conversion in a capillary-fixed bed reactor (reference catalyst, $T = 493$ K $P = 20$ bar, initial CO conversion = 54 %, initial $P_{\text{H}_2\text{O}}/P_{\text{H}_2} = 0.66$, GHSV in: $\text{Nml g}_{\text{cat}}^{-1} \text{h}^{-1}$).

4.3.3. Co-fed water

The deactivation model also provides a prediction for the effect of co-fed water on the rate cobalt sintering and catalytic activity. Reacting water-free syngas ($\text{H}_2/\text{CO} = 2$, GHSV = 25 000 $\text{Nml}/(\text{g}_{\text{cat}}\cdot\text{h})$) gives an initial conversion of 58%. When water was added to the reactor, the flow rate has to be increased to obtain similar initial conversion. This effect is similar with the influence of syngas dilution on carbon monoxide conversion.

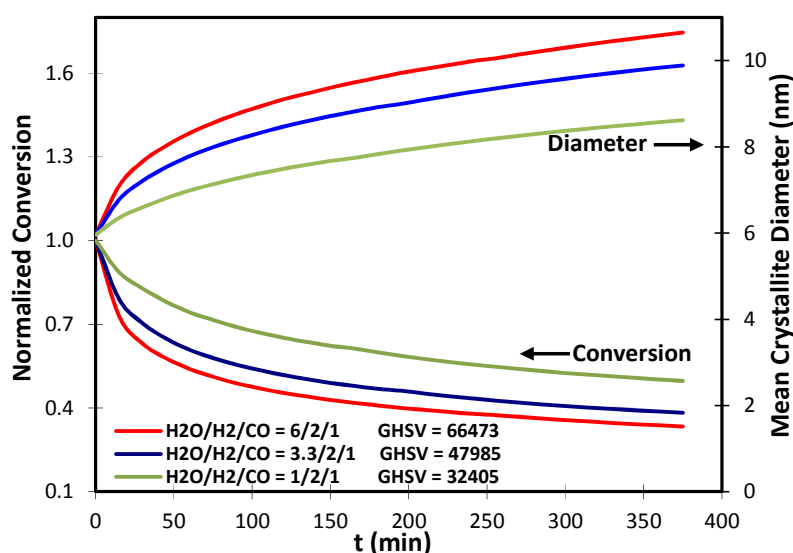


Figure 4.4 Effect of co-fed water on the evolution of surface-average particle diameter [in the middle of catalyst bed] as well as relative CO conversion [at the reactor outlet] with time at iso-conversion in a capillary-fixed bed reactor (reference catalyst, $T = 493$ K $P = 20$ bar, initial CO conversion = 54 %, initial $P_{\text{H}_2\text{O}} = 17.4, 15.5,$ and 11.0 bar for $\text{H}_2\text{O}/\text{H}_2/\text{CO} = 6/2/1, 3.3/2/1,$ and $1/2/1$ respectively, initial $P_{\text{H}_2\text{O}}/P_{\text{H}_2} = 8.17, 4.89,$ and 1.89 respectively, GHSV in: $\text{Nml g}_{\text{cat}}^{-1} \text{h}^{-1}$).

Fig. 4.4 shows the change in (a) the FT reaction rate as well as (b) particle size with time in the presence of water free syngas and syngas with co-fed water. Note that the sintering is significantly accelerated when water is added to the reaction. The cobalt particle size increases from 6 to more than 9 nm in the presence of co-fed water after 300 min of the reaction (Fig. 4.3), while this increase is less significant with a water-free syngas or in the presence of smaller amounts of water.

A much more rapid decrease in conversion can be seen in the presence of more significant amounts of water (Fig. 4.4). The predicted phenomena are interpreted in terms of variation of water pressure in the reactor. Indeed, water affects the ratio $P_{\text{H}_2\text{O}}/P_{\text{H}_2}$ as it brings about higher water partial pressure. Consequently it increases the CoO surface coverage in the short-term, leading to a more severe sintering and deactivation. As the water dilution amount increases the absolute water pressure in the reactor and more importantly $P_{\text{H}_2\text{O}}/P_{\text{H}_2}$ ratio which enhances cobalt sintering.

4.4. Validation of existing experimental runs

Once the operating parameters which influence the initial deactivation are identified, the model is used to study and be validated the experimental results. The simple model is first applied in order to study the capillary fixed bed reactor as it is considered a perfect piston flow reactor which does not include the complexities of hot and cold condensers. It is found that it could represent the evolution of average crystallite size as well as carbon monoxide conversion during the first period of FT synthesis (100 min on stream). Some microscopic improvements are then applied in the model in order to include the effect of size correction and coking. The model is then applied to the millimetric fixed bed reactor with hot and cold condensers.

4.4.1. Capillary fixed bed reactor model

Although the capillary fixed bed reactor is a reactor of choice for analyzing the crystallite growth and associated initial deactivation due to its simple configuration, its availability is limited due to difficulty of performing in-situ synchrotron-based experiments. Consequently the limited set of experiments is used to adjust the sintering constant in fixed bed reactors through the direct evolution of average Co particle size. Further analysis of operating conditions is found using the laboratory scale millimetric fixed bed reactor.

Fig. 4.5 displays the evolution of both crystallite average diameter and relative CO conversion with time for the experimental operando fixed bed configuration. The normalized

conversion is calculated by the CO conversion at any given time t divided by CO conversion at $t = 0$. The test conditions and details are given in Chapter 2. The experimental data are taken from Ref [7], while the calculated data are simulated using the model described in section 4.2 (Eq. 6).

As predicted by the model, the sintering rate is higher for small crystallites as can be seen by the sharper slope of $d(\text{Co})$ -time graph at $t = 0$ which reduces as the crystallites grow. It can be seen that cobalt sintering principally occurs during the first 100 min on stream, where the sintering model could realistically represent the initial deactivation. However, as the crystallite growth levels off, other deactivation mechanisms (e.g., carbon deposition, and carbidisation [8]) could also contribute. This suggests that other mechanisms in addition to sintering should be employed to describe long-term deactivation (TOS >100 min).

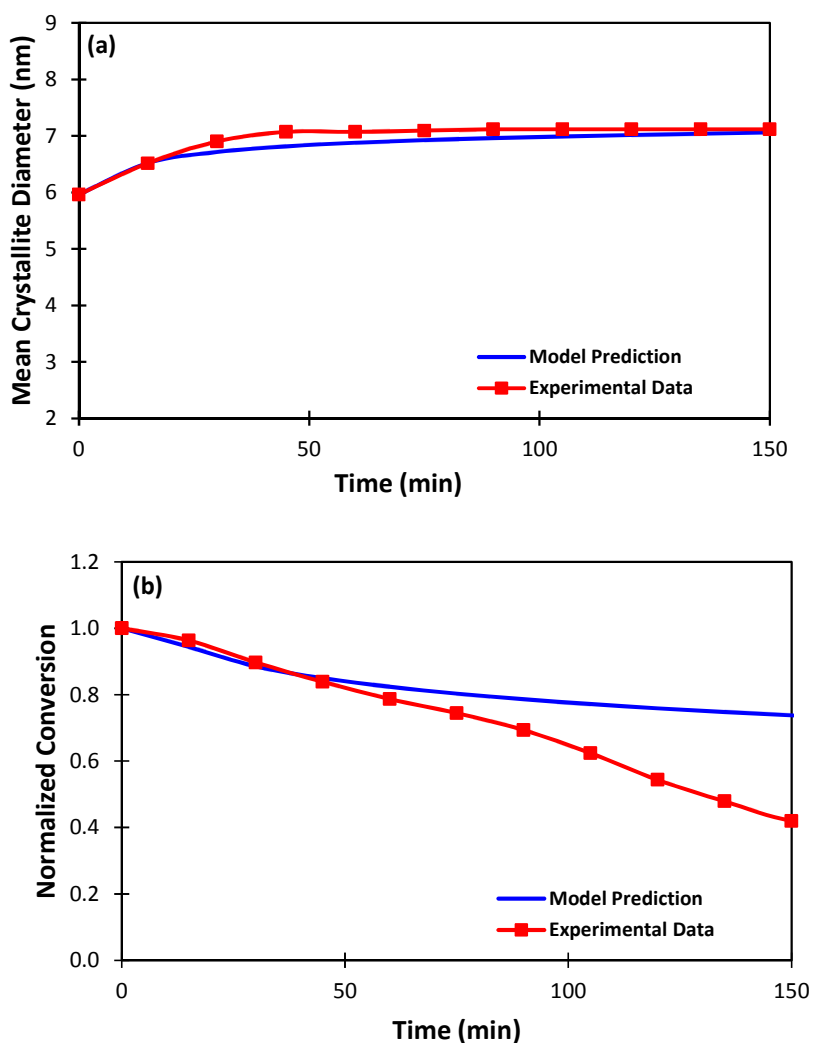


Figure 4.5 Evolution of surface-average particle diameter in the middle of catalyst bed (a) and relative CO conversion at the reactor outlet (b) with time for Co-Pt/ Al_2O_3 catalyst sample during FT synthesis ($T = 493 \text{ K}$, $P = 20 \text{ bar}$, $\text{H}_2/\text{CO} = 2$, $\text{GHSV} = 25000 \text{ Nml g}^{-1} \text{ h}^{-1}$) in a capillary-fixed bed reactor.

4.4.1.1. Effect of further microscopic catalyst properties on the catalytic activity

Although the simple FT reaction rate provided by Eq. 4.6 incorporates the microscopic phenomenon of crystallite growth, there are other phenomena that need to be included once a more appropriate reactor model is required for the fixed bed reactors. We will therefore add the dependency of the FT kinetic coefficients as well as surface carbon deposition to the previously developed FT reaction rate (Eq. 4.6) in order to represent the reactor in a better way.

There are certain evidences that there is a size dependency on the kinetics although no comprehensive quantitative approach has been already applied for the Co/Al₂O₃ catalysts. Recently it has shown [9] that the apparent turnover frequency (TOF) in FT synthesis could be smaller with cobalt particles smaller than 6 nm. Note that our proposed model involves intrinsic kinetic coefficients instead of TOF. It is clear that TOF is not a simple kinetic term, as it represents the reaction rate of each surface site. In other words, TOF depends not only on the particle sizes, but also on operating conditions as pressure, temperature, and composition. The intrinsic kinetic constants do not vary in the catalyst bed, while TOF changes from the inlet to the outlet of the reactor.

However, despite the lack of enough literature correlations, the empirical TOF-d(Co) dependence graph (depicted in Fig. 4.6) suggested by Bezemer et al. [9] could be used as a starting point to develop an intrinsic kinetic constant which varies with the mean Co crystallite size in Co/Al₂O₃ catalysts. A continuous exponential normalized function is therefore assumed for the k_a -d(Co) dependence and it is optimised in such a way that a reasonable fit between the experimental and the simulated FT reaction rates is achieved.

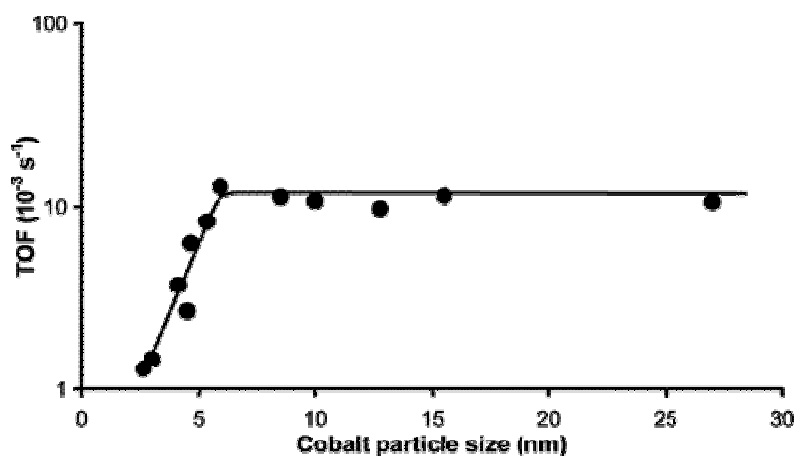


Figure 4.6 The influence of cobalt particle size on the TOF in Co/CNF catalysts (220 °C, H₂/CO = 2, 1 bar)

Eq. 4.8 gives the suggested form of kinetic diameter-dependant kinetic parameter which is further used in an improved version of Fischer-Tropsch rate expression (i.e. Eq. 4.9).

$$k_a = k_{a,0} \times (1 - e^{4.2 - \bar{d}_s}) \quad (4.8)$$

$$r_{FT} = \frac{(1 - e^{4.2 - \bar{d}_s})}{\bar{d}_s} \times \frac{k_{a,0} C_{CO} C_{H_2}}{(1 + k_b C_{CO})^2} \quad (4.9)$$

where $k_{a,0}$ gives the kinetic parameter value at $d_s = 6$ nm.

A graphical representation of Eq. 4.8 is depicted in Fig. 4.7.

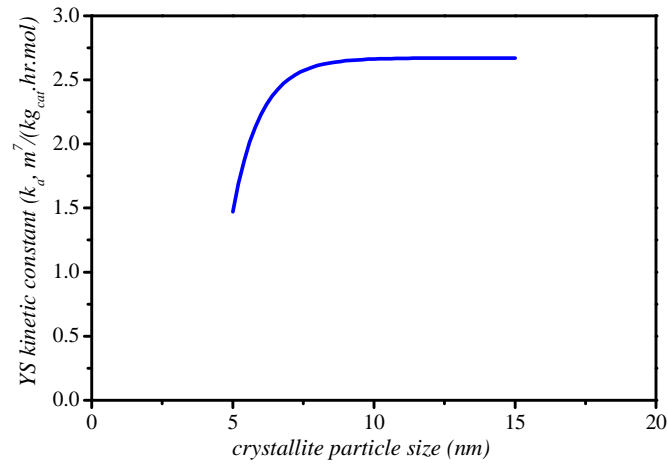


Figure 4.7 Suggested "exponential" size dependent kinetic parameter

Although this size correction is found not to influence the results in the case of capillary fixed bed reactor especially as the difference between the initial (6 nm) and final (7nm) Co crystallite size is small, the size correction is suggested as a necessary step in the more complicated reactor models i.e. milli-fixed bed reactors.

In addition we have added the coking as the main long-term deactivation phenomena. The previously improved FT reaction rate is therefore further modified to include the effect of coking on the CO conversion:

$$r_{FT} = \frac{(1 - e^{4.2 - \bar{d}_s}) \theta_*$$

The evolution of carbon-poisoned sites with time is given based on the correlations presented in Chapter 3. Note that as the coking activation energy is relatively high (150 kJ/mol) its contribution to deactivation is negligible at typical FT temperature of 493 K.

However once exposed to high temperatures, it leads to a rapid total deactivation of the catalyst.

Eq. 4.10 is the most complete form of intrinsic FT kinetic expression which could be used independent of the choice of the reactor configuration.

Although the application of Eq. 4.10 in the case of experimental capillary reactor is found to bring about some improvements, the difference with the simple form of Eq. 4.6 is not significant especially in the current set of operating conditions. Consequently, we will see better the effect of such improvements in the milli-fixed bed reactor set up

4.4.2. Milli-fixed bed reactor model with hot and cold condensers

The milli-fixed bed reactor (details given in Chapter 2) is used in the UCCS to study the performance of Co-based FT catalysts. It allows analyzing the effect of different operating parameters on the sintering severity. The full hydrocarbon distribution is measured with the GC while ex-situ XRD measurements were performed for both the fresh and used catalyst samples to follow the evolution of crystallite size after different working conditions.

One of the particularities of the milli-fixed bed reactor set-up is the existence of hot and cold condensers as explained in Chapter 2 and re-drawn again in Fig. 4.8. As a matter of fact, in contrary to the capillary reactor, the milli-fixed bed reactor is rarely used alone in experimental tests and in most cases the reactor effluents flow through the hot and cold condensers leading to some modifications in terms of reactor outlet composition. Consequently the experimental CO conversions measured through the integration of GC peaks are not the characteristics of the FT reactor only, but the total reactor+condensers assembly. Therefore the reactor model could not be simply applied in this case.

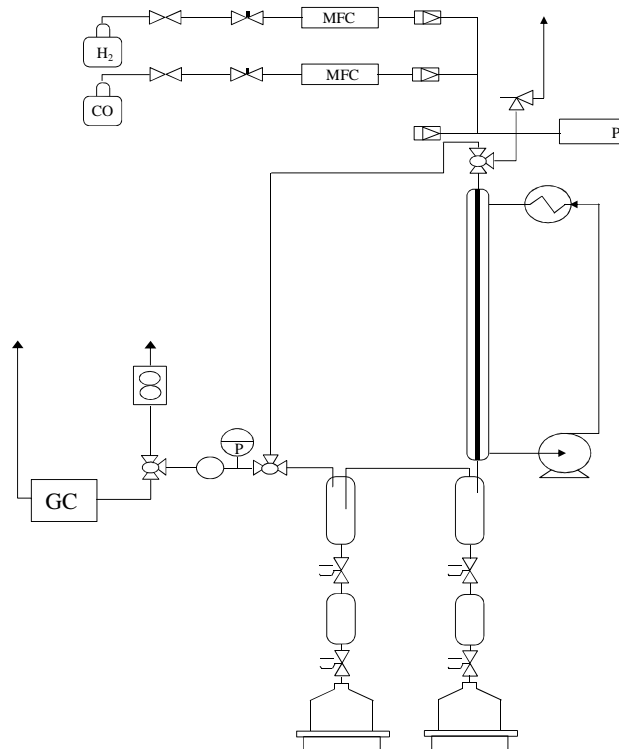


Figure 4.8 Scheme of experimental setup for FT synthesis in milli-fixed bed reactor (MFC = Mass flow controller; GC = gas chromatography; P = Pressure regulator)

It might be therefore necessary to recall some of the equations used in the “full profile” (i.e. reactor+condensers) modeling of milli-fixed bed reactor set-up. The full set of these equations is given in Chapter 2.

The reactor outlet composition is given by incorporating Eq. 4.10 in the reactor mass balance as follows:

$$\varepsilon \frac{\partial C_i}{\partial t} + \frac{\partial (C_i u)}{\partial z} - (1 - \varepsilon) \eta r_i \rho_{cat} = 0 \quad (4.11)$$

The reactor outlet compositions are then inserted into the overall mass balance of hot condenser in order to yield the gas composition at its outlet:

$$\frac{dn_{H \text{ condenser}}^G}{dt} = G_{reactor} y_{i, reactor} - G y_{H \text{ condenser}} \quad (4.12)$$

The final composition of the gas mixture is then obtained through the application of cold condenser overall mass balance:

$$\frac{dn_{C \text{ condenser}}^G}{dt} = G_{H \text{ condenser}} y_{i, H \text{ condenser}} - G y_{C \text{ condenser}} \quad (4.13)$$

We have studied both the effect of syngas ratio (section 4.4.2.1) and the temperature (section 4.4.2.3) on the rate of sintering and on the catalyst deactivation behavior.

4.4.2.1. Milli-fixed bed reactor tests under different syngas ratios

In order to study the effect of syngas ratios, experimental runs were conducted at three different syngas ratios in a laboratory milli-fixed bed reactor. We have use a non-diluted catalyst configuration already described in Chapter 2. The operating conditions are as follows: catalyst loading = 0.3 g, gas flow rate = 33 Nml/min ($H_2/CO = 1$), 66 Nml/min ($H_2/CO = 2$), 132 Nml/min ($H_2/CO = 4$); $T = 220\text{ }^\circ\text{C}$, $P = 20\text{ bar g}$.

Fig. 4.9 demonstrates the experimental CO conversion and methane selectivity with time for the three different syngas ratios. Although the GHSV was adjusted to obtain (almost) similar CO conversion level, higher H_2/CO ratio leads to higher initial catalytic activity, higher methane selectivity and also higher deactivation rate.

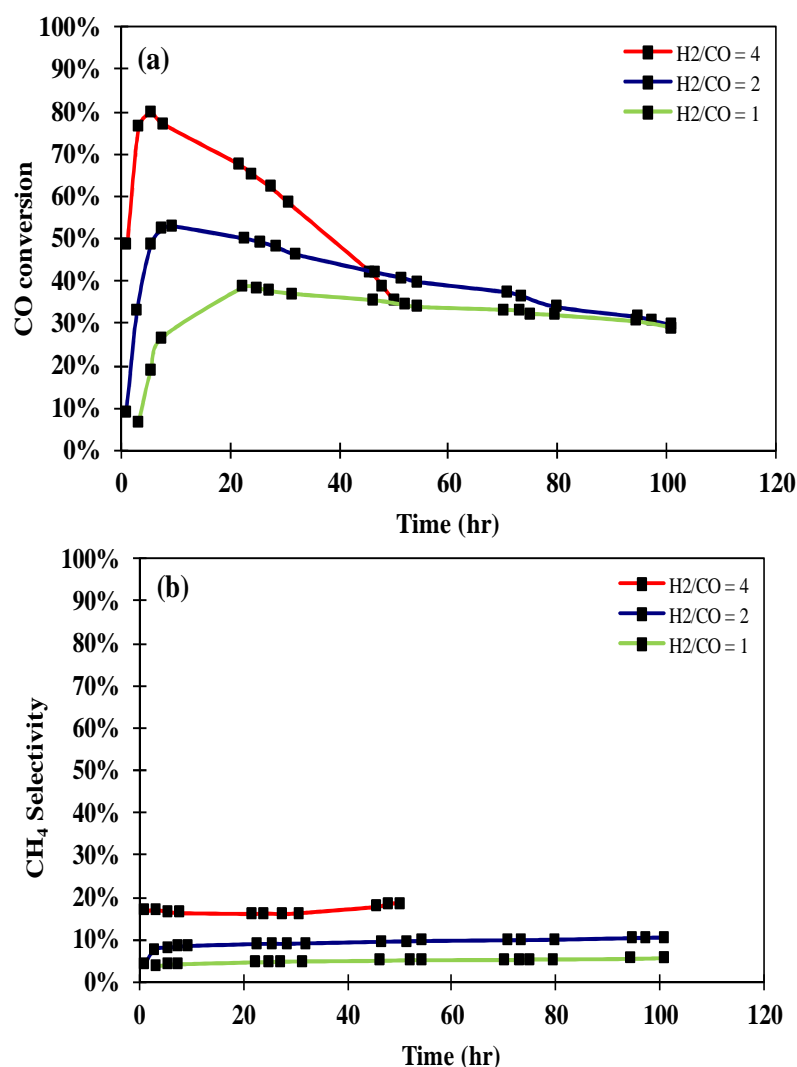
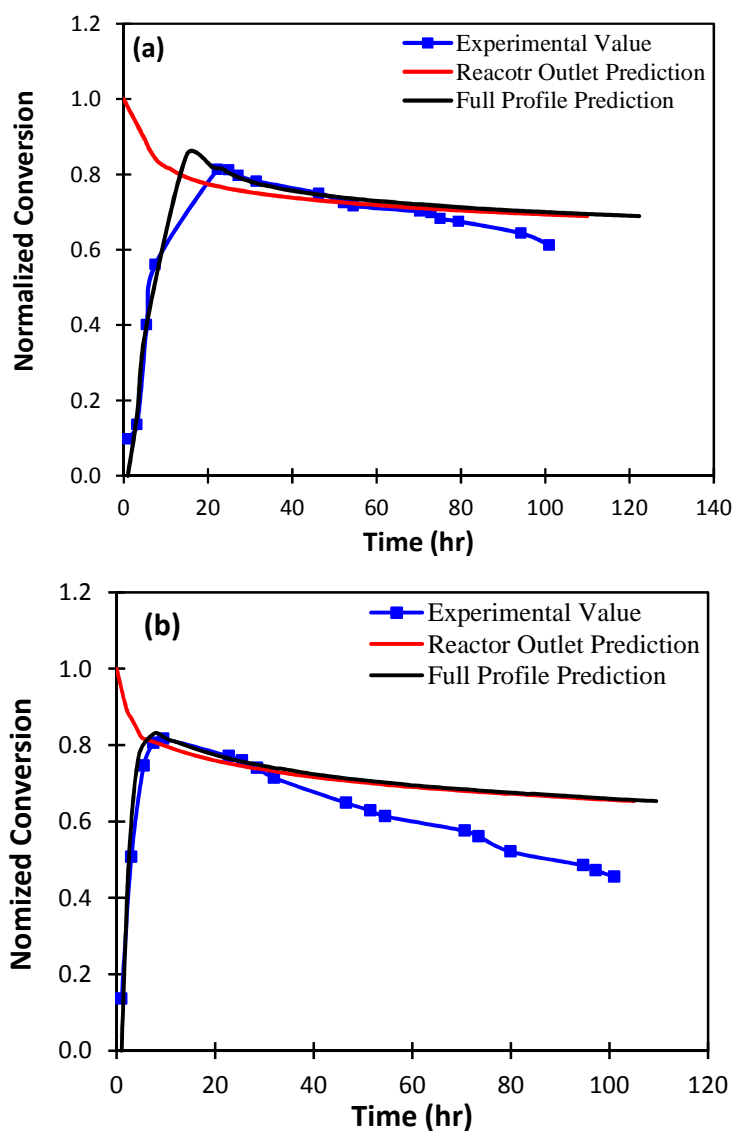


Figure 4.9 Experimental CO conversion (a) and methane selectivity (b) profiles of reference catalyst during FT synthesis: (i) $H_2/CO = 1$, $GHSV = 1.55 \times 10^6$ Nml/(mol_{Cobalt} · h⁻¹), (ii) $H_2/CO = 2$, $GHSV = 3.1 \times 10^6$ Nml/(mol_{Cobalt} · h⁻¹), (iii) $H_2/CO = 4$, $GHSV = 6.2 \times 10^6$ Nml/(mol_{Cobalt} · h⁻¹) - (milli-fixed bed reactor, $T = 493\text{ K}$, $P = 20\text{ bar}$)

As already explained in Chapter 2, the increase in the activity during the initial period seen by the GC signals is believed to be an experimental artifact due to the residence time distribution of the hot and cold condensers, and consequently it is not of kinetic/deactivation significance. Simultaneous analysis of the hydrodynamics of millimetric reactor system with condensers and sintering kinetics indicate that major modifications of catalysts structure occur during the initial period of the reaction when the apparent carbon monoxide conversion increases. .

Fig. 4.10 shows the experimental and calculated evolution of relative CO conversion with time under three different syngas ratios for the experimental milli-fixed bed configuration. Both the CO conversion at the outlet of FT reactors and at the input to the GC are shown in order to provide quantitative analysis of the model.



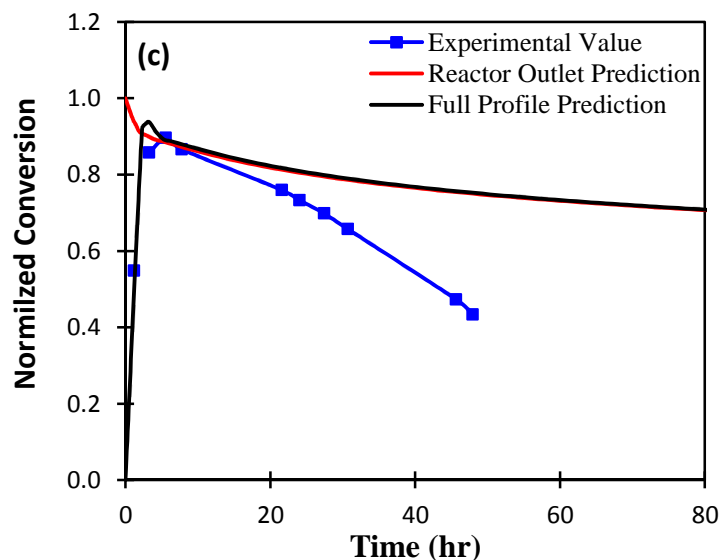


Figure 4.10 Experimental and calculated CO conversion profile of reference catalyst during FT synthesis using the improved model (milli-fixed bed reactor, reference catalyst, $T = 493\text{ K}$, $P = 20\text{ bar}$): (a) $\text{H}_2/\text{CO} = 1$, $\text{GHSV} = 1.55 \times 10^6\text{ Nml}/(\text{mol}_{\text{Cobalt}} \cdot \text{h}^{-1})$, (b) $\text{H}_2/\text{CO} = 2$, $\text{GHSV} = 3.1 \times 10^6\text{ Nml}/(\text{mol}_{\text{Cobalt}} \cdot \text{h}^{-1})$, (c) $\text{H}_2/\text{CO} = 4$, $\text{GHSV} = 6.2 \times 10^6\text{ Nml}/(\text{mol}_{\text{Cobalt}} \cdot \text{h}^{-1})$

The full profile model seems to give a realistic image of experimental CO conversion profile using syngas with lower H_2/CO ratio. As shown by Fig. 4.10 although it is not possible to testify by the experimental GC spectra, the catalyst is subject to more severe conditions inside the reactor itself. The initial reactor outlet conversion could be up to 20% more than the maximum activity seen by the experiment collected data point. This results in a much higher water partial pressure which leads to an easier crystallite growth. The higher crystallite growth rate leads to a much sharper activity reduction than what is observed by the GC data.

In addition, although the model is found to enhance the fit with the experimental data especially in the case of lower syngas ratios, higher ratios are found to deviate from the (full) model predictions. This is suggested to be due to the higher presence of water absolute partial pressure which could possibly lead to other mechanisms of irreversible catalyst deactivation.

Fig. 4.11 shows the calculated relative and absolute water partial pressures ($P_{\text{H}_2\text{O}}/P_{\text{H}_2}$ and $P_{\text{H}_2\text{O}}$) profiles for the three experimental cases. It is clear that in the low syngas ratio case of $\text{H}_2/\text{CO} = 1$, sintering could be considered as the main cause of deactivation as the $P_{\text{H}_2\text{O}}/P_{\text{H}_2}$ ratio is remarkably high. In the case of higher syngas ratios, the relative water partial pressure is not high enough to cause accelerate sintering and significant activity loss due to crystallite growth.

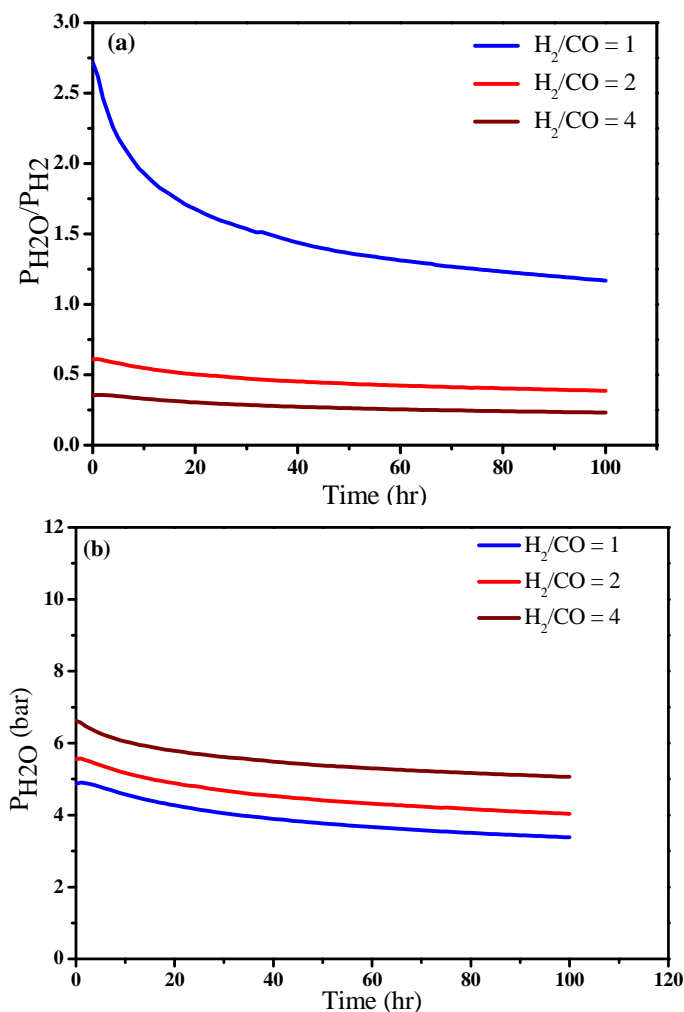


Figure 4.11 Calculated Relative (a) and absolute (b) partial pressures of water [at the reactor outlet] during FT synthesis in the milli-fixed bed reactor, reference catalyst, $T = 493$ K, $P = 20$ bar: (i) $H_2/CO = 1$, $GHSV = 1.55 \times 10^6$ $Nml/(mol_{Cobalt} \cdot h^{-1})$, (ii) $H_2/CO = 2$, $GHSV = 3.1 \times 10^6$ $Nml/(mol_{Cobalt} \cdot h^{-1})$, (iii) $H_2/CO = 4$, $GHSV = 6.2 \times 10^6$ $Nml/(mol_{Cobalt} \cdot h^{-1})$

Furthermore, the crystallite size profile evolution within the reactor was studied according to the full profile model. Fig. 4.12 shows the relative surface-average Co crystallite at three different times for the experimental case of $H_2/CO = 2$. Although the catalyst sample shows uniform particle size once put within the reactor ($t = 0$ hr), the average crystallite size deviates to larger values at the reactor outlet as the time on stream increases. The difference between the average crystallite diameter at the reactor entrance and outlet increases as the sintering proceeds more.

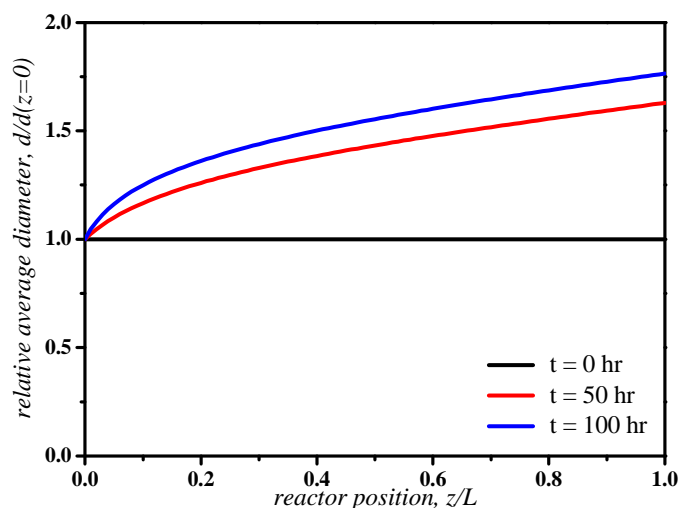


Figure 4.12 Evolution of relative surface-average crystallite diameter within the milli-fixed bed reactor during FT synthesis according to the improved model ($H_2/CO = 2$, $GHSV = 3.1 \times 10^6$ Nml/(mol_{Cobalt} · h⁻¹), $T = 493$ K, $P = 20$ bar, reference catalyst)

4.4.2.2. Milli-fixed bed reactor tests at higher temperatures

In order to accelerate sintering as well as other deactivation mechanisms, some experimental tests have been conducted at 240–280 °C using both diluted and non-diluted catalyst samples. The schematic view of both configurations is already given in Chapter 2. The operating conditions in both cases are as follows: catalyst loading = 0.05 g, gas flow rate = 65.8 Nml/min, $H_2/CO = 2$; $T = 240$ – 280 °C, $P = 20$ bar g.

Fig. 13 shows the experimental CO conversion as well as methane selectivity with time in three different temperatures in a non-diluted configuration. As expected high temperature regime has several parallel effects. First, as the Yates-Satterfield kinetic constants (k_a and k_b) are temperature-dependent, the initial activity (or CO conversion) is higher once operated at higher temperatures. The product selectivities are also affected including for example a higher methanation rate at higher temperatures. On the other side, sintering is suggested to be accelerated at high temperature as it is a thermochemical process. Consequently a sharper deactivation rate is observed. In addition, as the Fischer-Tropsch reaction is highly exothermic ($\Delta H_{rxn} = -165$ J/mol), high temperature may result in poor temperature control along the reactor. The poor heat transfer might result in local hotspots which could in turn increase the CO conversion to even 100%. This is also especially important as the initial real CO conversion is believed to be always higher than the maximum activity obtained from the experimental GC results.

The high initial conversion as well as rapid deactivation regime could be observed in Fig. 13. The methane selectivity is also quite high (70% compared to 20% at 220 °C) as methanation is accelerated in higher temperatures (Fig. 4.13).

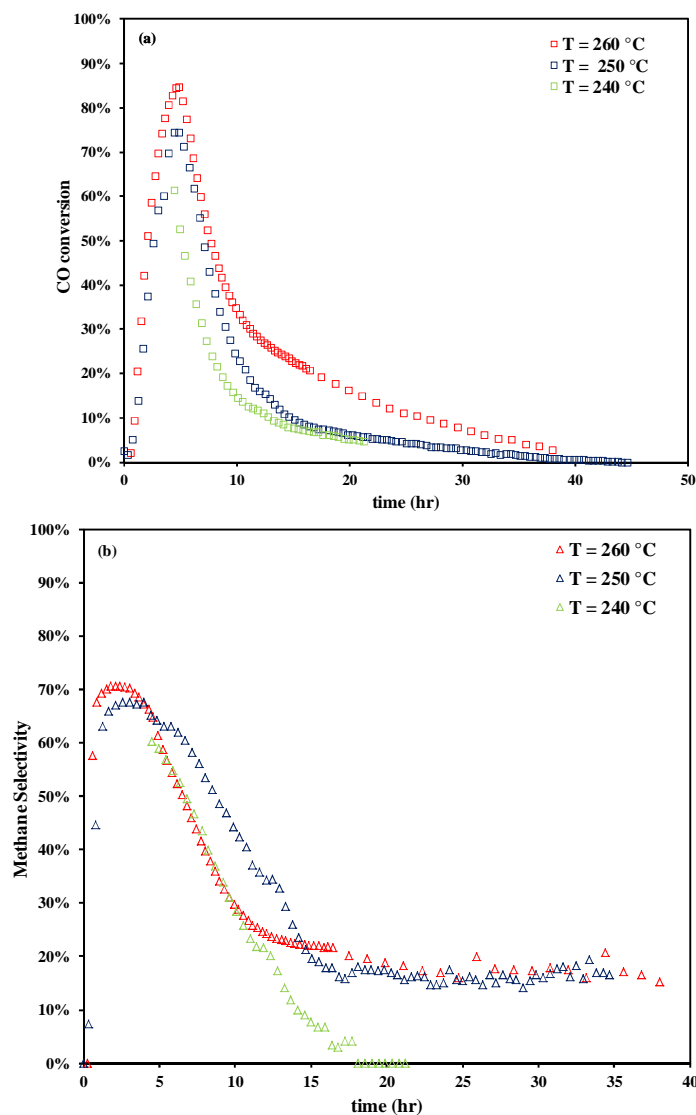


Figure 4.13 Experimental CO conversion (a) and methane selectivity (b) profiles of reference catalyst during FT synthesis as a function of time: millimetric fixed bed reactor, 0.05 g non-diluted reference catalyst, $H_2/CO = 2$, $P = 20$ bar, $GHSV = 1.9 \times 10^7$ $Nml/(mol_{Cobalt} \cdot h^{-1})$

The deactivation regime observed at high temperature suggests a contribution of two different deactivation mechanisms: an initial rapid deactivation followed by a long-term slow deactivation. Surprisingly the CO conversion approaches zero after 2 days on stream, the result which has been reproduced in several tests.

The use of a simple sintering mechanism therefore might not be appropriate to study deactivation in this case, as other mechanisms contribute to activity reduction as well. Consequently the complete form of FT reaction rate proposed by Eq. 4.10 is used which includes coking as the main phenomena for long-term catalyst deactivation.

4.4.2.2.1. Milli-fixed bed reactor model with coking

As already stated, the catalyst deactivation in higher temperatures seems to be a complex multi-phenomenon process which could not be only described by sintering. However as the appropriate in-situ characterization techniques are not yet commercially available in long-term, the use of a full mechanistic approach is not possible. Consequently a semi-mechanistic approach which could still fit the experimental data in long-term is employed as described in Chapter 3. The coking is proposed as the main cause of long-term deactivation and the evolution of carbon-poisoned sites with time is given. Eq. 4.10 is therefore used for the evolution of catalyst activity with time which includes both sintering and coke formation on the catalyst surface.

Fig. 4.14-4.15 show the calculated and experimental CO conversion profile in a milli-fixed bed reactor at 260 °C and 240 °C respectively using Eq. 4.10 as the CO consumption rate. Clearly, the sintering mechanism could not predict all the activity loss occurred in high temperature tests. However the coupled sintering-coking model results provide an acceptable fit with the experimental results.

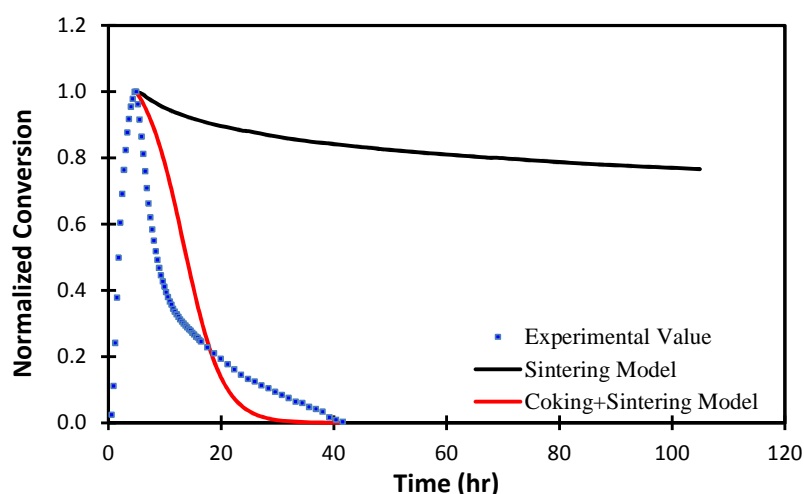


Figure 4.14 Experimental and simulated profile of normalized CO rate for reference catalyst during FT synthesis using the deactivating model including coking: milli-fixed bed reactor, reference catalyst, $H_2/CO = 2$, $GHSV=1.9 \times 10^7 \text{ Nm}^3/(\text{mol}_{\text{Cobalt}} \cdot \text{h}^{-1})$, $T = 260^\circ\text{C}$, $P = 20 \text{ bar}$

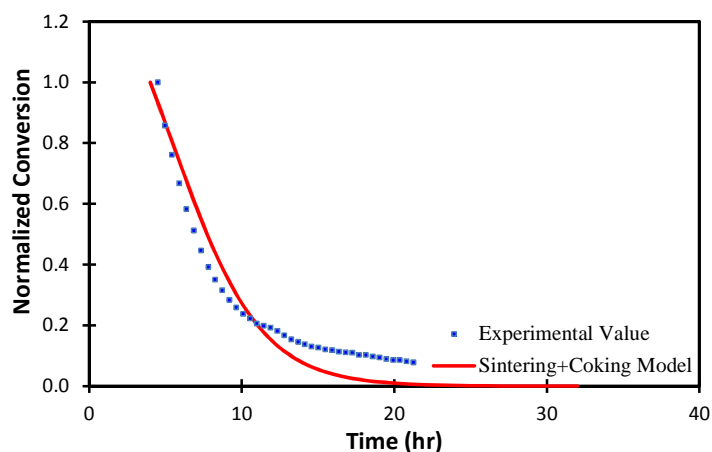


Fig. 4.15 Experimental and simulated CO conversion profile of reference catalyst during FT synthesis using the deactivating model including coking: milli-fixed bed reactor, reference catalyst, $H_2/CO = 2$, $GHSV=1.9 \times 10^7$ $Nml/(mol_{Cobalt} \cdot h^{-1})$, $T = 240^\circ C$, $P = 20$ bar

The calculated fraction of active sites on the catalyst surface is also found to decline to zero in 30-40 hours for both tests according to Fig. 4.16-4.17.

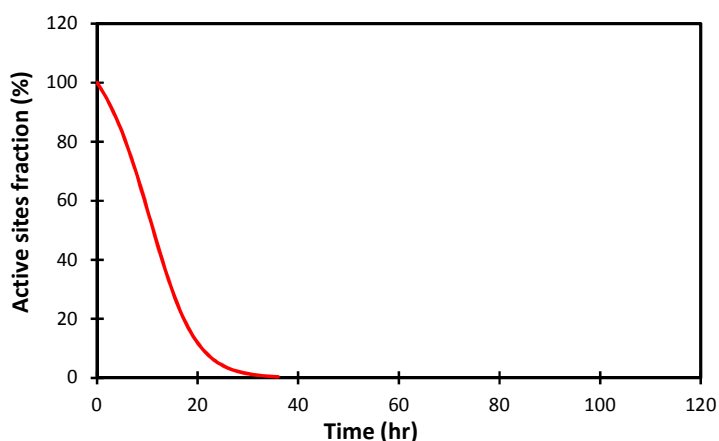


Fig. 4.16 Simulated profile of active site fraction on the reference catalyst during FT synthesis using the deactivating model including coking: milli-fixed bed reactor, $H_2/CO = 2$, $GHSV=1.9 \times 10^7$ $Nml/(mol_{Cobalt} \cdot h^{-1})$, $T = 260^\circ C$, $P = 20$ bar

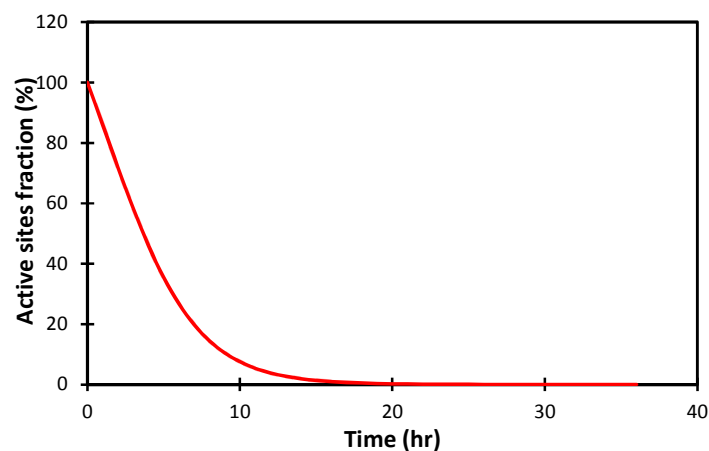


Fig. 4.17 Simulated profile of active site fraction on the reference catalyst during FT synthesis using the deactivating model including coking: milli-fixed bed reactor, $H_2/CO = 2$, $GHSV=1.9 \times 10^7$ $Nml/(mol_{Cobalt} \cdot h^{-1})$, $T = 240^\circ C$, $P = 20$ bar

4.5. Concluding remarks

Cobalt sintering of supported cobalt catalysts during FT reaction in the fixed bed reactor can be quantitatively described using a model which involves surface oxidation and diffusion of superficially oxidized cobalt nanoparticles. The model is applied within two laboratory scale fixed bed reactors.

The sintering model was used in order to study the effect of operating condition in a systematic way. The syngas ratio, syngas dilution, and water addition were changed in either constant initial conversion or gas space hourly velocity (GHSV). The kinetics of sintering is driven by a higher $P_{\text{H}_2\text{O}}/P_{\text{H}_2}$ ratio and consequently the sintering is accelerated if the operating conditions lead to higher water to hydrogen pressure ratio. The syngas ratio was found to be dominant in this case as a higher ratio of $\text{H}_2/\text{CO} = 4$ leads to the highest $P_{\text{H}_2\text{O}}/P_{\text{H}_2}$ possible and therefore the most severe activity loss in the case of different syngas ratios with the same space velocities. However, once syngas with different H_2/CO ratios are injected to the reactor at the same initial conversion of 58%, the syngas with a lower ratio of $\text{H}_2/\text{CO} = 1.5$ was found to be most affected by sintering as the water relative partial pressure is found to be at least 3 times higher in this case than in the case of higher syngas ratios. Water addition to the syngas has a significant effect on the sintering rate. The accelerated rate of sintering depends on the water content in the syngas. In constant initial conversion, a water co-fed syngas with a ratio of $\text{H}_2\text{O}/\text{H}_2/\text{CO} = 6/2/1$ leads to 67% crystallite size increase as well a 60% activity decreases in less than 400 min on stream in a capillary fixed bed reactor. This phenomenon could be also attributed to the higher $P_{\text{H}_2\text{O}}/P_{\text{H}_2}$ in this case as the co-fed water increases the water partial pressure inside the reactor. The addition of inert gas in the syngas, on the contrary, does not affect the sintering as it does not change the water relative partial pressure even added in high contents.

Once the effect of operating conditions on the sintering model is studied, the model is used to study deactivation in experimental reactors. The capillary fixed bed reactor is an ideal choice for analyzing the suitability of the model for the prediction of crystallite sizes with time on stream as it allows following the particle size evolution using in-situ XRD characterizations. The set-up also does not contain condensers and therefore the experimental results are the direct measures of catalytic activity at the reactor outlet. The CO conversion profile could be then correlated with the crystallite growth. The developed reactor model is thus been first applied to the capillary reactor. It was found that the model is able to give a correct image of particle size evolution and an estimated sintering constant. This is followed

by a realistic representation of CO activity loss during the first 100 minutes on stream which is well attributed to sintering. The model then deviates from the experimental results as other deactivation mechanisms are suggested to interfere. Consequently the catalyst coking is added to the model as the main cause of long-term deactivation. A new form of rate constant which depends on the crystallite size is also inserted in the model to account for the change in the average crystallite size.

The millimetric fixed bed reactor is then studied as it gives a wider window of operating conditions which could affect the initial and eventually the long-term deactivation behavior of cobalt catalysts in typical FT conditions.

However as the laboratory millimetric set-up includes the hot and cold condensers downstream of the FT reactor, the simple reactor model could not be used to describe the experimental results. As a matter of fact, the output signals measured by the GC are a combination of the reactor and condensers and therefore could not be considered as the real representation of the reactor performance. Consequently the hot and cold condensers should be added to the reactor model in order to obtain the “full profile” model results which could be compared with the experimental GC data.

Once the full profile model is developed, it is used to study the effect of operating conditions on the milli-fixed bed set-up. The syngas ratio and the reactor temperature are found to be the most sensible parameters which could affect the catalyst deactivation. Once operated in 220°C and different syngas ratios, the sintering model could be used to generate a realistic CO activity loss. The difference between the initial conversion at the reactor outlet and the apparent maximum conversion is found to be 20% in the case of low syngas ratios.

Experimental tests were then conducted at higher reactor temperature using a typical syngas ratio of 2. Although the catalyst mass is divided by a factor 6, the initial CO conversion was found to be surprisingly high when compared to tests at typical LTFT temperature ($T = 220^{\circ}\text{C}$). The high initial conversion was followed by a two-step deactivation regime and an activity reduction to zero in two days on stream was observed. This was suggested to be caused by a both higher sintering rate and a carbon deposition in high temperatures. Consequently the carbon poisoning (coking) mechanism previously developed was used to correct the FT reaction rate. It was found that once the sintering is coupled with coking, the full activity loss could be simulated in high temperature Fischer-Tropsch conditions.

4.6. References

- [1] J. Anfray, Acquisition de données pour la modélisation d'une colonne à bulles Fischer-Tropsch, in, University of Lyon, 2005.
- [2] O. Levenspiel, Chemical Reaction Engineering, 3rd Edition ed., Wiley, New York, 1999.
- [3] J.B. Butt, Catalyst Poisoning and Chemical Process Dynamics, in: B. Delmon, G.F. Froment (Eds.) Studies in Surface Science and Catalysis, Elsevier, 1980, pp. 21-41.
- [4] J.B. Butt, Catalyst poisoning and chemical process dynamics, in: J.L. Figueiredo (Ed.) Progress in Catalyst Deactivation, Nijhoff, Boston, 1982, pp. 153-208.
- [5] J.B. Butt, Catalyst deactivation: How we cannot yet subvert nature, in: C.H. Bartholomew, G.A. Fuentes (Eds.) Studies in Surface Science and Catalysis, Elsevier, 1997, pp. 69-86.
- [6] G.F. Froment, A Quantitative Approach of Catalyst Deactivation by Coke Formation, in: B. Delmon, G.F. Froment (Eds.) Studies in Surface Science and Catalysis, Elsevier, 1980, pp. 1-19.
- [7] H. Karaca, O.V. Safonova, S. Chambrey, P. Fongarland, P. Roussel, A. Griboval-Constant, M. Lacroix, A.Y. Khodakov, Structure and catalytic performance of Pt-promoted alumina-supported cobalt catalysts under realistic conditions of Fischer-Tropsch synthesis, *Journal of Catalysis*, 277 (2011) 14-26.
- [8] H. Karaca, J. Hong, P. Fongarland, P. Roussel, A. Griboval-Constant, M. Lacroix, K. Hortmann, O.V. Safonova, A.Y. Khodakov, In situ XRD investigation of the evolution of alumina-supported cobalt catalysts under realistic conditions of Fischer-Tropsch synthesis, *Chemical Communications*, 46 (2010) 788-790.
- [9] G.L. Bezemer, J.H. Bitter, H.P.C.E. Kuipers, H. Oosterbeek, J.E. Holewijn, X. Xu, F. Kapteijn, A.J. van Dillen, K.P. de Jong, Cobalt Particle Size Effects in the Fischer-Tropsch Reaction Studied with Carbon Nanofiber Supported Catalysts, *Journal of the American Chemical Society*, 128 (2006) 3956-3964.

CHAPTER

5

DEACTIVATION IN SLURRY REACTORS

5.1. Introduction

As already described in chapter 1, the slurry reactor is believed to be an optimum choice for the Fischer-Tropsch synthesis as it provides a better gas-liquid-solid mixing and an efficient heat transfer. However the use of slurry reactors is justified once a full catalyst reduction step as well as an efficient wax/catalysts separation are possible, as these factors could largely affect the FTS conversion and performance.

This chapter deals with the deactivation in slurry reactors. An attempt is made to find how the deactivation could be different in slurry and fixed bed reactors. The microscopic models are incorporated in the reactor model (described in Chapter 2) to enable us to follow the change in the carbon monoxide conversion with time. The sintering is the main deactivation mechanism considered in this study.

Similar to Chapter 4, the methodology starts with a quantitative analysis of the effect of the operating conditions on the deactivation rate in slurry reactors. In the lack of existing experimental runs that use the same reference catalyst previously employed in fixed bed reactor, a set of reactor simulations has been done. These “purely imaginary simulation runs” use the same reference catalyst with 25% cobalt loading that has been used in fixed bed reactors of Chapter 4. This helps to take the sintering constant for these runs the same as the one used in the case of fixed bed reactor (corrected by the effect of solubility in the liquid phase). The same approach is used for FT kinetic terms. Consequently only the reactor geometry is the parameter that has been changed, whereas the catalyst properties are kept the same. The list of kinetic and deactivation constants for this study is given in Table 5.1.

The final objective of such a methodology is to compare the behavior of the same catalyst in both fixed bed and slurry reactors in a systematic way. In addition, it could give the sensible parameters for the catalyst deactivation in slurry reactor as it was the case in Chapter 4.

The use of “simulated runs” allows identifying the sensible parameters on the rate of sintering as well a comprehensive comparison of deactivation behavior of the same catalyst in two reactors.

On the other hand for comparison of the modeling results with experimental data we used a commercial 15%Co/Al₂O₃ catalyst. A large number of kinetic experiments were conducted for this catalyst in a slurry reactor. The kinetic constants were extracted for this catalyst via fitting the kinetic and deactivation models with the experimental results. Again, the set of these constants is given in Table 5.1.

Finally a set of simulations are performed in order to investigate the difference in the deactivation behavior of fixed bed and slurry reactors. The results are given in Appendix C.

5.2. Effect of operating conditions on slurry reactor model

In order to study the effect of operating conditions, the slurry reactor model described in Chapter 2 is used. Sintering is considered as the main cause of initial deactivation. As the surface oxidation reaction which determines the rate of crystallite growth occurs in the liquid-solid interface in this case, Eq. 3.45 is used, re-written here as:

$$\frac{d\bar{d}_s}{dt} = k_s^L \frac{C_{H_2O}^L}{C_{H_2}^L} \cdot \frac{1}{\bar{d}_s^6} \quad (5.1)$$

where $C_{H_2O}^L$ and $C_{H_2}^L$ represent the water and hydrogen concentrations in the liquid phase, respectively.

As already stated in the introduction, this section gives only a simulation study of the sensibility analysis of the operating condition on the sintering rate. Consequently no experimental data is used in this part and only “pure simulation runs” are considered. The same reference catalyst used in fixed bed reactor is assumed for simulation with 25% cobalt loading. The further details of the reference catalysts are given in Table 2.2.

A sintering constant value similar to the one used in the case of the fixed bed reactors ($k_s = 0.416 \text{ nm}^6/\text{s}$) is therefore used which is corrected by the gas-liquid concentration coefficients. The value for the sintering constant of reference catalyst in slurry reactors (k_s^L) is thus given by:

$$k_s^L = k_s \frac{H_{H_2O}}{H_{H_2}} \quad (5.2)$$

where H_{H_2O} and H_{H_2} represent the Henry's coefficients with the dimensions of pressure divided by concentration for water and hydrogen respectively. The value for the ratio H_{H_2O}/H_{H_2} in the typical FT wax produced at $H_2/CO = 2$, $T = 220^\circ\text{C}$, $P = 20 \text{ bar}$ is calculated as 0.114. The details of such a calculation are given in section 2.4.3.1.

In addition to the sintering constant, the kinetic constants are also similar to the values used in the fixed bed reactor, corrected by the concentration and Henry's constants in the liquid phase. In this way the effect of reactor geometry on the rate of sintering is studied,

using similar set of kinetic and deactivation constants. In addition, the sintering constant for the fixed bed reactor has been determined (using operando XRD techniques). This constant could be used to study the effect of operating conditions on sintering in slurry reactor. The kinetic constants which will be used in the deactivation model which involves coking are also shown in Table 5.1

Table 5.1 List of kinetic and deactivation parameters used for slurry reactor

Description		Catalyst used	$k_{a,0}^L$ ($\text{m}^6/\text{kg}_{\text{Co}}\cdot\text{s}\cdot\text{mol}$)	k_b^L (m^3/mol)	k_S^L (nm^6/s)	k'_{CF} ($\text{m}^3/\text{mol}\cdot\text{hr}$)
Simulated runs		Reference 25%Co/Al ₂ O ₃	1.10×10^{-7}	1,475	0.047	---
Model validation with experimental runs	Set 1 sintering model	Industrial 15%Co/Al ₂ O ₃	3.46×10^{-7}	0.14185	0.047	---
	Set 2 sintering model	Industrial 15%Co/Al ₂ O ₃	3.46×10^{-7}	0.14185	0.19	---
	Set 1 sintering model with coking	Industrial 15%Co/Al ₂ O ₃	3.46×10^{-7}	0.14185	0.047	5×10^{-5}

The reactor geometry used to study the effect of operating conditions by simulation, has the following dimensions: inner diameter = 46 mm, total volume = 300 mL. As we are interested to compare the reactor performance at different operating conditions, the hot and cold condensers are not included in this part. The contribution of the condensers to the apparent CO conversion (detected by the GC) is found to be small in slurry set-up due to the comparable volumes of reactor and condensers (see Chapter 2).

The reactor is initially filled with 45 g of SX70, a long hydrocarbon cut of FT synthesis with a molecular weight of 464 g/mol. 5 g of reference 25%Co/Al₂O₃ catalyst with an initial Co crystallite size of 5.96 nm is then loaded into the reactor. Pure syngas with a molar flow rate of 210 Nml/min is fed into the reactor. The reactor is assumed to work at a constant temperature and pressure of 493 K and 20 bar respectively.

The proposed form of the FT kinetic rate which includes the crystallite growth as the main source of activity reduction is used. The reaction rate is expressed in terms of the reactant concentrations in the liquid phase and mean crystallite diameter as:

$$r_{FT} = \frac{(1 - e^{-4.2 - \bar{d}_s})}{\bar{d}_s} \frac{k_{a,0}^L C_{CO}^L C_{H_2}^L}{(1 + k_b^L C_{CO}^L)^2} \quad (5.3)$$

The FT reaction rate is then inserted in the “reactor model” presented in Chapter 2 where the change in the liquid and gas composition inside the CSTR is found by solving the ordinary differential equations of mass balance in line with the vapor-liquid equilibria and the geometrical limitation condition (Eq. 2.36-2.39).

Once the reactor model is developed, it is used to study the effect of operating conditions on the catalyst activity profile once exposed to the syngas. Similar to the fixed bed reactors, the syngas ratio and the presence of co-fed water seem to influence the (initial) catalyst deactivation.

5.2.1. Syngas ratio

As the syngas ratio plays an important role in the catalyst deactivation, the H₂/CO ratio is changed in both constant initial conversion (iso-conversion) and constant gas flow rate (iso-GHSV) in order to evaluate the sintering rate in both cases.

Fig. 5.1 shows the evolution of mean crystallite size as well as normalized CO conversion for three different syngas ratios (H₂/CO = 1.5 - 4) adjusted in a way to give an initial CO conversion of 60% at time $t = 0$. The results are in line with the study performed by Saib et al [1] where the sintering is shown to last up to ~5 days on stream in slurry reactors. The characteristic sintering time is thus much longer than in the case of fixed bed reactors.

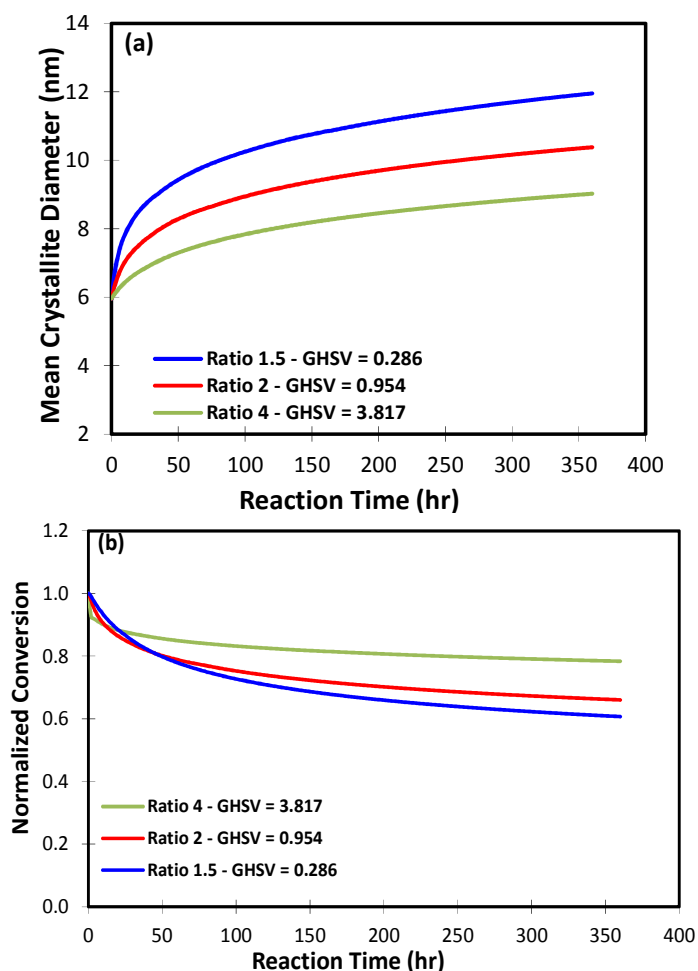


Figure 5.1 Effect of H₂/CO syngas ratio on evolution of surface-average particle diameter (a), and relative CO conversion (b) with time at iso-conversion in a completely stirred tank reactor (CSTR) (reference catalyst, T = 493 K, P = 20 bar, initial CO conversion = 60 %, GHSV in: Nm³ kg_{cat}⁻¹ h⁻¹)

Similar to the fixed bed reactors case, sintering is also more favorable for the low syngas ratios once operated at the same initial conversion, as in these conditions both the absolute and relative liquid water concentrations will be higher (Fig. 5.2) and consequently the sintering rate is increased. In addition, note that due to the uniform concentration inside the continuous stirred tank reactor (CSTR), there is no particle size profile within the reactor, and all the particles possess the same physico-chemical properties.

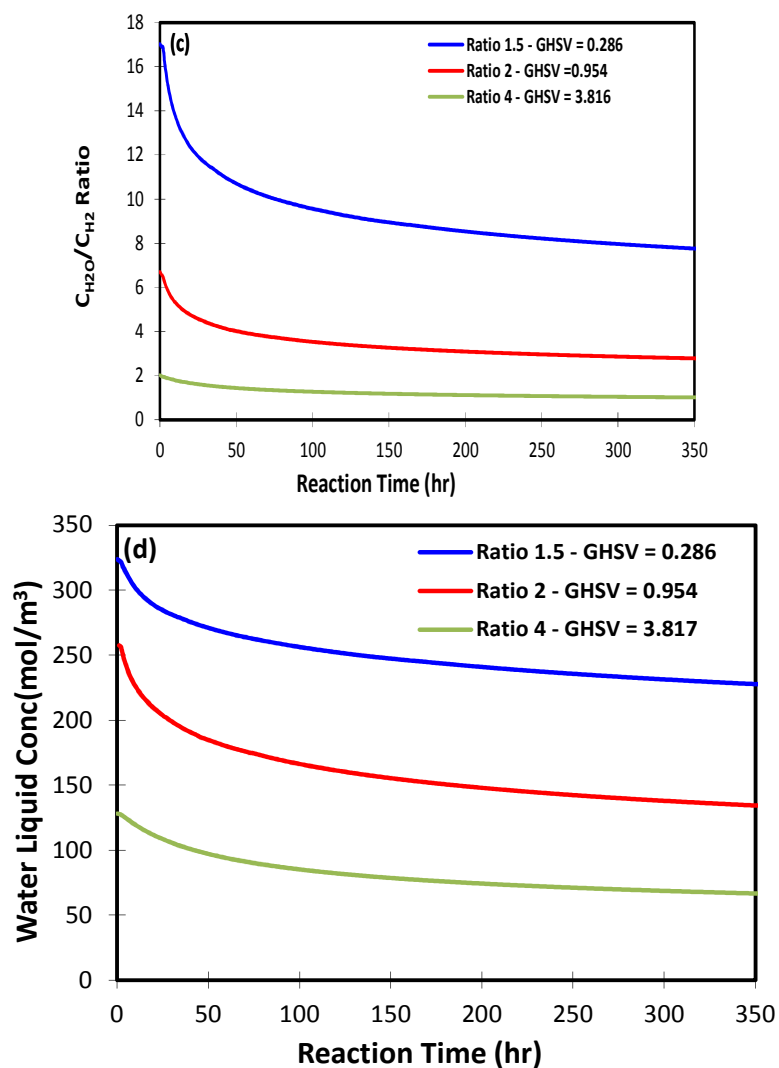


Figure 5.2 Effect of H₂/CO syngas ratio on evolution of water-to-hydrogen concentration in the liquid phase (c), and absolute water concentration in the liquid phase (d) with time at iso-conversion in a completely stirred tank reactor (CSTR) (reference catalyst, T = 493 K, P = 20 bar, initial CO conversion = 60 %, GHSV in: Nm³ kg_{cat}⁻¹ h⁻¹)

One could also consider the syngas streams with different H₂/CO ratios fed into the slurry reactor using the same GHSV, where we can observe that the sintering rate is higher for higher H₂/CO ratio in contrary to the previous case as shown in Fig. 5.3.

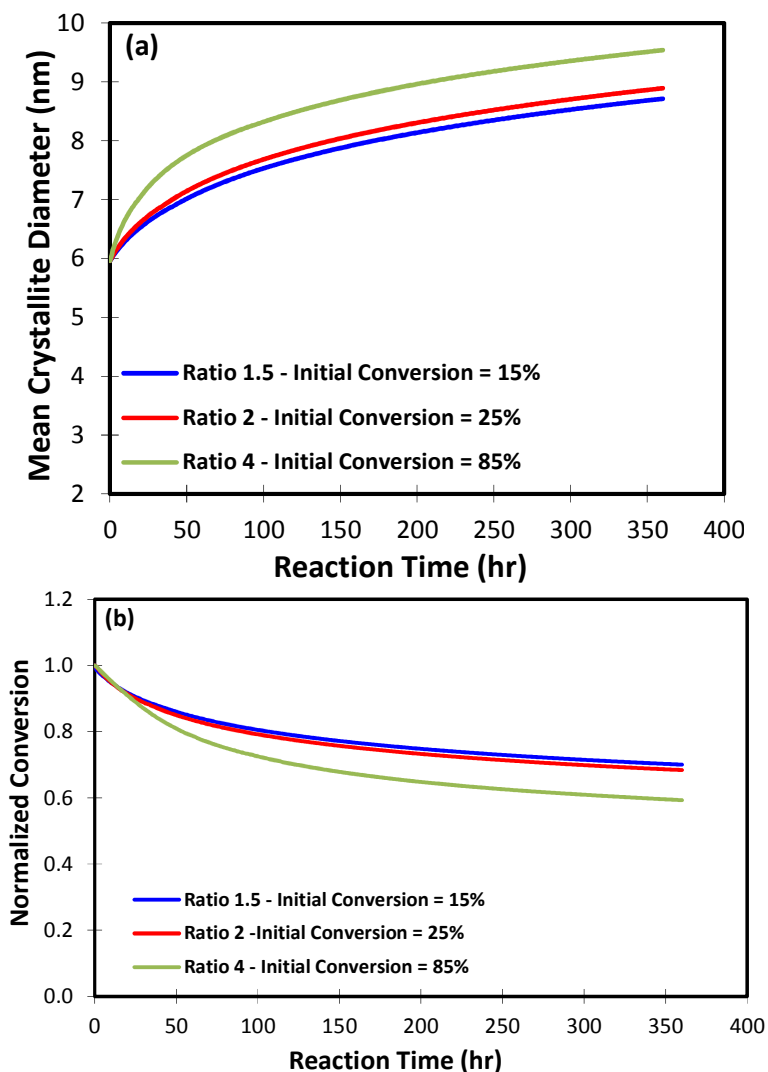


Figure 5.3 Effect of H₂/CO syngas ratio on evolution of surface-average particle diameter (a), and relative CO conversion (b) with time at iso-GHSV in a completely stirred tank reactor (CSTR) (reference catalyst, T = 493 K, P = 20 bar, GHSV = 2.76 Nm³ kg_{cat}⁻¹ h⁻¹)

This is in line with the results obtained for the fixed bed reactor at iso-GHSV conditions. Higher sintering rate is attributed to higher water-to-hydrogen concentration ratio in the liquid phase (Fig. 5.4). In addition, one could deduce that in a combined sintering effect, crystallite growth leads to a reduced activity and water production with time, which in turns slows down the crystallite growth. This effect combined with the higher diffusivity and surface energy of smaller crystallites leads to a sharp sintering rate at $t = 0$ which gradually approaches zero after ~5 days on stream.

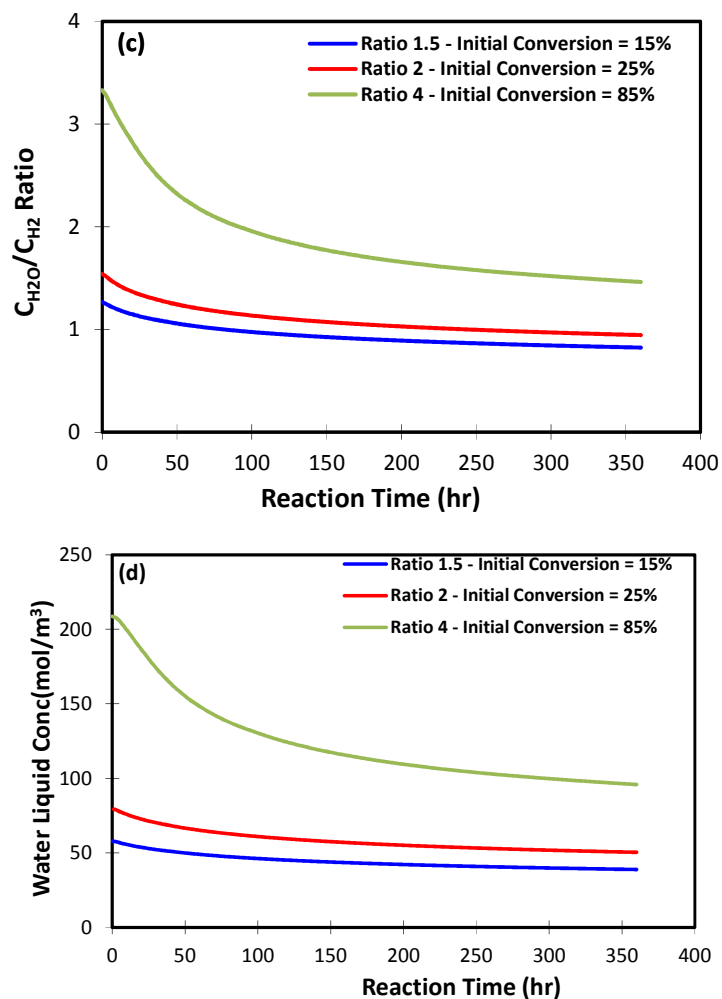


Figure 5.4 Effect of H₂/CO syngas ratio on evolution of water-to-hydrogen concentration in the liquid phase (a), and absolute water concentration in the liquid phase (b) with time at iso-GHSV in a completely stirred tank reactor (CSTR) (reference catalyst, T = 493 K, P = 20 bar, GHSV = 2.76 Nm³ kg_{cat}⁻¹ h⁻¹)

5.2.2. Co-fed water

The effect of co-fed water is also studied as the proposed sintering mechanism is assumed to be water-accelerated. Wet syngas is fed into the reactor by the ratio H₂O/H₂/CO = 1/2/1 and it is compared with the case where the dry syngas (H₂O/H₂/CO = 0/2/1) is used with the same total gas flow rate. It is observed that the initial CO conversion will be the same for both tests. However the wet FT test undergoes a sharper CO deactivation which is mainly due to larger Co crystallites formed (Fig. 5.5).

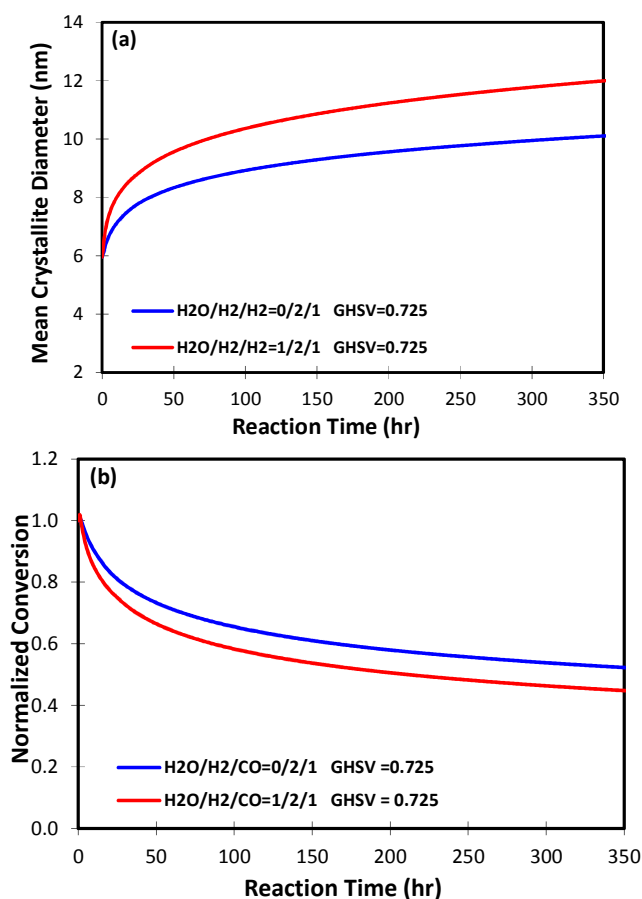


Figure 5.5 Effect of water co-feeding ratio on evolution of water-to-hydrogen concentration in the liquid phase (a), and absolute water concentration in the liquid phase (b) with time at iso-GHSV in a completely stirred tank reactor (CSTR) (reference catalyst, $T = 493$ K, $P = 20$ bar, initial CO conversion = 60 %, GHSV in: $\text{Nm}^3 \text{kg}_{\text{cat}}^{-1} \text{h}^{-1}$)

Obviously the co-fed water increases both the absolute and relative water concentrations within the reactor which enhance crystallite growth and sintering. We have found that the relative water concentration in the liquid phase could be more than three times higher when water is added in the syngas compared to the value calculated in the absence of co-fed water (Fig. 5.6). The absolute water concentration in the liquid phase could be also twice the value obtained in the case of dry syngas. These remarkably high concentrations of water inside the reactor are the main reason for 100% crystallite size increase (from 6 nm to 12 nm) when water is added in CO equimolar content (Fig. 5.5a).

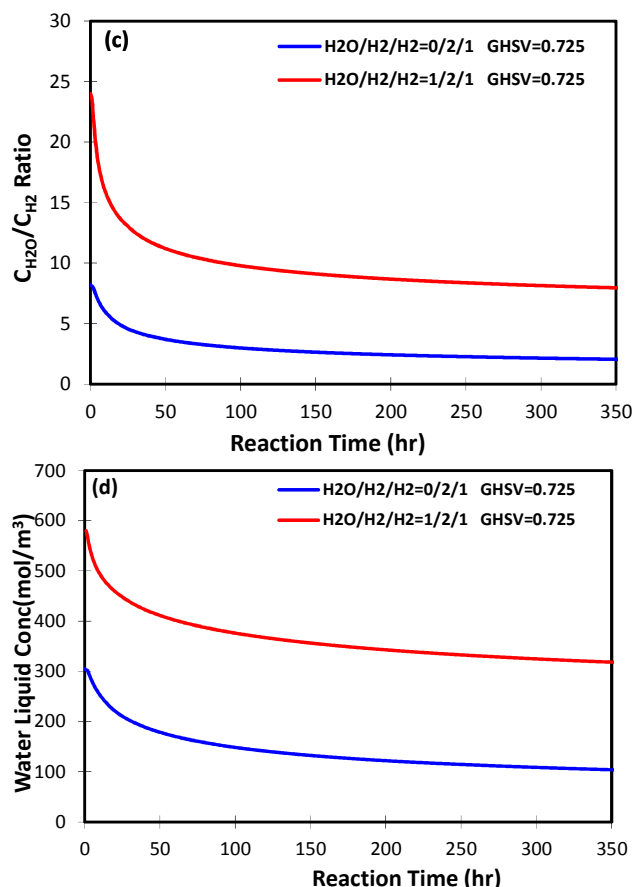


Figure 5.6 Effect of water co-feeding ratio on evolution of water-to-hydrogen concentration in the liquid phase (a), and absolute water concentration in the liquid phase (b) with time at iso-conversion in a completely stirred tank reactor (CSTR) (reference catalyst, $T = 493$ K, $P = 20$ bar, initial CO conversion = 60 %, GHSV in: $\text{Nm}^3 \text{kg}_{\text{cat}}^{-1} \text{h}^{-1}$)

5.3. Intermediate conclusions

In the previous section we have used the “pure simulation approach” to compare the deactivation behavior of reference 25%Co/Al₂O₃ catalyst in fixed bed and slurry reactor. Although the sintering time is found to be much longer in slurry reactor (~5 days in typical runs), the operating conditions are found to have similar effects on the catalyst deactivation behavior in both slurry and fixed-bed reactors. In addition sintering leads to much larger cobalt particles in slurry than in fixed bed reactors.

We speculate that this difference in sintering behavior of the same catalyst in two different reactor geometries could be due to three parallel effects: (a) in slurry reactor all the catalyst particles are subject to high conversions and high water fractions whereas the fixed bed reactor exhibits a concentration gradient with the average water concentration lower than the value in slurry reactor, (b) at comparable conditions, the H₂O/H₂ concentration ratio in the liquid phase is higher than in the gas phase due to the higher water solubility and (c) the sintering constant is corrected for the slurry reactors to account for VLE coefficients and

consequently a lower value is calculated compared to fixed bed reactor which could last in longer sintering period until a limiting particle size is reached. The list of sintering constants in fixed bed and slurry reactors is given in Table 5.2.

Table 5.2 List of sintering constants in fixed bed and slurry reactors

Description		Catalyst used	Sintering constant (nm ⁷ /s)	
Fixed bed reactor	Capillary reactor	Reference 25%Co/Al ₂ O ₃	0.416	
	Milli-fixed bed reactor	Reference 25%Co/Al ₂ O ₃	0.416	
Slurry reactor	Simulated runs		Reference 25%Co/Al ₂ O ₃	
	Model validation with experimental runs	Set 1 sintering model	Industrial 15%Co/Al ₂ O ₃	0.047
		Set 2 sintering model	Industrial 15%Co/Al ₂ O ₃	0.19
		Set 1 sintering model with coking	Industrial 15%Co/Al ₂ O ₃	0.047

Similar to the fixed bed reactor, sintering is also found to be accelerated at lower syngas ratios once operated at constant initial conversion, higher syngas ratios at constant GHSV, and in the presence of water in slurry reactor. All these conditions give a higher calculated value for H₂O/H₂ concentration ratio in the liquid phase and thus larger cobalt crystallites, which in turn lead to a higher deactivation rate.

5.4. Validation of existing experimental runs

The deactivation model developed in the preceding sections is also validated using experimental runs in slurry reactor conducted using a commercial 15%Co/Al₂O₃ catalyst. The kinetic constants were adjusted to fit the model with the experimental data (Table 5.1).

5.4.1. Continuous stirred tank (slurry) reactor

The developed reactor model is used to simulate the behavior of the experimental runs performed using an experimental laboratory-scale slurry reactor.

The details of the experimental set-up are provided in Chapter 2 which include a reactor geometry similar to the one presented in section 5.2. However note that the catalyst used in the experimental slurry reactor is different from the one used in fixed bed reactor. It

contains only 15% cobalt loading, whereas the reference catalyst used in fixed bed reactor contains 25% cobalt. The details of both catalysts are given in section 2.2.1.

As the catalysts are not the same in both reactors, their behavior to sintering could be also different and consequently different sintering constants might be necessary to model deactivation of the industrial catalyst in slurry reactor.

Consequently we have chosen to apply two sintering models in the validation stage, i.e. set 1 and set 2 models. The details of both models are given as follows.

A. Set 1 sintering model

In the set 1 model, it is assumed that the industrial catalyst used in “real experimental runs” shows the same sintering behavior as the reference catalyst used in “simulated runs” described in section 5.2. Consequently the same sintering constant is used. The kinetic terms are however optimized based on the initial experimental CO conversions. The list of deactivation and kinetic parameters used is given in Table 5.1.

B. Set 2 Sintering model

In the set 2 sintering model, the sintering constant is fitted so that it could predict all the activity reduction with only sintering. This corresponds to a value of sintering constant k_s^L equal to $0.19 \text{ nm}^6/\text{s}$, which is about 4 times higher than the value used in the set 1. Again the kinetic terms are optimized based on the initial experimental CO conversion, and therefore are identical to the values used in set 1 model. The full set of constants used for set 2 model is given in Table 5.1 as well.

Fig 5.7 shows a typical evolution curve of liquid mixture composition with time for the experimental runs. The model used for such a calculation is the set 2. We have simulated a reference experimental case where the industrial 15%Co/Al₂O₃ catalyst is exposed to a syngas ratio of H₂/CO = 2.6 at 493 K and 20 bar. In accordance with the simulation results reported by J. Anfray [2], we have found that the average carbon number is shifted from $n =$

33 to $n = 22$ after 15 days on stream. Further details of the assumptions and parameters used for the calculations are given in Chapter 2 (sections 2.4 and 2.5).

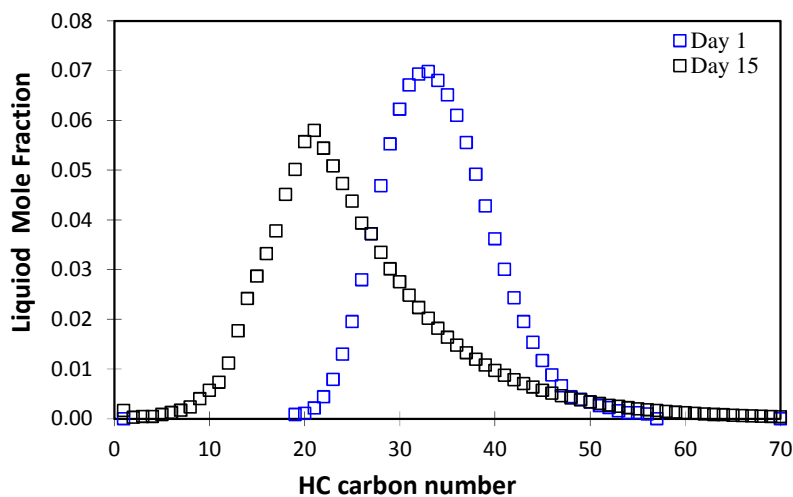


Figure 5.7 calculated evolution of liquid wax composition with time in a completely stirred tank reactor (CSTR) (15%Co/Al₂O₃ catalyst, T = 493 K, P = 20 bar, H₂/CO = 2.6, GHSV = 9.4×10⁵ Nml/(mol_{Cobalt}.h))

The following sections consider the change in the CO conversion with time once the catalyst is exposed to different operation conditions. The aim is to fit the model predictions with the experimental data in different reactor conditions.

5.4.1.1. Slurry reactor tests under different syngas ratios

In order to study the effect of syngas ratios, experimental runs were conducted at three different syngas ratios in a laboratory three-phase slurry reactor. The operating conditions are as follows: catalyst loading = 5 g, gas flow rate = 210 Nml/min, T = 220 °C, P = 20 bar g.

Fig. 5.8 demonstrates the experimental CO conversion with time for the three different syngas ratios. At the same GHSV, higher H₂/CO ratio leads to a higher initial catalytic activity, as well as a higher initial deactivation rate. This could be related to a higher water production rate in the case of H₂/CO = 4 which has a direct effect on the initial rate of catalyst deactivation (i.e. sintering).

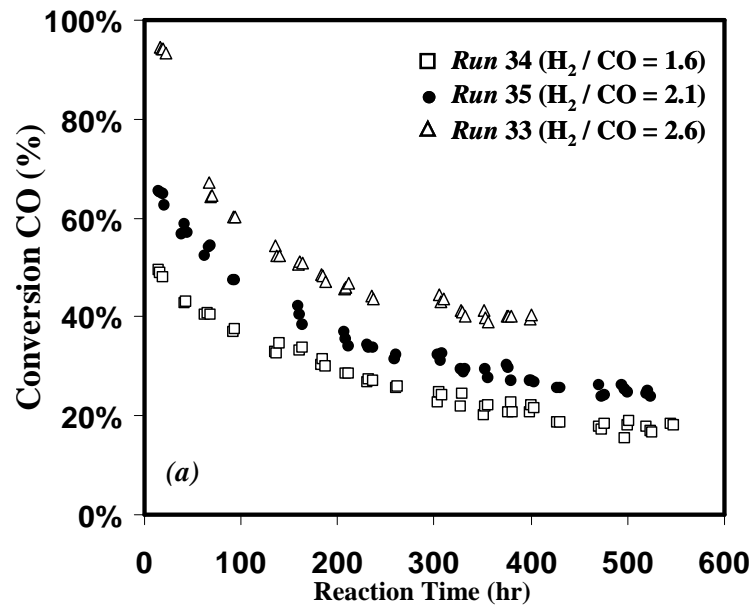
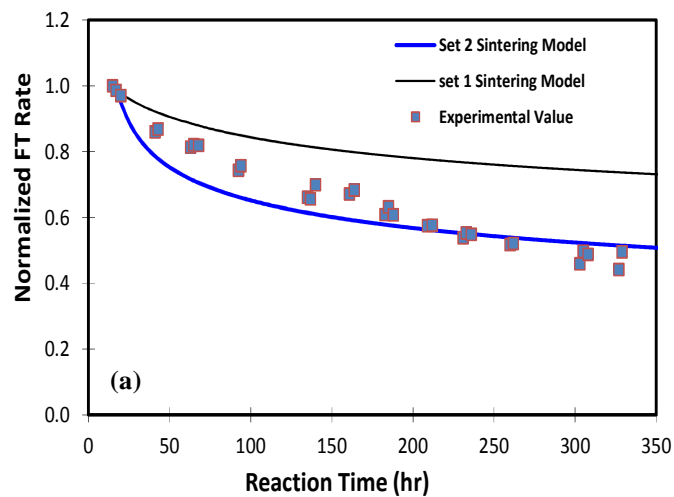


Figure 5.8 Effect of H_2/CO ratio on experimental catalyst activity in a completely stirred tank reactor (CSTR) (15%Co/ Al_2O_3 catalyst, $T = 493$ K, $P = 20$ bar, $GHSV = 9.4 \times 10^5$ Nml/(mol_{Cobalt}.h))

Fig. 5.9 shows the simulated and experimental values of catalyst activity for the three runs with different syngas ratios. Both the set 1 and set 2 models are used to compare the results.



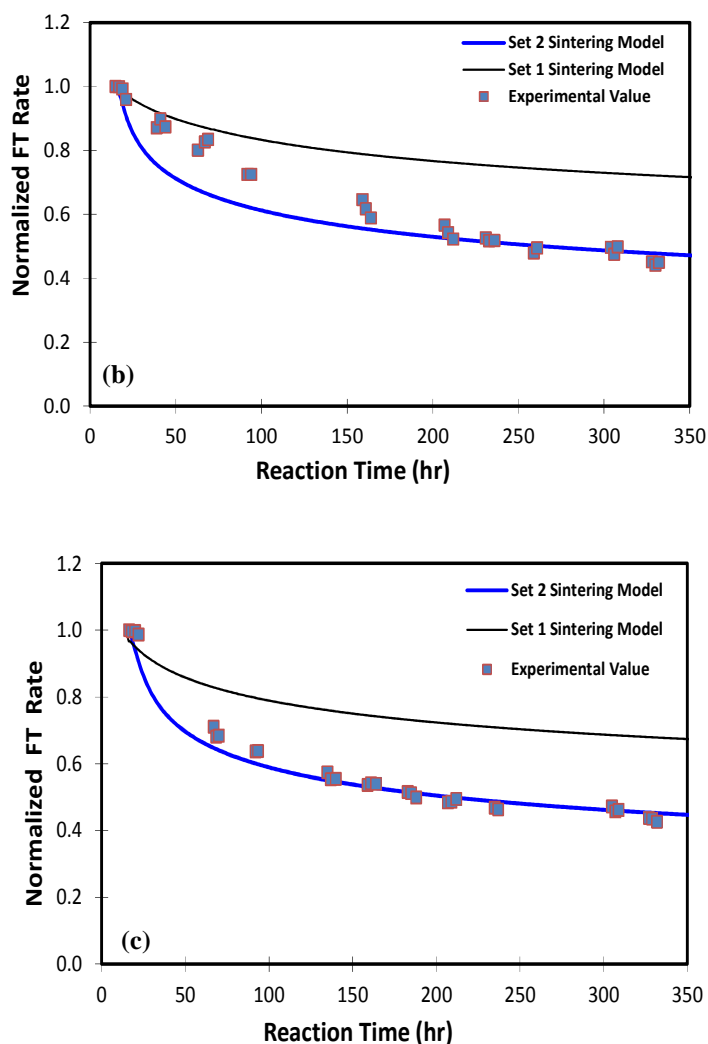


Figure 5.9 Effect of H_2/CO ratio on experimental and calculated FT reaction rate in the experimental slurry reactor (15%Co/ Al_2O_3 catalyst, $T = 493$ K, $P = 20$ bar, $GHSV = 9.4 \times 10^5$ $Nml/(mol_{Cobalt} \cdot h)$): (a) $H_2/CO = 1.6$, (b) $H_2/CO = 2.1$, and (c) $H_2/CO = 2.6$

As already predicted by the proposed sintering model, the initial deactivation slope is higher for the syngas ratio $H_2/CO = 2.6$ when the syngas flow rate is kept the same for all the ratios. However as discussed in section 5.2.1, the syngas ratio does not have a significant effect on the rate of sintering. Only 10-20% difference in the initial deactivation rate is observed when the syngas ratio is increased from 1.6 to 2.6. In addition, the set 2 sintering model is found to be able to predict the deactivation shape in a more realistic way whereas the set 1 sintering model could only predict 30-40% activity loss due to sintering. The use of set 2 sintering model is justified as the catalyst is used in the slurry reactor is different than the one used in fixed bed reactor and consequently the sintering constant should be different. As the sintering constant used in the set 2 model (for the industrial catalyst) is higher than the value used in the set 1 model (assuming the same constant as the reference catalyst), it is suggested

that the industrial 15% Co-based catalyst used in slurry reactor is more sensitive to sintering than the reference 25% Co-based catalyst used in fixed bed reactor.

5.4.1.2. Slurry reactor tests at different pressures

In order to study the effect of total pressure on the vapor-liquid equilibria which could affect the water liquid concentration and consequently sintering, some experimental tests have been conducted at 15-30 bar using the slurry reactor set-up. The operating conditions are similar to the previous section: catalyst loading = 5 g, gas flow rate = 210 Nml/min, $H_2/CO = 2$, $T = 220\text{ }^\circ\text{C}$.

Fig. 5.10 shows the evolution of experimental CO conversion with time at three different pressures. Total syngas pressure only slightly affects the initial CO conversion. The identical CO conversion at different pressures is expected as the reaction rate is governed by the reactants concentrations in the liquid phase and not in the gas phase. Indeed the hydrogen and carbon monoxide are poorly soluble components in the liquid mixture. In addition, as already mentioned in Chapter 2, the Fischer-Tropsch synthesis is not limited by the mass transfer as it is proposed to operate in the chemical regime under these conditions.

However the deactivation profile is found to be influenced by the total pressure. Fig. 5.10 shows that a higher deactivation rate is obtained once the pressure is higher, probably because it increases the water concentration in the liquid phase which could result in an accelerated crystallite growth and/or cobalt oxidation.

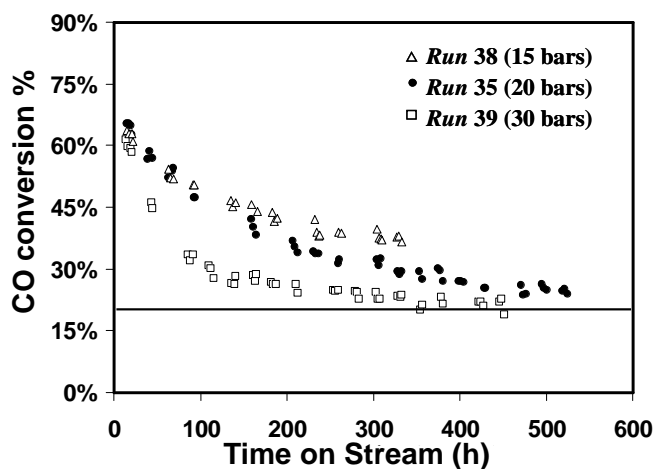


Figure 5.10 Effect of total syngas pressure on experimental catalyst activity in a completely stirred tank reactor (CSTR) (15%Co/Al₂O₃ catalyst, $T = 493\text{ K}$, $H_2/CO = 2.1$, $GHSV = 9.4 \times 10^5\text{ Nml}/(\text{mol}_{\text{Cobalt}} \cdot \text{h})$)

Fig. 5.11 shows the calculated and experimental profiles of CO conversion under three different syngas pressures. As it has been already shown that the set 2 model could give a better image of the deactivation profile, it is the only model used to fit the experimental data.

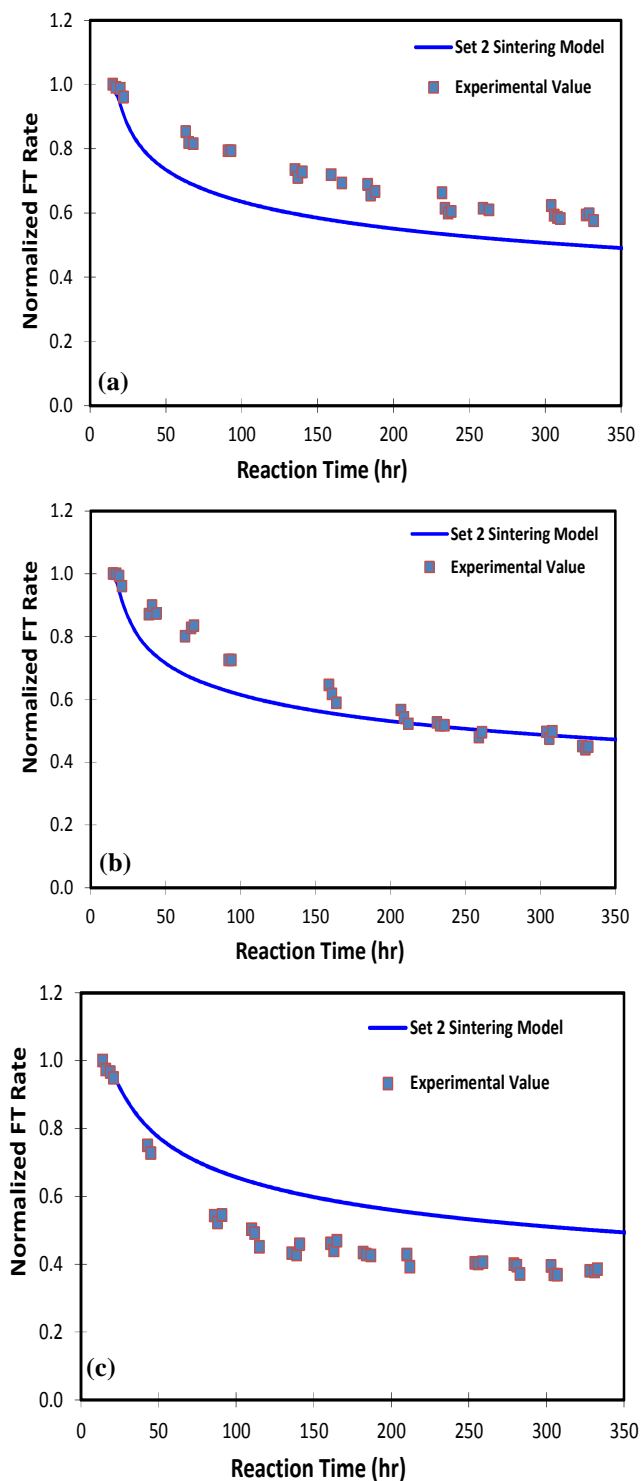


Figure 5.11 Experimental and calculated CO conversion in a slurry reactor (15%Co/Al₂O₃ catalyst, T = 493 K, H₂/CO = 2.1, GHSV = 9.4×10⁵ Nml/(mol_{Cobalt}·h)) at 15 bar (a), 20 bar (b) and 30 bar (c)

Although the simulations are able to represent the experimental CO conversion profile at 20 bar, the slurry model seems to deviate from the experimental data at higher or lower pressures. The most probable reason is that the effects of pressure on the liquid fugacity of different components and specially that of water are not well established in our developed reactor model. Indeed, the total pressure increases the solubility of the certain components in the liquid phase including water, which has a crucial role in the modified catalytic activity.

As already stated, we use the Henry's law for the water VLE in the reactor model which is the suggested to be the closest model which could give the equilibrium water composition in the liquid and gas phases. However it seems that the Henry's law is not well adapted in this case. Further sophisticated thermodynamic model should be applied which could represent the VLE in a more realistic way. In this way, one could improve the fit between the simulated and experimental deactivation profiles at high and low pressures.

5.4.1.3. Slurry reactor model with sintering and coking

The coking contribution has been added to the "set 1 sintering model" in order to evaluate the effect of coking on the catalyst deactivation in slurry reactor. The coking mechanism is described in Chapter 3 and the coking constant used in this section (k'_{CF}) is given in Table 5.1.

The operating conditions for the experimental run simulated here are as follows: catalyst loading = 5 g, gas flow rate = 210 Nml/min, $H_2/CO = 2.1$, $T = 220\text{ }^\circ\text{C}$, $P = 20\text{ bar g}$. Fig. 5.12 shows the simulation and experimental CO conversion curves using set 1 sintering model, set 2 sintering model and set 1 sintering model with coking.

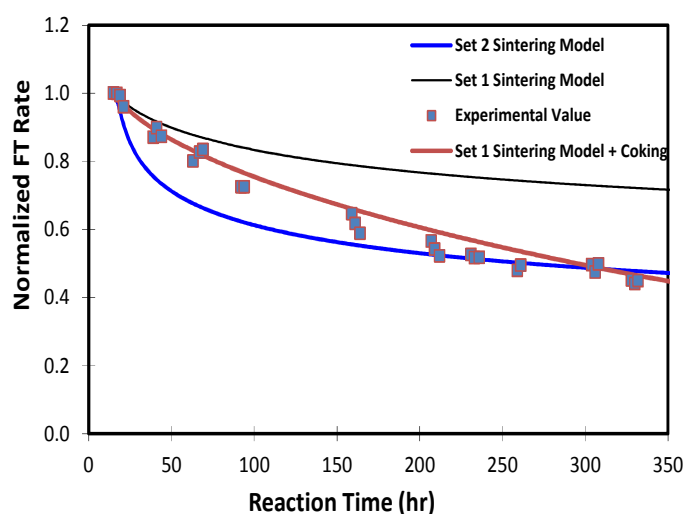


Figure 5.12 Experimental and calculated CO conversion in a slurry reactor (15%Co/Al₂O₃ catalyst, $T = 493\text{ K}$, $P = 20\text{ bar}$, $H_2/CO = 2.1$, $GHSV = 9.4 \times 10^5\text{ Nml}/(\text{mol}_{\text{Cobalt}} \cdot \text{h})$)

As Fig. 5.12 demonstrates, the set 1 sintering model + coking model seems to fit better the experimental CO conversion at least in this typical run. The results are coherent with the literature [1] where the sintering contribution is limited to the first 100 hours and the set 1 sintering model seems to level off at this stage. The contribution of coking mechanism then reduces the catalyst activity in the long-term close to the values observed by the experimental data. Further analysis of the combined sintering-coking models is possible in order to optimize both the sintering and coking constants and to model the deactivation in other operating conditions within the slurry reactor.

5.5. Concluding remarks

The deactivation behavior of the cobalt supported catalysts in continuously stirred tank reactors (CSTR) is studied. The main emphasis is put on the sintering as the main deactivation mechanism. According to the literature [1] crystallite growth could last up to 4-5 days in industrial slurry Fischer-Tropsch bubble column reactors.

As the reactor involves a three-phase mixture where the catalyst particles are dispersed within the liquid phase, the previously developed correlation proposed for crystallite growth is corrected using the water and hydrogen concentration in the liquid phase as the surface oxidation reaction takes place in the liquid-solid interface. The sintering constant is therefore corrected using the Henry's constant to balance the difference between the concentrations in the gas and liquid mixtures. The sintering constant is therefore calculated to be much lower for the same catalyst in the CSTR than in the FBR due to the differences in the solubilities of hydrogen and water in the liquid phase. This might explain why the sintering time is longer in CSTR and could last up to 5 days in typical tests.

Once the corrected correlation for predicting the rate of crystallite growth with time is established, it is used in the "reactor" model to simulate the catalytic activity once the catalyst is exposed to different operating conditions.

As the sintering constant has been determined for the reference catalyst in fixed bed reactors, the first part of this chapter deals with "simulated runs" where only simulation is considered to study the behavior of reference 25%Co/Al₂O₃ catalyst in slurry reactor. We use the reference 25%Co/Al₂O₃ for such a study in order to compare the deactivation behavior of the same catalyst in two different reactor configurations (i.e. slurry and fixed bed reactors). The characteristic sintering time is found to be much longer in slurry than fixed bed reactors for the same catalyst. This is explained by a much lower sintering constant for the same

catalyst in the slurry than in the fixed bed reactor, although the $\text{H}_2\text{O}/\text{H}_2$ concentration in the liquid phase is higher in the liquid phase than in the gas phase. Table 5.2 lists the sintering constants in fixed bed and slurry reactors.

Similar to the fixed bed reactor, the operating conditions are then modified in the “simulated runs” to find the sensible parameters for the catalyst deactivation. It is found that the syngas ratio could affect the sintering and deactivation although the change in the final normalized conversion is not significant once the H_2/CO ratio is changed from 1.5 to 4. At the same carbon monoxide initial conversion, the sintering is more pronounced in the tests with lowest syngas ratio. At the same GHSV, higher H_2/CO ratio in syngas lead to more significant sintering. Both cases seem to deliver a high $\text{H}_2\text{O}/\text{H}_2$ concentration ratio in the liquid phase and a high crystallite growth rate. This is coherent with sintering in fixed bed reactors. In addition, the co-fed water is shown to accelerate sintering even if added in small amounts. Water added by a ratio of $\text{H}_2\text{O}/\text{H}_2/\text{CO} = 1/2/1$ could lead to 100% crystallite size increase which leads to a dramatic catalytic loss when compared to the case of dry syngas. This size increase is much more pronounced when compared to the effect seen in fixed bed reactors. The co-fed water is found to increase the water relative and absolute liquid concentration to at least twice the values calculated in the absence of added water. Consequently the water has the higher effect in the predicted rate of crystallite growth as it increases the CoO surface coverage in short term.

Once the effect of operating conditions on the CSTR model is studied, “real experimental tests” using a commercial 15%Co/ Al_2O_3 catalyst are performed in an experimental slurry reactor to validate and to fit the model. As the catalyst used in the experimental reactor is different from the one used in fixed bed reactors (i.e. reference catalyst), a new set of kinetic and deactivation constants is required. Although the kinetic terms are optimized based on the initial CO conversions (Table 5.1), the choice of sintering constants is challenging.

Two sintering models are therefore proposed for experimental test of industrial catalyst in slurry reactor. In the set 1 sintering model, a sintering constant identical to the value used for the reference catalyst is assumed for the industrial catalyst. This constant is found not to be able to fit the experimental data. Then the set 2 sintering model is proposed which uses an optimized sintering constant for the industrial catalyst. The value for the sintering constants in both models is given in Table 5.1.

The use of both set 1 and 2 models allows comparing the sintering behavior of the reference 25% Co-based and the industrial 15% Co-based catalysts in slurry reactor. It has

been therefore suggested that the industrial 15%Co/Al₂O₃ catalyst is more sensitive to the sintering than the reference one as the fitted value used for the sintering constant in the set 2 model is 4 times higher than the value in the case of reference catalyst in the set 1 model. The set 2 sintering model is also found to be able to predict the full deactivation profile in several experimental cases. The wax replacement process is also predicted by the model and it is suggested that the FT products replace the initial paraffinic solvent in ~15 days with a shifted average carbon number from 33 to 22.

In agreement with the “simulated runs”, the “real experimental runs” suggest that the syngas ratio has a smaller effect on the rate of catalyst deactivation. Indeed the syngas with a H₂/CO = 4 at constant gas flow rate shows only 10% difference in deactivation rate with the case of H₂/CO = 1.5. However the total syngas pressure could modify the experimental deactivation curve although the initial CO conversion is not much. The change in the deactivation profile with pressure could not be easily fitted with the proposed slurry model which is basically due to unsuitability of the use of Henry’s law to predict the vapor-liquid equilibria for several components including water. In fact the high pressure could increase the water content in the liquid phase and consequently a higher deactivation rate, although such an effect is not well represented in our model. Consequently the improvement of the thermodynamic model could be considered in the perspective works.

In addition, it has been shown that the combination of sintering and coking for the long-term catalyst decay could still enhance the quality of deactivation model fit with the experimental data. The addition of this mechanism to further analysis of deactivation in slurry reactors is therefore recommended in the future studies.

5.6. References

- [1] A.M. Saib, D.J. Moodley, I.M. Ciobîcă, M.M. Hauman, B.H. Sigwebela, C.J. Weststrate, J.W. Niemantsverdriet, J. van de Loosdrecht, Fundamental understanding of deactivation and regeneration of cobalt Fischer–Tropsch synthesis catalysts, *Catalysis Today*, 154 (2010) 271-282.
- [2] J. Anfray, Acquisition de données pour la modélisation d’une colonne à bulles Fischer-Tropsch, in, University of Lyon, 2005.

CHAPTER

6

CONCLUSION AND PERSPECTIVES

6.1. Introduction

The current thesis focuses on the deactivation behavior of cobalt-based catalysts under typical Fischer-Tropsch synthesis conditions. The main objective is to find the mechanistic approaches which could explain the experimentally observed activity decline with time.

The thesis starts with a bibliographic review of the Fischer-Tropsch synthesis, including the typical industrial processes and catalysts, kinetic and thermodynamic aspects of the process, as well as the deactivation aspects. Several deactivation mechanisms are presented including poisoning, cobalt oxidation, sintering, coke deposition, and metal-support interactions. The few existing deactivation models are then presented which include either microscopic or macroscopic models.

The second chapter gives the details of the methodology and tools employed in the thesis to study the FT catalyst deactivation. The experimental setups used for testing the cobalt-based catalysts are detailed and the choice of experimental protocol and catalyst is explained. The data treatment is explained using the gas chromatography (GC) and the effect of the residence time distribution on the catalytic activity is discussed. The reactor models for both the fixed bed and slurry reactor are developed and the effect of the condensers on the apparent catalytic activity is investigated.

The proposed mechanistic models for deactivation are later presented at the catalyst scale. Both sintering and coking models are developed to account for initial and long-term activity loss. The sintering is proposed to be accelerated by water through the intermediate step of surface oxidation which is supported by both characterization and thermodynamic techniques. The coking or carbon deposition mechanism is also suggested to cause irreversible active site poisoning especially in higher temperatures.

The microscopic models are then integrated in the reactor models to study the effect of operating conditions on the rate of deactivation in both fixed bed and slurry reactors. The effect of syngas ratios, syngas dilution by either inert or co-fed water, temperature, and pressure are studied. The experimental tests provide the necessary tools to validate and fit the simulation results and to optimize the models.

The following sections represent the main conclusions of the thesis as well the perspective proposed for future works.

6.2. General conclusions

As already explained, this work is aimed at explaining the deactivation behavior of the cobalt catalyst once exposed to syngas under typical FT conditions. The quantitative mechanistic correlations are therefore proposed for both initial and long term activity decline. However the main emphasis is put on sintering as the main source of initial deactivation as this is proposed by several authors in the literature although the causes of long-term deactivation are quite contradictory. In addition, the availability of in-situ characterization tools including synchrotron-based radiation in the initial stage of Fischer-Tropsch synthesis allows the catalyst properties to be followed as a function of time. .

Sintering is therefore studied in a comprehensive manner in this thesis. Sintering is driven by the thermodynamic reasons as larger crystallites have a lower surface energy and therefore a higher thermodynamic stability. The cobalt crystallite growth is suggested to be accelerated by the water produced during FT synthesis. The production of surface cobalt oxide is suggested from thermodynamic calculations at typical FT conditions. The produced CoO layer helps to reduce both the surface energy and increase the mobility of small Co crystallites and consequently increases the rate of sintering. The particle growth is suggested to proceed through a Particle Migration and Coalescence (PMC) type as the particle dispersion evolution during sintering could be correlated using a Generalized Power Law Expression (GPLe) and the particle size distribution during/after sintering follows a Log-Normal Distribution Function (LNDF).

The proposed sintering mechanism involves therefore an initial stage of surface oxidation follows by the main steps of PMC mechanism including crystallite diffusion through the support pores, crystallite collision, and agglomeration. The larger crystallites formed are finally reduced to metallic cobalt as the surface oxidation is supposed to be reversible under typical FT conditions. This mechanism therefore allows investigating the effect of water through a quantitative correlation for crystallite growth. The correlation suggests that the crystallite sintering is driven by the water-to-hydrogen partial pressure ratio (or liquid concentration ratio in the case of slurry reactors) and consequently higher sintering is expected in any conditions that favor a higher H_2O/H_2 ratio.

Catalyst coking is also suggested to occur at longer periods on stream, especially when the temperature is sufficiently high for irreversible carbon deposition on the surface. The change in the active sites is therefore described by a differential equation where the relative

partial pressures (or liquid concentrations in the slurry reactor) of CO, H₂O, and H₂ are involved.

The effect of both sintering and coking on catalytic activity are then incorporated in the FT reaction rate modified expression which involves the average crystallite size and the fraction of free active sites. The developed expression is later used in the reactor models for both fixed bed and slurry reactors to study the effect of different parameters on the catalyst deactivation.

The following sections discuss how the operation conditions and reactor geometry could affect the deactivation behavior of Fischer-Tropsch catalyst.

6.2.1. Effect of operating conditions on catalyst deactivation

Syngas ratio is found to affect sintering as any change in the inlet syngas mole fraction leads to a modified effluent composition and especially the relative H₂O/H₂ molar ratio, which could in turn change the crystallite growth and sintering rate. Simulations are therefore conducted with modified syngas ratios in a capillary-fixed bed reactor either at constant initial CO conversion or constant gas space velocity. Simulations indicate that the highest syngas ratio could cause the highest deactivation rate once operated at constant GHSV as the H₂O/H₂ partial pressure ratio is sufficiently high in this case once compared to lower syngas ratios (0.37 for H₂/CO = 4, 0.09 for H₂/CO = 1.5), although the change in deactivation rate is not significant in the range of H₂/CO = 1.5-2. On the other hand, the syngas with the lowest ratio produces the highest rate of initial deactivation when injected to the FT reactor at constant initial conversion of 58% again due to higher P_{H₂O}/P_{H₂} ratio in this case (2.58 for H₂/CO = 1.5, 0.22 for H₂/CO = 1.5). The effect of syngas ratio on the sintering rate is similar in both fixed bed and slurry reactors as shown in Chapter 5. "Pure simulation runs" are considered with the same reference 25%Co/Al₂O₃ catalyst in order to study the effect of reactor geometry on the deactivation behavior of the same catalyst in both reactors. The same sintering constant obtained in the fixed bed reactor is therefore used in the simulations, corrected by the solubility effects. Sintering period is found to be longer for the same catalyst in slurry reactor than in the fixed bed one. The calculated crystallites growth range in constant initial conversion regime is 6 - 12 nm for H₂/CO = 1.5 and 6 - 8.2 nm for H₂/CO = 4 during the first 300 h on stream in slurry reactor. The Co crystallites exposed to syngas at constant space velocity however grow from 6 nm to 9.3 nm for H₂/CO = 4 and to 8.2 for H₂/CO = 1.5, again in slurry reactor.

The syngas dilution with an inert gas is found not to affect the deactivation profile of the reference catalyst even when added in high contents. The syngas dilution at constant H_2/CO ratio lowers the absolute CO and H_2 partial pressure within the reactor and consequently the water absolute partial pressure in fixed bed reactor. However the relative water partial pressure is found to be identical to the case where the non-diluted syngas is used. Consequently the crystallite growth rate is not modified upon inert dilution and consequently the deactivation profile is kept the same. Similar effect is predicted for the slurry reactor.

The co-fed water is found to have a significant effect on the deactivation profile of cobalt catalysts in both fixed bed and slurry reactors. Simulations are performed with water added to the inlet syngas either at constant initial conversion in fixed bed reactors or constant gas space velocity in slurry reactors. In both cases the catalyst deactivation is accelerated. The added water induces a higher absolute and relative water partial pressure within the reactor, which results in a higher deactivation rate due to crystallite growth. The cobalt particle size in the reference catalyst with 25% cobalt loading increases from 6 to more than 9 nm in the presence of co-fed water after 300 min of the reaction in the case of capillary fixed-bed reactor. The calculations show that particles grow from 6 nm to 12 nm in size when exposed to a co-fed water syngas after 350 h inside the slurry reactor through the use of “pure simulated runs”.

6.2.2. Effect of reactor configuration on deactivation profile

The effect of reactor configuration on the catalyst deactivation behavior is also studied with an aim of understanding the influence of the reactor setup on the activity decline with time in a quantitative manner.

As already explained in section 6.2.1, the effect of operating condition on the initial deactivation rate is similar in both fixed bed and slurry reactors. Higher syngas ratios in constant gas space velocity, lower syngas ratios in constant initial CO conversion, and the presence of co-fed water in the syngas, are the three factors that lead to a higher sintering rate.

Different hydrodynamics of the FBR and CSTR is believed to be the main reason responsible for their different deactivation behavior and sintering time.

In addition to the reactor configuration, the reactor scale is also found to affect the catalyst deactivation. Both capillary and millimetric fixed bed reactor are considered. The respective bed lengths are 9 mm and 16 cm (in the non-diluted catalyst configuration). The

simulation results in line with experimental data suggest that sintering lasts longer in millifixed bed reactor. Cobalt crystallites growth is limited to the first 100 min on stream for capillary reactors. The crystallites also exhibit a size gradient from the inlet to the outlet when the bed is sufficiently long.

The effect of condensers on the apparent observation of the catalytic activity is also investigated. The hot and cold condenser located downstream of the FT reactor could lead to some experimental artifact reading of CO conversion as measured by the GC. The initial filling of the condensers with pure syngas during the syngas ratio stabilization phase gives a time delay in the FT conversion observation by the GC which is not a characteristic of the reaction. Consequently an initial apparent boost (or so-called the induction period) is observed by the GC spectra corresponding to the gas replacement period inside the condensers by the reactor effluents (products). The induction period is a function of the relative reactor/condensers volume, the syngas flow rate, temperature and pressure. A detailed Residence Time Distribution (RTD) is therefore performed to study the effect of condensers. The millimetric fixed bed reactor configuration is found to be the most affected setup by the induction period basically due to the large difference in reactor/condenser volumes (reactor volume = 1 mL, condensers overall volume = 600 mL). Consequently the condensers are incorporated in the full FT process modeling and the apparent conversion profile is fitted with the simulation findings. It is found that although it cannot be seen by the GC spectra the initial conversion at the reactor outlet could be higher than the maximum observed conversion and the sintering principally occurs in the first stages of the reaction although it might be overlooked by referring to the GC results.

6.3. Perspectives

The current thesis should be considered as the first step in understanding the fundamental steps of catalyst deactivation during Fischer-Tropsch synthesis. The complexity of the subject requires further analysis both from experimental and modeling points of view.

As the catalyst deactivation is a characterization-oriented subject, further catalyst characterization tools are essential in improving our understanding at catalyst scale. The readiness of advanced in-situ characterization tools such as synchrotron radiation and magnetic measurement help to follow the crystallite size with time under different FT conditions. The use of high pressure X-ray photoelectron spectroscopy (XPS) could reveal

important information about the surface evolution during Fischer-Tropsch synthesis. High-resolution microscopy is another powerful tool which allows comparing particle size distribution and morphology once exposed to syngas.

The fundamental *ab-initio* studies should be also developed as a tool to predict the extent of surface oxidation as under different water partial pressures. The Density Functional Theory (DFT) methods could be coupled with the thermodynamic calculation to predict the conditions which are prone to surface oxidation. Cobalt oxidation still remains a challenging issue in Fischer-Tropsch synthesis and therefore further investigations are required in this field.

The modified product selectivity with deactivation is another challenge to explore in future works as this could affect the process productivity and economic aspects. The interactions between the catalyst activity and selectivity should be analyzed and the mechanistic models that could explain the modification in catalysts selectivity with time could be derived. The change in catalyst selectivity with time should be considered in different reactor configurations.

The effect of catalysts properties (morphology, initial crystallite size, active metal content, preparation methods) are further areas to investigate. Characterization tools and modeling study could improve our insight in the catalyst-catalytic activity relations. Such a study could also propose solutions to limit the deactivation by using enduring catalyst samples.

APPENDIX

A

LIST OF CATALYTIC TESTS

A.1. List of FT tests in capillary fixed bed reactor

Table A.1 Overview of performed catalytic tests in capillary-fixed bed reactor (P = 20 bar)

Reference	GHSV, Nml/(mol _{Cobalt} ·h)	T (°C)	H ₂ /CO ratio	X _{CO} (%)
H. Karaca (10 mg catalyst)	5.5×10 ⁶	220	2:1	59.7 (t = 0 min) 18.5 (t = 375 min)

A.2. List of FT tests in millimetric fixed bed reactor

Table A.2 Overview of performed catalytic tests in milli-fixed bed reactor (P = 20 bar)

Reference	GHSV, Nml/(mol _{Cobalt} ·h)	T (°C)	H ₂ /CO ratio	X _{CO} (%)	S _{CH₄} (%)	S _{CO₂} (%)
J. Hong (0.3 g non- diluted catalyst)	1.6×10 ⁶	220	1:1	38.5 (t = 22.3 h) 29.0 (t = 101 h)	4.6 (t = 22.3 h) 5.6 (t = 101 h)	0.2 (t = 22.3 h) 0.2 (t = 101 h)
	3.1×10 ⁶	220	2:1	52.9 (t = 9.5 h) 29.5 (t = 101 h)	8.5 (t = 9.5 h) 10.5 (t = 101 h)	0.1 (t = 9.5 h) 0.1 (t = 101 h)
	6.2×10 ⁶	220	4:1	79.8 (t = 5.6 h) 38.6 (t = 48 h)	16.5 (t = 5.6 h) 18.5 (t = 48 h)	0.1 (t = 5.6 h) 0.1 (t = 48 h)
	6.2×10 ⁶	240	2:1	72.4 (t = 6.5 h) 45.6 (t = 55.5 h)	12.1 (t = 6.5 h) 12.2 (t = 55.5 h)	0.5 (t = 6.5 h) 0.2 (t = 55.5 h)
S. Chambrey (0.5 g non- diluted catalyst)	3.0×10 ⁶	280	2:1	99.8 (t = 19 h)	28.9 (t = 19 h)	13.5 (t = 19 h)
	5.8×10 ⁶	280	2:1	96 (t = 2 h)	28.1 (t = 2 h)	12 (t = 2 h)
	1.2×10 ⁷	280	2:1	60.8 (t = 4 h)	27.9 (t = 4 h)	4.1 (t = 4 h)
S. Chambrey (0.1 g non- diluted catalyst)	1.8×10 ⁷	280	2:1	78.6 (t = 16 h)	20.5 (t = 16 h)	0 (t = 16 h)
	3.5×10 ⁷	280	2:1	55.7 (t = 1.1 h) 0 (t = 23.7 h)	20.8 (t = 1.1 h) 0 (t = 23.7 h)	1.7 (t = 1.1 h) 0 (t = 23.7 h)
S. Chambrey (0.1 g diluted catalyst in 0.4 g SiC)	3.5×10 ⁷	280	2:1	65.3 (t = 2h)	31.4 (t = 2h)	8.1 (t = 2h)
	7.1×10 ⁷	280	2:1	40.0 (t = 0.5 h) 0 (t = 19 h)	20.5 (t = 0.5 h) 0 (t = 19 h)	2.1 (t = 0.5 h) 0 (t = 19 h)
S. Chambrey (0.05 g diluted catalyst in 0.45 g SiC)	2.0×10 ⁷	260	2:1	42.0 (t = 4.9 h) 21.6 (t = 20.4 h)	15.5 (t = 4.9 h) 16.9 (t = 20.4 h)	0.5 (t = 4.9 h) 0 (t = 20.4 h)
	2.0×10 ⁷ In-situ Regeneration (350°C)	260	2:1	4.5 (t = 1 h) 7.4 (t = 4.5 h)	0 (t = 1 h) 14.3 (t = 4.5 h)	0 (t = 1 h) 0.3 (t = 4.5 h)
S. Chambrey (0.05 g non- diluted catalyst)	1.9×10 ⁷	260	2:1	88.1 (t = 6.0 h) 0 (t = 32.2 h)	62.3 (t = 6.0 h) 0 (t = 32.2 h)	19.6 (t = 6.0 h) 0 (t = 32.2 h)
	1.9×10 ⁷	260	2:1	84.7 (t = 4.9 h) 6.3 (t = 32 h)	61.5 (t = 4.9 h) 17.6 (t = 32 h)	20.3 (t = 4.9 h) 0.8 (t = 32 h)
	1.9×10 ⁷	250	2:1	75.5 (t = 4.9 h) 0 (t = 40 h)	64.3 (t = 4.9 h) 0 (t = 40 h)	20.0 (t = 4.9 h) 0 (t = 40 h)
	1.9×10 ⁷	240	2:1	69.9 (t = 3.5 h) 0 (t = 43 h)	67.7 (t = 3.5 h) 0 (t = 43 h)	23.1 (t = 3.5 h) 0 (t = 43 h)
S. Chambrey (0.1 g diluted catalyst in 0.4 g SiC)	3.5×10 ⁷	250	2:1	25.6 (t = 1.3 h) 0 (t = 41.3 h)	13.6 (t = 1.3 h) 0 (t = 41.3 h)	0.3 (t = 1.3 h) 0 (t = 41.3 h)
	3.5×10 ⁷	260	2:1	33.6 (t = 1.2 h) 7.3 (t = 22.2 h)	16.3 (t = 1.2 h) 14.0 (t = 22.2 h)	0.5 (t = 1.2 h) 0 (t = 22.2 h)

A.3. List of FT tests in slurry reactor

Table A.3 Overview of performed catalytic tests in slurry reactor

Reference	GHSV, Nml/(mol _{Cobalt} .h)	T (°C)	P (bar)	H ₂ /CO ratio	X _{CO} (%)	S _{CH₄} (%)
S. Piche (5 g catalyst)	9.4×10 ⁵	220	20	2.1 (Run 20)	63.2 (t = 18.5 h) 33.0 (t = 326.5 h)	6.3 (t = 18.5 h) 12.2 (t = 326.5 h)
	9.4×10 ⁵	220	20	2.1 (Run 27)	54.6 (t = 15.0 h) 32.2 (t = 279 h)	5.5 (t = 15.0 h) 9.6 (t = 279 h)
	9.4×10 ⁵	220	20	2.1 (Run 29)	62.9 (t = 18.5 h) 20.1 (t = 617 h)	5.5 (t = 18.5 h) 14.9 (t = 617 h)
	9.4×10 ⁵	220	20	2.1 (Run 30)	65.1 (t = 17.5 h) 51.9 (t = 112 h)	5.9 (t = 17.5 h) 8.2 (t = 112 h)
	9.4×10 ⁵	220	20	2.1 (Run 31)	62.4 (t = 20.5 h) 45.7 (t = 206.5 h)	5.8 (t = 20.5 h) 8.2 (t = 206.5 h)
	9.4×10 ⁵	220	20	2.6 (Run 33)	94.5 (t = 16.5 h) 40.2 (t = 332 h)	17.3 (t = 16.5 h) 11.5 (t = 332 h)
	9.4×10 ⁵	220	20	1.6 (Run 34)	49.5 (t = 15.0 h) 17.1 (t = 473 h)	4.7 (t = 15.0 h) 13.4 (t = 473 h)
	9.4×10 ⁵	220	20	2.1 (Run 35)	65.3 (t = 15.0 h) 15.9 (t = 670 h)	6.5 (t = 15.0 h) 10.6 (t = 670 h)
	9.4×10 ⁵	210	20	2.1 (Run 36)	46.5 (t = 19.0 h) 25.1 (t = 233 h)	6.2 (t = 19.0 h) 10.0 (t = 233 h)
	9.4×10 ⁵	230	20	2.1 (Run 37)	95.0 (t = 13.0 h) 11.7 (t = 495 h)	22.2 (t = 13.0 h) 15.0 (t = 495 h)
	9.4×10 ⁵	220	15	2.1 (Run 38)	63.6 (t = 15.0 h) 38.1 (t = 236 h)	6.9 (t = 15.0 h) 9.2 (t = 236 h)
	9.4×10 ⁵	220	30	2.1 (Run 39)	61.5 (t = 14.0 h) 22.8 (t = 283 h)	4.9 (t = 14.0 h) 15.5 (t = 283 h)

APPENDIX

B

HISTOGRAM ANALYSIS

Table B.1 Details of histogram analysis of fresh and spent catalyst samples

Fresh Catalyst Sample					
min bin diameter (nm)	max bin diameter (nm)	bin size, Δd (nm)	Bin center diameter d_i (nm)	Number of particles in bin, N_i (-)	
1.35	2.70	1.35	2.0	34.0	
2.70	4.05		3.4	370.9	
4.05	5.40		4.7	513.3	
5.40	6.75		6.1	341.5	
6.75	8.10		7.4	165.4	
8.10	9.45		8.8	69.0	
9.45	10.80		10.1	26.8	
10.80	12.15		11.5	10.1	
12.15	13.50		12.8	3.8	
13.50	14.85		14.2	1.4	
14.85	16.20		15.5	0.5	
16.20	17.55		16.9	0.2	
17.55	18.90		18.2	0.1	
Spent Catalyst Sample					
2.57	3.91		1.34	3.2	3.0
3.91	5.25	4.6		29.1	
5.25	6.59	5.9		90.1	
6.59	7.93	7.3		157.6	
7.93	9.27	8.6		199.4	
9.27	10.61	9.9		206.9	
10.61	11.95	11.3		188.8	
11.95	13.29	12.6		157.9	
13.29	14.63	14.0		124.4	
14.63	15.97	15.3		94.0	
15.97	17.31	16.6		69.0	
17.31	18.65	18.0		49.5	
18.65	19.99	19.3		35.0	
19.99	21.33	20.7		24.5	
21.33	22.67	22.0		17.0	
22.67	24.01	23.3		11.8	
24.01	25.35	24.7		8.1	
25.35	26.69	26.0		5.6	
26.69	28.03	27.4		3.9	
28.03	29.37	28.7		2.7	
29.37	30.71	30.0	1.8		
30.71	32.05	31.4	1.3		
32.05	33.39	32.7	0.9		
33.39	34.73	34.1	0.6		

APPENDIX

C

**REACTOR GEOMETRY
AND
CATALYST DEACTIVATION**

In order to study the effect of reactor geometry on the deactivation rate, several simulations are considered all with the same reference 25%Co/Al₂O₃ catalyst.

Sintering was considered as the main deactivation phenomena and a set of different scenarios are considered as described in Table C.1.

Table C.1 List of cases studied for the effect of reactor geometry on deactivation rate

Description	Reactor type	Phase(s) within reactor	X _{CO,i} (%)	GHSV (Nm ³ kg _{cat} ⁻¹ h ⁻¹)	V _{reactor} (mL)	m _{cat} (g)	P _{H₂,i} (bar)	P _{CO,i} (bar)
Case 1	CSTR	gas-liquid	63	0.73	283	10	8.42	4.69
Case 2.1	CSTR	gas	83.7	0.73	283	10	3.35	2.38
Case 2.2	CSTR	gas	82.9	0.73	249	10	3.44	3.73
Case 2.3	CSTR	gas	63	1.43	249	10	6.98	3.61
Case 3	mFBR	gas	54	3.33	0.25	0.3	13.68 (z/L=0) 11.72 (z/L=0.5) 8.78 (z/L=1)	6.71 (z/L=0) 5.90 (z/L=0.5) 4.72 (z/L=1)
Case 4.1	CSTR	gas	54	1.77	283	10	9.10	4.91
Case 4.2	CSTR	gas	54	1.71	4.94	10	9.15	4.94
Case 4.3	CSTR	gas	54	1.73	0.25	0.3	9.19	4.96

Note: i denotes initial condition.

The list of kinetic/deactivation constants used for different cases is also given in Table C.2. Note that the constants are assumed the same for all cases and independent of the reactor type. The phase contribution is also taken into account while considering the gas-liquid CSTR in order to have the same intrinsic coefficients in order to have comparable results for all cases.

Table C.2 List of kinetic/sintering constants used for the effect of reactor geometry on deactivation rate

Description	Kinetic coefficients		Sintering constant k _s (nm ⁷ /hr)
	k _{a,0} (mol/m ³ .hr.Pa ²)	k _b (1/Pa)	
Case 1	6.78 x10 ⁻⁷	1.45 x10 ⁻⁴	1.3 x10 ⁴
Cases 2.1- 2.3	4.581 x10 ⁻⁷	8.341 x10 ⁻⁵	5.1994 x10 ⁴
Case 3	4.581 x10 ⁻⁷	8.341 x10 ⁻⁵	5.1994 x10 ⁴
Case 4.1-4.3	4.581 x10 ⁻⁷	8.341 x10 ⁻⁵	5.1994 x10 ⁴

C.1. Effect of reacting phase within the slurry reactor

As the fixed bed reactor studied in chapter 4 is assumed to work in a gas-phase regime, the first step to compare both reactors is to see the effect of reacting media within a typical slurry reactor. We have therefore defined Case 2.1 as a gas-phase slurry reactor with the same reactor volume and catalytic mass in the reference case (Case 1). Consequently all

the FT products are assumed to be in gas phase in Case 2.1 and the same GHSV is imposed on the system.

C.1.1. Constant GHSV and reactor volume

The results indicate a higher initial conversion for the gas-phase CSTR compared to gas-liquid reactor. This is suggested to be due to the fact that for the three-phase reactor the $H_2 + CO$ mixture is distributed between two phases and only the dissolved syngas reacts on the catalyst surface whereas for the gas-phase CSTR, all the syngas molecules can react on the catalyst surface. The contribution of liquid phase in Case 1 therefore results in an initial conversion value of only 63% compared to 83% for Case 2.1 (completely gas-phase CSTR).

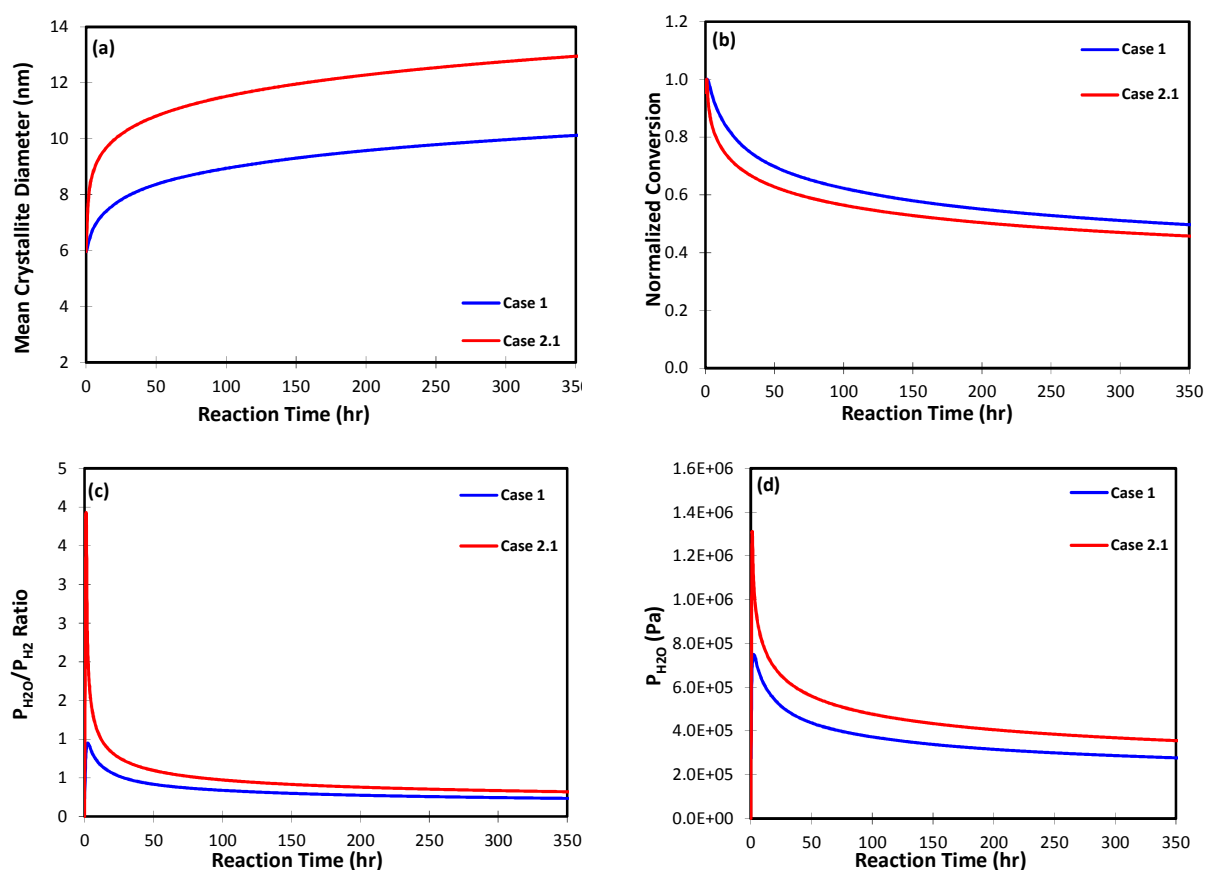


Figure C.1 Evolution of crystallite size (a), normalized CO conversion (b), water to hydrogen pressure ratio (c), and absolute water partial pressure (d) with time at constant gas space velocity and reactor volume for a gas-liquid completely stirred tank reactor (case 1) and a gas-phase completely stirred tank reactor (case 2.1)

As shown in Fig. C.1, a higher activity for the gas-phase CSTR leads to a higher water and lower hydrogen partial pressure within the reactor, thus a much higher H_2O/H_2 partial pressure ratio for the gas-phase CSTR. This leads to a much higher sintering rate which

results in a final crystallite size of about 12.92 nm for the gas-phase CSTR compared a typical value of 10.08 nm for the gas-liquid CSTR.

C.1.2. Constant GHSV and gas volume

As the gas volume is different for gas-phase and gas-liquid CSTRs studied above, case 2.2 is defined where the volume of the reactor is reduced in order to have identical gas volume for both gas-phase and gas-liquid CSTRs. As given in Table C.1 this result in 100% initial conversion once operating with the same space velocity.

Comparing case 2.2 with both case 1 and case 2.1 allows studying either the reacting phase or the reactor volume on the deactivation rate (Fig. C.2).

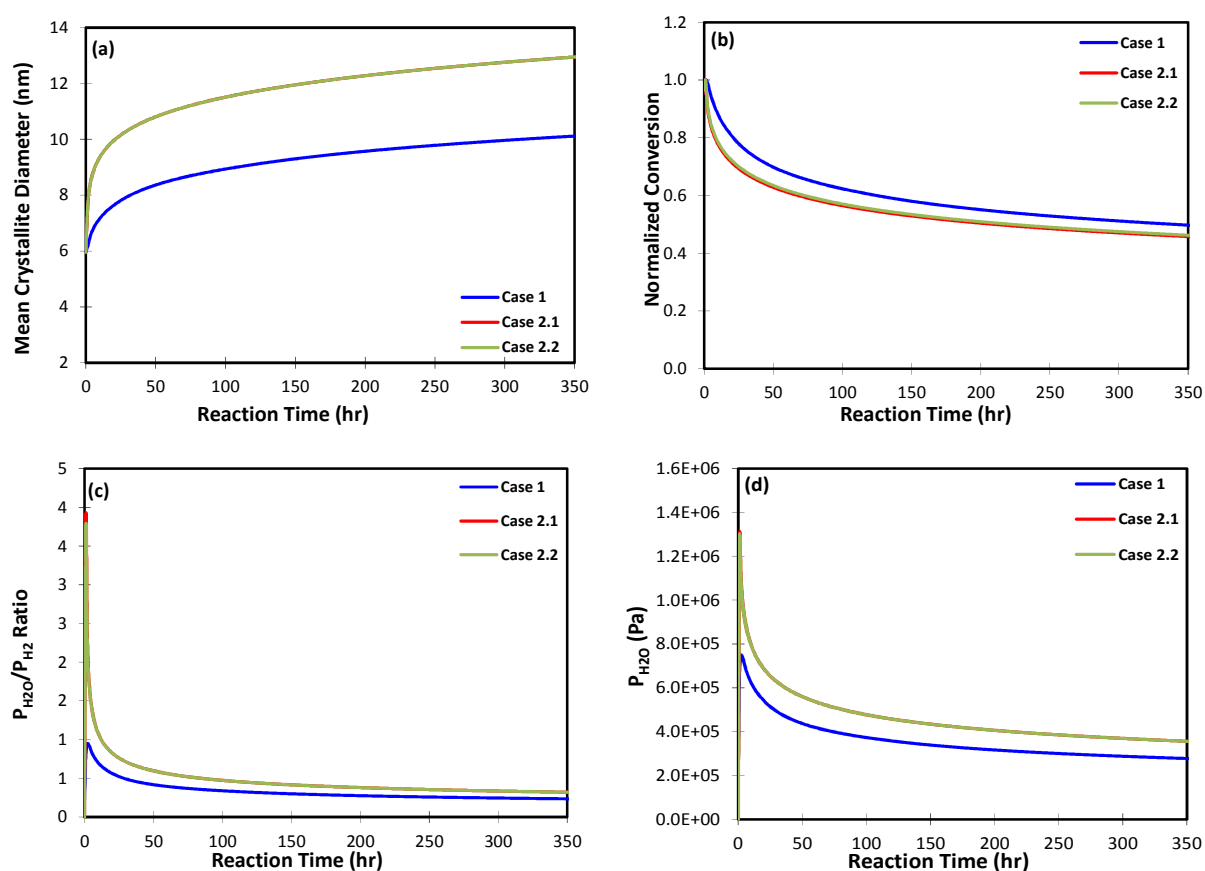


Figure C.2 Evolution of crystallite size (a), normalized CO conversion (b), water to hydrogen pressure ratio (c), and absolute water partial pressure (d) with time at constant gas space velocity for a gas-liquid completely stirred tank reactor (case 1) and a gas-phase completely stirred tank reactor (case 2.1 and 2.2)

As depicted in Fig. C.2, for the same gas-phase CSTR, reducing reactor volume (Case 2.2) does not affect the reactor performance considerably. Indeed a higher volume increases the conversion as shown in Fig.C.3. However in the range of 249 – 289 mL the change is not significant.

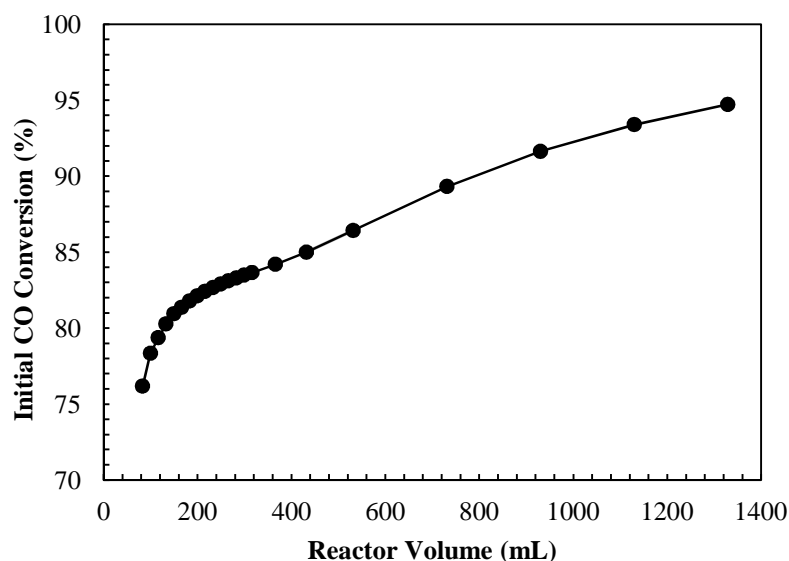


Figure C.3 Effect of reactor volume on the initial CO conversion in a gas-liquid completely stirred tank reactor ($T = 493 \text{ K}$, $P = 20 \text{ bar}$, $\text{GHSV} = 0.725 \text{ Nm}^3 \text{ kgcat}^{-1} \text{ h}^{-1}$, reference catalyst)

While comparing the gas-phase and gas-liquid CSTRs with the same gas volume (Cases 1 and 2.2), similar trends as the ones observed in section C.2 are found: higher initial conversion in the gas-phase CSTR leads to a larger $P_{\text{H}_2\text{O}}/P_{\text{H}_2}$ ratio, which in turn gives higher crystallite size values.

C.1.3. Constant gas volume and conversion

Once the gas volume is adjusted for both the gas-phase and gas-liquid CSTRs, the simulations are followed to have the same initial conversion for the different phases within the reactor and to see how this could change the deactivation curves. Therefore the GHSV used for Case 2.2 is increased to yield an initial conversion of 65% in Case 2.3. Fig. C.4 shows how the change in the space velocity modifies the initial conversion within the gas-phase GHSV.

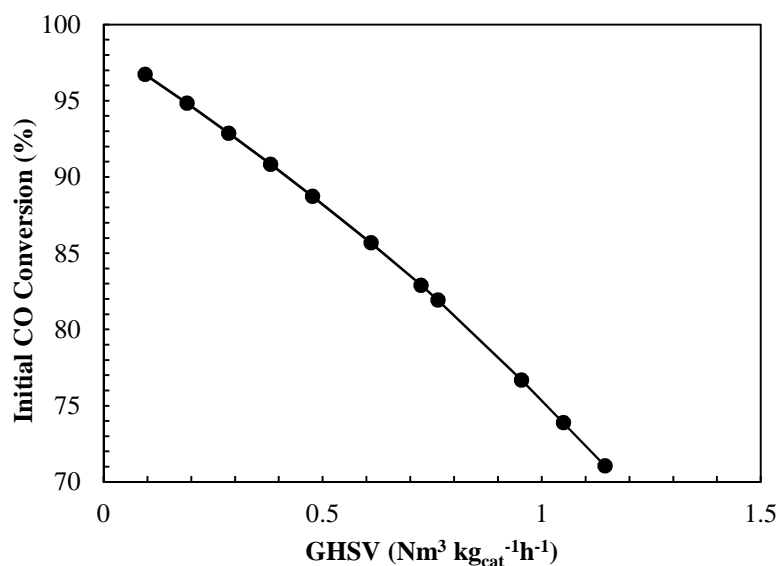
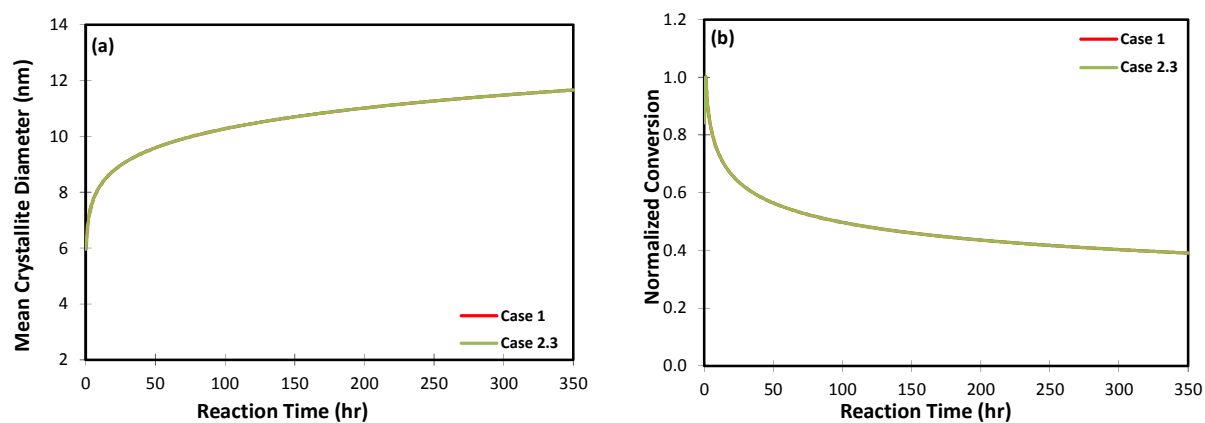


Figure C.4 Effect of gas space velocity on the initial CO conversion in a gas-liquid completely stirred tank reactor (T = 493 K, P = 20 bar, reactor volume = 249 mL, reference catalyst)

Fig. C.5 shows the profile of different parameters for both Cases 1 and 2.3 with time. As expected, the curves superimpose for all the parameters as the kinetics are deactivation constants are corrected for the vapor-phase equilibria in both cases. Therefore we suggest that the reacting phase does not affect the deactivation rate for the comparable conditions.



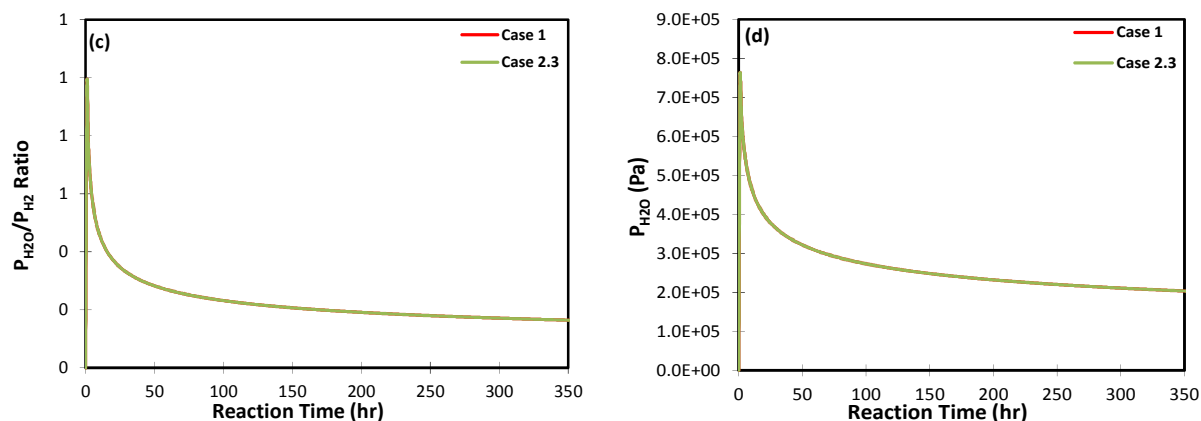


Figure C.5 Evolution of crystallite size (a), normalized CO conversion (b), water to hydrogen pressure ratio (c), and absolute water partial pressure (d) with time at constant gas space velocity and initial CO conversion for a gas-liquid completely stirred tank reactor (case 1) and a gas-phase completely stirred tank reactor (case 2.3)

C.2. Effect of reactor hydrodynamics

Once the effect of reacting phase on the deactivation rate is investigated, the study continues by looking into the reactor hydrodynamics. Consequently we have tried to compare fixed bed and slurry reactors through Case 3 (mFBR) and the 4.1-4.4 (CSTR) as defined in Table C.1.

In this way several scenarios are studied as follows:

C.2.1. Constant initial conversion

The first step to study the reactor behavior on the deactivation rate is to consider the fixed bed and slurry reactor with their typical dimensions and catalyst loading, while operating under the same initial conversion (Cases 3 and 4.1-4.2).

Table C.1 shows that the same initial conversion could be obtained in the fixed bed reactor with a much higher GHSV than in the CSTR.

In general, the lower GHSV in the slurry reactor than in the fixed bed reactor is justified by the difference in the reactor hydrodynamics. This difference has been first investigated by Satterfield in 1985 [1] who suggested that the catalyst activity in the fixed-bed appears to have been moderately higher than in the slurry reactor. Although in an experimental viewpoint, this could be due to an optimal fixed bed catalyst reduction, the reactor hydrodynamic seems to be the dominant factor. The partial pressures of H_2 and CO are much lower in the CSTR than in the fixed bed reactor (especially at the inlet point), as there is no concentration (or partial pressure) profile within the CSTR and the pressures are

instantly reduced to the outlet pressures as soon as the syngas enters the reactor. Consequently, a higher residence time (i.e. lower space velocity) is required to maintain the same (initial) conversion. On the contrary the FBR benefits from a partial pressure profile along the catalyst bed which help to maintain the syngas partial pressure higher at the first part of the bed, and therefore higher GHSV (i.e. lower residence time) could be applied to have similar conversion. Our calculations show that this could be up to twice the GHSV used in a comparable CSTR.

Fig. C.5 gives the variation of initial CO conversion for both a typical mFBR and CSTR as a function of GHSV.

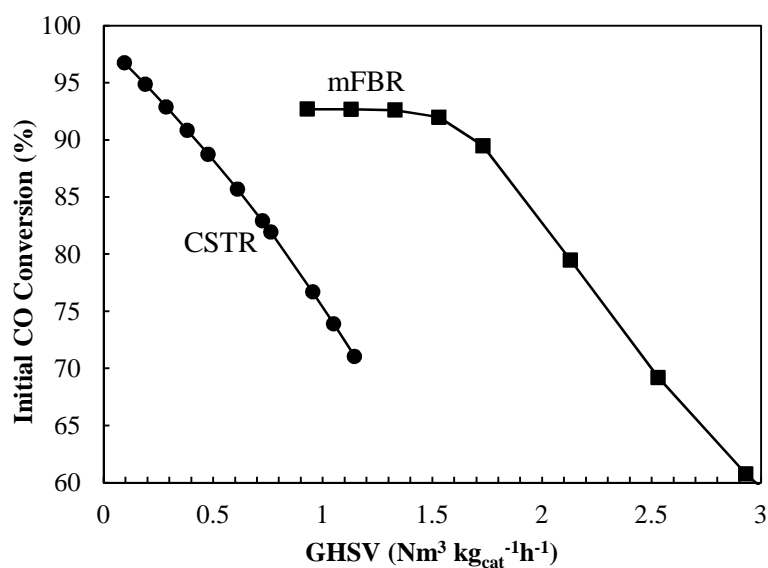


Figure C.5 Effect of gas space velocity on the initial CO conversion in a gas-liquid completely stirred tank reactor ($T = 493$ K, $P = 20$ bar, reactor volume = 249 mL, reference catalyst) and a millimetric fixed bed reactor ($T = 493$ K, $P = 20$ bar, reactor volume = 0.25 mL, reference catalyst)

Fig. C.6 shows the evolution of different reactor parameters with time on stream for Cases 3 and 4.1-4.2. Note that as there is axial profile for all parameters with the mFBR, these parameters are given only at the reactor outlet as this provides an acceptable approach for reactor comparison.

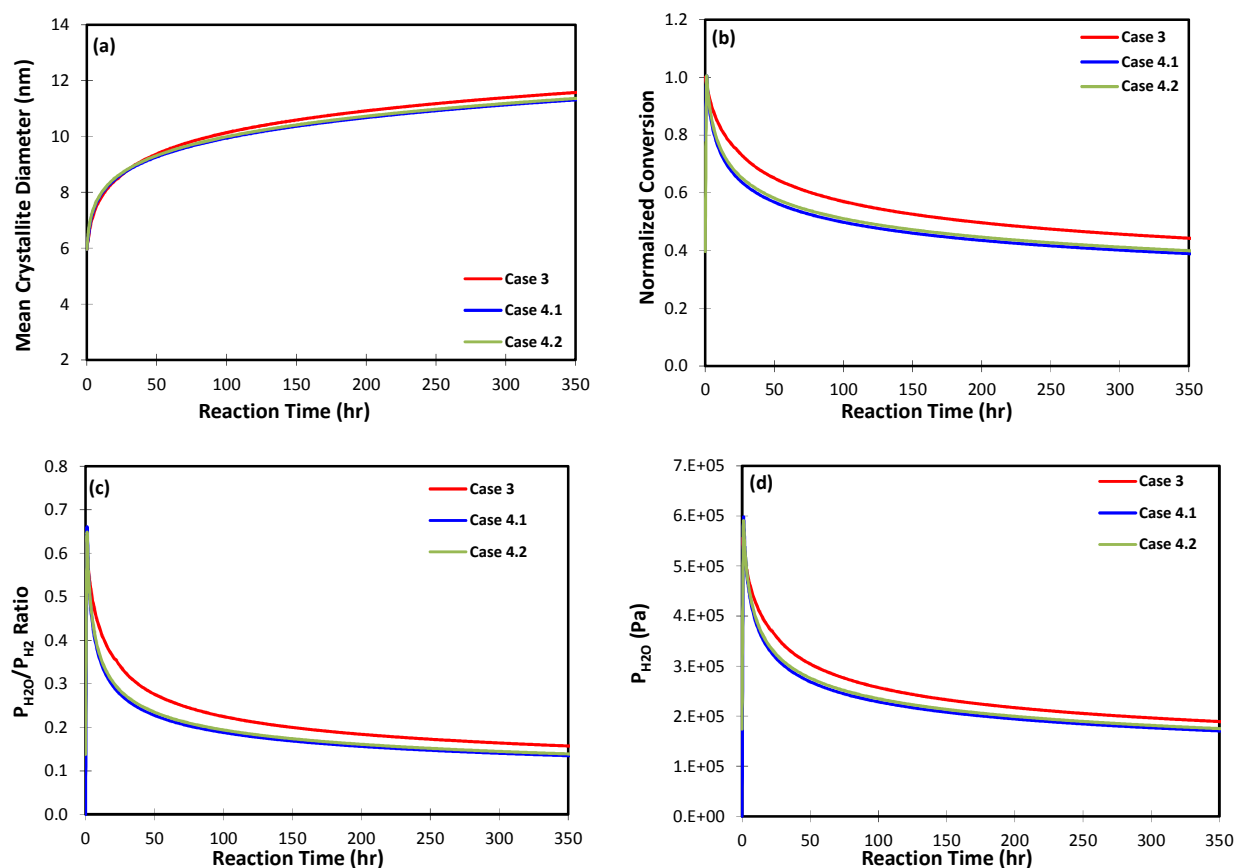


Figure C.6 Evolution of crystallite size (a), normalized CO conversion (b), water to hydrogen pressure ratio (c), and absolute water partial pressure (d) with time at initial CO conversion for a millimetric fixed bed reactor (case 3) and a gas-phase completely stirred tank reactor (cases 4.1 and 4.2)

The results indicate a sharper initial activity decline in the CSTR than in the FBR. This is justified by the reactor hydrodynamics as all the catalyst particles are exposed to the highest water to hydrogen partial pressure in the CSTR, whereas only a fraction of particles at the mFBR outlet are exposed to these conditions. Therefore although the crystallite size curves move in the same directions for both reactors, the effect of sintering on the CO conversion is more pronounced in the CSTR, which in turn reduces the reaction rate much faster and the consequently water absolute and relative partial pressures are lower than the corresponding values found at the mFBR outlet.

It should be also noted that the curves for both Cases 4.1 and 4.2 are superimposed in Fig. C.6. Case 4.2 is the lowest possible reactor volume that could have 10 gr of industrial catalyst. Consequently the CSTR volume again does not play an important role in the range of 4.94 – 283 mL for the deactivation rate.

C.2.2. Constant initial conversion, reactor volume, and catalyst loading

Although the previous section revealed some differences in the deactivation behavior of fixed bed and slurry reactor, the use of “comparable” conditions could better show such a difference in reactor performances.

Consequently we have defined Case 4.3 in which the slurry reactor is modified in a way to have the same reactor volume, reacting phase, catalyst mass and initial CO conversion, as the mFBR defined by Case 3. Note again that the GHSV required maintaining an initial conversion of 54% is two times in the mFBR compared to the CSTR.

Fig. C.7 shows the evolution of different parameters in the two cases (Case 3 and 4.3) as a function of time on stream.

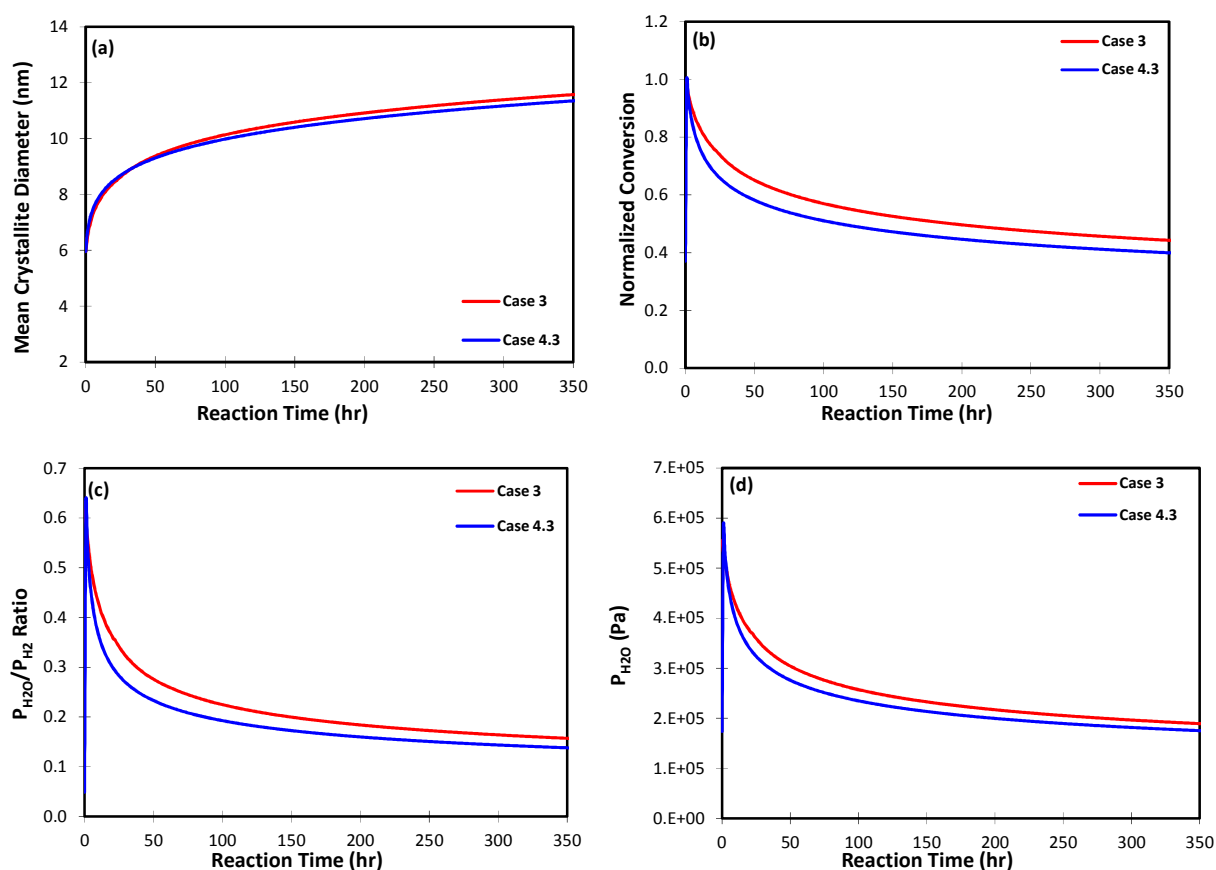


Figure C.7 Evolution of crystallite size (a), normalized CO conversion (b), water to hydrogen pressure ratio (c), and absolute water partial pressure (d) with time at initial CO conversion, catalyst loading and reactor volume for a millimetric fixed bed reactor (case 3) and a gas-phase completely stirred tank reactor (cases 4.1 and 4.2)

These results are coherent with the ones obtained in the previous section. An increased initial activity decline as well as lower water absolute and relative partial pressures are observed for the CSTR although the difference with the mFBR is not significant.

C.2.3. Normal operating conditions

The final step is to compare how the slurry and fixed bed reactors behave under their typical operating conditions (e.g. reactor volume, catalyst mass, reacting phase, GHSV, etc.) although they might be different. This is a good practice as the typical industrial reactors differ in operating conditions depending on their type. Therefore cases 1 and 3 are compared in terms of deactivation rate as Fig. C.8 demonstrates.

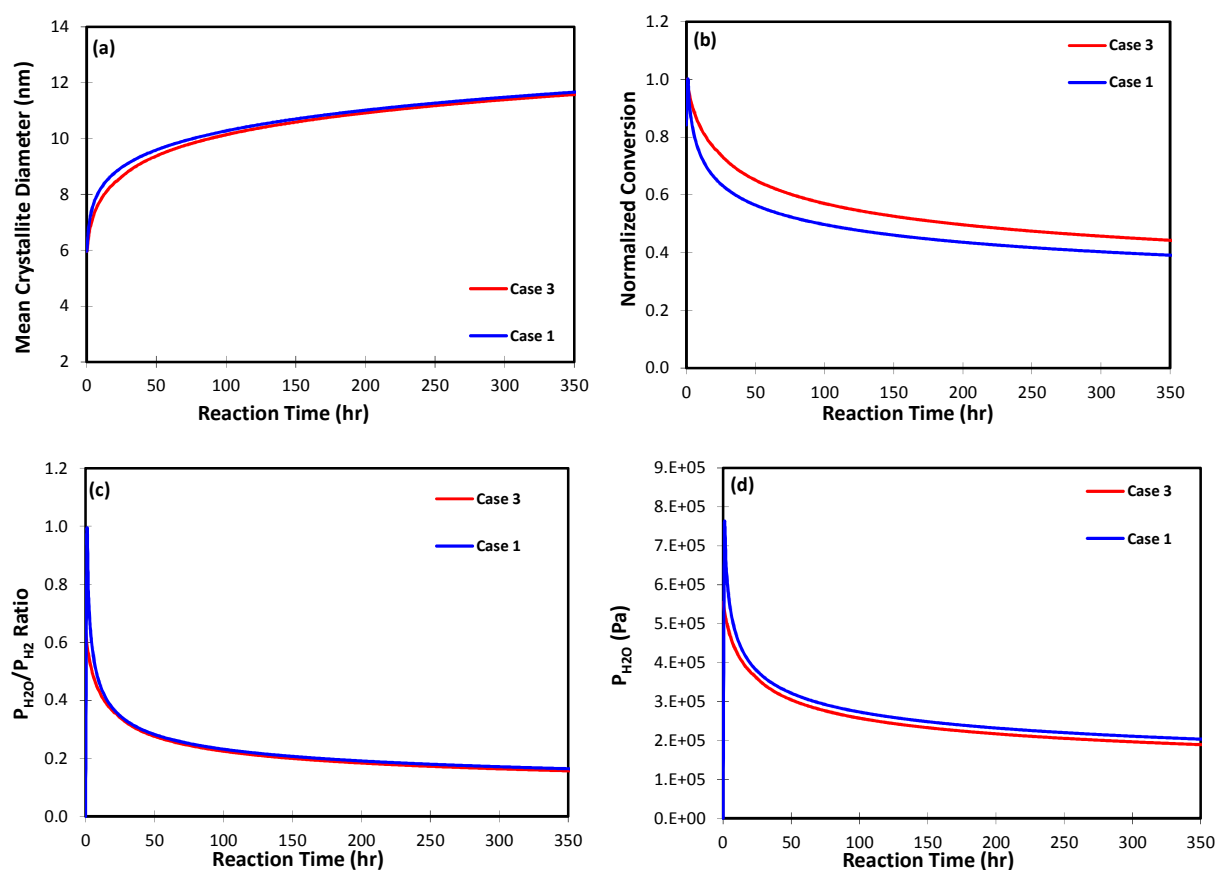


Figure C.8 Evolution of crystallite size (a), normalized CO conversion (b), water to hydrogen pressure ratio (c), and absolute water partial pressure (d) with time for a millimetric fixed bed reactor (case 3) and a gas-liquid completely stirred tank reactor (case 1)

The results indicate similar trends as observed in the previous section. Higher initial deactivation rate in the CSTR compared to the FBR gives a sharper activity decline and a higher crystallite size. However, in the long-term both reactors move in the same direction; although the final crystallite size is slightly larger in the CSTR than in the FBR.

C.3. References

1. Fox, J.M.; Degen, B.D.; Cady, G.; Deslate, F.D.; Summers, R.L.; Slurry Reactor Design Studies. Slurry vs. Fixed-Bed Reactors for Fischer-Tropsch and Methanol: Final Report. DEO Report DE91005752, 1990.